Characterization of NETosis Dynamics in Hypertension and Associated Mechanisms of Renal and Vascular Injury

Chloé Landry

Department of Cellular and Molecular Medicine
Faculty of Medicine
University of Ottawa
Ottawa, Ontario, Canada

January 2026

This thesis is submitted to the University of Ottawa
in partial fulfillment of the requirements for the
Ph.D. program in Cellular and Molecular Medicine

Abstract

Neutrophil extracellular trap (NET) release is an innate immune process involving chromatin extrusion that has been linked to hypertension and associated vascular and kidney injury. However, reliance on endpoint measurements limits mechanistic insight into NETosis regulation and dynamics. To address this, we developed a live-cell imaging assay and semi-automated, CellProfiler-based analysis pipeline for high-throughput quantification of NETosis progression. This pipeline enables single-cell feature extraction and machine-learning–based classification of NETosis stages, allowing quantitative assessment of stimulus- and dose-dependent NETosis dynamics. The approach was validated in neutrophil-differentiated HL-60 cells and primary mouse bone marrow neutrophils and reliably captured responses to common NETosis inducers and pharmacological inhibitors.

We applied this pipeline to an angiotensin II (Ang II)–induced model of hypertension to examine NETosis dynamics across bone marrow and kidney neutrophil compartments. In parallel, the contribution of NETs to renal immune cell recruitment and kidney injury was assessed in Ang II–treated *Padi4*$^{-/-}$ mice. Although NETs did not accumulate in the kidney and did not contribute to blood pressure elevation or overt kidney injury in this model, temporal single-cell analysis revealed stage-specific alterations in NETosis dynamics in male bone marrow and kidney neutrophils, suggesting altered neutrophil priming originating in the bone marrow that does not translate to tissue injury in this context.

Given the established link between NETs and endothelial injury, we next examined the transcriptional response of HUVECs treated with HL-60–derived NETs using bulk RNA sequencing. Pathway and gene set enrichment analyses revealed suppression of G2/M cell cycle regulators alongside upregulation of inflammatory pathways, consistent with activation of a senescence-associated transcriptional program, as supported by Human Universal Senescence Index (hUSI) scoring. Markers of G2/M arrest and senescence were further evaluated in NET-treated HUVECs, with variable support across assays. Together, these findings indicate that NET exposure induces an early senescence-like transcriptional response that precedes, but does not yet manifest as, stable cell cycle exit and bona fide senescence after 24 hours.

Table of contents

List of figures

List of tables

Abbreviations

ACE	Angiotensin II-converting enzyme
ANCA	Anti-neutrophil cytoplasmic antibody
Ang II	Angiotensin II
AUC	Area under the curve
BP	Biological process
CC	Cellular component
CCC	Lin's concordance correlation coefficients
CCNA2	Cyclin A2
CCNB1	Cyclin B1
CCNB2	Cyclin B2
CD3	Cluster of differentiation 3
CDK1	Cyclin-dependent kinase 1
cDNA	Complementary DNA
CitH3	Citrullinated histone H3
CLR	Centered log-ratio
CPA	Cell Profiler Analyst
CXCL12	C-X-C motif chemokine ligand 12
CXCR4	C-X-C motif chemokine receptor 4
DAMPs	Damage-associated molecular patterns
DC	Dendritic cell
DDR	DNA damage response
dHL-60	Differentiated HL-60
DMSO	Dimethyl sulfoxide
ECs	Endothelial cells
ELISA	Enzyme-linked immunosorbent assay
eNOS	Endothelial nitric oxide synthase
ERK1/2	Extracellular signal–regulated kinase 1/2
FBS	Fetal bovine serum
FDR	False discovery rate

GAPDH	Glyceraldehyde-3-phosphate dehydrogenase
G-CSF	Granulocyte colony-stimulating factor
GM-CSF	Granulocyte-macrophage colony-stimulating factor
GO	Gene Ontology
GSDMD	Gasdermin D
GSEA	Gene Set Enrichment Analysis
G2/M	G2 to mitosis
HMGB1	High-mobility box 1
HRP	Horseradish peroxidase
hUSI	Human universal senescence index
HUVECs	Human Umbilical Vein Endothelial Cells
ICAM-1	Intercellular adhesion molecule-1
ICAM-2	Intercellular adhesion molecule-2
ICC	Intraclass correlation coefficient
IFN-α	Interferon-α
IFN-1	Type 1 interferon
IFN-γ	Interferon-γ
IL-10	Interleukin-10
IL-17	Interleukin-17
IL-18	Interleukin-18
IL-1β	Interleukin-1β
IL-8	Interleukin 8
IMDM	Iscove's Modified Dulbecco's Medium
iNOS	Inducible nitric oxide synthase
IQR	Interquartile range
KEGG	Kyoto Encyclopedia of Genes and Genomes
LME	Linear mixed-effects model
LPS	Lipopolysaccharide
MAE	Mean absolute error
MAPK	Mitogen-activated protein kinase
MCM	Minichromosome maintenance

MEK	Mitogen-activated protein kinase kinase
MF	Molecular function
MMP-9	Matrix metalloproteinase-9
MMPs	Matrix metalloproteases
MPO	Myeloperoxidase
mRNA	Messenger RNA
mTORC2	Mechanistic target of rapamycin complex 2
NE	Neutrophil elastase
NES	Normalized enrichment scores
NETs	Neutrophil extracellular traps
NF-κB	Nuclear factor κB
NGAL	Neutrophil gelatinase-associated lipocalin
NLR	Neutrophil-to-lymphocyte ratio
NLRP3	NOD-like receptor family pyrin domain containing-3
NO	Nitric oxide
NOX2	NADPH oxidase 2
PAD4	Peptidylarginine deiminase 4
PCA	Principal component analysis
PERMANOVA	Permutational Multivariate Analysis of Variance
PI3K	Phosphoinositide 3-kinase
PKC	Protein kinase C
PLK1	Polo-like kinase 1
PMA	Phorbol 12-myristate 13-acetate
PR3	Proteinase-3
RAAS	Renin-angiotensin-aldosterone system
RMSE	Root mean square error
ROS	Reactive oxygen species
RT-qPCR	Real-time quantitative PCR
SA-β-gal	Senescence-associated β-galactosidase
SARS-CoV-2	Severe acute respiratory syndrome coronavirus 2
SASP	Senescence-associated secretory phenotype

SBP	Systolic blood pressure
SEM	Standard error of the mean
SIRPα	Signal-regulatory protein α
SLE	Systemic lupus erythematosus
Syk	Spleen tyrosine kinase
TAK1	Transforming growth factor β- activated kinase 1
Th1	T helper 1
Th17	T helper 17
TIMP-1	Tissue inhibitor of metalloprotease-1
TLR	Toll-like receptor
TLR2	Toll-like receptor 2
TLR4	Toll-like receptor 4
TLR9	Toll-like receptor 9
TNF-α	Tumor necrosis factor-α
Tregs	Regulatory T cells
TREX	Three Prime Repair Exonuclease
TREX1	Three Prime Repair Exonuclease1
WB	Western blot
WT	Wild-type

Acknowledgments

This PhD was made possible through the unwavering support and guidance of my supervisor, peers, friends, and family.

First and foremost, I would like to thank my supervisor, Dr. Dylan Burger, who introduced me to research nearly nine years ago and has guided me through the many ups and downs of this journey ever since. Through working alongside him and collaboratively teasing out any (of the many) issues that arose, I developed the way I think about, communicate, and approach science. Thank you, Dylan, for your trust, guidance, and for fostering the confidence that allowed me to grow as a scientist.

I would also like to thank my TAC members for their guidance throughout the years. Their insightful feedback and support have played an important role in shaping this thesis.

I am grateful to Julie (Lihua) and Fengxia for their support, whether through assistance with experiments or by generously answering my many questions. I would also like to thank Liyuan and Chloë at the CBIA Core for teaching me and guiding me through the art of scientific imaging and analysis. Their eagerness to teach and continued support have meant so much.

I am also deeply grateful to my fellow lab members and peers for being alongside me throughout this journey. Whether through joking around or letting me talk through scientific ideas, their presence made all the difference. In particular, I would like to thank Mayra and Rob, who have been with me through it all, and Emma, who joined the lab one year ago and quickly became an integral part of it, for their encouragement, perspective, and most of all, their friendship.

To my friends, Danika and Claudia, who have listened to me talk about my research, helped me prepare scientific presentations, and offered steady emotional support, your encouragement has meant the world to me. I also cannot forget my cat, Ivy, who in her own way provided emotional support and was always by my side through countless hours of writing.

Finally, I would like to thank my parents. Their unwavering trust and support have meant everything to me and made this journey possible.

Chapter 1

General Introduction

1.1 Neutrophils

1.1.1 Origin and Maturation of Neutrophils

Neutrophils are terminally differentiated granulocytes that constitute the predominant population of circulating leukocytes and serve as frontline effectors of the innate immune system (1,2). Their rapid activation and short response time positions them as central players in coordinating ensuing immune responses by modulating both innate and adaptive immunity (1).

Neutrophils are generated in the bone marrow through granulopoiesis, a tightly regulated process that produces approximately 10^{11} cells per day (2). During granulopoiesis, neutrophils arise from hematopoietic stem cells that differentiate into multipotent progenitors and subsequently into lymphoid-primed multipotent progenitors. Under the control of granulocyte colony-stimulating factor (G-CSF), cells then commit to the granulocytic lineage, developing into myeloblasts that begin to form neutrophil-specific granules. Neutrophil maturation then progresses through the promyelocyte, myelocyte, metamyelocyte, band cell, and mature neutrophil stages (Fig. 1.1), each defined by the acquisition of distinct granule subsets. The final compartment to form is the secretory vesicle pool, which enables neutrophil activation and adhesion, marking the transition to a fully mature, functional neutrophil (2).

Neutrophil release into the circulation is governed by the C-X-C motif chemokine receptor 4 (CXCR4)- C-X-C motif chemokine ligand 12 (CXCL12) axis. Decreased CXCR4 expression on maturing neutrophils and increased CXCL12 expression by surrounding osteoblasts and stromal cells facilitate their egress from the bone marrow (1,2). Elevated levels of G-CSF further promote neutrophil release by downregulating CXCR4 on neutrophils thereby disrupting the CXCR4-CXCL12 interaction (3,4).

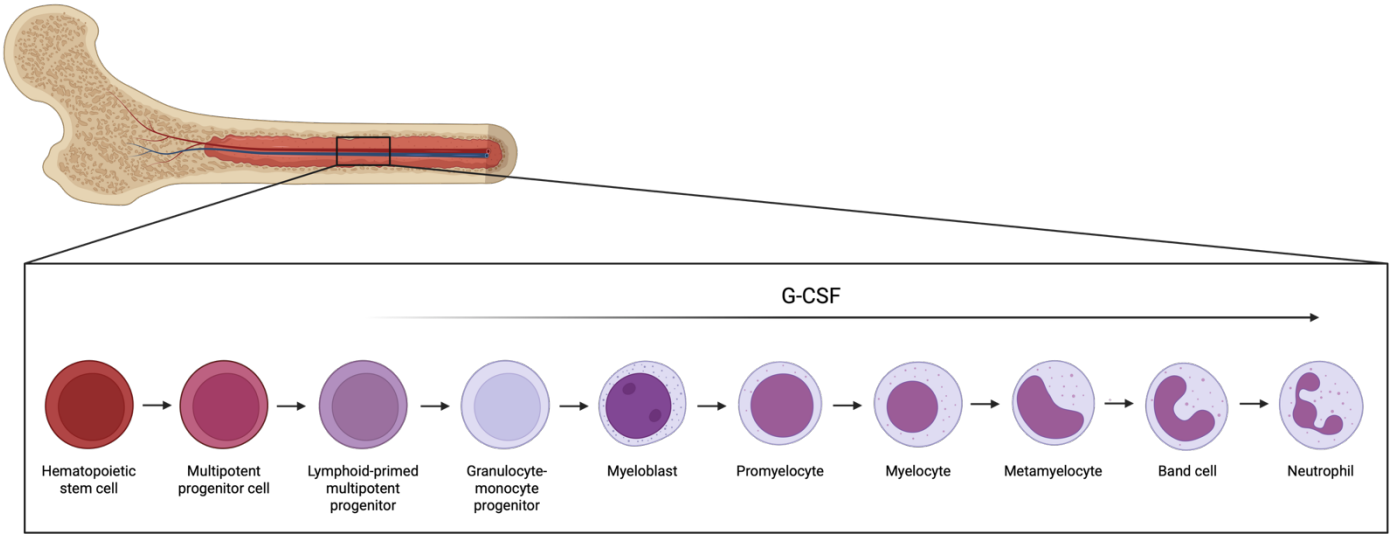

Figure 1.1: Stages of neutrophil development during granulopoiesis.

Schematic representation of granulopoiesis, depicting progression from early myeloid progenitors through myeloblast, promyelocyte, myelocyte, metamyelocyte, band cell, and terminally differentiated segmented neutrophils. Maturation occurs under the influence of granulocyte colony-stimulating factor (G-CSF) and is accompanied by nuclear remodeling and segmentation, increased cytoplasmic granularity, and acquisition of neutrophil effector functions.

Beyond the bone marrow, neutrophil subpopulations are also found in peripheral tissues such as the lungs, spleen, liver and lymph nodes, enabling rapid antimicrobial response upon tissue injury or infection (2).

1.1.2 Effector Functions of Neutrophils

Neutrophils are equipped with an arsenal of intracellular granules that perform diverse functions in the antimicrobial response (5,6). The tightly regulated activation of these granules enables neutrophils to execute key effector functions, including phagocytosis, degranulation and the release of neutrophil extracellular traps (NETs) (2). Given their many functions, neutrophil phenotypes are highly heterogenous and can adapt at sites of injury or infection to execute specific tasks and modulate the immune response accordingly (2).

The diverse intracellular granules, which store a wide array of enzymes, antimicrobial peptides, and membrane receptors, define the neutrophil's effector potential and enable rapid adaptation to distinct inflammatory environments. Based on their molecular composition and the timing of formation during granulopoiesis, these granules are classified into four main types: azurophilic (primary), specific (secondary), gelatinase (tertiary), and secretory vesicles (6,7). Notably, these granules are mobilized in the reverse order of their formation during neutrophil activation, allowing a graded release of effector components in response to escalating inflammatory stimuli (5,8).

Secretory vesicles, the smallest and most readily exocytosed granules, supply membrane-associated receptors essential for endothelial adhesion and directed migration (9,10). Their rapid mobilization during activation is triggered by the leukocyte adhesion cascade, which guides neutrophils to the sites of injury and inflammation (11). E- and P-selectins, adhesion receptors expressed on activated endothelial cells (ECs), bind to glycoprotein ligands on neutrophils, mediating transient rolling interactions along the vessel wall (12). This is followed by firm

adhesion through integrins binding to intercellular adhesion molecule-1 (ICAM-1) and intercellular adhesion molecule-2 (ICAM-2) on ECs, a critical step that precedes neutrophil transmigration into peripheral tissues (2,13,14).

Following adhesion, neutrophils rely on gelatinase granules to degrade vascular barriers and enable tissue entry. These granules, mobilized upon contact with the endothelium, contain matrix-degrading enzymes that facilitate extravasation into peripheral tissue by breaking down components of the vascular basement membrane (15,16). Gelatinase granules are enriched in proteolytic enzyme matrix metalloproteinase-9 (MMP-9) and are equipped with membrane-associated receptors and trafficking proteins, including CD11b/CD18 (Mac-1), CD67, CD177**,** fMLF-R**,** SCAMPs, and VAMP2 (1,2). Collectively, these components coordinate neutrophil adhesion, migration, and tissue infiltration during the early stages of inflammation.

Once within tissues, specific granules contribute to direct microbial killing and immune amplification. Among their diverse contents, lactoferrin is a major specific granule protein that disrupts microbial cell membranes by sequestering iron in biological fluids (17). Beyond its antimicrobial role, lactoferrin amplifies innate immune responses by activating azurophilic enzymes such as cathepsin G and serine proteases (18,19). Neutrophil gelatinase-associated lipocalin (NGAL), another key component of specific granules, exerts complementary antimicrobial effects by neutralizing bacterial siderophores, thereby limiting iron bioavailability to pathogens generated by microorganisms (20,21).

Finally, azurophilic granules provide the most potent enzymatic machinery for intracellular killing (1). These granules are enriched in myeloperoxidase (MPO), which facilitates pathogen neutralization by inducing toxic oxidative reactions within phagolysosomes

during phagocytosis, the process by which neutrophils engulf and degrade pathogens intracellularly (22). This compartmentalized reaction enables efficient microbial killing while minimizing host tissue damage (23). In addition to MPO, azurophilic granules also contain neutrophil elastase (NE), cathepsin G, proteinase 3, defensins, and lysozyme (1). Upon neutrophil activation by stimuli such as Toll-like receptor (TLR) ligands, granulocyte-macrophage colony-stimulating factor (GM-CSF), tumor necrosis factor-α (TNF-α), or immunoglobulin/Fc receptor signaling, their contents can be also released into the extracellular space through degranulation, amplifying inflammatory signaling and contributing to host defense (8,24).

Beyond degranulation, granular enzymes and antimicrobial peptides are also externalized during the formation of NETs, which are physical networks of chromatin and protein that can physically immobilize and neutralize pathogens (25). These antimicrobial effectors remain enzymatically active upon NET release, allowing them to carry out their microbicidal function in the extracellular space (26).

1.1.3 Neutrophil Cell Death Pathways and Regulation

Despite the central role of neutrophils in antimicrobial defense and inflammation, their activity must be tightly regulated due to the highly cytotoxic nature of their granular contents and the potential for collateral host tissue injury (23). In addition to their antimicrobial arsenal, neutrophils release granule-derived molecules that exert regulatory functions to limit inflammation and promote tissue homeostasis. Specific granule proteins such as resistin, olfactomedin-4, and signal-regulatory protein α (SIRPα) modulate neutrophil accumulation, oxidative activity at sites of injury, and lifespan (2,27,28).

The short lifespan of neutrophils and the mechanisms regulating their clearance are critical for preventing aberrant neutrophil activity (29). Under homeostatic conditions, neutrophil

survival is regulated by apoptosis, a non-lytic and non-inflammatory form of programmed cell death (30). This process can be initiated by intracellular stress factors or by membrane-mediated signaling in response to external stimuli. Both intrinsic and extrinsic pathways result in the assembly of the apoptosome and subsequent activation of effector caspase-3 and -7 (30–32). Morphologically, apoptosis is characterized by cell shrinkage, plasma membrane blebbing, chromatin condensation, and nuclear DNA fragmentation (29). Importantly, membrane integrity is preserved during apoptosis, thereby preventing the leakage of neutrophil contents and minimizing local tissue injury (33,34).

Under certain conditions, neutrophils can undergo alternative forms of cell death, including necroptosis, necrosis, pyroptosis, autophagy-mediated cell death, and NETosis (29). Necrosis and necroptosis are both associated with a marked increase in reactive oxygen species (ROS), ultimately leading to the rupture of the plasma membrane (35). Cell lysis is also a hallmark of pyroptosis, a caspase-1- or caspase-11-dependent process in which inflammasome activation promotes gasdermin-mediated membrane pore formation and the release of interleukin-1β (IL-1β) (29,35,36).

In contrast to these lytic pathways, autophagy-mediated cell death is typically non-inflammatory and is characterized by the formation of autophagic intracellular vesicles that sequester and degrade cellular contents (37). Although autophagy primarily functions as a survival mechanism to remove damaged organelles, sustained activation can shift this process toward self-digestion and cell death via autophagy (38).

NETosis, the most recently described form of programmed cell death in neutrophils, culminates in the release of NETs. A defining feature of this process is the rupture of the nuclear envelope, which allows chromatin to mix with granular and cytoplasmic components prior to the

disintegration of the plasma membrane (39). This sequence of events leads to neutrophil death and the extrusion of a highly microbicidal extracellular network that contributes to pathogen neutralization (40).

Following neutrophil death, macrophages play a critical role in maintaining neutrophil homeostasis by clearing apoptotic neutrophils through efferocytosis, a process that promotes the resolution of inflammation (29,41,42). This clearance suppresses granulopoiesis and the further release of neutrophils from the bone marrow by downregulating G-CSF production (43). The presence of senescent neutrophils in the circulation also induces upregulation of CXCR4, facilitating their return to the bone marrow for final clearance (44).

1.2 Neutrophil Extracellular Traps

1.2.1 Discovery and Immune Function of NETs

NETs were first discovered and described by Volker Brinkmann and Arturo Zychlinsky in 2004 (40). They described NETs as extracellular web-like structures composed of decondensed chromatin decorated with granular and cytoplasmic proteins released from activated neutrophils. These structures were shown to entrap and neutralize pathogens by providing locally concentrated antimicrobial enzymes and peptides and acting as physical barriers that limit pathogen dissemination (40). Importantly, Brinkmann and colleagues also recognized the potential pathogenic consequences of NET formation, noting that the extracellular exposure to nuclear and granular contents could contribute to host tissue injury and autoimmune disease.

This process was later termed NETosis, a distinct form of regulated cell death in which NET extrusion occurs concomitantly with the death of the neutrophil (39). NETosis can be distinguished from other types of neutrophil death by its characteristic sequence of morphological changes. Neutrophil activation first triggers actin cytoskeletal rearrangement,

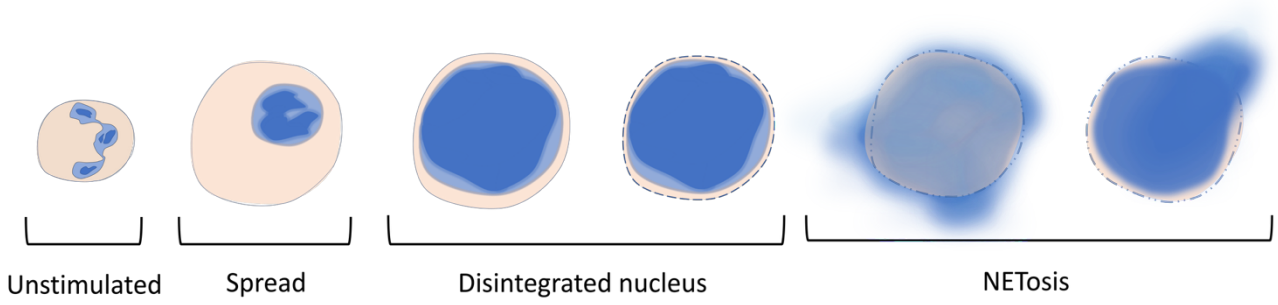

Figure 1.2: Sequential morphological stages of NETosis.

Schematic representation of the progressive morphological stages of NETosis. NET release proceeds through sequential morphological changes, previously described as Spread, Disintegrated nucleus, and NETosis. Neutrophil activation initiates cytoskeletal rearrangements that promote cell spreading, followed by chromatin decondensation and nuclear swelling that expands to fill the cell body and allows mixing of nuclear and cytosolic contents. Terminal NETosis culminates in the externalization of chromatin structures into the extracellular space, occurring through localized membrane pores or widespread loss of membrane integrity, resulting in diffuse, cloud-like NET release.

causing the cell body to flatten (45). Chromatin then decondenses and expands, leading to the loss of the lobulated nucleus and breakdown of the nuclear envelope. The simultaneous disintegration of granular membranes allows mixing of nuclear and granular content within the cytoplasm, which are then expelled into the extracellular space, either diffusely following complete plasma membrane rupture or through a localized pore (39,45). These steps have been classified into distinct stages of NETosis: (1) Spread, (2) Disintegrated nucleus, and (3) NETosis (39,45) (Fig. 1.2), with their timing dependent on the type and intensity of the activating stimulus.

The composition of NETs is heterogenous and appears to depend on the nature of the activating stimulus (25). The antimicrobial activity of NETs has been attributed to several key components released during NETosis, including histones, granular proteases such as NE, MPO and, lactoferrin (46). Variability in NET protein cargo has been well documented. While initial proteomic analyses of PMA-induced NETs identified 24 core proteins, subsequent studies have shown that the NET proteome is modulated by the stimulus, with exposure to different strains of *Pseudomonas aeruginosa* inducing the release of up to 50 distinct proteins (47,48).

NET formation thus allows neutrophils to maintain antimicrobial activity post-mortem and was shown to be as effective as phagocytosis in eliminating certain pathogens (39). Since their discovery, extensive work has focused on elucidating the role of NETs in host defense. Given their antimicrobial properties, NET release can be triggered by a wide range of stimuli, including bacteria, fungi, parasites, and viruses (25,49), often in response to microbial components such as lipoteichoic acid and lipopolysaccharide (LPS), and other cell surface molecules. NETs primarily function to immobilize and eliminate pathogens that are too large or resistant to phagocytosis (46,50,51). Through electrostatic interactions, NETs can physically

bind both Gram-positive and Gram-negative bacteria, as well as fungi, thereby limiting dissemination and enhancing microbial killing (52).

Beyond physical entrapment, NETs exert potent bactericidal effects through the activity of their associated granular components. NE, bound to the chromatin backbone, can cleave virulence factors of *Shigella flexneri*, *Salmonella typhimurium*, and *Yersinia enterocolitica* (40,53,54). Similar proteolytic activity has been reported for cathepsin G and proteinase 3 (55). MPO also remains catalytically active following NET release, generating ROS that are instrumental in NET-mediated killing of *Staphylococcus aureus* (25,26). Additionally, externalized histones exhibit potent bactericidal activity (56), and the web-like NET structures can serve to disrupt bacterial biofilms, preventing further dissemination, as demonstrated for *Pseudomonas aeruginosa* (57).

NETs also participate in antiparasitic, antiviral and antifungal immune responses. Against parasites, NET release promotes immobilization but appears insufficient for complete eradication (58). Viral exposure can also trigger NET formation (59,60). Notably, NETs have been shown to bind and inactivate HIV-1 virions (61). This antiviral activity has been attributed to chromatin-bound antimicrobial proteins MPO and α-defensin, which can target both enveloped and non-enveloped viruses (61).

Similarly, NETs can eliminate fungal pathogens through mechanisms mediated by calprotectin and MPO (48,62). The physiological relevance of these mechanisms is highlighted by the occurrence of recurrent fungal infections in MPO-deficient individuals (48), and by the observation that calprotectin restoration in granulomatous disease patients protects against invasive fungal infections (63). In humans, NETs are particularly important for the clearance of

fungal infections and other pathogens capable of evading phagocytosis, yet NETs display variable antimicrobial efficiency across infections *in vivo* (46).

NETs also engage in crosstalk with neutrophils and innate immune cells to modulate the ensuing immune responses. They have been shown to stimulate neighboring neutrophils and enhance granule exocytosis, ROS generation, and phagocytic activity, an effect suggested to occur through activation of p38 mitogen-activated protein kinase (MAPK), Akt, and extracellular signal–regulated kinase 1/2 (ERK1/2) phosphorylation pathways (64). Moreover, NETs play a key role in macrophage modulation by inducing polarization toward a pro-inflammatory phenotype via Toll-like receptor 9 (TLR9)-dependent nuclear factor κB (NF-κB) signaling (65), facilitating the transfer of neutrophil-specific antimicrobial peptides and triggering macrophage pyroptosis through high-mobility box 1 (HMGB1) release (66,67). These interactions enhance macrophage antimicrobial activity, particularly by promoting phagocytosis (68). NETs have also been shown to promote the differentiation of monocytes into M2 macrophages by downregulating IL-4 receptor expression, which may serve to limit chronic inflammation induced by monocyte-derived dendritic cells (DCs) (69).

NETs further influence DC responses by inducing the production of interferon-alpha (IFN-α) through TLR9 signaling (70). However, their effect appears to be dichotomous. While NET-associated granular proteins can stimulate plasmacytoid DCs to release antiviral factors, NET exposure under certain conditions can impair DC differentiation and maturation, dampening their immunostimulatory potential (71). Additionally, NETs have been observed to supress natural killer cell function, further emphasizing their dual role in regulating innate immunity (49).

Beyond their impact on innate immune cells, NETs can also modulate adaptive immune responses by engaging T and B lymphocytes. NETs interact with T cells through their receptors, inducing elevated expression of activation markers (72,73). This interaction lowers the activation threshold of T cells and enhances antigen-specific immune responses (74). In B cells, NETs promote activation and proliferation through p38 MAPK and TLR9 signaling (75), supporting their role in bridging innate and adaptive immune mechanisms.

While NETs can amplify inflammation and contribute to tissue injury through their cytotoxic proteome, they may also participate in the resolution of inflammation. NET-associated proteases can degrade cytokines and chemokines to help dampen immune activation (76). Collectively, these findings highlight the dual nature of NETs as antimicrobial and immunomodulatory effectors, essential for host defense yet potentially pathogenic when dysregulated. Following their discovery as a novel antimicrobial strategy, subsequent studies have focused on elucidating the cellular and molecular mechanisms underlying their formation.

1.2.2 Mechanisms of NETosis

Foundational research has established NETosis as a distinct form of programmed cell death involving the orchestrated activation of signaling networks that include protein kinase C (PKC), Raf–mitogen-activated protein kinase kinase (MEK)–ERK, and NADPH oxidase pathways, culminating in peptidylarginine deiminase 4 (PAD4)-dependent chromatin decondensation and extracellular DNA release (40,77,78). The relative contribution of each pathway depends on the nature of the stimulus and cellular context, leading to the characterization of distinct mechanisms of NET release.

The classical pathway of NET formation, known as suicidal NETosis, involves a robust oxidative burst that initiates a cascade of intracellular events resulting in neutrophil death and DNA release (46). This process has been well characterized in response to phorbol 12-myristate

13-acetate (PMA), which triggers an NADPH oxidase 2 (NOX2)-mediated signaling cascade via activation of PKC (79,80). Physiological stimuli such as cytokines TNF-α, IL-1β, or interleukin-8 (IL-8) can also induce NET formation through this pathway (81).

PKC and the Raf-MEK-ERK pathway both phosphorylate cytosolic p47 to induce the assembly of the active NOX2 complex at the phagosomal or plasma membrane (78,80,82). The resulting production of ROS triggers MPO activation, leading to the cytosolic release of NE, which sequestered at the surface of azurophilic granules within mulprotein complexes known as azurosomes (83,84). This release represents a key initiating step in NET formation (25). Accordingly, suppression of ROS with antioxidants such as vitamin C significantly reduces NET release (85,86)

NE is a central effector of canonical NETosis, mediating both chromatin decondensation and activation of gasdermin D (GSDMD), a pore-forming enzyme that facilitates DNA extrusion while concurrently inducing cell death (87,88). Cytosolic NE contributes to NETosis by disassembling the actin cytoskeleton, degrading F-actin to promote neutrophil activation and immobilization (83,89). It can also enter the nucleus via passive diffusion where it synergizes with MPO to cleave and inactivate histone subunits, driving chromatin decondensation (84,87). Consistent with this, NE deficiency prevents NET formation during bacterial challenge (87).

MPO activation serves as an important inducer of NE release and further enhances chromatin decondensation along with other cationic proteins such as DEK, which bind to and neutralize histone charge (84,90). Yet, blocking MPO only delays NETosis rather than preventing it (84). NE release can occur independently of MPO through ROS-mediated disruption of azurosomes, promoting NE translocation to the nucleus and chromatin decondensation even in the absence of MPO activity (83).

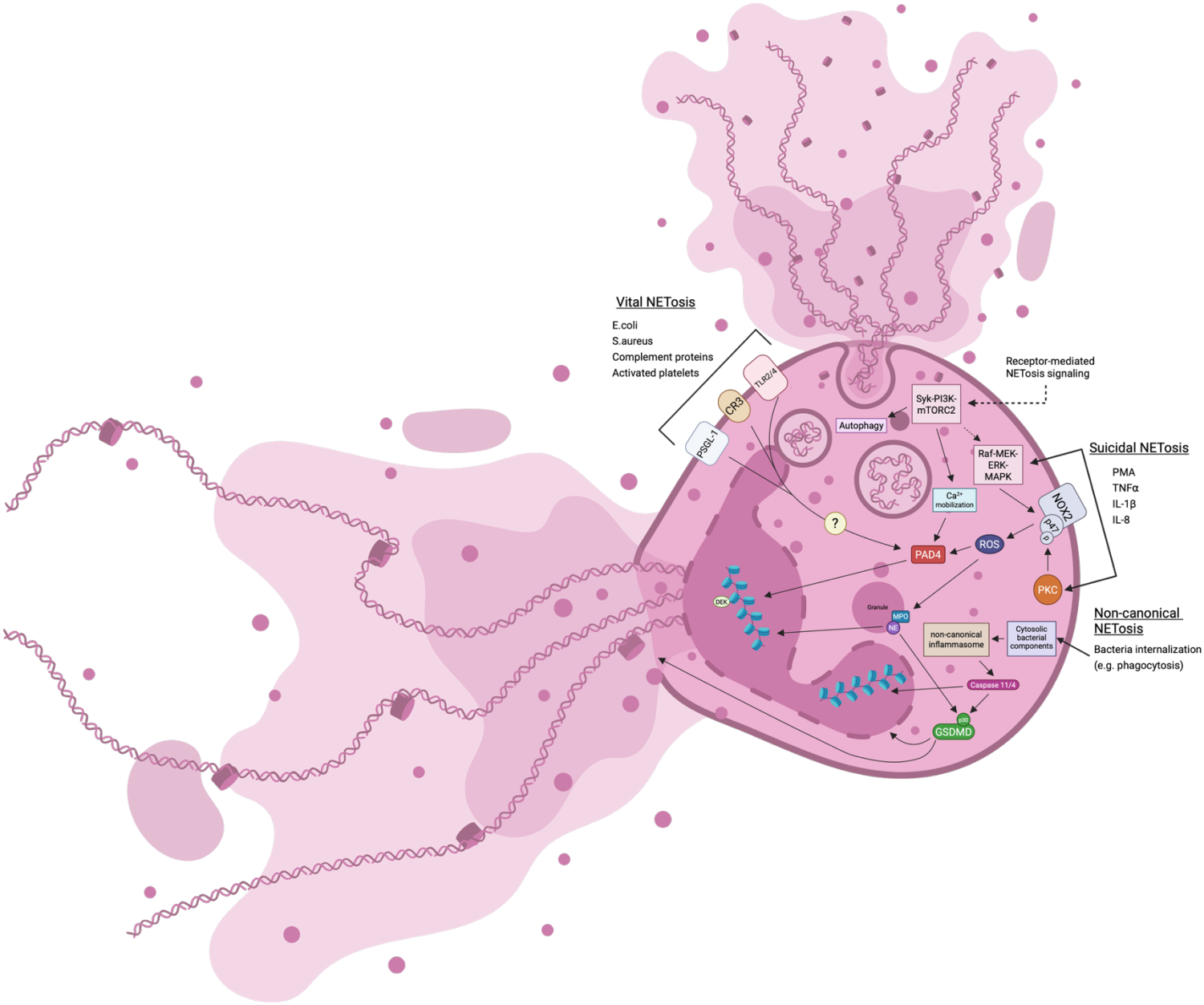

Figure 1.3: Signaling pathways and cellular outcomes contributing to NET formation.

Schematic overview of major signaling pathways and cellular processes implicated in neutrophil extracellular trap (NET) formation. Receptor-mediated activation engages upstream signaling modules, including Syk–PI3K–mTORC2 and MAPK (Raf–MEK–ERK), which promote cytoskeletal remodeling, calcium mobilization, and reactive oxygen species (ROS) generation via NADPH oxidase 2 (NOX2). Suicidal NETosis is triggered by ROS- and calcium-dependent signaling that converges on activation of protein kinase C (PKC) and peptidylarginine deiminase 4 (PAD4), driving histone modification and chromatin decondensation. In suicidal NETosis, extensive chromatin decondensation, nuclear envelope breakdown, and loss of plasma membrane integrity culminate in extracellular DNA extrusion decorated with granule proteins such as neutrophil elastase (NE) and myeloperoxidase (MPO). In parallel, a non-canonical inflammasome–dependent pathway can be initiated following bacterial internalization (e.g. phagocytosis), leading to cytosolic sensing of bacterial components, activation of caspase-11/4, gasdermin D (GSDMD) pore formation, and NET release. In contrast, vital NETosis is depicted as an alternative outcome in which neutrophils release DNA through vesicles while retaining plasma membrane integrity and cellular viability, allowing continued effector functions, and has been associated with Toll-like receptor (TLR) activation as well as complement- and P-selectin-mediated signaling. Dashed arrows indicate indirect or stimulus-dependent signaling relationships.

Proteases such as NE further contribute to NET release by cleaving inactive GSDMD in the cytosol, generating the pore-forming fragment GSDMD-p30 (91). This fragment inserts into granular and plasma membranes, creating pores that promote their rupture and facilitate extracellular DNA release (88).

The progression of NETosis also involves temporally distinct kinase signaling events (92). Its early onset depends on transforming growth factor β-activated kinase 1 (TAK1), p38 MAPK, and MEK activation, which drive PAD4-dependent histone citrullination and initiate chromatin decondensation (92,93). In contrast, later stages rely on spleen tyrosine kinase (Syk)–phosphoinositide 3-kinase (PI3K)–mechanistic target of rapamycin complex 2 (mTORC2) signaling to coordinate calcium mobilization and complete chromatin relaxation (93,94). Syk activation also regulates autophagy through the PI3K–mTORC2–rubicon-like autophagy-enhancer pathway, linking receptor-driven signaling to metabolic control of NETosis (94–96). Inhibition of autophagic flux disrupts proper NET formation, underscoring the importance of this pathway in sustaining the process. Moreover, Syk-dependent Ca^{2+} mobilization can further enhance PAD4 activity at later stages, facilitating complete chromatin decondensation and DNA extrusion (93,97). Calcium mobilization therefore represents a key convergence point between kinase signaling and chromatin decondensation in suicidal NETosis, as PAD4 activation and histone citrullination are intrinsically calcium-dependent (98).

Although canonical NETosis is classically dependent on NOX-derived ROS, residual NET formation observed in NOX-deficient models under certain stimuli suggests that additional, ROS-independent mechanisms can also mediate NET release (99).

In addition to its role in canonical NETosis, GSDMD also mediates non-canonical NETosis, a mechanism that occurs independently of NOX-derived ROS as well as MPO and NE

activity (91). In this pathway, cytosolic bacterial components are sensed through non-canonical inflammasome signaling, leading to the activation of caspase-11/4 (100). Activated caspases cleave GSDMD, producing the pore-forming N-terminal fragment that inserts into cellular membranes, a process mechanistically analogous to pyroptosis but resulting in DNA extrusion, thereby defining a distinct form of NETosis (88,91,101). GSDMD pore formation enables caspase-11 to access chromatin and promote histone degradation, while altered ionic gradients may facilitate PAD4 activation (89).

GSDMD plays multiple roles in the NETosis process, contributing both to its progression and to its bactericidal function. Its pore-forming activity facilitates the release of NET-associated cytokines that recruit additional neutrophils, while the GSDMD-p30 fragment can directly disrupt bacterial membranes to induce killing (25). Consequently, GSDMD deficiency impairs NETosis and reduces peripheral immune cell infiltration (102).

While canonical and non-canonical NETosis ultimately result in neutrophil lysis and death, an alternative mechanism of NET release that preserves neutrophil viability and function has also been described, termed vital or non-lytic NETosis (103). This process involves rapid vesicular extrusion of chromatin through nuclear blebbing, enabling NET release without plasma-membrane rupture, and may contain both histone-rich nuclear DNA and mitochondrial DNA (104). Unlike suicidal NETosis, neutrophils undergoing vital NETosis remain viable and capable of effector functions such as migration, phagocytosis, and bacterial killing while simultaneously releasing NETs (105).

Similar to non-canonical NETosis, vital NETosis proceeds independently of NE and MPO and can often occur without PAD4 activation (106). However, the involvement of PAD4 remains a matter of debate, as PAD4 inhibition has been shown to prevent ionomycin- and *S.*

aureus-induced vital NETosis, suggesting that PAD4 may act as an overlapping mediator across distinct NETosis mechanisms (107). Vital NETosis is primarily a receptor-mediated process involving Toll-like receptor 2 (TLR2) and Toll-like receptor 4 (TLR4) signalling and complement-mediated opsonization (105,108,109). It can be triggered by LPS exposure or by platelet interactions that depend on platelet TLR4 expression and platelet- neutrophil engagement via P-selectin (108). Activation of complement component C3a, reported in response to β-glucan exposure, also promotes this form of NETosis by engaging C3a receptors on neutrophils and enhancing their activation (85,109,110) This process has been observed during Gram-positive bacterial infection, where neutrophils remain anuclear yet intact, and continue to crawl and engage pathogens (105).

Across these mechanistic variants, chromatin decondensation remains a defining event, centrally orchestrated by PAD4, whose activation and regulation are discussed in the following section.

1.2.3 PAD4-mediated Chromatin Decondensation

PAD4 is a well-established calcium-dependent enzyme that catalyzes the post-translational deamination of peptidyl-arginine residues to citrulline on histones and protein substrates. Briefly, PAD4 hydrolyzes the imine group of arginine into a neutral ureido group with the release of ammonia, thereby eliminating the positive charge and reducing protein stability (111). In the context of histones, PAD4-induced citrullination weakens the histone-DNA interaction and promotes chromatin decondensation (80,112).

PAD4 is one of five enzymes in the PAD family, a group of enzymes that share conserved catalytic domains but differ in tissue distribution and subcellular localization. The PADI genes encoding these enzymes are clustered on chromosome 1p36.1 in humans and chromosome 4pE1 in mice (111). PADs 1, 3, and 6 are primarily expressed in epidermal and

reproductive tissues, while PAD2 displays broad expression across neural, muscular, and immune systems. PAD4 is predominantly expressed in granulocytes and is also detected in certain cancer cell lines and oocytes (111,113). Interestingly, PAD4 is the only isoform to contain the classic nuclear localization sequence 56-PPAKKKST-63, enabling it to be trafficked to the nucleus and therefore mediate histone citrullination (114).

Structurally, PAD4 is a 74 kDa protein that forms a head-to-tail dimer (115). Each monomer contains two N-terminal immunoglobulin-like domains and a C-terminal catalytic domain that adopts the α/β propeller fold characteristic of the deiminase superfamily (116). PAD4 activation requires the cooperative binding of five calcium ions, with two binding sites located within the C-terminal catalytic domain (Ca1 and Ca2) and three within the N-terminal domain (Ca3, Ca4, and Ca5) (112). These interactions induce conformational rearrangements that align catalytic residues, enabling substrate access and enzymatic activity (115).

However, the calcium concentrations required for PAD4 activation exceed those typically present in the homeostatic cytoplasm, implying the enzymatic activation depends on upstream signaling pathways that promote calcium influx (115,117,118). Calcium-dependent PAD4 activation has been observed in neutrophils following exposure to ionophores, bacterial products, or increases in extracellular pH (119,120). In certain contexts, this may be mediated through PKC-dependent signaling or the Syk-PI3K-Ca^{2+} axis, which couples receptor activation to PAD4 enzymatic function (93,97)

Due to its distinct functions in granulocytes, PAD4 has garnered particular interest for its immunomodulatory functions and has been positioned as a driver of inflammatory and autoimmune diseases (112). The generation of anti-citrullinated protein antibodies, a hallmark of rheumatoid arthritis, implicates PAD4 overexpression as a promoter of citrullinated autoantigens

that prime autoimmune responses (121,122). Elevated PAD4 activity has also been associated with multiple sclerosis, systemic lupus erythematosus (SLE), and sepsis (112).

Beyond generating autoantigens, PAD4 is a central mediator of NET formation (77,123). Once activated in the cytosol, PAD4 translocates to the nucleus, where it catalyzes histone citrullination, weakening electrostatic interactions between histones and DNA to drive chromatin decondensation and NET release. Its crucial role in this process is reflected by the markedly impaired NET formation observed in PAD4$^{-/-}$ mice (107,124). PAD4-mediated histone citrullination may also enhance the pro-inflammatory potential of NETs by modifying histones to increase their immunogenicity, thereby further contributing to NET-associated pathologies (125). Consistent with this, PAD4 inhibition or deficiency exerts broad immunomodulatory effects and is protective against vascular injury, atherosclerotic plaque progression, thrombosis, and inflammatory arthritis (126–128). Consequently, dysregulation of PAD4 activity and defective NET clearance have been implicated in chronic inflammation and autoimmunity, underscoring the importance of mechanisms that restrain NET formation and facilitate their removal.

1.2.4 Regulation and Clearance of NETs

NETosis is a regulated process with multiple checkpoints that determine whether a neutrophil will undergo NET release or pursue other antimicrobial strategies. One key control mechanism is the microbe-sensing capacity of neutrophils, which allows them to determine when NET formation is required (129). Phagocytosis itself also serves as an inhibitory signal that prevents NETosis, enabling neutrophils to eliminate pathogens intracellularly instead (25).

The decision between phagocytosis and NET release is largely dictated by pathogen size and behaviour. Small microorganisms are efficiently engulfed within phagosomes that fuse with azurophilic granules. This process sequesters NE and prevents its translocation to the nucleus, thereby blocking chromatin decondensation (129). In contrast, when neutrophils encounter large

pathogens, NE is mobilized into the nucleus through the slower azurosome-mediated pathway, initiating NET formation (25,46). Moreover, some microbes have evolved mechanisms to evade phagocytosis, which triggers neutrophils to resort to NET release instead (130,131).

Given the cytotoxic and pro-inflammatory potential of NET components, efficient mechanisms exist to degrade and clear NETs once their antimicrobial purpose is fulfilled. DNases play a central role in this process by cleaving the double-stranded DNA backbone of NETs, facilitating the subsequent removal of residual protein by phagocytes (132,133). Both extracellular DNase I and lysosomal DNase II participate in NET degradation (134). DNaseI hydrolyzes phosphodiester bonds in extracellular chromatin structures, while DNase II, localized in macrophage lysosomes, degrades phagocytosed DNA fragments (135,136). DNase activity has been shown to limit intravascular NET accumulation and prevent thrombus formation during sepsis (135).

In addition, the 3'-exonucleases of the Three Prime Repair Exonuclease (TREX) family contribute to NET clearance, particularly by degrading oxidized DNA species that are resistant to DNase I and II (135,137). Three Prime Repair Exonuclease 1 (TREX1), expressed in macrophages, facilitates intracellular degradation of NETs following phagocytosis (138). Importantly, physiological concentrations of DNase I alone may be insufficient for complete NET removal, highlighting the cooperative role of macrophages and nucleases in maintaining immune homeostasis (133,138). In fact, macrophage and dendritic cell activation enhances NET uptake and degradation, and local macrophage density has been shown to inversely correlate with NET accumulation in aortic aneurysms (134,139)

Impaired clearance or excessive formation of NETs can result in their persistence within tissues and circulation, promoting chronic inflammation and contributing to a wide spectrum of pathological conditions.

1.2.5 Pathological Role for NETs in Disease

Despite their protective role in infection, NETs exhibit a dichotomous impact on the host, contributing to pathogen clearance while simultaneously promoting collateral tissue injury (140). During sustained inflammatory stimulation, excessive or dysregulated NET release drives tissue damage and systemic inflammation, contributing to sepsis and multi-organ failure (141,142). Much of this injury stems from NET-bound histones and proteolytic enzymes, which are cytotoxic to surrounding tissues and amplify inflammatory signaling cascades (143,144). In severe infections such as sepsis and severe acute respiratory syndrome coronavirus 2 (SARS-CoV-2), NETs also contribute to coagulopathy through interactions with platelets, coagulation factors, and fibrin networks, placing them at the center of immunothrombotic complications (145–147).

NETs also serve as reservoirs of modified autoantigens that can drive the production of autoantibodies and perpetuate immune complex formation (148). These structures further amplify autoimmunity by activating complement and antigen-presenting cells (149–151). Consequently, impaired NET clearance prolongs autoantigen exposure, promoting the onset and progression of autoimmune diseases such as SLE, arthritis and anti-neutrophil cytoplasmic antibody (ANCA)-associated vasculitis (152–154).

Importantly, NET-driven injury is not limited to infection but also occurs in sterile inflammatory conditions triggered by endogenous and environmental cues such as IL-8, immune complexes, damage-associated molecular patterns (DAMPs), and microcrystals (49). Among

these, microcrystal-mediated NETosis has been implicated in the pathogenesis of atherosclerosis, arthritis and pancreatitis (49,155). Moreover, metabolic disturbances such as diabetes further exacerbate NET formation by upregulating PAD4 expression (156,157), linking NET dysregulation to diabetic complications and chronic inflammation (158,159).

Consistent with their immunothrombogenic nature, excessive NET formation has been implicated in thrombus development across multiple thrombotic disorders, including atherosclerosis, ischemic stroke, and deep venous thrombosis (160–162). The prothrombotic properties of NETs also extend to cancer-associated thrombosis (163), where NETs have been detected within coronary, cerebral and pulmonary thrombi of cancer patients (164,165). Beyond their contribution to thrombosis, NET components exert protumorigenic effects by promoting tumor cell proliferation, metastasis, immunosuppression, and angiogenesis (166).

Dysregulation of PAD4 activity has been observed across autoimmune, metabolic, and thrombotic diseases (106). Pharmacological inhibition or genetic deletion of PAD4 reduces NET formation and neutrophil infiltration, improving outcomes in models of diabetes, atherosclerosis, and lupus (123,167,168).

1.2.6 Experimental Models of NET Formation

Given the diverse functions of NETs and their broad involvement in disease pathogenesis, substantial efforts have been made to develop reliable models to study their formation and function. *In vitro* NETosis models have been instrumental in dissecting the isolated mechanisms and consequences of NET release (87). While primary human neutrophils remain the gold standard for studying NETosis, the use of neutrophil-directed HL-60 cells has gained increasing popularity as a practical and reproducible alternative (169,170).

The HL-60 promyelocytic leukemia cell line offers several advantages, including rapid proliferation in culture and the ability to bypass the technical and ethical challenges associated

with isolating primary neutrophils or using hematopoietic stem cells (171). Upon differentiation with polar compounds such as dimethyl sulfoxide (DMSO), HL-60 cells acquire neutrophil-like characteristics (170,172). These differentiated HL-60 (dHL-60) cells exhibit key neutrophil functions including degranulation, phagocytosis, chemotaxis, oxidative burst, and NETosis (171,173). Their transcriptional profile closely aligns with that of human neutrophils and, in some contexts, may be more reflective of human physiology than murine neutrophils (173). However, dHL-60 cells do not fully capture all features of primary neutrophil physiology, including nuclear segmentation, granule composition, and rapid activation dynamics, and therefore should be interpreted as a simplified system for studying NETosis (173). Nonetheless, dHL-60 cells have become a valuable tool in neutrophil biology, contributing to major advances in understanding NET formation and its regulatory pathways (174–177).

To study the broader implications of NETs *in vivo*, PAD4-defient mice, which display abrogated capacity for NET formation, are commonly employed (123). PAD4 catalyzes histone citrullination, a crucial step in chromatin decondensation during NETosis, and its genetic deletion effectively prevents NET formation (123). Comparisons between wild-type (WT) and $PAD4^{-/-}$ mice have been instrumental in linking NET formation to diverse pathological processes including thrombosis, sepsis, and ischemia-reperfusion injury (178). However, PAD4 also participates in other cellular pathways such as gene regulation and macrophage function, and thus phenotypic differences in PAD4-deficient mice should be interpreted with caution (114,179).

The established involvement of PAD4 in NET release has been further investigated through the use of pharmacological inhibitors and stimulants. Selective PAD4 inhibitors such as GSK484 and the pan-PAD inhibitor Cl-amidine are commonly employed *in vitro* and *in vivo* to

delineate PAD4-dependent mechanisms of NETosis and assess the downstream consequences of NET inhibiton on tissue injury and inflammation (107,126,180). These modulators have helped demonstrate the contribution of PAD4 to NETosis-driven pathology, including thrombosis and organ damage.

To induce NET formation, neutrophils are commonly stimulated with PMA, a potent activator of PKC that triggers suicidal NETosis. PMA stimulation has been widely used to define sequential stages of NET release and to generate abundant NETs for isolation and downstream applications (39,40,181).

To confirm the specificity of NET-mediated effects, experiments are often performed in parallel using DNase-treated NETs, in which the extracellular DNA backbone is degraded, effectively dismantling the NET structure. This approach has been pivotal in distinguishing NET-specific effects both *in vitro* and *in vivo*, contributing to the identification of NET-dependent mechanisms in models of ischemia-reperfusion injury and deep vein thrombosis (181,182).

1.3 Identifying and Quantifying NETs

1.3.1 Conventional Approaches for NET Detection

With the growing interest in NET research, several methodologies have been developed to detect and quantify NETs across different sample types (183). Among these, the detection of cell-free DNA remains one of the most widely used measures of NET levels, despite its inability to discriminate NET-derived DNA from that released during necrosis (184,185). This approach typically relies on fluorescent binding of DNA in bodily fluids using nucleic-acid stains or probes in a 96-well plate assay format. Although simple and high throughput, its specificity and interpretative value have been questioned due to its indiscriminate nature (183)

To improve specificity, cell-free DNA detection is often combined with MPO to identify MPO-DNA complexes using capture enzyme-linked immunosorbent assay (ELISA) (185,186). ELISA-based approaches are widely applied in NET research and can be adapted to quantify various NET-associated markers (185). Notably, citrullinated histone H3 (citH3) serves as a common indicator of PAD4 activity and NET release (185,187). In addition to ELISA, citH3 and other NET components are frequently analyzed using flow cytometry or immunofluorescent microscopy. Using flow cytometry, fluorescently labeled antibodies against neutrophil markers such as MPO and NE are paired with nucleic-acid dyes to identify cells undergoing NETosis (188). Similarly, immunofluorescent staining enables visualization of NET-associated structures in cultured cells and tissue sections (183,185,189).

Although these methods provide increased specificity compared to DNA-based assays, they are often costly, labor intensive, and require extensive sample handling that may disrupt the delicate NET structures (190). As such, a standardized method for detection and quantification of NETs has yet to be established in the research community.

1.3.2 Limitations of Current Quantification Methods

The accurate and translatable quantification of NETs requires standardized and reproducible methodologies. However, current approaches in NET research often lack the rigor and defined parameters necessary to achieve inter-laboratory reproducibility (191). Assays such as ELISA and DNA-based fluorescence approaches require extensive optimization and standardization, which can vary substantially between laboratories and compromise comparability across studies (183,191). Moreover, these methods are not always translatable between *in vitro* and *in vivo* experimental contexts (191), and discrepancies in NET quantification outcomes can arise depending on the methodology used (192).

As previously discussed, more specific techniques such as flow cytometry and immunofluorescent imaging require significant sample manipulation, which may damage NET structures and impair accurate quantification. In the case of flow cytometry, measurements are inherently biased toward pro-NETotic cells, since the method primarily detects cell-associated NET components rather than free extracellular NETs (183). Imaging- based methods can capture a broader spectrum of NET phenotypes, but their quantitative outcomes are highly dependent on field of view and observer subjectivity (183,191).

To reduce user bias and improve reproducibility, recent efforts have focused on automating image-based NET quantification. Advances in computational pipelines for fluorescence microscopy have facilitated the analysis of NET formation, yet the heterogeneity of NETs poses a challenge for establishing comprehensive and reproducible analyses (193,194). Current pipelines for *in vitro* NET analysis largely rely on measuring the surface area of DNA stained with cell-impermeant fluorescent DNA dyes (i.e. SYTOX) or a chromatin antibody, reporting on NET counts or area, and inferring the percentage of NETting cells by normalizing to total cell count (189). However, NETs are defined by varying DNA staining features across different methods. Some studies quantify NETs as the total DNA-positive area, while others use metrics such as the size or integrated density of DNA-positive regions to define NETs (189,195), leading to inconsistent data interpretation. Although some approaches are more comprehensive and incorporate multiple DNA stain features (196), they still rely exclusively on a limited set of predefined DNA staining metrics, a constraint that can reduce specificity and risk overfitting.

Collectively, these methodological limitations underscore the need for standardized, dynamic, and unbiased tools capable of capturing NET formation in real time across diverse

experimental contexts, as the current lack of methodological consensus continues to hinder data interpretation and comparability between studies.

1.3.3 Recent Advances in Quantitative NET Analysis

In response to these methodological gaps, recent advances in live-cell imaging and computational analysis incorporating machine-learning algorithms have begun to address the need for standardized and unbiased approaches to NET quantification. Live-cell fluorescence microscopy enables the continuous monitoring of NET formation in real time, providing dynamic insights that static endpoint assays cannot capture (197).

The application of machine learning algorithms for single-cell NET labeling allows automated thresholding to measured parameters or the learning of classification boundaries directly from image data using convolutional neural networks (198,199). While these methods increase specificity and reduce bias introduced by manual thresholding, they have so far been applied using limited staining panels or narrowly focused deep learning-algorithms (198,200). These constrains hinder the development of generalizable classifiers capable of accurately resolving distinct phenotypes and distinguishing NETosis from other forms of cell death (199).

Several factors contribute to the phenotypic variability among NETting cells, making it challenging for stringent models or fixed parameters to capture the full spectrum of NETosis across cells of different origins. To address this, we present a comprehensive experimental framework integrating live-cell imaging to machine learning-assisted pixel and object classification for broad-spectrum identification of NETs and clear distinction from other types of cell death. The coupling of live-cell imaging with automated image analysis and machine-learning algorithms offers a powerful framework for high-throughput, reproducible assessment of NETosis dynamics across experimental contexts.

1.4 Hypertension

1.4.1 Overview and Epidemiological Context

Hypertension, defined as a sustained systolic blood pressure (SBP) ≥ 140 mm Hg or diastolic blood pressure (DBP) ≥ 90 mm Hg (201), remains the leading preventable risk factor for cardiovascular morbidity and mortality worldwide (202). It is broadly classified as primary or secondary hypertension. Primary hypertension accounts for approximately 90–95% of cases and arises without an identifiable cause, whereas secondary hypertension results from specific underlying conditions such as renal or endocrine disorders (203).

Affecting more than 30% of adults globally, elevated blood pressure contributes substantially to the overall burden of cardiovascular disease by promoting end-organ damage in the vasculature, kidneys, and heart (204,205). This damage underlies the increased incidence of ischemic heart disease, ischemic and hemorrhagic stroke, and chronic kidney disease among hypertensive individuals, making hypertension a major driver of premature death globally (204). Despite advances in detection and treatment, the prevalence of hypertension continues to rise with population aging and urbanization. While rates have declined in many high-income countries, they remain stable or are increasing in low- and middle-income regions (205).

1.4.2 Mechanisms of Hypertension

Blood pressure is regulated by a complex integration of renal, neural, endocrine, and vascular mechanisms that together maintain circulatory homeostasis (206). Among these, the renin-angiotensin-aldosterone system (RAAS) has long been recognized as a central regulator of blood pressure. The enzyme renin, primarily synthesized by juxtaglomerular cells in the afferent arteriole of the kidney, catalyzes the conversion of circulating angiotensinogen produced by the liver into angiotensin I, which is subsequently converted to angiotensin II (Ang II) by angiotensin-converting enzyme (ACE) in the pulmonary endothelium (207). Ang II acts as

a potent vasoconstrictor and stimulates aldosterone release from the adrenal cortex, which promotes sodium retention and extracellular fluid expansion (208,209). Beyond its classical renal effects, aldosterone also contributes to vascular dysfunction by activating mineralocorticoid receptors in endothelial and smooth muscle cells, leading to oxidative stress and impaired nitric oxide (NO) signaling (210).

Renal sympathetic nerve activation also contributes to blood-pressure elevation by enhancing renin release, promoting tubular sodium reabsorption, and reducing renal blood flow (211). Sustained stimulation can even induce phenotypic changes in vascular smooth muscle cells of the afferent arteriole, increasing local renin production (212).

The kidney's sodium-handling mechanisms are also critical in long-term blood-pressure regulation. Sodium transporters along the nephron govern natriuresis and diuresis, thereby determining circulating blood volume (213). In hypertension, alterations in the expression or localization of these transporters disrupt sodium balance and sustain elevated blood pressure (214). Such shifts in transporter activity can be mediated by Ang II, inflammatory cytokines, impaired NO bioavailability, and enhanced adrenergic signaling (206)

An increase in sympathetic outflow from the central nervous system is a common feature of hypertension (215). These efferent signals, which can be stimulated by central Ang II signaling, contribute to elevated blood pressure by promoting vasoconstriction and vascular remodeling, enhancing renal renin production and sodium retention, and triggering immune activation (215). In addition to these efferent mechanisms, afferent signals from adipose tissue can further enhance sympathetic activity, creating a feed-forward loop that sustains hypertension (216).

Oxidative stress acts as a unifying amplifier of the mechanisms underlying hypertension. Generation of ROS, enhanced by Ang II signaling and high salt intake, sustains elevated blood pressure by enhancing vascular tone and remodeling (217–219). ROS promote vascular stiffening through several mechanisms, including direct NO oxidation and inactivation, increased renal sodium reabsorption, and stimulation of sympathetic outflow (220). Collectively, oxidative pathways reinforce the maladaptive feedback loops that lead to endothelial dysfunction and perpetuate hypertension.

1.4.3 Vascular Dysfunction and End-Organ Damage

Notable structural and functional changes occur in the vasculature during hypertension, both as a consequence of elevated blood pressure and a driver of its pathogenesis. Increased systemic vascular resistance arises from enhanced local concentrations of vasoconstrictor hormones including Ang II, catecholamines, and vasopressin, as well as from impaired endothelium-dependent vasorelaxation due to reduced NO bioavailability (221). Sustained activation of these pathways promotes vascular remodeling, characterized by hypertrophy of vascular smooth muscle cells and luminal narrowing (222), by increasing the activity of matrix metalloproteinases and collagen deposition (206).

The vascular alterations characteristic of hypertension are both hallmarks and drivers of subsequent cardiac, cerebral, and renal complications (223). Vascular stiffness enhances the transmission of pressure into the microcirculation, predisposing to barotrauma and endothelial damage in target organs (224). Accordingly, increased pulse wave velocity, reflecting aortic stiffening, can precede the onset of hypertension and serves as a strong predictor of stroke, myocardial infarction, and renal failure (225).

Endothelial dysfunction is key feature of hypertensive vascular injury, marked not only by diminished NO-mediated vasorelaxation but also by a phenotypic shift toward an activated,

pro-inflammatory, and pro-thrombotic state. In this context, ECs display increased proliferation, altered morphology, upregulated adhesion molecule expression, and enhanced thrombogenicity, further compromising vascular homeostasis and promoting leukocyte adhesion and infiltration (226,227). Together, these endothelial alterations promote atherosclerosis and increase the incidence of cardiovascular events (228–230).

Sustained hypertension progressively damages the microvasculature, with small artery remodeling representing one of the earliest manifestations of end-organ damage (229). Microvascular remodeling contributes to vessel rarefaction, defined by a reduction in vessel density that can become irreversible with sustained vasoconstriction and immune activation (231,232). Progressive endothelial dysfunction further impairs microvascular regeneration, resulting in hypoxia that drives renal ischemia, interstitial fibrosis, and ischemic-hypoxic injury in cerebral white matter (233). These target-organ injuries lead to renal dysfunction and cerebral autoregulatory impairment, which in turn exacerbate cardiovascular risk factors such as dyslipidemia, diabetes, and atherosclerosis, and contribute to cognitive decline and dementia (232,234)

1.4.4 Inflammatory and Immune Contributions

While genetic predispositions, dietary habits and environmental factors are well-established contributors, emerging evidence identifies chronic low-grade inflammation as a hallmark of hypertension and a major driver of its pathogenesis (220,235). The immune landscape of hypertension involves both innate and adaptive immune cells. Prominent roles have been described for T and B lymphocytes, monocytes, and macrophages, whose activation leads to the release of pro-inflammatory mediators such as interleukin-17 (IL-17), interleukin-18 (IL-18), interferon-γ (IFN-γ) and tumour necrosis factor, collectively sustaining vascular inflammation and remodeling (236).

Innate immune cells are activated early in hypertension, releasing cytokines and chemokines that recruit and activate T and B cells (237,238). Activated T cells subsequently differentiate into T helper 1 (Th1) and T helper 17 (Th17) effector subsets that modulate inflammation and vascular dysfunction, further exacerbating hypertension (239–241). In contrast, regulatory T cells (Tregs) exert protective effects by suppressing immune cell activation through the release of interleukin-10 (IL-10), which limits vascular injury (242).

T cell activation in hypertension can also be driven by neoantigens generated under oxidative stress, such as isolevuglandin-modified proteins and heat shock protein 70 (236). These neoantigens stimulate antigen-presenting dendritic cells, which further activate and recruit T cells to target organs (237). The neuroimmune axis represents another mechanism of immune modulation in hypertension, whereby increased sympathetic nerve activity enhances the proliferation and trafficking of T cell subsets to peripheral tissues (243,244).

Tissue sodium accumulation also acts as an immunostimulatory signal. Elevated interstitial sodium concentrations activate monocytes, drive macrophages toward a pro-inflammatory M1-like phenotype and promote IL-17A production by T cells (245–247). The hypertensive milieu further alters the transcriptional profile of immune cells, increasing chemokine receptor expression and pro-inflammatory cytokine production (236).

Effector cytokines such as IL-17 and IFN-γ directly contribute to endothelial dysfunction by reducing nitric oxide bioavailability through inhibition of endothelial nitric oxide synthase (eNOS) and by promoting oxidative stress (248,249). In contrast, Tregs counteract these effects via IL-10-mediated suppression of inflammatory signaling (242).

Both the kidney and vasculature serve as major sources and targets of immune activation in hypertension (228), exhibiting increased homing of myeloid and T cells (236). The activated

endothelium facilitates monocyte adhesion and transmigration, allowing for their differentiation into macrophages and dendritic cells that further amplify T cell activation and cytokine release (250). Upregulation of pattern recognition receptors, including TLR2 and TLR4, in hypertensive tissues enhances NOD-like receptor family pyrin domain containing-3 (NLRP3) inflammasome activation, promoting leukocyte recruitment and perpetuating vascular inflammation (236,251,252).

Collectively, these immune mechanisms establish a self-perpetuating cycle of inflammation, vascular dysfunction, and end-organ injury that underlies the progression of hypertension (220). While much of this immune response has been attributed to lymphocytes and macrophages, increasing evidence points to an important yet underexplored role for neutrophils in mediating vascular inflammation (253,254). In hypertension, neutrophils adopt a pro-inflammatory and activated phenotype, but their precise contribution to disease progression remains incompletely understood (255,256)

1.4.5 Neutrophils and NETs in Hypertension

Among the inflammatory changes associated with immune dysregulation, marked shifts in granulocytic populations have been reported and may influence disease progression. One prominent change is the emergence of a pro-inflammatory neutrophil phenotype. In hypertensive patients, the neutrophil-to-lymphocyte ratio (NLR), a common biomarker of systemic inflammation, is elevated and often accompanied by increased circulating neutrophil counts (257). Evidence from both clinical and experimental models indicates that neutrophils in hypertension adopt a heightened oxidative and pro-inflammatory phenotype, reflected by increased ROS generation in patients (258), and elevated inducible nitric oxide synthase (iNOS) and MPO activity in spontaneously hypertensive rats (259). This heightened activation can lead

to aberrant neutrophil function, including increased degranulation and ROS production, ultimately promoting host-tissue injury (260).

A key mechanism underlying neutrophil-mediated damage is the formation of NETs (261). NET release is increased in the vasculature and peripheral tissues of hypertensive subjects, and NETosis deficiency ($PAD4^{-/-}$) has been shown to reduce blood pressure, implicating NETs as active contributors to hypertension pathogenesis (262). PAD4 activation is stimulated by elevated blood pressure and oxidative stress, leading to chromatin decondensation and NET release through ROS-dependent pathways (263). Consistent with this, increased circulating NET levels have been detected in hypertensive patients (264).

Although the precise mechanisms driving this response remain incompletely understood, some evidence indicates that NET accumulation is associated with vascular smooth muscle cell proliferation and medial thickening, linking NETs to vascular remodeling (265). Hypertensive mechanical stretch of the endothelium promotes its activation and the release of ROS and pro-inflammatory mediators, which have been associated with increased NETosis (262).

Ang II has also emerged as a potential inducer of NETosis, with *in vitro* studies reporting NET release following exposure to Ang II and plasma from patients with essential hypertension (266–268). Recent evidence showed that treatment with Ang II receptor blockers reduces levels of circulating NETs in hypertensive patients, further supporting a possible role for Ang II in neutrophil activation (267).

Current evidence thus links neutrophilia and neutrophil dysfunction to hypertensive cardiovascular inflammation, with several studies suggesting a direct involvement of neutrophils in blood pressure regulation (269,270). While exposure to mechanical stretch and Ang II are recognized triggers of aberrant neutrophil activity (267,269), substantial heterogeneity reported

among neutrophil subpopulations, spanning differences in maturation stage, effector function and transcriptional profile, suggest that these changes may extend beyond transient activation and may reflect a more fundamental reprogramming of neutrophil function (269,271,272)

1.5 NETs in Vascular Injury

1.5.1 NETs in Vascular Inflammation

NETs act as potent drivers of vascular inflammation by engaging multiple immune and vascular cell types within the vessel wall (273). ECs sense various NET components through pattern-recognition receptors such as TLR2 and TLR4, activating NF-κB signaling and shifting the endothelium toward a pro-inflammatory phenotype characterized by increased IL-1β production and upregulation of adhesion molecules including vascular cell adhesion molecule-1 (VCAM-1) and ICAM-1 (274–277). This activated endothelial state enhances leukocyte adhesion and promotes cytokine and chemokine release, creating a local inflammatory environment within the vessel wall (278–280)

Beyond ECs, NET structures directly recruit and activate immune cells. Histone-rich DNA scaffolds promote monocyte, macrophage, and lymphocyte adhesion through charge-dependent interactions and histone-mediated binding mechanisms (273). NET-derived antimicrobial peptides such as LL-37 further enhance leukocyte recruitment by binding to endothelial surfaces and reinforcing chemokine production (281). These interactions amplify local immune cell accumulation and inflammatory signaling within the vascular microenvironment (282).

A central mechanism linking NETs to vascular inflammation is activation of the NLRP3 inflammasome (283). NET components stimulate NLRP3 activation in various immune cells and ECs (284,285). This process involves TLR-dependent sensing of histones and cathelicidin, which activates NF-κB and promotes IL-1β maturation and release (286–288).

In macrophages, NET-induced release of IL-1β via inflammasome activation activates a Th17 response that drives further leukocyte recruitment to the vessel wall (273,289). Exposure to NET-derived MPO and LL-37 also prompts macrophages to release ROS and other pro-inflammatory factors that promote the formation of foam cells, that can compromise the integrity of the endothelium (290,291).

NET components also activate DCs and B lymphocytes through their DNA-protein cargo, inducing robust type I interferon (IFN-1) responses that propagate vascular inflammatory signaling (273,292). Mitochondrial DNA released during NETosis can further amplify inflammation by promoting additional NETosis and upregulation of NET-associated mediators such as NE and ROS (290).

Complement activation represents another major pathway through which NETs intensify vascular inflammation (293). MPO-rich NETs can interact with ANCAs, forming MPO–ANCA complexes that activate the complement cascade to promote vascular injury (294,295). This establishes a feed-forward loop wherein complement activation promotes additional NETosis, further amplifying leukocyte recruitment and inflammatory mediator release within affected vascular beds (296)

Together, these mechanisms position NETs as central coordinators of vascular inflammation. Through endothelial activation, immune cell recruitment, inflammasome engagement, dendritic cell stimulation, and complement-driven amplification, NETs orchestrate a self-sustaining inflammatory network that disrupts vascular homeostasis and contributes to chronic vascular inflammatory diseases.

1.5.2 NET-induced Endothelial Dysfunction

NETs released into the circulation can impair endothelial function through both direct and indirect mechanisms (49). During sustained inflammatory stimulation, excessive NET

release increases vascular permeability and tissue injury, contributing to the development of sepsis and multi-organ failure (142,276). Several NET components induce EC pyroptosis and apoptosis and disrupt the endothelial glycocalyx, resulting in profound structural and functional impairment of the vascular barrier (275–277,297). Consistent with these effects, NETs have been implicated as drivers of vascular necrosis in inflammatory diseases (132,298).

Many endothelial-injurious effects of NETs arise from the cytotoxic activity of NET-bound histones and granular enzymes. Histones bind to phospholipids within endothelial membranes and disrupt intercellular junctions, inducing membrane permeabilization and excessive calcium influx via TLR4-dependent pathways, culminating in EC death (143,299,300). Citrullinated histones produced during NETosis further amplify EC inflammation, as observed in acute inflammatory states such as sepsis (301)

In addition to membrane disruption, several NET-associated proteases degrade key extracellular matrix components and compromise endothelial structural integrity. MPO and matrix metalloproteases (MMPs) bind endothelial glycosaminoglycans and degrade matrix proteins, promoting endothelial activation and facilitating leukocyte recruitment (302,303). NE amplifies matrix injury by activating MMP-9 and degrading its inhibitor metalloproteinase-1 tissue inhibitor (TIMP-1), thereby enhancing proteolytic damage (304). NET-associated MPO and LL-37 further damage exposed endothelial matrix surfaces and promote additional MPO attachment (273). Proteinase-3 (PR3) can also bind directly to ECs, inducing cellular senescence and apoptosis (305). Together, these NET-associated enzymes drive structural endothelial injury, loss of barrier homeostasis, and direct EC death (299).

Beyond inducing cell death, NETs modulate endothelial function through inflammatory signaling pathways. Histone-mediated TLR2/4 activation upregulates endothelial tissue factor

expression via NF-κB and activator protein-1, promoting a pro-coagulant phenotype and contributing to vascular dysfunction (274,306). NETs can also directly activate the NLRP3 inflammasome within ECs, increasing levels of cleaved IL-1β and driving endothelial stress and dysfunction (286,307).

NETs further impair endothelial vasodilatory function by disrupting NO signaling. Exposure to NETs reduces eNOS expression and phosphorylation, effects partly mediated by NET-associated MPO (285,308). MPO-derived oxidants impair L-arginine uptake and activate μ-calpain, which inhibits eNOS phosphorylation and reduces NO bioavailability, resulting in blunted endothelial-dependent vasodilation (309).

Collectively, NET components act through cytotoxic, proteolytic, and inflammatory pathways to impair endothelial integrity and promote vascular dysfunction.

1.5.3 PAD4-Dependent Mechanisms of Vascular Injury

Despite the existence of alternative NETosis pathways, PAD4 remains a central mediator of NET formation and NET-driven vascular injury. Pharmacological or genetic inhibition of PAD4 markedly reduces NET release and has been shown to improve vascular inflammation and endothelial function across multiple disease models (310,311).

PAD4 inhibition limits NET-associated activation of IFN-1 signaling and the inflammasome, thereby preserving endothelial membrane and preventing NET-induced increases in vascular permeability (285,310). Consistent with this, PAD4 blockade reduces neutrophil infiltration and mitigates downstream endothelial injury, underscoring the importance of PAD4-dependent NETosis in the development of vascular dysfunction (180,285).

1.5.4 NET-induced Endothelial Senescence

Senescence is a stress-induced program of permanent cell cycle arrest that prevents the propagation of damaged cells yet becomes maladaptive when persistent during chronic injury

(312,313). Although non-proliferative, senescent cells remain metabolically active and acquire a pro-inflammatory secretory phenotype that disrupts tissue homeostasis.

Senescence is initiated through activation of the p53/p21 and $p16^{INK4a/Rb}$ tumor suppressor pathways in response to DNA damage, oxidative stress, or chronic inflammatory signals (313). These pathways enforce irreversible cell cycle exit and promote transcriptional reprogramming through NF-κB signaling and inflammasome activation (314,315). This reprogramming leads to the development of the senescence-associated secretory phenotype (SASP), marked by heightened expression of pro-inflammatory cytokines, chemokines, and matrix-modifying enzymes that alter the local microenvironment and can induce senescence in neighboring cells, impairing tissue repair and function (316,317)

Endothelial senescence contributes to vascular injury by impairing angiogenesis and barrier repair while creating a chronic inflammatory and pro-thrombotic microenvironment (318,319). Senescent ECs exhibit increased inflammatory signaling, reduced NO bioavailability, and compromised tight junction integrity, all of which promote endothelial dysfunction and the development of cardiovascular diseases (320–322). Accordingly, endothelial senescence has been linked to stroke, atherosclerosis, diabetes, and hypertension (323). In addition, SASP-associated MMPs degrade extracellular matrix components and increase arterial stiffness, further exacerbating vascular dysfunction and elevating the risk of hypertension (324).

Emerging evidence links NETs to impaired endothelial regeneration and vascular repair during inflammatory injury, suggesting that NETs may contribute to endothelial senescence (325,326). NET exposure has been shown to induce cell cycle stasis and p21 upregulation in ECs (326). Conversely, senescent ECs can attract leukocytes and promote NET release within diseased vessels, indicating a bidirectional relationship in which NETs may both induce

senescence and participate in the clearance of senescent cells (327). Given the overlap between NET-induced endothelial activation and functional impairment with senescent-associated changes, clarifying whether NETs drive true endothelial senescence and defining the mechanisms involved is an important next step.

1.6 Thesis Objectives and Hypotheses

NETs have gained increasing attention over the past two decades for their essential antimicrobial functions as well as their deleterious effects across a wide range of diseases (46). Although key molecular mediators of NET formation have been identified, important gaps remain in our understanding of how NETs are regulated across different biological contexts, limiting the development of therapeutics. Addressing these gaps requires methodological tools capable of resolving the dynamics and heterogeneity of NET formation. Thus, **Chapter 3** of this thesis describes the development and validation of an improved NETosis assay that overcomes limitations of existing methodologies and enables quantitative analysis of NET release.

Beyond their role in host defense, NETs have been strongly implicated in cardiovascular and renal pathology, including hypertension (263,264). While associations between elevated NET formation and increased blood pressure have been reported, the mechanistic basis linking NETosis to hypertension remains poorly understood (262). Given the central role of the kidney in blood pressure regulation and the emerging evidence that NETs contribute to kidney injury (328,329), **Chapter 4** of this thesis investigates how NETosis is altered in Ang II–induced hypertension and whether changes in NET formation are associated with renal injury.

We **hypothesized** that Ang II–induced hypertension alters NETosis dynamics, leading to increased NET release in the kidney, thereby promoting renal leukocyte recruitment and kidney injury, and that NET deficiency would protect against these outcomes.

NETs are also known to impair endothelial function, promoting inflammation, barrier disruption, and defective vascular repair (132,298). Recent evidence demonstrating that NETs suppress endothelial regeneration raises the possibility that NETs promote a senescence-like program in ECs, thereby contributing to vascular dysfunction (326). Accordingly, **Chapter 5** of this thesis characterizes the transcriptional and functional responses of ECs to NET exposure, with a focus on determining whether NETs induce early features of endothelial senescence.

We **hypothesized** that NET exposure initiates transcriptional reprogramming in ECs involving dysregulation of cell cycle control and senescence-associated pathways, and that this early transcriptional response promotes senescence-like features and impaired endothelial replication.

Overall, the **central hypothesis** of this thesis is that dysregulated NET formation contributes to vascular and renal injury through context-dependent mechanisms that include altered NETosis dynamics in hypertension and the induction of senescence-associated pathways in ECs.

Chapter 2

Materials & Methods

2.1 Animals

2.1.1 Mouse Model and Husbandry

PAD4-deficient (Padi4$^{-/-}$) mice were obtained from The Jackson Laboratory (strain: B6.Cg-Padi4$^{tm1.1Kmow}$/J) and initially maintained on a C57BL/6J background. To generate Padi4$^{-/-}$ mice on an FVB/N background, the line was backcrossed with WT FVB/N mice for more than 12 generations. For colony maintenance, Padi4$^{-/-}$ homozygous mice were bred with WT FVB/N mice to sustain the colony and to generate heterozygous breeders. Both male and female homozygous Padi4$^{-/-}$ and WT littermates were used for experiments. All animal procedures were conducted in accordance with the guidelines of the Canadian Council on Animal Care and approved by the University of Ottawa Office of Animal Ethics and Compliance.

2.1.2 Genotyping

Ear clips were collected at weaning for genomic DNA extraction. Tissue samples were processed using the Extract-N-Amp™ Tissue PCR Kit (Millipore-Sigma) according to the manufacturer's instructions. Genotyping PCR was performed on a thermocycler under the following conditions: initial denaturation at 94°C for 3 minutes, followed by 35 cycles of denaturation at 94°C for 30 seconds, annealing at 68°C for 30 seconds, and extension at 72°C for 1 minute, and a final extension at 70°C for 10 minutes. Amplified PCR products were run on a 1.8% agarose gel containing GelRed® Nucleic Acid Stain (Millipore-Sigma) and visualized under UV illumination. Genotyping primers for *Padi4* are listed in Table 2.1.

2.1.3 Osmotic Minipump Insertion

To induce hypertension, osmotic minipumps (Alzet) containing Ang II were surgically implanted subcutaneously. Twenty-four hours prior to surgery, Ang II (Bachem) solutions were prepared in sterile 0.9% NaCl at a concentration calculated from the average mouse weight to

deliver 1000 ng/kg/day. Each pump was filled with 100 uL of the Ang II solution and incubated in sterile saline at 37°C for 24 hours to ensure proper priming.

One hour prior to surgery, mice received a subcutaneous injection of slow-release buprenorphine (1 mg/kg). Anaesthesia was induced and maintained with 2-3% isoflurane, and each mouse received a 1 mL subcutaneous injection of sterile 0.9% NaCl. Ophthalmic ointment was applied to both eyes to prevent corneal drying. Minipumps were inserted subcutaneously in the subscapular region through a small incision made perpendicular to the spine, with the delivery portal positioned first. The wound was closed using a single subcuticular 6-0 Prolene suture and secured with a wound clip. Following surgery, mice were placed in a heated recovery chamber until fully awake and were monitored for 48 hours post-procedure. Ang II minipumps remained implanted for two weeks prior to euthanasia.

2.1.4 Blood Pressure Measurement

Blood pressure was measured by tail-cuff plethysmography using the BP-2000 Blood Pressure Analysis System (Visitech Systems). Mice were acclimated to the system for five consecutive days prior to baseline measurements to reduce stress-related variability. Measurements were taken at baseline (before pump implantation), one week post-implantation, and at endpoint. For each session, five preliminary practice measurements were measured to allow mice to acclimate, followed by ten recorded measurements. The reported blood pressure value for each mouse represents the mean of the ten recorded readings.

2.1.5 Cardiac Puncture Blood Collection

At the experimental endpoint, blood was collected via cardiac puncture under anesthesia with 2-3% isoflurane. The thoracic area was sterilized with 70% ethanol, and a 1 mL syringe was coated with heparin and fitted with a 25-gauge needle which inserted through the thoracic wall into the left ventricle. Gentle suction was applied to collect approximately 0.8–1.0 mL of blood.

Blood samples were centrifuged at 2000 x g for 10 min to separate plasma, which was then stored at -80°C until analysis. Following cardiac puncture, mice were euthanized by cervical dislocation in accordance with the Canadian Council on Animal Care guidelines and approved institutional protocols.

2.2 Histology

2.2.1 Tissue Collection and Processing

The right kidneys were extracted and bisected longitudinally. One half was fixed in 10% neutral buffered formalin for 24 hours and then transferred to 70% ethanol for storage at 4°C. Fixed samples were sent to the University of Ottawa Louise Pelletier Histology Core Facility for processing, paraffin embedding, and sectioning at 5 μm. The remaining half was fresh-frozen in optimal cutting temperature (OCT) compound using liquid nitrogen and stored at -80°C until sectioning.

2.2.2 Immunohistochemistry

Paraffin-embedded tissue sections were deparaffinized in xylene and rehydrated through graded ethanol washes. Heat-induced antigen retrieval was performed by submerging slides in 10 mM sodium citrate buffer (pH 6.0) and boiled in the microwave for 20 minutes. Sections were then incubated with 0.3% hydrogen peroxide in PBS for 10 minutes to quench endogenous peroxidase activity. Non-specific binding was blocked using 10% normal donkey serum in 1% BSA in PBS for 40 minutes at room temperature. The appropriate primary antibody, outlined in Table 2.2, was diluted in 1% BSA in PBS and incubated with the sections overnight at 4°C in a humidity chamber. After three washes in PBS, sections were incubated with ImmPRESS™ Horse Anti-Rabbit IgG HRP polymer reagent (Vector Laboratories) for 30 minutes at room temperature. Signal was developed using in DAB substrate for 5 minutes, and nuclei were

counterstained with Mayer's hematoxylin for 40 seconds. Slides were dehydrated in ethanol, cleared and mounted with Acrytol® Mounting Medium.

2.2.3 Immunofluorescence

Fresh-frozen kidneys were sectioned at 10 μm using a cryostat, mounted on microscope slides, and fixed in 4% PFA for 10 minutes at room temperature. Non-specific binding was blocked using 2.5% normal horse serum in 1% BSA in PBS for 40 minutes at room temperature. The primary antibody (Table 2.2) was diluted in 1% BSA in PBS and incubated with the sections overnight at 4°C in a humidity chamber. After three washes in PBS, sections were incubated with the appropriate fluorescently conjugated secondary antibodies for 1 hour at room temperature in the dark. Sections were counterstained with Hoescht (1 μg/mL) in double-distilled water for 10 minutes in the dark, followed by a rinse in deionized water. Slides were mounted with Vectashield® Mounting Medium (Vector Laboratories) and imaged using a Zeiss Axio Observer 7 fluorescence microscope.

2.3 Cell Culture

2.3.1 Kidney Neutrophil Isolation

At animal study endpoint, the renal capsule was removed from the left kidney, which was then placed in sterile PBS on ice. Kidneys were promptly transferred to digestion media containing Iscove's Modified Dulbecco's Medium (IMDM) supplemented with 10% fetal bovine serum (FBS, Wisent), 1% penicillin-streptomycin, 10 μg/mL Type 1 collagenase (Millipore-Sigma), 10 μL/mL DNase (Thermo Fisher Scientific) and 0.1 mM β-mercaptoethanol. Digestion media was injected at 5-6 distinct sites per kidney using a 1 mL syringe and 25-gauge needle prior to incubation at 37°C with gentle agitation. After 30 minutes, the tissue was mechanically dissociated using the plunger of a sterile 3 mL syringe, followed by an additional 15-minute

incubation. The reaction was stopped stop by adding ice-cold PBS, and the tissue was gently triturated using a 1 mL pipette until no visible fragments remained.

The cell suspension was filtered through a 70 µm nylon mesh sieve and centrifuged at 250 x g for 5 minutes at 4°C twice, washed once with complete MACS buffer, and centrifuged again under the same conditions. The resulting pellet was resuspended in 600 µL MACs buffer and incubated with 40 µL CD11b MicroBeads (Miltenyi Biotec) for 15 minutes at 4°C.

After incubation, the suspension was centrifuged at 200 x g for 2 minutes, resuspended in 5 mL MACS buffer, and passed through a 40 µm cell strainer into an equilibrated LS column (Miltenyi Biotec) mounted on a magnetic holder, as per the manufacturer's instructions. $CD11b^+$ cells were eluted by removing the column from the magnetic separator and flushing with 5 mL MACS buffer.

2.3.2 Bone Marrow Neutrophil Isolation

At animal study endpoint, bone marrow was isolated from the femur according to a previously described protocol (330). Briefly, muscle and connective tissue were removed from the femoral bone, and the condyles, the patella, and the epiphysis were excised with scissors to expose the metaphysis. The femur was placed knee end down in a 0.5 mL microcentrifuge tube nested in a 1.5 mL microcentrifuge tube and centrifuged at ≥10,000 x g for 15 seconds to collect the bone marrow.

Bone marrow cells were processed for negative immunomagnetic selection of neutrophils using the Mouse Neutrophil Isolation Kit (Miltenyi Biotec), in which all non-neutrophil populations were depleted by incubation with a cocktail of biotinylated antibodies and anti-biotin magnetic microbeads, followed by magnetic column separation, according to the manufacturer's instructions. Typical yields ranged from 2-9 x 10^6 neutrophils per femur.

2.3.3 Promyelocytic HL-60 Cell Line

HL-60 cells, a human promyelocytic leukemia cell line, were cultured in IMDM with phenol red (Thermo Fisher Scientific), supplemented with 10% FBS and 1% penicillin-streptomycin. Cells were maintained at a density between 1-5 x 10^5 cells/mL by diluting cultures every 2-3 days to ensure optimal viability. Cultures were incubated at 37 °C in a humidified atmosphere containing 5 % CO_2.

Differentiation toward neutrophil-like cells was induced by transferring cells into complete culture medium containing 1.25% dimethyl sulfoxide (DMSO) at a final density of 4x10^5 cells/mL, followed by incubation under the same conditions for five days, as previously described (331). After differentiation, cell viability was assessed using Trypan Blue exclusion, and differentiated cultures with ≥75% viability were used for subsequent experiments.

2.3.4 NET Isolation

To induce NET release, 9 x 10^6 neutrophil-differentiated HL-60 cells were seeded in a 150 mm culture dish at a density of 3 x 10^5 cells in serum-free IMDM medium (Thermo Fisher Scientific) supplemented with 1% penicillin-streptomycin. Cells were stimulated with 200 nM PMA (Millipore-Sigma) for 4 hours at 37°C in a humidified incubator with 5% CO_2.

Following stimulation, the culture medium containing released NETs was collected into a 50 ml tube. The dish was then gently washed with cold sterile PBS without Ca^{2+} and Mg^{2+} to recover any adhered cells and NETs. The wash was combined with the initial supernatant.

The pooled suspension was first centrifuged at 450 x g for 10 minutes at 4 °C to pellet and remove any remaining intact cells. The resulting supernatant was centrifuged again at 2500 x g for 10 minutes at 4 °C to eliminate any cell debris, yielding a cell-free, NET-rich supernatant.

To isolate NETs, the supernatant was centrifuged at 18 000 x g for 10 minutes at 4 °C. The supernatant was discarded, and the resulting pellet was washed with 1 mL of cold PBS and

centrifuged again under the same conditions. The final NET pellet was resuspended in 25 µl of ice-cold PBS, generating a cell-free NET stock used to treat cells for subsequent experiments.

The concentration of NET-associated DNA in the resuspended pellet was determined using the Quant-iT™ PicoGreen dsDNA Assay Kit (Thermo Fisher Scientific) according to the manufacturer's instructions. Fluorescence was measured using a microplate reader (excitation/emission: 480/520 nm) and absorbance was normalized to the standard curve. NET preparations were normalized to a final concentration of 10 ng/µL DNA and stored at –80 °C until use.

2.3.5 HUVEC Cell Line

Human Umbilical Vein Endothelial Cells (HUVECs) were obtained from ATCC and maintained in complete EndoMax™ culture medium (Wisent) supplemented with 1% penicillin-streptomycin. Cells were cultured at 37 °C in a humidified incubator with 5% CO_2. The medium was replaced every 2-3 days, and cells were passaged as needed at ~80-90% confluence using 0.05% trypsin-EDTA. HUVECs between passages 4 and 8 were used for all experiments to ensure consistent endothelial phenotype and avoid senescence-related alterations.

2.3.6 Viability Assay

To assess cell viability, 1 x 10^3 HUVECs were seeded per well of a 96-well plate and allowed to adhere overnight. Cells were then treated with NETs for 24 hours. Cell viability was quantified using the Presto Blue™ Cell Viability Reagent (Thermo Fisher Scientific) according to the manufacturer's instructions. Fluorescence was measured 10 minutes after reagent addition using a microplate reader (excitation/emission: 560/590 nm). Alternatively, viability was assessed using the XTT assay (Cayman Chemical) according to the manufacturer's instructions.

All samples were analyzed in technical duplicate and repeated in at least three independent experiments.

2.3.7 Proliferation Assay

To assess cell proliferation, 1 x 10^3 HUVECs were seeded per well of a 96-well plate and allowed to adhere overnight. Cells were then treated with NETs for 48 hours. Cell proliferation was quantified using the BrdU Cell Proliferation Assay Kit (Roche) following the manufacturer's protocol. BrdU labelling solution was added during the final 24 hours of incubation, and absorbance was measure at 270 nm using a microplate reader. All samples were analyzed in technical triplicate and repeated in at least three independent experiments.

2.3.8 Senescence Assay

Senescence-associated β-galactosidase activity was measured using the Senescence Assay β-Galactosidase Activity Assay Kit (Cell Signaling Technology) according to the manufacturer's protocol. HUVECs were seeded to a 12- or 24-well plate to ~80% confluence, allowed to adhere, and treated with NETs for 24 hours. After treatment, the cells were lysed with the buffer provided with the kit. Protein concentration was determined using the DC Protein Assay (Bio-Rad) according to manufacturer's instructions. For the β-galactosidase assay, protein lysates were diluted to a final concentration of 0.02 mg/mL and incubated with the assay buffer in a black 96-well plate for 2 hours at 37°C. Fluorescence was then measured using a microplate reader (excitation/emission:360/465 nm). All samples were analyzed in technical duplicate and repeated in at least three independent experiments.

2.3.9 Senescence Imaging

HUVECs were seeded at 5 x 10^4 cells per well in a 12-well plate and allowed to adhere overnight. Cells were then treated with NETs for 24 hours. Senescence-associated β-galactosidase levels were visualized using the Senescence β-Galactosidase Staining Kit (Cell

Signaling Technology) according to the manufacturer's instructions. After treatment, cells were fixed and incubated with the β-galactosidase staining solution for 24 hours at 37°C in a dry incubator. Stained cells were imaged under brightfield illumination using an EVOS FL Auto 2 imaging system (Thermo Fisher Scientific) at 20x magnification. All samples were analyzed in technical triplicate and repeated in at least three independent experiments.

2.3.10 NETosis Assay

Assay preparation

Each well of a 96-well flat bottom culture microplate (Corning) was coated with 0.1 mg/mL fibronectin from bovine plasma (Millipore-Sigma) in PBS and incubated at room temperature for 1 hour. The assay culture medium consisted of serum-free IMDM (phenol red-free) supplemented with 250 nM Incucyte® Cytotox Green Dye (Sartorius) and 30 ng/mL PE Annexin V (Biolegend). Neutrophils were resuspended in this medium and seeded at a density of 2 x 10^4 cells per well. Treatments were added to a final volume of 200 µL per well.

Cells and treatments

Neutrophil differentiated HL-60 cells, as described above, were used to compare NETosis dynamics between different inducers and to assess the contribution of PAD4 with both PMA and ionomycin stimulation. The NETosis assay was repeated five times using independent batches of differentiated cells, with three replicate wells per treatment. Cells were either left untreated or treated with 0.2, 2, 20, or 200 nM PMA (Millipore-Sigma) or 5 µM ionomycin (Millipore-Sigma). In separate wells, cells were pre-treated with 20 µM GSK484 (Cayman Chemical), a selective PAD4 inhibitor (107), for 30 minutes prior to stimulation with either 200 nM PMA or 5 µM ionomycin.

Isolated mouse kidney and bone marrow neutrophils were also subjected to the live-cell NETosis assay and either left untreated or stimulated with 100 nM PMA, with three replicate wells per animal.

Live-cell imaging

Images were acquired using the Incucyte® S3 Live-Cell Imaging and Analysis System (Sartorius) at 20x magnification in the green, red, and phase contrast channels. For each well, 2-3 fields of view were captured every hour over a total duration of 12 or 24 hours. Default acquisition settings were used, with exposure times of 300 ms for the green channel and 400 ms for the red channel, and standard focus offsets applied by the Incucyte software (v2023A). The imaging system was maintained at 37°C with 5% CO_2 throughout the experiment.

2.4 Protein and RNA Expression Analysis

2.4.1 Protein Extraction

Cells were lysed in radioimmunoprecipitation assay (RIPA) buffer containing 150 mM sodium chloride, 1% Triton X-100, 0.5% sodium deoxycholate, 0.01% sodium dodecyl sulfate (SDS), 50 mM Tris (pH 8.0), supplemented with 1:100 dilution of protease inhibitor cocktail (Millipore-Sigma). Lysates were incubated at 4°C for 30 minutes with gentle agitation, followed by sonication for 1 minute to ensure complete cell disruption. Samples were then centrifuged at 12 000 rpm for 10 minutes at 4°C to pellet and remove insoluble debris. Protein concentrations were determined using the DC Protein Assay (Bio-Rad) according to manufacturer's instructions.

2.4.2 Western blotting

For each sample, 20-30 ng of protein was mixed with Laemmli SDS sample buffer (Alfa Aesar) and topped up with RIPA buffer to a final volume of 25 µL. Samples were denatured at 95°C for 5 minutes and loaded onto a 12% polyacrylamide gel. Electrophoresis was performed

for 1 hour at 120 V in SDS running buffer, after which proteins were transferred onto a nitrocellulose membrane at 100 V for 40 minutes in transfer buffer.

Membranes were blocked with 5% milk in TBS-T (20 mM Tris-HCl, 150 mM NaCl, 0.1% Tween-20, pH 7.6) for 40 minutes and incubated overnight at 4°C with the appropriate primary antibodies (Table 2.2) diluted in 5% milk in TBST-T with gentle agitation. Following incubation, membranes were washed three times with TBS-T for five minutes each at room temperature.

The appropriate horseradish peroxidase (HRP)-conjugated secondary antibodies (Table 2.2) were diluted in 5% milk in TBS-T and incubated with the membranes for 1 hour at room temperature with gentle agitation. Membranes were then washed three times with TBS-T for 5 minutes each. Protein bands were visualized using Pierce™ ECL Western Blotting Substrate (Thermo Fisher Scientific) and imaged using a ChemiDoc Imaging System (Bio-Rad) with the optimized exposure settings. Band intensities were quantified using Image Lab (Bio-Rad) and normalized to β-tubulin as a loading control.

2.4.3 RNA Extraction

Total RNA was isolated using the RNeasy Mini Kit (Qiagen) according to the manufacturer's protocols. Cells and tissues were disrupted and homogenized in RLT buffer provided with the kit, then passed through QIAShredder columns (Qiagen) to ensure complete homogenization. The resulting lysates were applied to RNeasy spin columns to complete RNA extraction and purification. RNA was eluted in RNase-free water and quantified using a spectrophotometer by measuring absorbance at 260/280 nm.

Equal amounts of RNA from each sample were subjected to DNase I digestion using amplification-grade DNase I (Thermo Fisher Scientific) according to the manufacturer's instructions. Purified RNA samples were stored at -80°C until use.

2.4.4 Reverse Transcription and cDNA Synthesis

Complementary DNA (cDNA) was synthesized from purified RNA using the High-Capacity cDNA Reverse Transcription Kit (Applied Biosystems) according to the manufacturer's instructions. For each reaction, equal amounts of total RNA (5 ng) were added to PCR tubes containing the appropriate kit components. Reverse transcription was performed on a thermal cycler under the following cycling conditions: primer annealing at 25°C for 10 minutes, reverse transcription at 37°C for 120 minutes, and enzyme inactivation at 85°C for 5 minutes. The resulting cDNA samples were stored at –80 °C until use.

2.4.5 Quantitative Real-time PCR

Real-time quantitative PCR (RT-qPCR) was performed using the PowerUp™ SYBR™ Green Master Mix (Applied Biosytems) supplemented with 1.5 µL of the appropriate forward and reverse primers (10 µM). For each sample, duplicate reactions were prepared by dispensing the master mix into PCR tubes and adding 5 ng of cDNA template. Amplification was carried out on a CFX Opus 96 Real-Time System (Bio-Rad) under the following cycling conditions: 50°C for 2 minutes, 95°C for 2 minutes, followed by 40 cycles of denaturation at 95°C for 15 seconds and annealing and extension at 60°C for 1 minute.

Relative messenger RNA (mRNA) expression levels were calculated using the $2^{-\Delta\Delta CT}$ method, with glyceraldehyde-3-phosphate dehydrogenase (GAPDH) serving as the internal reference gene. All primer sequences used for RT-qPCR are listed in Table 2.1.

2.4.6 Library Preparation and Sequencing

Total RNA from HUVECs treated with 10 ng/mL of NETs or a vehicle control were submitted to Genome Québec (Montréal, Canada) for poly(A)-enriched stranded RNA sequencing. Libraries were prepared using the NEBNext Ultra II Directional RNA Library Prep Kit (New England Biolabs) and indexed with NEBNext dual indices. Sequencing was performed on an Illumina NovaSeq 6000 platform (2 × 100 bp paired end reads) with a run concentration of 140 pM. Each library yielded approximately 80–95 million read pairs with > 98% passing filter (PF) reads aligned to the *Homo sapiens* GRCh38 reference genome (average quality = Q39, median insert size ≈ 350 bp).

2.5 Bioinformatics

2.5.1 NETosis Assay Image Analysis Pipeline

Following image acquisition, uncalibrated images were exported as 8-bit PNG files for the phase-contrast channel and as 16-bit TIFF files for the green and red fluorescence channels.

ilastik cell segmentation

To facilitate cell segmentation in CellProfiler, phase-contrast images were first processed in ilastik (v.1.4.0; https://www.ilastik.org/) using the Pixel Classification workflow to generate segmentation probability maps (332). Separate workflows and segmentation algorithms were generated for each of the cell types (i.e. neutrophil-directed HL-60 cells and mouse bone marrow neutrophils). For each workflow, 5-9 representative images spanning all treatment conditions were selected as training data. All multi-scale image features were enabled for pixel characterization, including smoothed pixel intensity, edge filter, and texture descriptors, with each scale corresponding to the Gaussian sigma applied prior to filtering. Training images were manually annotated with two binary labels, *Cells* and *Background*. Using ilastik's Live Update function, pixels were iteratively annotated until accurate segmentation was achieved, capturing

all cell morphologies while excluding background. Each pixel was assigned a feature vector comprising values for each selected image feature, used to train a Random Forest classifier (Vigra's RandomForestClassifier from the C++ Python for image-processing and machine-learning library). The trained classifier assigned each to a class based on these features and annotations, producing semantic segmentation probability maps for each label. Batch processing was then used to apply the classifier to all unseen images. Resulting probability maps were exported as 32-bit multi-channel TIFF images and imported into CellProfiler, where pixel-probability thresholding was used to generate binary masks for segmentation.

CellProfiler image processing pipeline

Images were processed using CellProfiler™ cell image analysis software (v4.2.6; https://cellprofiler.org) for segmentation of cells, DNA, Annexin V and NETs, as well as for the extraction of morphological and quantitative object features from phase-contrast, green fluorescence, and red fluorescence images (333). Cell segmentation was facilitated by ilastik-generated probability maps, which were imported into CellProfiler and applied to the corresponding phase-contrast images. This pipeline enabled broad NET quantification by extracting image-level metrics, including NET counts, total area, and fluorescence intensity from the segmented extracellular DNA regions. All resulting object feature measurements were exported as a database file compatible with CellProfiler Analyst (CPA) for subsequent single-cell classification.

Metadata: Image metadata were extracted from folder and file names to provide CellProfiler with information on the imaging channel, well, field of view, and time point for each image. Accordingly, folders were organized and named by image type (i.e. Phase, Green, Red, and Probability) and images were saved using the default Incucyte naming format:

Plate_Well_Image_Day_Hours_Minute. The following regular expression was used in CellProfiler to extract file name metadata: *^(?P<Plate>.*)_(?P<Well>[A-P][0-9]{1,2})_(?P<Image>[0-9])_(?P<day>[0-9]{2})d(?P<hours>[0-9]{2})h(?P<minute>[0-9]{2})m)*. To incorporate per-well treatment information, a separate CSV file was created listing each well alongside its associated treatment and uploaded using the *Import from file* metadata extraction method in CellProfiler.

Probability maps: The ilastik probability maps were imported into the pipeline as RGB images and subsequently split to grayscale images using the CellProfiler *ColorToGray* module. In these maps, background pixels are black, and pixels classified as cells appear progressively whiter with increasing classification certainty, enabling CellProfiler to interpret pixel intensities as probability values for segmentation.

The grayscale probability maps were smoothed using the *EnhanceOrSuppressFeatures* module (Suppress mode, feature size=10 pixels) to reduce small-scale noise and intensity variations. The *IdentifyPrimaryObjects* module was used to segment cells based on the intensity values of ilastik-identified ROIs. Cells were identified as white regions ≥15 pixels that did not touch the image border. Adaptive Otsu thresholding (two classes) was applied with a threshold correction factor of 0.3 and a 50-pixel adaptive window. A 10-pixel smoothing filter was used to distinguish clumped objects by shape, with dividing lines determined by intensity gradients. Internal holes within segmented objects were filled.

Segmented cell borders were overlaid on the corresponding phase-contrast images using the *OverlayOutlines* module as a quality control step to validate segmentation accuracy during pipeline optimization.

Green fluorescence images: For DNA segmentation, the green fluorescence images were first log-transformed (base 2) using the *ImageMath* module to enhance low-intensity regions and facilitate the detection of faint DNA signals.

All true DNA areas were segmented using a separate *IdentifyPrimaryObjects* module applied to the processed green fluorescence images. Objects ≤1,000 pixels that did not touch the image border were included. Adaptive Otsu thresholding (two classes) was applied with a threshold correction factor of 0.8 and a 50-pixel adaptive window. Intensity threshold limits were optimized per dataset to account for background variation, with the lower inclusion limit ranging from 0.005-0.03. A 10-pixel smoothing filter was used to distinguish clumped objects by shape, with dividing lines determined by intensity gradients. Internal holes within segmented objects were filled.

Identified DNA areas overlapping with segmented cells were saved as a new object set to filter out aberrant signals, with cells designated as parent objects and segmented DNA as child objects in the *RelateObjects* module. The filtered object set was linked to parent cells using a second *RelateObjects* step, after which all separate DNA objects were merged per-parent cell using the *SplitOrMergeObjects* module. These merged objects were then related back to their parent cells in a final *RelateObjects* step.

Red fluorescence images: Prior to Annexin V segmentation, the red fluorescence images were processed using the *EnhanceOrSuppressFeatures*module to enhance speckles with a feature size of 20 pixels, a characteristic size of Annexin V signals, thereby improving their distinction from background noise.

Annexin V objects ≤1,000 pixels that did not touch the image border were segmented using a third *IdentifyPrimaryObjects* module. Adaptive Otsu thresholding (three classes, with

middle intensity classified as foreground) was applied on a smoothed image (default smoothing: 1.3488) with threshold bounds set between 0.0002-1, a correction factor of 1, and a 50-pixel adaptive window. Clumped objects were distinguished based on shape using the smoothed image automatically generated by CellProfiler, with dividing lines determined by intensity gradients. Internal holes within segmented objects were filled.

Identified Annexin V areas overlapping with segmented cells were saved as a new object set to filter out aberrant signals, with cells designated as parent objects and segmented Annexin V as child objects in the *RelateObjects* module. The filtered object set was linked to parent cells using a second *RelateObjects* step, after which all separate Annexin V objects were merged per-parent cell using the *SplitOrMergeObjects* module. These merged objects were then related back to their parent cells in a final *RelateObjects* step.

NET segmentation: To enable NET segmentation, the *MaskObjects* module was applied with the per-cell unmerged DNA objects set as the objects to be masked and the segmented cells as the masking objects. The mask was inverted to retain only DNA regions outside the cell borders. Segmented NET objects were expanded by 1 pixel using the *ExpandOrShrinkObjects* module to ensure overlap with their parent cells, enabling subsequent relational mapping with the *RelateObjects* module.

The area of each individual NET was measured using the *MeasureObjectSizeShape* module, after which the *RelateObjects*module was applied to filter objects by size (≥150 pixels) and to keep only those associated with at least one parent cell. The filtered NET object set was linked to parent cells using a second *RelateObjects* step, after which all separate NETs were merged per-parent cell using the *SplitOrMergeObjects* module. These merged objects were then related back to their parent cells in a final *RelateObjects* step.

Image masks: Prior to object measurement and data extraction steps, all identified objects (i.e. cells, merged DNA, merged Annexin V, and merged NETs) were applied as masks on the phase-contrast, green fluorescence, and red fluorescence images using a series of *MaskImage* modules, to enable data extraction for each object across all imaging channels.

Object feature data extraction: A series of object measurements were performed to characterize the morphological and compositional features of each object, with intensity and texture metrics extracted across all imaging channels to assess cross-channel signal associations.

The granularity spectrum of each object was measured using the *MeasureGranularity* module, which applies a series of top-hat filters with structuring elements sized 1-16 pixels to quantify texture coarseness at different spatial scales.

Several intensity features were extracted from each object across all imaging channels using the *MeasureObjectIntensity*module: maximum intensity, minimum intensity, mean intensity, median intensity, lower quartile intensity, upper quartile intensity, intensity standard deviation and, intensity median absolute deviation (MAD).

The spatial distribution of signal intensities within each DNA and NET object was quantified using the *MeasureObjectIntensityDistribution* module, with the cell edges defined as the center point and 4 radial bins applied. This module reports the fraction of total object intensity at each radius, expressed as mean fractional intensity and the coefficient of variation of intensity within each concentric ring. Area and shape features are extracted from the objects using the *MeasureObjectSizeShape* module, including area, volume, perimeter, eccentricity, radius, and Zernike shape features.

The degree and nature of texture within objects were assessed using the *MeasureTexture* module, with quantifies object roughness or smoothness by analyzing the distribution of pixel

intensities over 256 greyscale levels and calculating Haralick features, including contrast, correlation, variance, and entropy.

To report image-level NET features, the total NET area was measured using the *MeasureImageAreaOccupied* module, while NET intensity features were quantified from the green fluorescence images using the *MeasureImageIntensity*module, including total fluorescence intensity for comparison between treatment groups.

Overlay images highlighting the cells and segmented objects were generated for visualization of analysis output. The phase-contrast, green fluorescence, and red fluorescence grayscale images were converted to RGB format using the *GrayToColor* module, with cells assigned to the blue channel, DNA to the green channel, and Annexin V to the red channel. The OverlayOutlines module was then used to outline the outer borders of NETs in fuchsia on the RGB images, which were then saved as 8-bit integer TIFF files using the *SaveImages* module.

All extracted image- and object-level data were exported as an SQLite database file using the *ExportToDatabase* module, with a single object table created for seamless integration with CPA. A CellProfiler properties file was also generated at this stage to enable subsequent single-cell classification with CPA, specifying *object* as the classification type and defining cells as the individual object locations. Finally, all images were batch processed by selecting *Analyze Images* in the bottom left of the CellProfiler user interface.

Single-cell NETosis stage classification

Each cell identified during CellProfiler segmentation was classified into one of the predefined NETosis stages (negative, dead, spread, disintegrated nucleus, or NETosis) using the machine-learning classifier in CellProfiler Analyst™ (CPA, 3.0.4; https://cellprofileranalyst.org) (334). Cell phenotype categories were primarily defined according to the morphological stages

described by Inozemtsev et al. (45), in which the spread stage consists of cells with a flattened morphology and a compact nucleus, the disintegrated nucleus stage refers to cells with DNA dispersed throughout the cytoplasm, and NETosis is characterized by DNA extrusion into the extracellular space, either forming a disperse “cloud” or emerging through a membrane pore, with the cell perimeter becoming Annexin V-positive, as described by Fuchs et al. (39). Cells lacking any detectable fluorescent signal were classified as negative, and Annexin V and DNA positive cells showing a shrunken and irregular morphology as dead.

For each individual experiment and dataset, a Random Forest classifier was trained by manually annotating 100-200 cells per phenotype category. Features extracted from segmented objects (per_object table) in the CellProfiler database file and its included features, as described in the CellProfiler image analysis pipeline above, were used to train the algorithm and identify informative features for distinguishing cell phenotypes. Overall classifier accuracy and per-class accuracy were evaluated for each dataset using the CPA confusion matrix, which reports the proportion of manually labeled cells correctly predicted cells by the algorithm. Classifier performance was assessed using 5-fold cross-validation in CPA, with an 80/20 train-test split ratio in each fold. Accuracy metrics, including precision, recall, and F1-score, were calculated and reported as the average across all 5 folds. Each dataset was batch processed separately to account for experiment-specific phenotypic variations and to minimize the risk of overfitting.

Following cell classification, an image-level per-class cell count table (HitTable) was generated in CPA. Outliers were identified and removed on a per-experiment, per-treatment, and per-time-point basis within each phenotypic class using the interquartile range (IQR) method, implemented in Python (v3.11) using pandas. Data points outside were excluded from downstream analyses. The remaining values were normalized to the total cell count per image

(*Image_Count_Cells*) to calculate the percentage of each NETosis stage, which was then averaged across all fields of view (*Image_Metadata_Image*), and stratified by treatment (*Image_Metadata_Treatment*) and time point (*Image_Metadata_Hours*).

2.5.2 RNA sequencing Processing and Differential Expression

RNA-seq data processing and analysis were performed by the Bioinformatics Core Facility at the Ottawa Hospital Research Institute (OHRI) following their standardized RNA-seq analysis pipeline (https://gitlab.com/ohri/2024-scn-rnaseq-workshop). Briefly, read quality was assessed using FastQC**,** and adapter sequences and low-quality bases were removed with Trim Galore. High-quality reads were aligned to the Homo sapiens reference genome (GRCh38) using STAR (v2.7.x) with default parameters. Gene-level quantification was performed with featureCounts (Subread v2.0.x) to generate a raw count matrix. Downstream analysis was conducted in R (v4.3.1) using DESeq2 (v1.40.2). Counts were normalized using DESeq2's variance-stabilizing transformation (rlog), and principal component analysis (PCA) was performed on the top 500 most variable genes to visualize global expression patterns and detect potential batch effects. Differential expression was evaluated using the Wald test with Benjamini–Hochberg correction for multiple comparisons, and genes with an adjusted p-value < 0.05 were considered significantly differentially expressed.

2.5.3 Gene Ontology and KEGG Pathway Enrichment Analysis

Differential expression results from DESeq2 were analyzed using g:Profiler (https://biit.cs.ut.ee/gprofiler/). Enrichment was performed for the *Homo sapiens* gene set across the Gene Ontology Biological Process (GO:BP), Molecular Function (GO:MF), Cellular Component (GO:CC), and Kyoto Encyclopedia of Genes and Genomes (KEGG) databases. The built-in *g:SCS* algorithm was applied to control for multiple testing, and terms with adjusted p-value < 0.05 were considered significantly enriched.

2.5.4 Gene Set Enrichment and Pathway Activity Inference

To assess pathway-level activity, differential expression results from DESeq2 were analyzed using the fgsea algorithm (v1.30.0) implemented in R and executed through a Python interface. Genes were pre-ranked by $\log_2$ fold change, and enrichment was evaluated against Hallmark and Reactome gene sets from the Molecular Signatures Database (MSigDB v7.5.1). In parallel, curated senescence-related gene sets representing cell cycle arrest, DNA damage response, chromatin regulation, and SASP signaling were assembled from the literature and analyzed using the same gene set enrichment analysis (GSEA) framework on the same transcriptomic data. Normalized Enrichment Scores (NES) and Benjamini–Hochberg adjusted p-values (false discovery rate (FDR) < 0.05) were used to identify significantly enriched pathways. Leading-edge subsets were extracted to define the core genes driving each enrichment.

2.5.5 Computing the Senescence Index Score

To further quantify senescence-associated transcriptional changes, a human universal senescence index (hUSI) score was calculated using the framework described by Wang et al.(335) and implemented in Python. Normalized bulk RNA-sequencing data from each sample were used as input to compute hUSI scores based on the curated senescence-associated gene set defined in the original study. Gene-level expression values were aggregated according to the published scoring scheme to generate a senescence score for each sample. Statistical differences in hUSI scores between experimental conditions were assessed using an unpaired two-tailed Welch's t-test.

2.6 Statistical Analysis and Data Collection

2.6.1 General Statistical Framework

All *in vitro* experiments were performed using a minimum of three independent biological replicates. *In vivo* studies included 6-7 mice per group. Animal experiments were

conducted in both males and females, which were analyzed separately. For each dataset, data distribution and variance were evaluated using the Shapiro-Wilk and Brown-Forsythe tests, respectively. Comparisons between two groups were performed using a two-tailed student's or Welch's t-test, while comparisons involving more than two groups were analyzed using a one-way ANOVA followed by Tukey's post-hoc test, or a Kruskal–Wallis test with appropriate post-hoc corrections for non-normally distributed data.

Error bars on all graphs represent standard error of the mean (SEM), and statistical significance was defined as $p \leq 0.05$. For histological quantification, two sections of tissues were sectioned and stained, and at least 10 randomly selected fields of view from were used for the quantification.

All statistical analyses were conducted using Python (v3.11) or GraphPad Prism (v10.1.1). Python-based analyses incorporated *pandas*, *numpy*, *scipy*, *statsmodels*, and related packages.

2.6.2 NET Assay Data Analysis and Interpretation

Image-level data extraction and visualization

A *per_image* table was generated as part of the database file, containing all image-level extracted data. For broad NET assessment at this stage, the metrics *Image_Count_NETs_merged* (NET count per image),*Image_AreaOccupied_AreaOccupied_NETs_merged* (NET area in pixels per image), and*Image_Intensity_TotalIntensity_DNA_NETs_merged* (NET intensity (A.U.) per image) were used. Outliers were identified and removed on a per-experiment, per-treatment, and per-time-point basis for each metric using the IQR method, implemented in Python (v3.11) using pandas. Data points outside were excluded from downstream analyses. Remaining values were normalized to the total cell count per image (*Image_Count_Cells*), averaged across all fields of

view (*Image_Metadata_Image*), and stratified by treatment (*Image_Metadata_Treatment*) and time point (*Image_Metadata_Hours*).

A global Kruskal-Wallis test was performed to assess overall differences in image-level metrics across treatments, followed by pairwise Mann-Whitney U tests with Holm correction for multiple comparisons.

Comparison to hand counts

NET counts from 9 representative images (3 per treatment group) were quantified by two independent manual annotators and by the CellProfiler pipeline. Agreement and bias between methods was assessed using Kruskal-Wallis tests with appropriate post-hoc corrections, Bland-Altman plots, and intraclass correlation coefficients (ICC2 and ICC3) to evaluate inter-rater absolute agreement and consistency.

Global classifier and accuracy metrics

The CPA training datasets from all sample sets (n=5 for HL-60 cells and n=4 for mouse bone marrow neutrophils) were compiled into combined training datasets containing all cell-level features extracted using the CellProfiler pipeline. The HL-60 combined dataset comprised 4886 total cells (negative: 818 cells, spread: 735 cells, disintegrated nucleus: 763 cells, NETosis: 607 cells, dead: 1963), while the mouse neutrophil dataset included a total of 2183 cells (negative: 441 cells, spread: 496 cells, disintegrated nucleus: 364 cells, NETosis: 247 cells, dead: 635). These datasets were used to train Random Forest classifiers (scikit-learn v1.3, Python v3.11) with 100 decision trees using stratified random sampling and a fixed random seed (42) to ensure reproducibility. A single representative decision tree, restricted to a maximum depth of 5, was generated using Graphviz to highlight key decision nodes and illustrate how features contributed to phenotype classification.

Feature importance scores were computed based on the mean reduction in Gini impurity for each feature across all trees in the Random Forest, resulting in ranked and normalized importance values. The top ten features contributing most to classification accuracy were plotted to compare relative rankings and to visualize their value distributions across the five NETosis stages. Univariate statistical comparisons of feature values were performed across all pairwise class combinations using the Mann-Whitney U test, with Bonferroni correction applied to adjust p-values for multiple comparisons. Statistical significance was defined as $p < 0.05$ after correction.

Classifier performance was evaluated using stratified 5-fold cross-validation, ensuring balanced representation of all five phenotypes within each fold. In each iteration, 80% of the data were used for training, while the remaining 20% were reserved as unseen data for testing. Performance metrics, including precision, recall and F1-scores for each class, were calculated using the function from scikit-learn, and results were averaged across all folds. Confusion matrices were computed for each fold, summed across folds, and row-normalized to visualize the proportion of correct and incorrect predictions per class. The aggregated confusion matrix was plotted as a heatmap.

Comparison of agreement between CPA trainers

Two independent users trained separate CPA Random Forest classifiers on the same CellProfiler input dataset to assess user-specific bias and variability in the resulting cell count values. Training datasets were manually annotated into the five predefined NETosis stages, according to the previously described classification guidelines. A total of 1755 images (~5.2 x 10^5 cells) from all reported treatment conditions were included in this dataset and scored using the resulting classifiers.

Classification results were compared using Wilcoxon signed-rank tests with appropriate false discovery rate correction and rank-biserial effect sizes. Agreement and bias between classifiers were assessed using Bland-Altman and scatter plots and quantified using Spearman's correlation coefficient (r) and ICC2 and ICC3 to evaluate inter-rater absolute agreement and consistency. Discrepancies between trainers were further characterized using mean absolute error (MAE) and root mean square error (RMSE).

Comparison of NET quantification methods

To evaluate the agreement of CPA-derived NET counts with CellProfiler-derived counts and mean manual annotations, NET counts from 9 representative images (3 per treatment group) were compared using a non-parametric Friedman test with appropriate post-hoc tests and FDR correction.

Statistical comparisons were then repeated using the mean CPA-derived NET counts from both classifiers, and relationships between methods were visualized with scatter plots and Bland-Altman plots to highlight any deviations. Rank-based agreement was quantified using Spearman's correlation coefficient (r) to assess monotonic relationships between each pair of quantification methods, and Lin's concordance correlation coefficients (CCC) were computed to evaluate overall agreement.

Analysis of differences in NETosis dynamics

Hourly proportions of each NETosis stage were calculated by normalizing cell counts to the total cell count per image. For each treatment condition, the median percentage of each cell class was calculated from the mean values per well. Median line plots over time (0-12 hours) with 95% percentile intervals were generated to visualize the temporal progression of NETosis stages. A mixed-effects model with independent experiments as a random intercept was used to

account for per-experiment variability. Post-hoc pairwise comparisons between relevant treatment groups were performed with FDR correction.

The area under the curve (AUC) for each cell-state feature was calculated across all replicates using the trapezoidal rule. Median AUC values (expressed as % x hour) were computed for each treatment and NETosis stage to capture the overall magnitude of each phenotype. To assess treatment effects, a global linear mixed-effects model (LME) was fitted separately for each cell-state feature with Treatment as a fixed factor and Experiment as a random intercept, following the formula: AUC∼C(Treatment)+(1|Experiment). Pairwise post-hoc comparisons between treatments were performed using reduced LME models restricted to two treatments, with appropriate multiple testing correction.

The temporal composition of NETosis stages was visualized using stacked area plots and analyzed following centered log-ratio (CLR) transformation to generate 3-component composition vectors (after adding pseudo-counts where necessary), where each vector represents the overall abundance and duration of the three NETosis cell phenotypes per replicate. Compositional differences between treatments were assessed using global and pairwise Permutational Multivariate Analysis of Variance (PERMANOVA, 999 permutations) based on Euclidean distances of CLR-transformed data, with p-values adjusted for multiple testing. The difference between treatment centroids in CLR space was calculated, and the relative contribution of each cell-state phenotype to the overall composition difference was determined as: $\%\text{contribution}=\sum j(\Delta CLRj)^2/(\Delta CLRi)^2\times 100$.

Univariate LME models were applied to median AUC values for predefined treatment pairs, with treatment as a fixed factor and experiment as a random intercept. Median AUC

differences were reported to indicate the direction and magnitude of change between treatments. All p-values were corrected for multiple testing.

Key temporal metrics (Onset10, t_{50}, and centroid) for each NETosis stage were derived from the time-course data using custom NumPy functions. Median values and IQR for each temporal metric were visualized using error-bar plots. To test for treatment effects on NETosis timing, LME models were fitted for each metric and cell feature, with treatment as fixed factor and experiment as a random intercept. We assessed monotonic trends across PMA doses, performed pairwise comparisons of PMA and ionomycin, and compared each stimulus with or without GSK484 pre-treatment. P-values were corrected for multiple comparisons.

Table 2.1: List of primers for genotyping and RT-qPCR analyses.

Primer names, applications, and sequences (5'–3') are shown. Expected amplicon sizes are provided for genotyping PCR to distinguish wild-type and mutant alleles. RT-qPCR, real-time quantitative PCR.

Primer	Application	Sequence (5' to 3')	Expected amplicon size
Mouse-*Padi4gl* Mutant-F	Genotyping	TCATGACCCCCAACACTCA	~300 bp
Mouse-*Padi4gl* WT-F	Genotyping	AGCTTTGTAAGGGGCATCCT	165 bp
Mouse-*Padi4gl* Common-R	Genotyping	TCAAAGTACCTGATGTGTTGACTG	-
Mouse-*Havcr1(KIM-1)*-F	RT-qPCR	AAACCAGAGATTCCCACACG	-
Mouse-*Havcr1(KIM-1)*-R	RT-qPCR	GTCGTGGGTCTTCCTGTAGC	-
Mouse-*Lcn2(NGAL)*-F	RT-qPCR	CAAGCAATACTTCAAAATTACCCTGTA	-
Mouse-*Lcn2(NGAL)*-R	RT-qPCR	GCAAAGCGGGTGAAACGTT	-
Human-*CDK1*-F	RT-qPCR	TACAGGTCAAGTGGTAGCCA	-
Human-*CDK1*-R	RT-qPCR	GAGATATAACCTGGAATCCTGCA	-
Human-*CCNB2*-F	RT-qPCR	ATGCGTGCCATCCTAGTG	-
Human-*CCNB2*-R	RT-qPCR	AGAGCAGAGCAGTAATCCCA	-
Human-*CCNA2*-F	RT-qPCR	TGGACCCAGAAAACCATTGG	-
Human-*CCNA2*-R	RT-qPCR	CCTCCATTTCCCTAAGGTATGTG	-
Human-*PLK1*-F	RT-qPCR	GACGGGGAGAGGAAGAAGAC	-
Human-*PLK1*-R	RT-qPCR	GCAAGAAGTCTCAAAAGGTGGT	-
Human-*CCNB1*-F	RT-qPCR	TTAAACTTTGGTCTGGGTCGG	-
Human-*CCNB1*-R	RT-qPCR	AGAAGGAGGAAAGTGCACCA	-
Human-*MCM5*-F	RT-qPCR	GCTGCCCTCCCAAATGTCTA	-
Human-*MCM5*-R	RT-qPCR	GATGTCTCCTCGGCGAGTAA	-
Human-*MCM4*-F	RT-qPCR	CAGCAGCAGAAGATATAGTGGC	-
Human-*MCM4*-R	RT-qPCR	ACATTAATCTCCCCAAGTCGTTG	-
Human-*MCM2*-F	RT-qPCR	CATCTCCCACCTGCCTCTG	-
Human-*MCM2*-R	RT-qPCR	CCCAGGACGAAATTGCACTT	-

Table 2.2: List of antibodies for Western blot and immunostaining protocols.

Listed are primary and secondary antibodies used in this study, including application, supplier, and catalog number. WB, Western blot; IHC, immunohistochemistry; IF, immunofluorescence.

Antibody	Application	Supplier	Catalog number
Mouse monoclonal anti-beta Tubulin	WB	Abcam	ab131205
Mouse monoclonal anti-p21	WB	Thermo Fisher Scientific	MA5-31479
Rabbit monoclonal anti-PLK1	WB	New England Biolabs	4513
Mouse monoclonal anti-CKD1[A17]	WB	Abam	ab18
Goat anti-Mouse IgG (H + L), HRP	WB	Bio-Rad	170-6516
Goat anti-Rabbit IgG, HRP	WB	Millipore Sigma	9169
Rabbit monoclonal anti-CD3 epsilon [SP7]	IHC	Abcam	ab16669
Rabbit monoclonal anti-F4/80 [EPR26545-166]	IHC	Abcam	ab300421
Rabbit monoclonal anti-MPO [EPR20257]	IHC	Abcam	ab208670
ImmPRESS™ Horse Anti-Rabbit HRP polymer reagent	IHC	Vector Labs	MP-7401-15
Rabbit polyclonal anti-Histone H3 (citrulline R2 + R8 + R17)	IF	Abcam	ab5103
Goat anti-Rabbit IgG (H+L), Alexa Fluor 647	IF	Thermo Fisher Scientific	A-21245

Chapter 3

Development and validation of a semi-automated imaging and analysis pipeline for quantifying NETosis dynamics

This chapter is based on a manuscript that has been submitted to Frontiers in Immunology and is currently under review.

3.1 Introduction and Rationale

NETs are widely recognized not only as mediators of host defense but also as drivers of tissue injury across a range of diseases (46). Their broad functional roles underscore the need to better characterize the mechanisms governing NET formation across different contexts and conditions, as well as the downstream biological impacts of this process. As the mechanisms that regulate NETosis become increasingly defined, there is a growing need for tools that can precisely resolve this process and facilitate efficient screening of its modulators (183). Existing approaches often lack the sensitivity or scope necessary to investigate the mechanistic implications of NETosis (184,185,192). Prior work has identified sequential stages of neutrophil activation and NET release (39,45), each governed by distinct, temporally ordered signaling event that provide important mechanistic insight (92). Consequently, end-point measurements of NET release alone often fail to capture stimulus-dependent differences in NETosis (197), highlighting the value of live-cell imaging and the need to define NETosis with temporal resolution.

The phenotypic heterogeneity of NETs already complicates their accurate identification, and incorporating distinct NETosis stages adds an additional layer of complexity that is difficult to address with classic image-analysis methods (336). These approaches often lack the capacity to discriminate subtle morphological transitions and can substantially increase the risk of manual-annotator bias. The growing availability of efficient machine-learning tools offers a promising approach to address these challenges (334,337).

In this chapter, we present a high-throughput methodology and analysis pipeline for real-time tracking of NET release across its defined morphological stages. By leveraging machine learning, this approach enables characterization of NETosis dynamics and supports inference of the underlying mechanisms governing stage progression.

3.2 NET Assay and Analysis Pipeline Overview

We developed a high-throughput live-cell imaging assay and semi-automated analysis pipeline to quantify NETosis dynamics over time (Fig. 3.1a). This approach enables real-time tracking of NET release and progression through distinct NETosis stages, providing detailed insight into both temporal patterns and phenotypic features. By combining phase-contrast imaging with fluorescence detection of extracellular DNA and Annexin V, the assay captures key morphological and functional changes of NETosis (Fig. 3.1b). This information helps distinguish NETting cells from dying cells, while detecting a broader range of NET phenotypes than traditional assays. The pipeline integrates open-source tools: *ilastik* for pixel classification (332), *CellProfiler* for object segmentation (333), and CPA for downstream classification of NETosis stages (334) (Fig. 3.1c). Total-image NET characteristics such as count, area and fluorescence intensity can be quantified to provide a broad assessment of NETosis (Fig. 3.1d). Additionally, single-cell features obtained from CellProfiler are used to train classifiers in CPA, enabling the assignment of each cell to a NETosis stage and quantification of stage distributions over time (Fig. 3.1e). This method enables mechanistic studies by revealing when and how specific treatments alter NETosis, and its 96-well format supports large-scale screening of NETosis modulators.

To demonstrate the capabilities of the analysis pipeline, we first validated it using neutrophil-directed HL-60 cells and characterized the dynamics of NETosis in response to two stimuli that act through distinct pathways, in the presence and absence of PAD4 inhibition. We

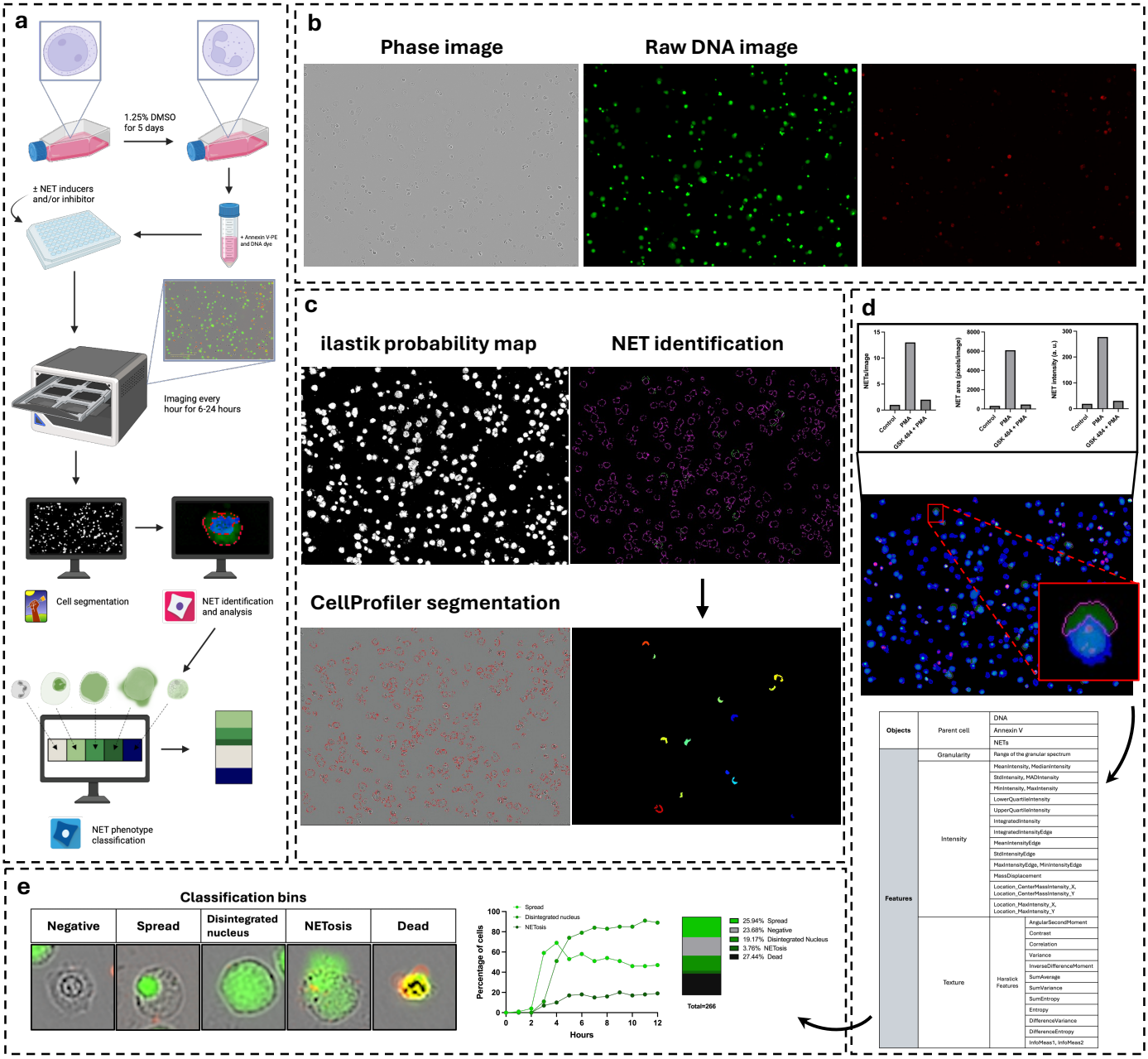

Figure 3.1: Overview of the experimental workflow and analysis for NETosis quantification.

a, Schematic of the workflow with differentiated HL-60 cells. Created in BioRender (https://BioRender.com/9rvj2i1). **b**, Live-cell imaging is performed every hour for 12 hours using three channels: Phase contrast, green fluorescence (DNA), and red fluorescence (Annexin V). **c**, A segmentation probability map is generated from each phase image using *Ilastik*. All images, including the segmentation probability map, are processed in a custom *CellProfiler* pipeline to identify individual cells, DNA and Annexin V. NETs are defined as regions of green fluorescence located outside of the cell body, and all identified objects are mapped back to the parent cell. **d**, NET count, area, and fluorescence intensity are measured per image. For each individual cell and its associated DNA, Annexin V, and NET structures, morphological (e.g., shape, size), textural, granular, and intensity-based features are extracted and saved as a CSV file. **e**, Extracted object-level features are used by *CellProfiler Analyst* to train a Random Forest classifier on user-annotated images. The classifier is then used to categorize cells into different NETosis stages, enabling quantitative assessment of NETosis dynamics and phenotype distributions over time.

then applied the pipeline to primary neutrophils to assess its adaptability to cells of different origins. NETosis was characterized in bone marrow–derived neutrophils from wild-type and *Padi4*$^{-/-}$ mice to further investigate PAD4-dependent differences in NET formation. Together, these applications highlight the flexibility and broad utility of the pipeline for analyzing NETosis across experimental models and interventions.

Cells were seeded to 96-well plates and incubated with SYTOX (green) and Annexin V (red). Distinct treatments were added to designated wells, and plates were imaged using the Incucyte S3 live-cell imaging system. Images were acquired every hour for 12-24 hours in the phase-contrast, green fluorescence (DNA) and red fluorescence (Annexin V) channels.
To assist with accurate cell segmentation in the phase contrast images, ilastik's pixel classification was used to generate segmentation probability maps. All available feature layers were included to capture variability in cell morphology. Manual annotations for foreground (cell) and background regions were done on a series of representative images and used to train a Random Forest classifier. The resulting probability maps yielded cell counts comparable to manual annotation (Fig. 3.2). These probability maps were exported and used as inputs for downstream object segmentation in CellProfiler.

In CellProfiler, individual cells were segmented from the probability maps and identified as primary objects. Signals from the green and red fluorescence channels were used to identify extracellular DNA and Annexin V, respectively, and were mapped to the corresponding parent cell objects. NETs were defined as regions of extracellular DNA not overlapping with or contained within cell bodies. A wide array of features, including object area, shape, texture, granularity, and fluorescence intensity, were extracted for each object across all three channels.

Object-level feature data was exported from CellProfiler as a database file (*.db) and imported into CPA for single-cell classification. For each experiment, a representative subset of cells was manually classified into five NETosis-related phenotypic categories: negative, dead, spread, disintegrated nucleus, and NETosis (Fig. 3.1E). These labels were used to train a Random Forest classifier which was then applied across all images to assign each cell to a phenotype bin. This classification enabled quantification of NETosis dynamics by tracking changes in the proportion of each cell type over time and across treatment conditions.

Data generated by this pipeline, which include readouts on the cell count of each cell type at each hour post-stimulation, can be interpreted to provide insights into the dynamics of each cell type over time, the magnitude of their response, the onset and progression of NETosis, and the overall shifts in cell composition across conditions. Combined with modulators of NET release, this pipeline can help identify the timing and extent of their effect, providing insights into the specific stages at which they act.

We evaluated the accuracy of the CellProfiler object segmentation-based pipeline and CPA classification in identifying NETs, using manual counts as the reference standard. The performance of the CPA classifier is assessed, and inter-rater variability in the training data and resulting classifiers is evaluated by comparing counts across NETosis stages. Differences in NETosis dynamics induced by PMA and ionomycin, with or without pre-treatment using GSK484, a selective PAD4 inhibitor (107), will be described. This includes changes in the hourly distribution of NETosis stages, overall response magnitude to each stimulus, compositional shifts in cell populations and temporal variations in the progression of NETosis. Finally, we present an adapted version of the pipeline for use with mouse bone marrow-derived

neutrophils and apply it to compare NETosis dynamics in wild-type and *Padi4*-deficient mice, reporting similar temporal and compositional readouts as described above.

3.3 CellProfiler NETosis object segmentation accurately identifies NETs

The pipeline was initially developed and validated using dHL-60 cells. Representative images illustrate the responsiveness of untreated cells and cells treated with 200 nM PMA, along with the subsequent image processing steps performed in CellProfiler (Fig. 3.3). Cell segmentation was performed on phase-contrast images using ilastik-generated probability maps, with cell boundaries outlined in red (Fig. 3.3a). DNA objects were segmented from green fluorescence images and merged with their corresponding parent cells (Fig. 3.3b). A similar process was applied to the red fluorescence images to identify and assign per-cell Annexin V objects (Fig. 3.3c). NETs were then identified by segmenting extracellular DNA and applying a size threshold, followed by merging these objects to their respective parent cells (Fig. 3.3d). PMA-treated cells show increased levels of DNA objects, many of which appear enlarged, reflecting elevated NET release (Fig. 3.3b). While some level of spontaneous NETosis is observed in the control image, the representative PMA-treated image demonstrates a marked increase in both the number and size of segmented extracellular DNA structures (Fig. 3.3d).

The pipeline was applied to quantify NET parameters in cells treated with 200 nM PMA and compared to untreated cells or those pre-treated with 20 μM GSK484 for 30 minutes prior PMA stimulation, to confirm that the pipeline accurately detected the expected reduction in NETosis with PAD4 inhibition. Representative overlay images generated by CellProfiler show clear NET release in PMA-treated cells whereas GSK484 pre-treatment shows complete suppression of extracellular DNA release (Fig. 3.4a), highlighting the sensitivity of the pipeline in detecting biologically relevant changes in NETosis.

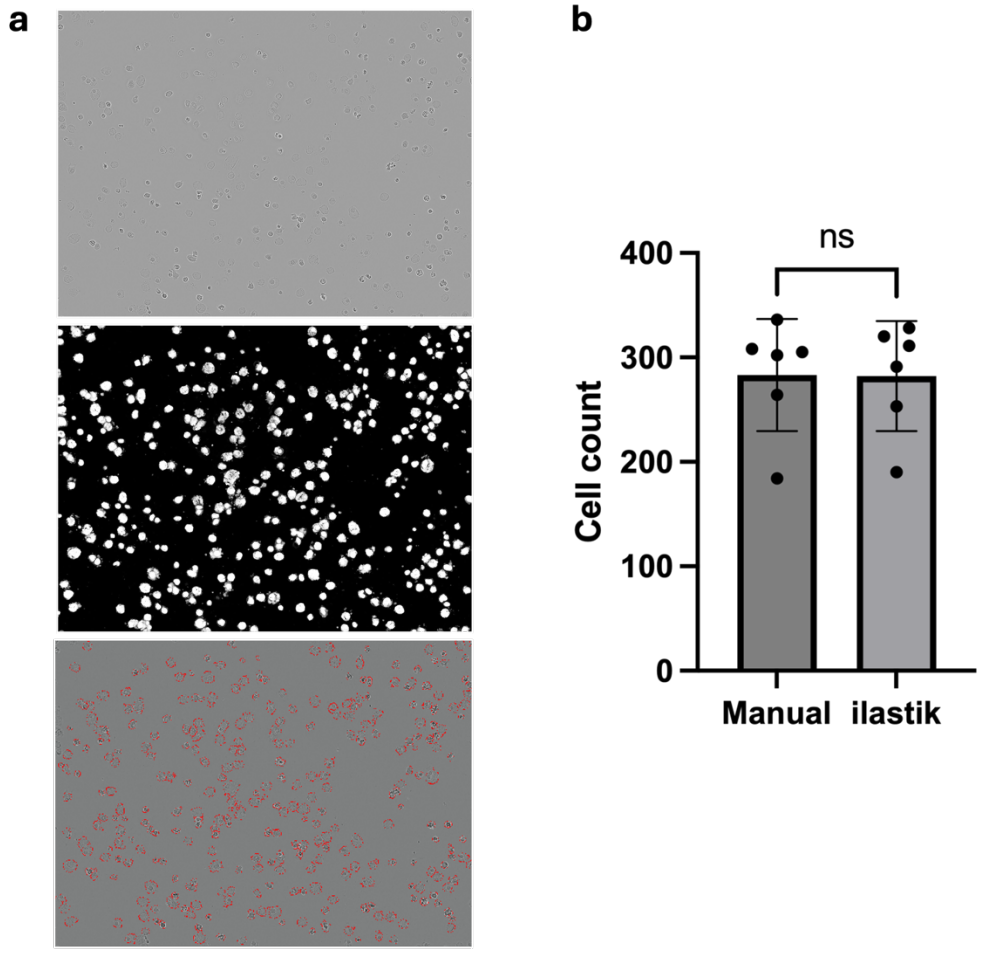

Figure 3.2: Comparison of ilastik-generated image cell counts with manual counts.

a, Representative example showing a phase contrast image, the corresponding probability map generated by ilastik, and resulting cell segmentation in CellProfiler. **b**, Barplot comparing automated cell counts and manual cell counts, with statistical significance assessed by paired t-test result. N = 9 images.

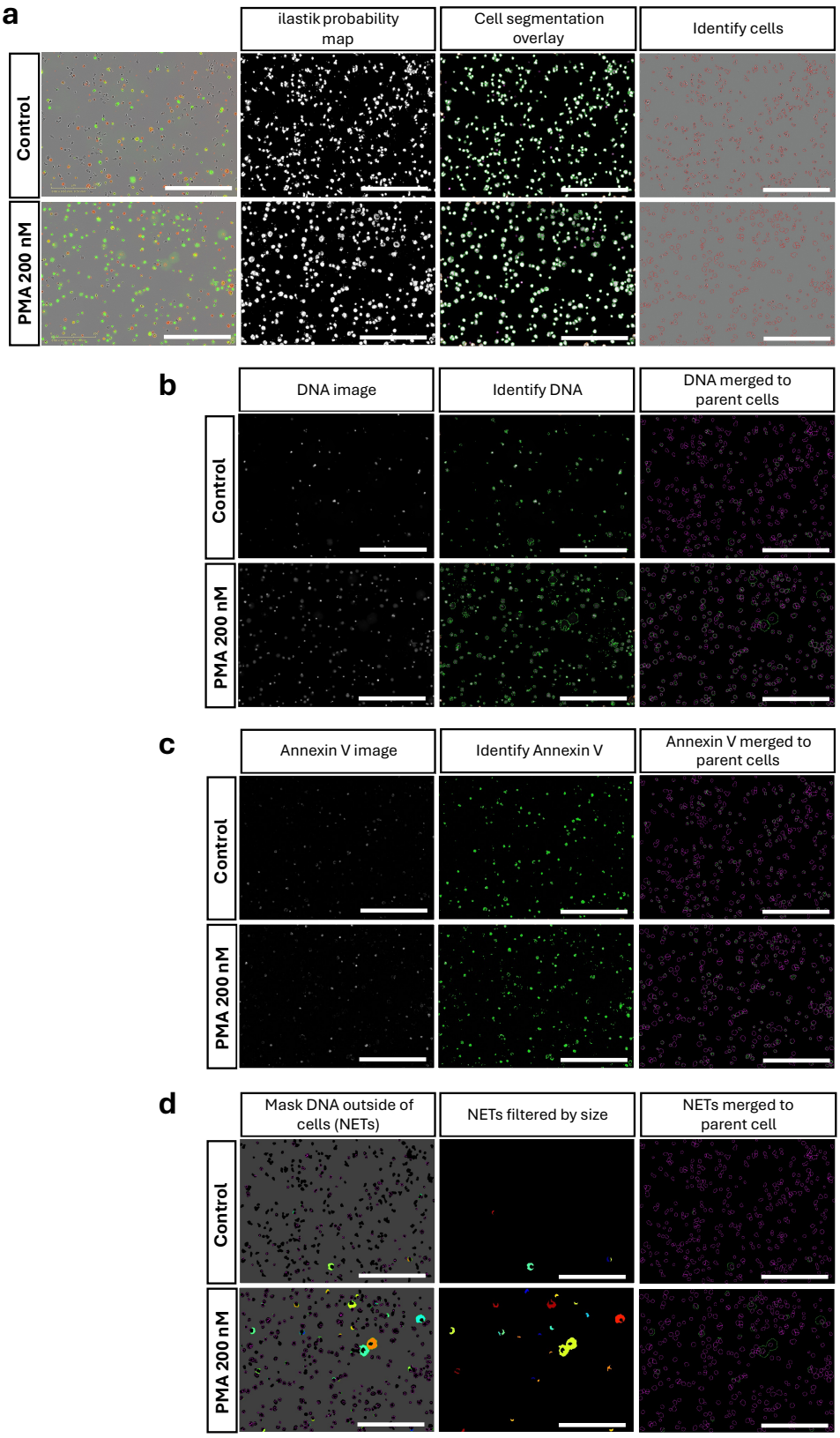

Figure 3.3: CellProfiler object-based segmentation pipeline steps.

a-d, Representative steps of the CellProfiler pipeline for segmenting cells, DNA, Annexin V and NETs, shown for untreated cells and cells treated with 200 nM of PMA at 8 hours. Scale bar = 30 µm. **a**, Ilastik-generated probability maps and corresponding CellProfiler segmentations overlaid on phase contrast images. **b**, Raw green fluorescence images (DNA) image, DNA object identification by CellProfiler and mapping to parent cells. **c**, Raw red fluorescence images (Annexin V), CellProfiler-identified Annexin V-positive regions, and their association with parent cells. **d**, NET segmentation from masking of DNA areas outside of segmented cells in CellProfiler and mapping to parent cells.

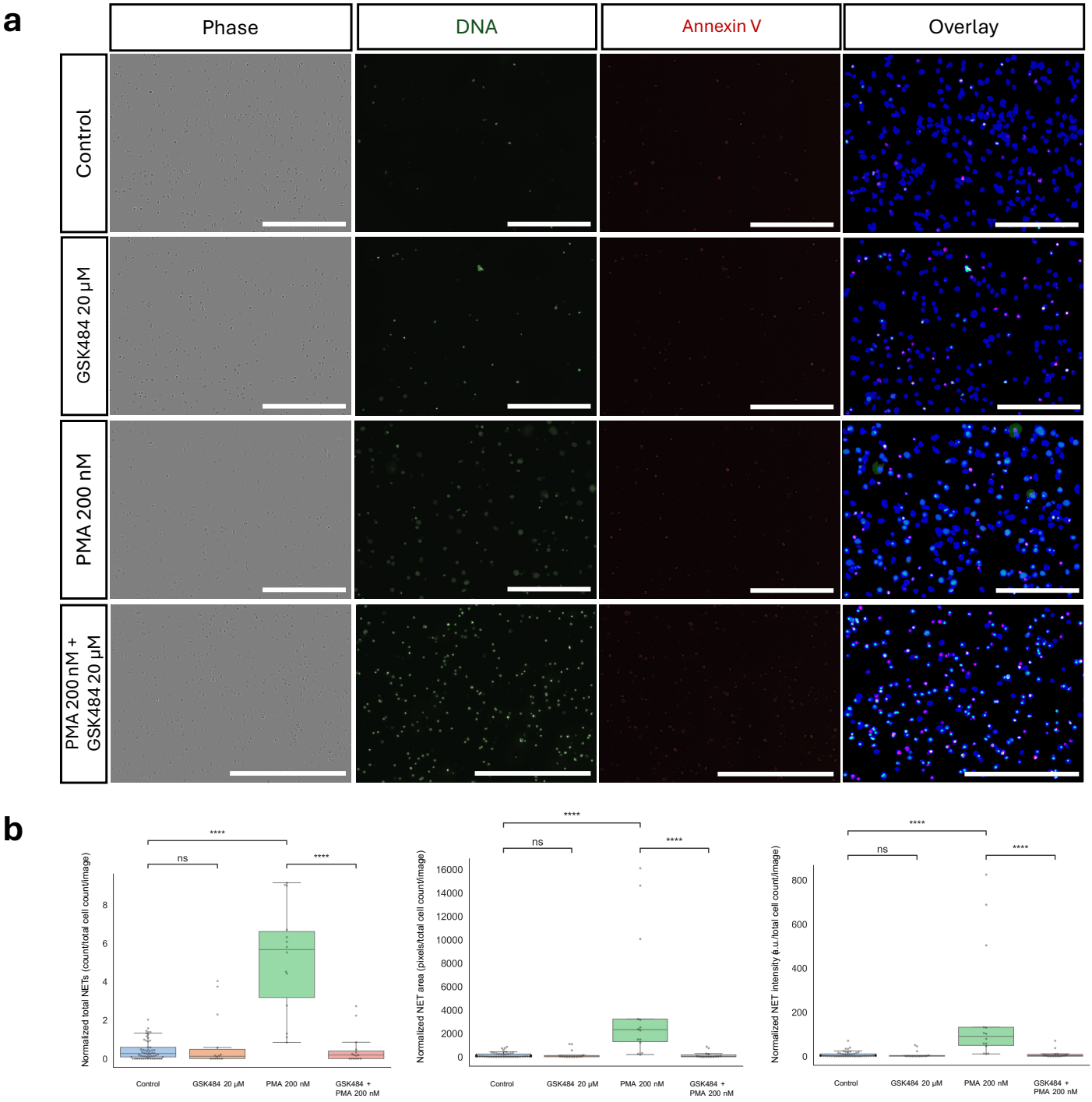

Figure 3.4: CellProfiler validation of NET segmentation biological relevance.

a, Composite overlays showing segmented cells (blue), DNA (green) and Annexin V (red) with NETs outlined in red. Representative images are shown for control, 20 µM GSK484, 200 nM PMA, and GSK484 + PMA (30-min pre-treatment) conditions. **b**, Quantification of NET count, total area, and fluorescence intensity per image across all four treatments. N=15, n=5. ****P<0.0001; ns, not significant.

Total image-level NET features extracted from CellProfiler confirmed the expected effects of PMA and PAD4 inhibition (Fig. 3.4b). PMA markedly increased NET count, area, and fluorescence intensity, whereas GSK484 pre-treatment alone did not induce NET release and reduced PMA-induced NETosis to near-baseline levels.

3.4 CellProfiler NETosis object segmentation is comparable to manual counts

To assess the accuracy of the CellProfiler pipeline in identifying NETs, automated NET counts were compared to manual counts performed by two independent annotators across 3 representative images from the control, 200 nM PMA and GSK484 + PMA treatment groups (Fig. 3.5). The pipeline demonstrated good overall agreement with hand counts, with no significant differences in NET counts across treatments (Fig. 3.5a). Bland-Altman plots comparing CellProfiler-derived NET counts to those from manual annotations demonstrated strong agreement, with only minimal bias toward undercounting by CellProfiler (mean difference −0.22 relative to Hand Count User 1 and −1.78 relative to Hand Count User 2; Fig. 3.5b). Inter-rater variability between manual annotators was also assessed and showed a comparable mean bias (−1.56; Fig. 3.6), underscoring the inherent subjectivity of manual counting and highlighting the value of automated pipelines in reducing user-dependent variability.

To further evaluate the agreement between CellProfiler-generated NET counts and manual NET counts, ICCs were calculated and indicate very strong agreement in absolute NET counts and high consistency in relative trends between methods (Fig. 3.5c).

3.5 Single-Cell NETosis Stage classification demonstrates high performance

Data from five independent experiments were used to train Random Forest Classifiers in CPA. The CPA interface enables the manual creation of phenotype bins, into which unlabelled cells can be sorted for each dataset. Cells were classified into one of 5 phenotypes: negative, spread, disintegrated nucleus, NETosis or dead (Fig. 3.7a). Care was taken to include a broad

a

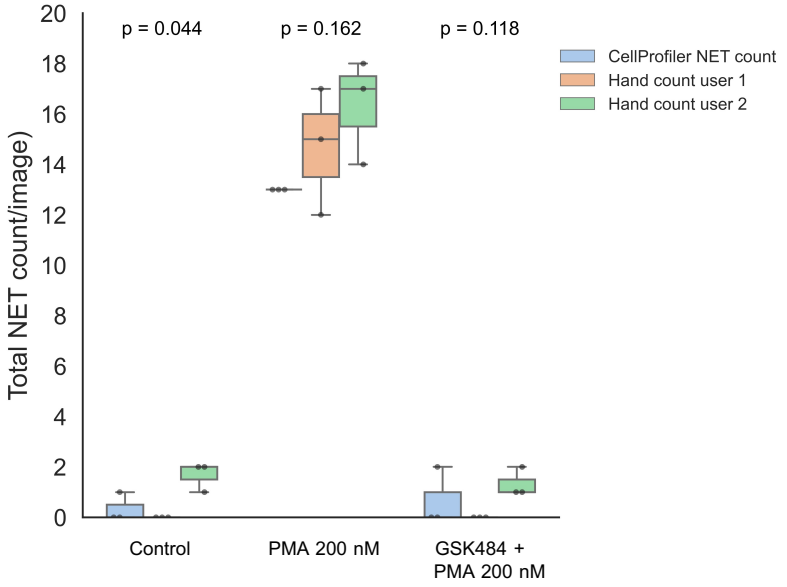

b

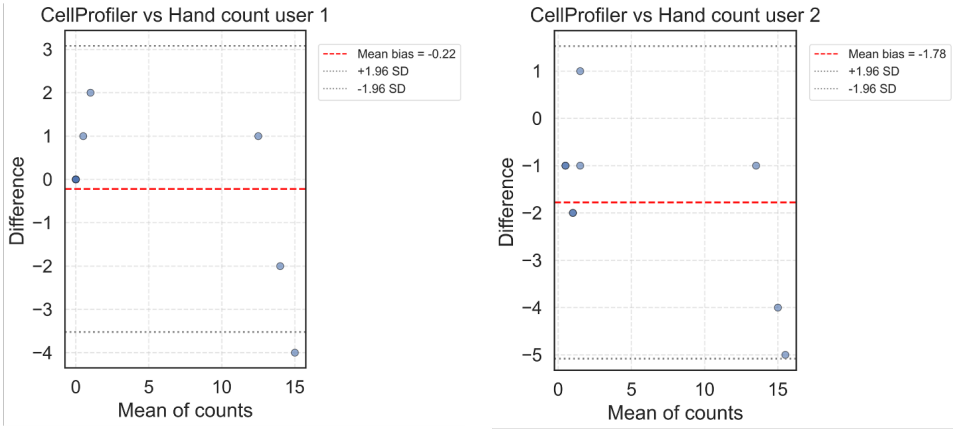

c

Intraclass Correlation Coefficient (ICC)				
Type	**ICC**	**CI95%**	**F**	**p-value**
ICC2	0.96	[0.84, 0.99]	134.0	3.46e-13
ICC3	0.98	[0.93, 0.99]	134.0	3.46e-13

Figure 3.5: Agreement between CellProfiler-generated and manual NET counts.

a, Boxplot comparing NET counts from the CellProfiler pipeline with manual hand counts by two independent users. Kruskal-Wallis test results are shown above each treatment (N=3 per treatment). **b**, Bland-Altman plots illustrating the agreement and mean bias between the CellProfiler NET counts and each manual quantifier (N = 9 images). **c**, Intraclass Correlation Coefficients between CellProfiler NET counts and manual counts (N= 9 images).

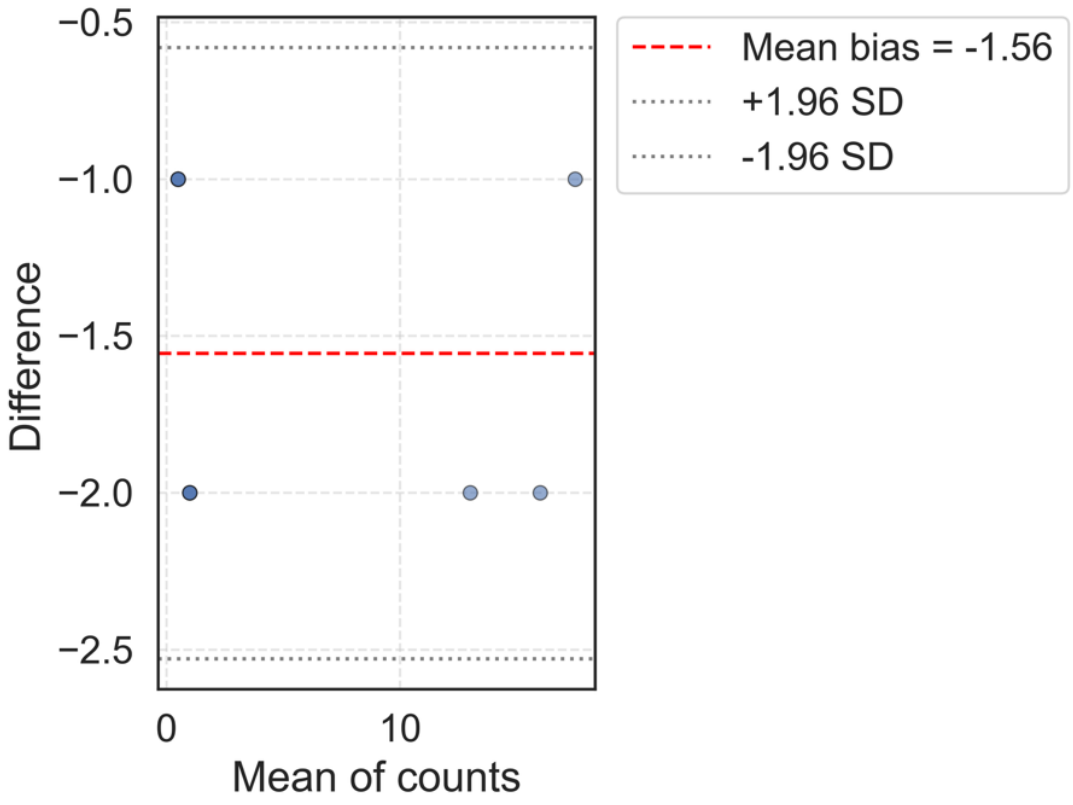

Figure 3.6: Agreement in NET counts between manual annotators.

Bland-Altman plot illustrating the agreement and mean bias in NET counts between two independent manual quantifiers (N = 9 images).

range of phenotypes during training to capture the full spectrum of cell morphology within each class. Rather than applying a single global model, a common base model was retrained separately for each experiment to account for inter-experiment variability and avoid overfitting. Classification accuracy for individual phenotypes varied between experiments, with overall classifier performance ranging from 90 to 95% accuracy (Fig. 3.8a). Spread and NETosis phenotypes showed greater variability, though still high-performing, with F1-scores ranging from 0.86 to 0.95 and 0.84 to 0.92, respectively (Fig. 3.8b). Training datasets from individual experiments were combined (N=4886 cells) to generate a single representative Random Forest Classifier tree, allowing for evaluation of classifier performance across the full dataset and assess generalizability across experiments (Fig. 3.7).

The classifier was characterized based on its top-ranking features across experiments to evaluate their contribution to phenotype discrimination. Features extracted from phase-contrast images, DNA signal, and Annexin V signal within cell bodies were among the most informative for single-cell classification (Fig. 3.7b). Annexin V and DNA MAD intensities ranked the highest, with their upper quartile intensities also appearing among the top features. Additional important predictors included DNA granularity and several DNA texture features, such as contrast, inverse difference moment, and sum variance. These results highlight the value of DNA and Annexin V staining for distinguishing NETosis stages. The top three classification features, cell Annexin V MAD intensity, DNA MAD intensity and Annexin V upper-quartile intensity, differed significantly across phenotypes, except for DNA MAD intensity, which overlapped between dead and spreading cells ($p=0.0746$), making these two phenotypes more challenging to separate (Fig. 3.7b).

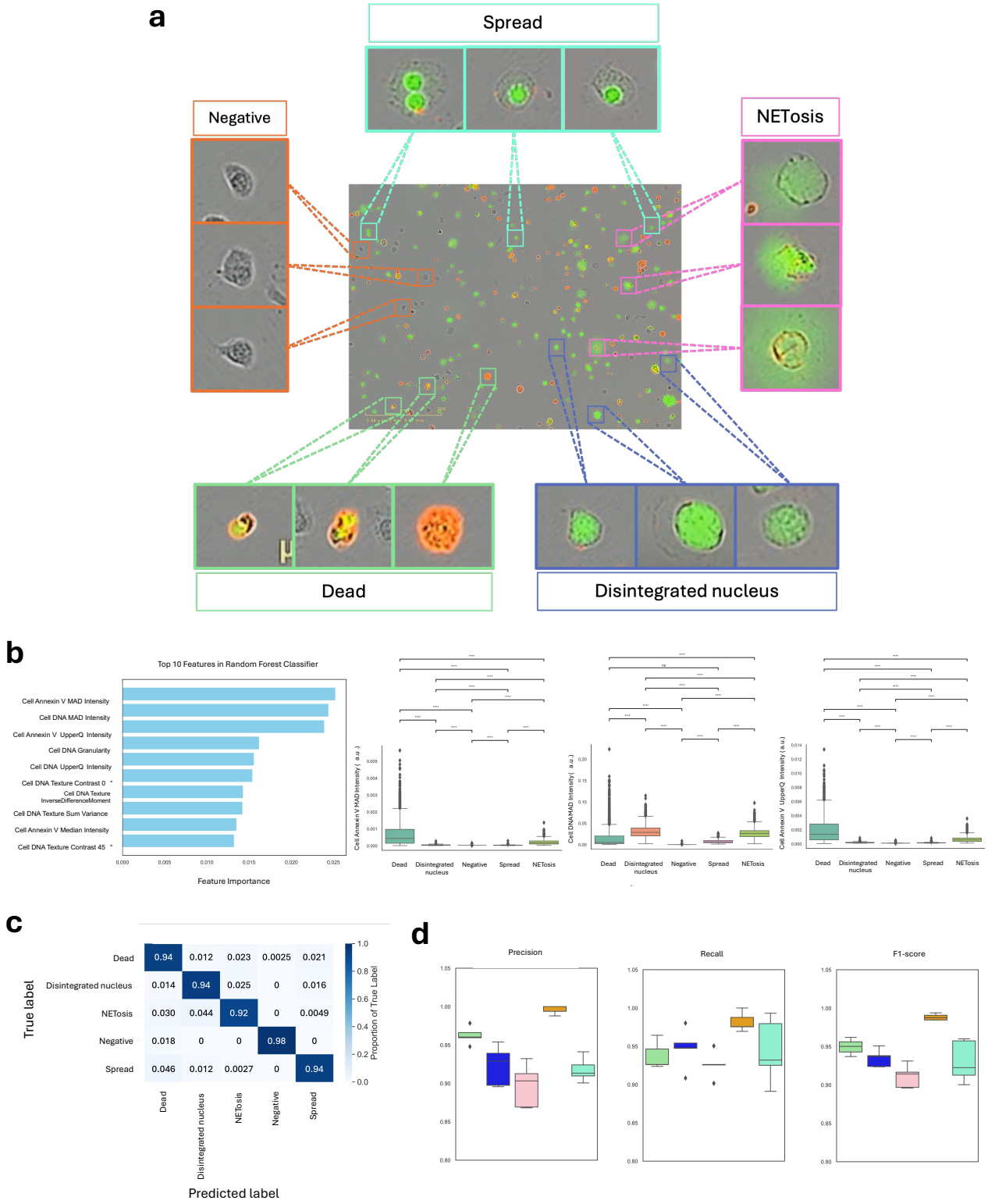

Figure 3.7: CellProfiler Analyst classification performance with neutrophil-directed HL-60s.

a, Representative images for each classification bin: Negative, Spread, Disintegrated nucleus, NETosis and Dead. **b**, Top 10 classification features ranked by importance in the Random Forest model, with boxplots showing the distribution of the top 4 features across classified cell types (n = 5 experiments, N = 4,886 cells) Mann-Whitney test and Bonferroni correction performed ****p<0.0001. **c**, Classifier Confusion Matrix on unseen, stratified test data from 5-fold cross validation (k=5). **d**, Classification performance metrics (precision, recall, and F1-score) for each cell type evaluated on stratified test data.

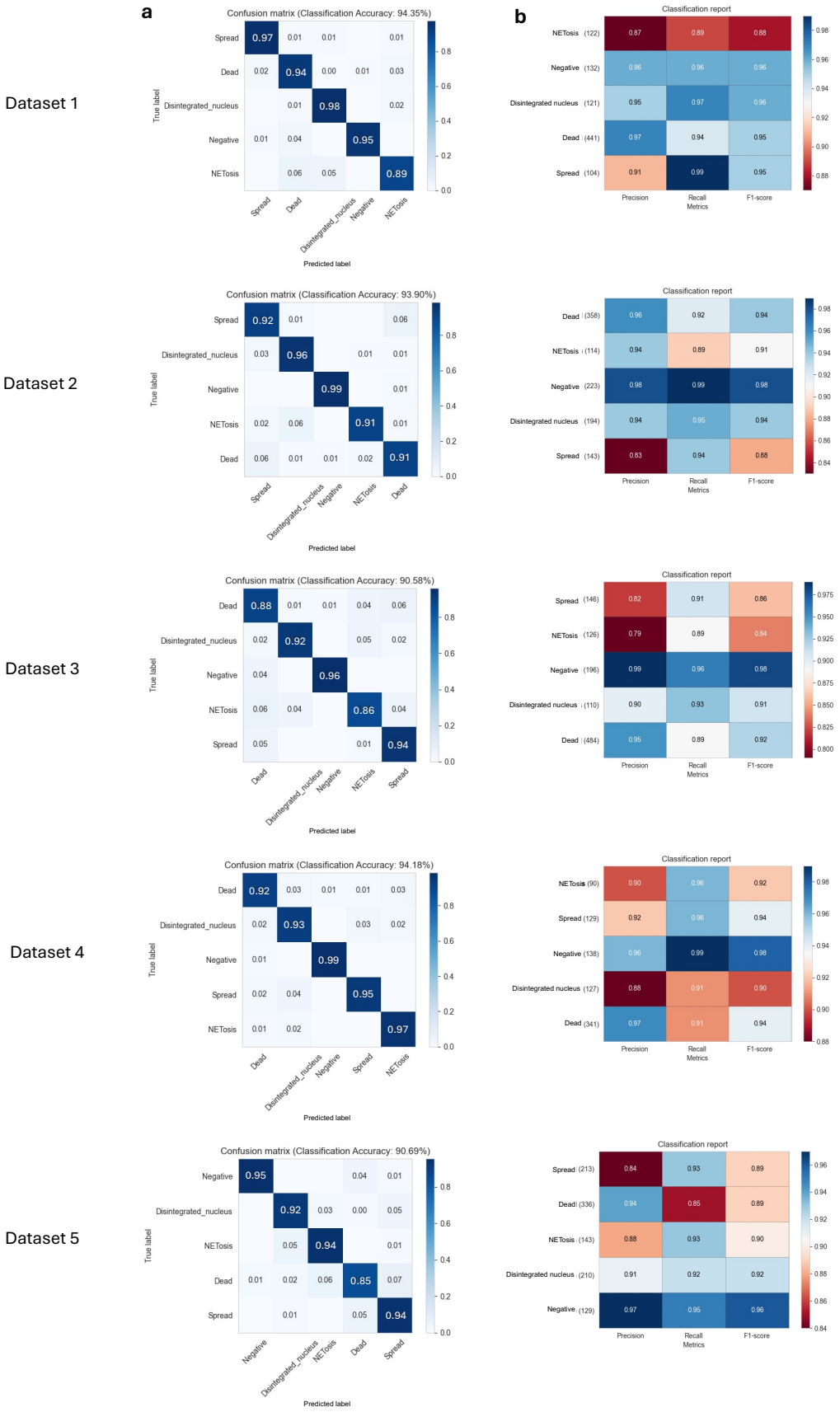

Figure 3.8: CellProfiler Analyst classification performance across independent dHL-60 experimental replicates. **a**, Confusion matrices and **b**, corresponding performance metrics (precision, recall, and F1-score) obtained from CPA models trained on individual dHL-60 datasets. Model performance was evaluated using stratified test k-fold cross-validation (k=5) for each of the five experimental replicates. Overall classification accuracy for each dataset is indicated above the corresponding confusion matrix.

To assess the power of these features and the overall performance of the Random Forest classifier in reliably sorting cells, classification accuracy was evaluated on unseen data using stratified test set evaluation. Classification metrics showed high accuracy in correctly identifying each of the cell phenotypes. Cell labels were consistent with the training annotations 98% of the time for negative cells, 94% for dead, spread and disintegrated nucleus cells, and 92% for NETosis (Fig. 3.5c). Accordingly, the median F1-scores followed a similar trend, with values highest to lowest for negative (0.988), dead (0.95), disintegrated nucleus (0.937), spread (0.923), and NETosis (0.914). Spread classification shows the greatest variability in F1-score, driven by inconsistent recall, suggesting variable sensitivity of the classifier in detecting this phenotype. Precision was most variable for disintegrated nucleus and NETosis classifications, reflecting inconsistent rates of false positives across folds (Fig. 3.7d).

3.6 Single-Cell NETosis stage classification shows some inter-rater variability but remains comparable to other quantification methods

To evaluate the impact of inter-rater variability, two independent annotators labeled the same dataset, and the resulting annotations were used to compared CPA training outcomes, classifier performance, and cell phenotype quantification. A noticeable skew in results was observed across several phenotypes, driven by consistent user-specific biases during classifier training, which led to significant differences in the resulting cell counts. Specifically, counts of negative, spread, dead and disintegrated nucleus cells differed significantly, whereas NETosis counts did not ($p=0.051$) (Fig. 3.9a).

Scatter plot analysis demonstrated strong agreement between image-level NETosis counts generated by classifiers trained by independent annotators, with high overall correlation (Spearman$r\approx0.93$), with minimal inter-rater bias (Fig. 3.9b-c). Counts for negative and disintegrated nucleus phenotypes showed consistently high concordance between trainers,

whereas spread and dead cell classification exhibited greater variability and systematic deviations in opposite directions, suggesting that these phenotypes are sensitive to subjective interpretation during classifier training.

Bland-Altman plots further supported these trends (Fig. 3.9b). NETosis counts showed minimal bias, reinforcing the consistency of classification for this phenotype. The mean differences in disintegrated nucleus (-3.73) and negative (-15.7) cell counts were marginal but consistent across the range of mean counts. Spread and dead cells displayed strong proportional bias, with differences increasing alongside the mean cell counts. Mean differences were -20.6 for spread and 39.9 for dead cells, indicating systematic under- and overestimation, respectively, between trainers.

To further quantify classifier agreement and prediction error, ICCs and absolute error metrics were evaluated across phenotypes (Fig. 3.9c). NETosis exhibited the strongest agreement (ICC≈0.99), with minimal prediction error, indicating reproducible classification. Negative and disintegrated nucleus cells also showed high agreement with moderate error, consistent with limited inter-user bias. In contrast, dead and spread cell classification displayed lower agreement and higher prediction error, with spread cell showing the weakest concordance overall (ICC≈0.4-0.5), suggesting that this phenotype is the most inconsistently interpreted and may benefit from clearer standardized annotation criteria to improve classification robustness.

To assess the accuracy of the CPA classifiers trained by two independent annotators in identifying NETs, automated NET counts were compared to those obtained from the CellProfiler segmentation pipeline and to the average manual counts across 3 representative images from the control, 200 nM PMA and GSK484 + PMA treatment groups, as shown in Fig. 3.4a. Automated

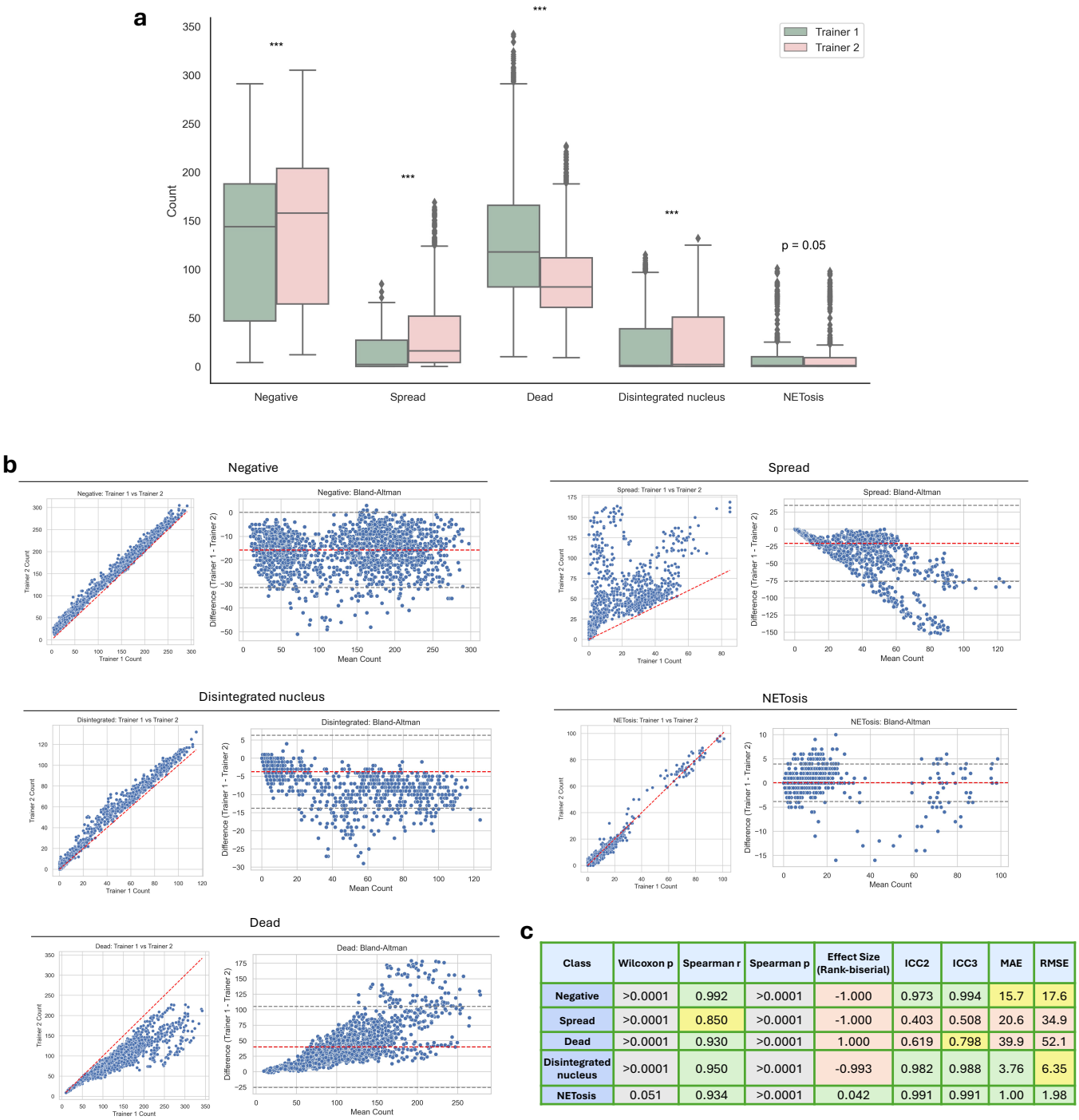

c

Class	Wilcoxon p	Spearman r	Spearman p	Effect Size (Rank-biserial)	ICC2	ICC3	MAE	RMSE
Negative	>0.0001	0.992	>0.0001	-1.000	0.973	0.994	15.7	17.6
Spread	>0.0001	0.850	>0.0001	-1.000	0.403	0.508	20.6	34.9
Dead	>0.0001	0.930	>0.0001	1.000	0.619	0.798	39.9	52.1
Disintegrated nucleus	>0.0001	0.950	>0.0001	-0.993	0.982	0.988	3.76	6.35
NETosis	0.051	0.934	>0.0001	0.042	0.991	0.991	1.00	1.98

Figure 3.9: CellProfiler Analyst inter-rater classification agreement across NETosis stages.

a, Boxplots showing variability in predicted cell counts across two independently trained CPA classifiers. Paired Wilcoxon test with Benjamin-Hochberg correction performed (***p<0.0001). **b**, Scatterplots and Bland-Altman plots showing agreement between two independently trained CPA classifiers for each NETosis stage. **c**, Summary of agreement metrics between the two CPA classifiers trained using independent annotation sets, including MAE, RMSE, Spearman ρ and p, ICC2, Wilcoxon p-values, and rank-biserial effect size.

NET counts generated by the CPA classifiers did not differ significantly from each other, from the hand count mean or CellProfiler-derived NET counts across treatments (Fig. 3.7a).

To evaluate the correlation of reported NET counts across all methods, scatter plots were generated, and Spearman correlation coefficients calculated for each of the pairwise comparison of methods (Fig. 3.10). Average NET counts from the CPA classifiers showed slightly stronger correlation with manual counts than those obtained directly from the CellProfiler pipeline. The highest correlation was observed between the CellProfiler pipeline and CPA classifier outputs (r=0.98), showing consistency in automated methods (Fig. 3.10b).

Bland-Altman plots comparing mean differences in NET counts across each pairwise combination of methods revealed a modest bias toward underestimation by both automated methods relative to manual counts. In contrast, the comparison between CellProfiler and CPA classifier average showed strong concordance, with a minimal mean bias (Fig. 3.10d).

Overall agreement between methods, as measured by CCC, was excellent between CellProfiler and CPA (CCC=0.978) and remained strong between CPA and manual counts, indicating that CPA classifiers provide reliable quantification when benchmarked against both manual and automated methods (Fig. 3.10b).

3.7 Time-course analysis reveals PMA dose-dependent changes in NETosis stages

The assay was applied to characterize NETosis in neutrophil-differentiated HL-60 cells stimulated with PMA at 0.2, 2, 20 or 200 nM, allowing for evaluation of dose-dependent responses. Representative overlay images show areas of NETs segmented by the CellProfiler pipeline at 8 hours post-treatment, delimited by red outlines (Fig. 3.11a).

Cells exhibited increased NET formation in response to elevating PMA concentrations. However, quantitative analysis of CellProfiler-extracted data revealed significant

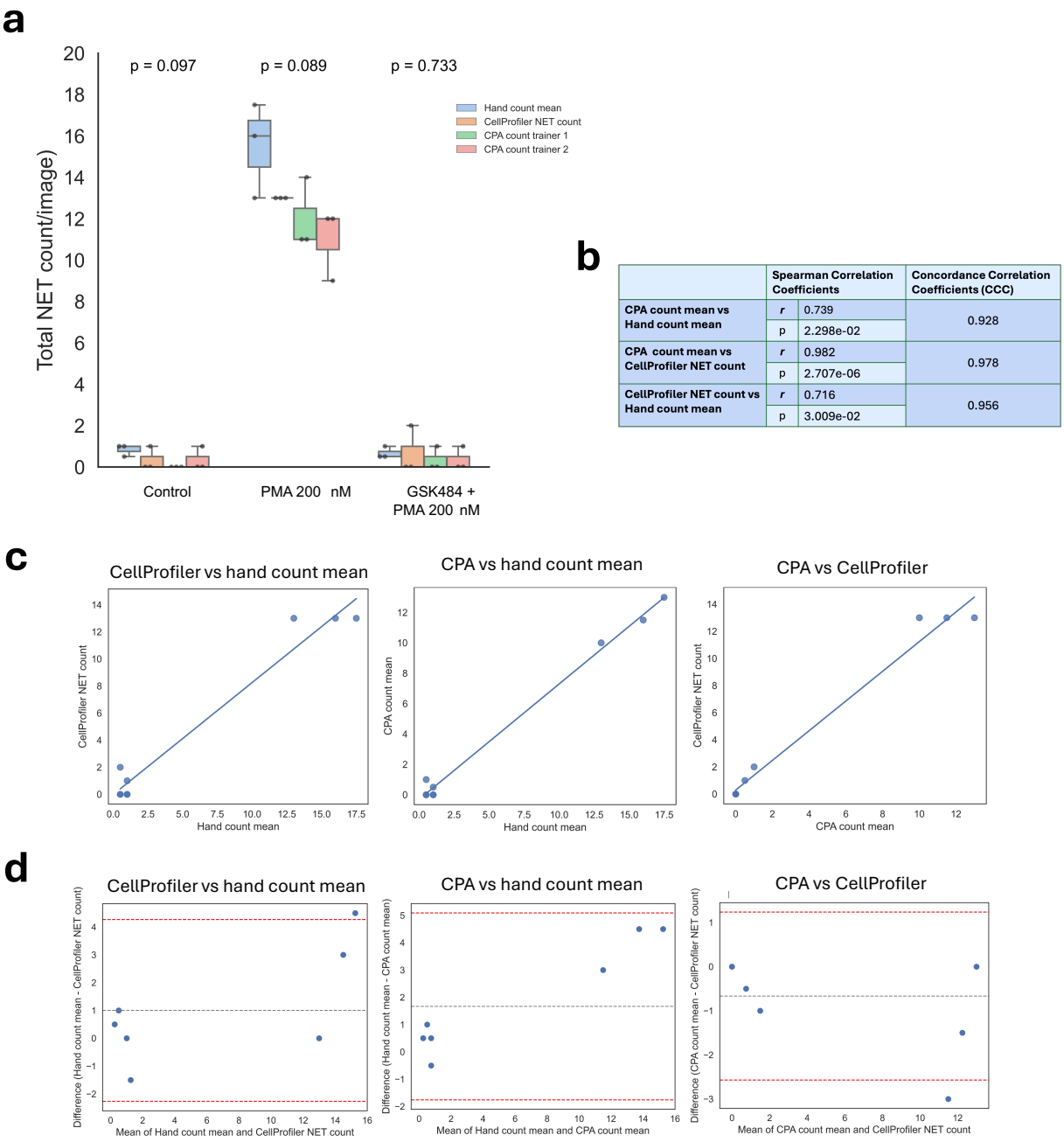

Spearman Correlation Coefficients		**Concordance Correlation Coefficients (CCC)**
CPA count mean vs Hand count mean	*r* 0.739	0.928
	p 2.298e-02	
CPA count mean vs CellProfiler NET count	*r* 0.982	0.978
	p 2.707e-06	
CellProfiler NET count vs Hand count mean	*r* 0.716	0.956
	p 3.009e-02	

Figure 3.10: Agreement of CellProfiler Analyst NET counts with other quantification methods.

a, Boxplots comparing NET counts obtained from CellProfiler, two independently trained CPA classifiers, and the average of manual counts (n = 9 images). Statistical comparisons were performed using the Friedman test, with results annotated above each group. **b**, Summary of agreement between automated and manual NET counts assessed with Spearman correlation and Lin's concordance correlation coefficients, n =9 images. **c**, Scatterplots comparing NET counts for each pairwise combination of NET quantification methods. **d**, Bland-Altman plots assessing agreement between each pair of quantifiers.

increases in NETosis metrics (counts, area, and intensity) compared to control beginning at 2 nM PMA, with no discernible differences between higher concentrations (Fig. 3.12).

The lack of detectable dose-dependent effects suggested limited sensitivity of the pipeline or an inability to capture earlier NETosis phenotypes, which were detected when analyses were combined with the CPA classifier (Fig. 3.11).

Temporal and compositional changes in NETosis dynamics were compared across PMA concentrations using the CPA classifier to quantify hourly levels of all three NETosis stages, enabling time-resolved comparisons between concentrations (Fig. 3.11b).

Spreading induced by PMA significantly differed from untreated cells starting immediately after treatment onset. The three highest PMA doses (2, 20 and 200 nM) led to significantly more spreading than the lowest dose, with divergence emerging around 1-4 hours post-treatment. Differences in spread cell percentages between the top three doses were minimal, indicating a similar degree of cell activation at doses above 2 nM (Fig. 3.11b, panel 1).

Nuclear disintegration following PMA treatment became significantly elevated relative to control starting at 2 hours. By 3 hours, dose-dependent differences emerged, with the three highest PMA concentrations exhibiting greater nuclear disintegration than 0.2 nM. As the experiment progressed, significant distinctions between the higher doses became apparent. However, nuclear disintegration remained comparable between 20 and 200 nM PMA throughout the time course(Fig. 3.11b, panel 2).

NETosis became significantly elevated in PMA-treated groups relative to control starting at 3 hours, with successive PMA dose groups reaching statistical significance in a stepwise manner at approximately 1-hour intervals (Fig. 3.11b, panel 3. Dose-dependent differences

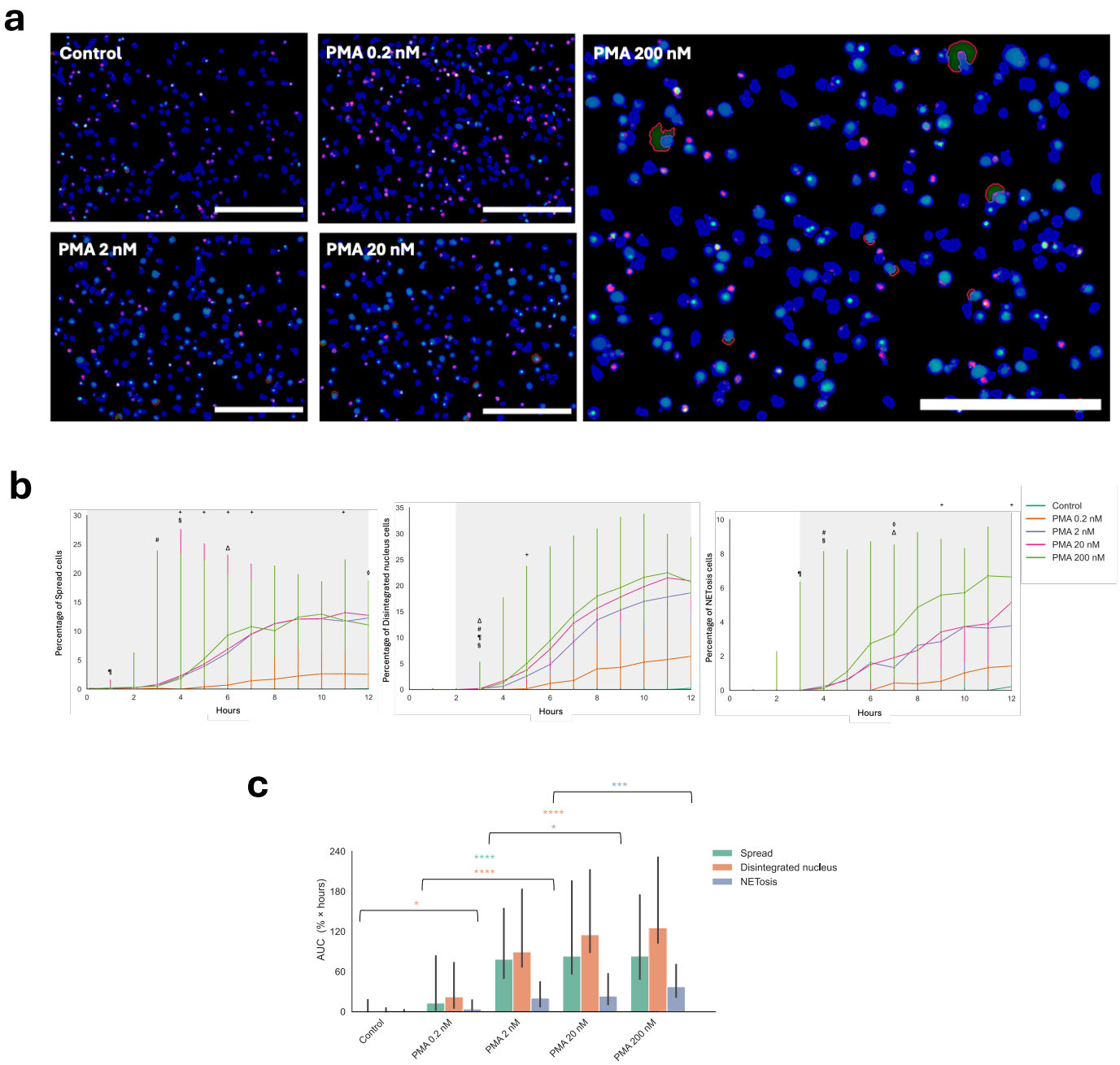

Figure 3.11: Time-course of NETosis dynamics in response to increasing concentrations of PMA.

a, Composite overlays showing segmented cells (blue), DNA (green) and Annexin V (red) with NETs outlined in red. Representative images are shown for all PMA concentrations (0.2-200 nM) after 8 hours. **b**, Line plots showing the median percentage of each NETosis stage over time with increasing PMA concentrations. Mixed-effects models were used with experiment as a random intercept, followed by Bonferroni-corrected pairwise comparisons. Symbols are shown only at the first significant time point if significance is maintained for all subsequent time points; otherwise, the symbol is shown at each significant time point. Grey boxes highlight time points where any PMA concentration is significantly higher than control. Pairwise comparisons: § PMA 0.2 vs 2 nM, ¶ PMA 0.2 vs 20 nM, # PMA 0.2 vs 200 nM and PMA 2 vs 20 nM, Δ PMA 2 vs 200 nM, ◊ PMA 20 vs 200 nM (n = 5 experiments, N = 15 replicates). **c**, Area under the curve (AUC) for each cell type with mixed-effects modeling with Holm step-down correction. n=5 experiments, N=15 replicates. *p<0.05, **p<0.01, ***p<0.001, ****p<0.0001.

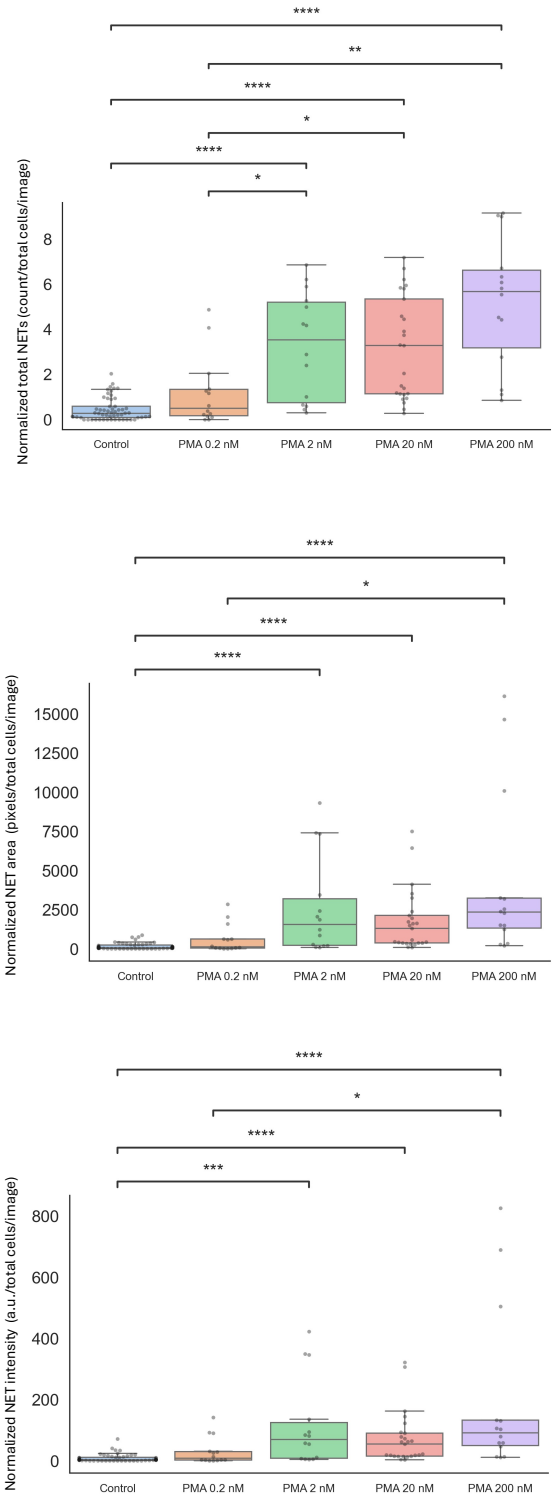

Figure 3.12: CellProfiler-generated NET metrics in response to increasing concentrations of PMA.
Quantification of NET count, area, and fluorescence intensity per image across PMA concentrations. N=12-15, n=4. *P<0.05, **P<0.01, ***P<0.001, ****P<0.0001.

emerged around 3-4 hours, with the three highest PMA concentrations inducing greater NETosis than 0.2 nM. NETosis levels were comparable between 2 and 20 nM throughout most of the experiment, although 20 nM PMA produced higher NETosis by 12 hours (5.15% vs 3.77%, $p<0.0001$). In contrast, 200 nM induced significantly more NETosis than all other doses starting at 7 hours, reaching a median of 6.64% of cells in NETosis by 12 hours (Fig. 3.11b, panel 3).

This time-course analysis revealed that while NETosis initiation is comparable in both timing and magnitude across PMA doses from 2 to 200 nM, higher doses lead to divergence at progressively later stages. Specifically, 20 nM induced more nuclear disintegration than 2 nM, whereas 200 nM surpasses 20 nM only at the stage of NET formation.

To assess differences in the magnitude of effect on each cell stage in response to increasing PMA concentrations, AUC values were calculated (Fig. 3.11c). Increasing PMA concentrations led to progressive shifts in the proportion of cells in each phenotype. The cumulative percentage of disintegrated nucleus cells increased significantly starting from the lowest concentration tested (Control=1.1 vs 0.2 nM=22.1, $p=0.048$), despite minimal and non-significant NETosis at this dose. The magnitude of nuclear disintegration continued to rise with increasing PMA concentrations, peaking at 20 nM and plateauing at 200 nM.

The largest increase in cumulative cell spreading occurred between 0.2 and 2 nM (0.2 nM=12.88 vs 2 nM=78.42, $p<0.0001$), after which levels remained relatively stable at higher concentrations. In contrast, cumulative NETosis increased at higher PMA doses, becoming significantly elevated between 2 and 20 nM and rising further at 200 nM (Fig. 3.11c).

3.8 Temporal kinetics of NETosis are modulated by PMA concentration

To assess temporal dynamics in NETosis progression across varying doses of PMA, timing metrics for each cell type were compared between concentrations. Specifically, we tested for dose-dependent monotonic trends in the onset, T_{50} and centroid (Fig. 3.13). The initiation

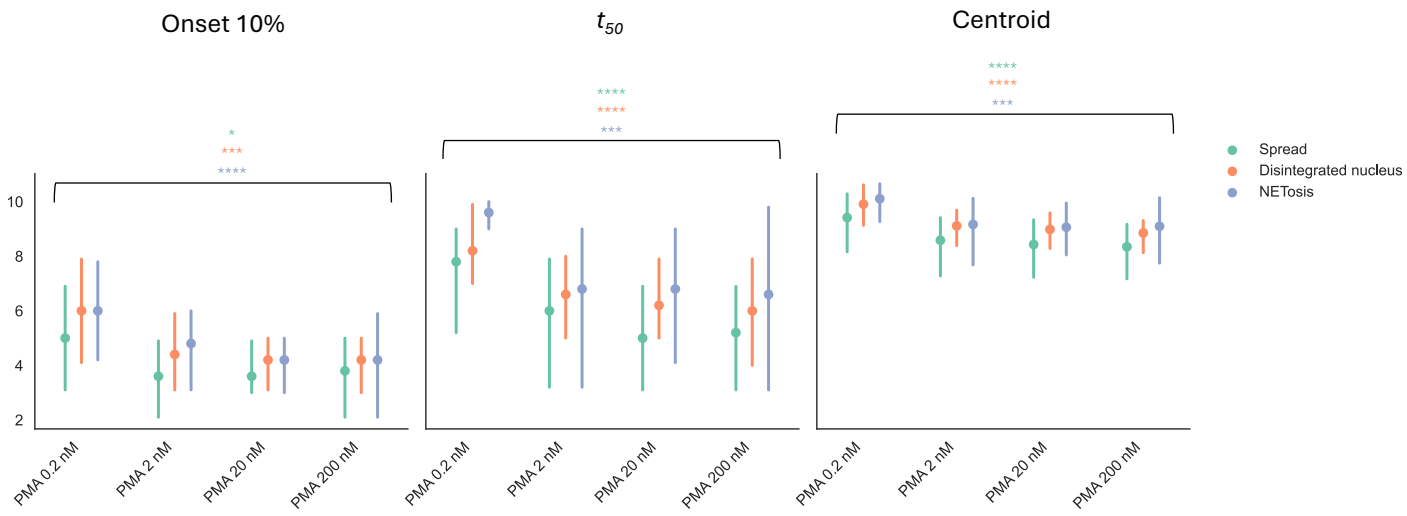

Figure 3.13: NETosis progression timing in response to increasing PMA concentrations.

Temporal metrics trend analysis (0nset 10%, t50 and centroid) across PMA concentrations (0.2-200 nM), shown as medians with 95% confidence intervals. Differences between groups were tested using mixed-effect models with experiment used as a random intercept n=experiments and Benjamini-Hochberg applied (n = 5 experiments, N = 15 replicates/treatment).

and progression of each NETosis stage accelerated in a dose-dependent manner. At the lowest concentration, cell spreading, nuclear disintegration and NETosis initiated sequentially over several hours, while higher PMA concentration (200 nM) advanced the onset of each stage by approximately 1 hour. Higher PMA concentrations also accelerated progression across all phenotypes, with cell spreading, nuclear disintegration and NETosis reaching half-maximal levels 1 to 3 hours earlier at 200 nM compared to 0.2 nM. The overall temporal distribution of the response for each cell type, as measured by the centroid, closely mirrored the T_{50} trend, occurring progressively earlier with increasing PMA concentration (Fig. 3.13), indicating a globally accelerated NETosis response with higher stimulation levels.

3.9 Time-course analysis reveals stimulus and PAD4-dependent changes in NETosis stages

Stimuli-dependent responses were assessed by comparing PMA- and ionomycin-induced NETosis (Fig. 3.14). Both activators were assessed in the presence or absence of PAD4 inhibition with GSK484 to determine the contribution of PAD4 activity in each activation pathway. Overlay images from cells treated with 200 nM PMA or 5 μM ionomycin, with or without a 30-minute pre-treatment with 20 μM GSK484, display comparable levels of NETosis between both NET inducers, while GSK484 pre-treatment fully suppressed NETosis under both conditions (Fig. 3.14a). Quantitative data extracted from CellProfiler corroborated these observations (Fig. 3.15).

As observed in Figure 3.15b, all treatments led to elevated cell spreading compared to control, even in the presence of PAD4 inhibition (Fig. 3.14b, panel 1). Stimulation with PMA or ionomycin, with or without GSK484 pre-treatment, significantly increased the proportion of spread cells starting at 1-hour post-treatment. GSK484 alone also induced cell activation, reflected by a significant increase in spread cells compared to control beginning at 5 hours.

PAD4 inhibition with GSK484 dampened the magnitude of spreading in PMA-treated cells, with a significant reduction observed starting at 6 hours (PMA = 9.3% vs GSK484 + PMA = 3.61%, $p = 0.0033$). In contrast, GSK484 pre-treatment followed by ionomycin stimulation produced a synergistic effect, resulting in significantly more cell spreading compared to ionomycin alone starting at 10 hours (4.82% vs 8.74%, $p = 0.022$), and surpassing levels in the GSK+PMA group.

Treatment with 200 nM PMA resulted in a faster accumulation of spread cells than ionomycin, with significantly higher levels observed between 8 and 11 hours post-treatment (10 hours: PMA =12.94% vs ionomycin= 4.82%, p=0.00013).

An earlier onset of nuclear disintegration was observed with ionomycin, which significantly diverged from control starting at 1 hour post-treatment, whereas this occurred at 2 hours with PMA (Fig. 3.14b, panel 2). However, from 5 hours onward, PMA treatment led to higher levels of nuclear disintegration than ionomycin (5 hours: PMA=5.02% vs ionomycin=1.77%, p=0.041).

PAD4 inhibition with GSK484 almost completely suppressed nuclear disintegration in PMA-treated cells, with significantly lower levels compared to PMA alone beginning at 3 hours. Contrastingly, co-treatment with GSK484 and ionomycin still resulted in detectable nuclear disintegration, which was significantly higher than control starting at 3 hours, though significantly reduced compared to ionomycin alone starting at 6 hours (ionomycin=4.5% vs GSK484 + ionomycin=2.03%, p=0.021). Accordingly, GSK484 + ionomycin led to a significantly greater proportion of cells with a disintegrated nucleus than GSK484 + PMA starting at 8 hours.

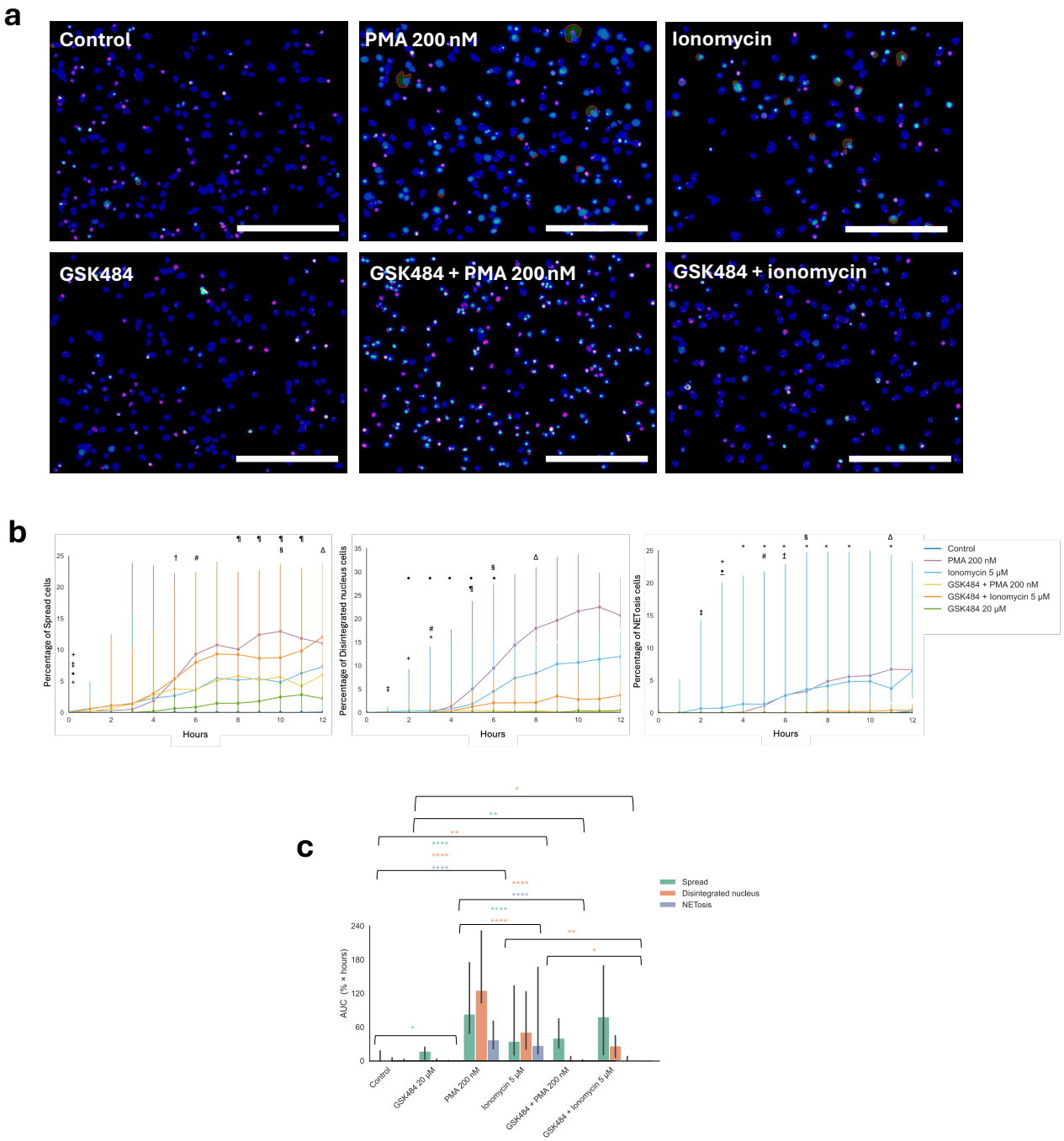

Figure 3.14: Time-course of NETosis dynamics in response to distinct stimuli and PAD4 inhibition.

a, Composite overlays showing segmented cells (blue), DNA (green) and Annexin V (red) with NETs outlined in red. Representative images are shown for stimulation with 5 µM ionomycin or 200 nM PMA, with or without pre-treatment with GSK484 (30 minutes), after 8 hours. **b**, Line plots showing the median percentage of each NETosis stage over time with pharmacological stimulation with ionomycin or PMA ± GSK484. Mixed-effects models were used with experiment as a random intercept, followed by Bonferroni-corrected pairwise comparisons. Symbols are shown only at the first significant time point if significance is maintained for all subsequent time points; otherwise, the symbol is shown at each significant time point. Pairwise comparisons: * Control vs GSK484 + Ionomycin, • Control vs GSK484 + PMA, † Control vs GSK484, ‡ Control vs Ionomycin, + Control vs PMA, Δ GSK484 + Ionomycin vs GSK484 + PMA, § GSK484 + Ionomycin vs Ionomycin, # GSK484 + PMA vs PMA, ¶ Ionomycin vs PMA (n = 5 experiments, N = 9 replicates). **c**, Area under the curve (AUC) for each cell type with mixed-effects modeling with Holm step-down correction. n=5 experiments, N=15 replicates. *p<0.05, **p<0.01, ***p<0.001, ****p<0.0001.

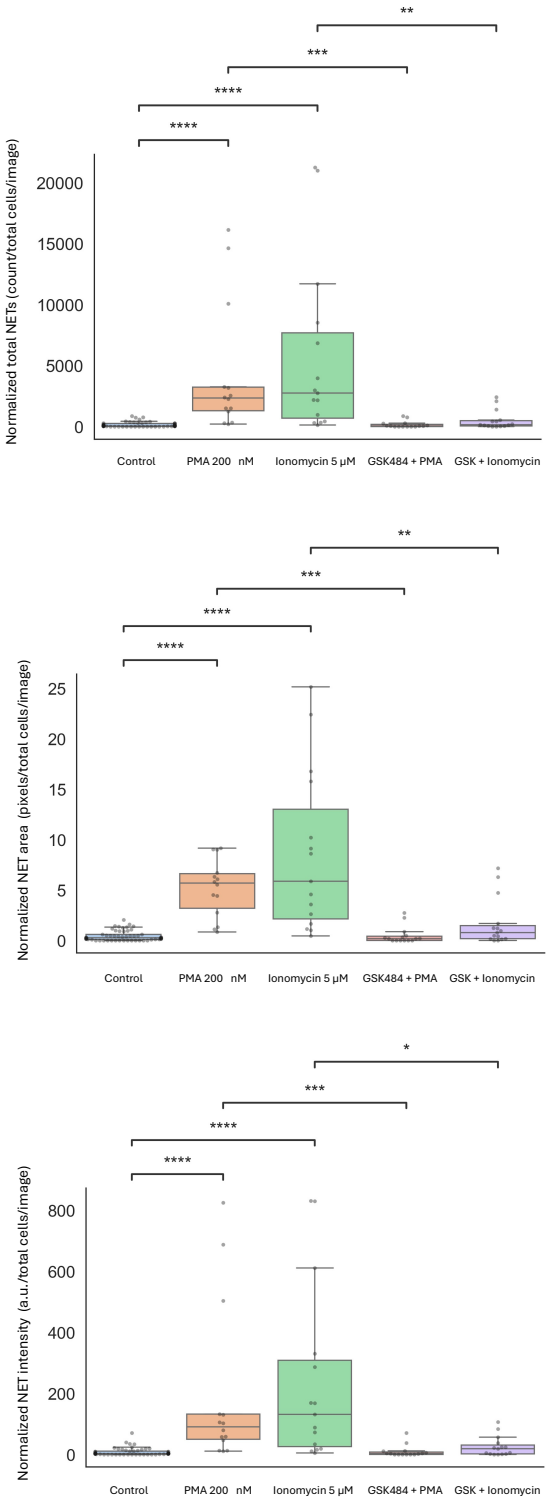

Figure 3.15: CellProfiler-generated NET metrics in response to various pharmacological stimuli. **(a-b)**, Quantification of NET count, area, and fluorescence intensity per image across **a**, PMA concentrations and **b**, PMA and ionomycin with or without PAD4 inhibition. N=12-15, n=4. *P<0.05, **P<0.01, ***P<0.001, ****P<0.0001.

In addition to an earlier onset of nuclear disintegration, ionomycin induced NETosis earlier than PMA, with significant increases relative to control observed at 2 hours and compared to PMA at 3 hours (Fig. 3.14b, panel 3). Despite this earlier onset, PMA and ionomycin resulted in similar levels of NETosis by 12 hours of stimulation, with 6.64% and 6.44% of cells affected, respectively. PAD4 inhibition with GSK484 significantly suppressed NETosis in both treatments, with significant divergence starting at 5 hours for PMA ($p=0.00047$) and at 7 hours for ionomycin ($p=0.034$). Although minimal, NETosis was still detected in ionomycin-treated cells despite PAD4 inhibition, with 0.37% of cells affected at 12 hours, which was significantly higher than the GSK484 + PMA group ($p<0.0001$).

To assess differences in the magnitude of effect on each cell stage under different stimuli with or without PAD4 inhibition, the AUC was compared between relevant treatment groups (Fig. 3.14c). Treatment with 200 nM PMA significantly increased the magnitude of induction across all NETosis stages compared to control. In contrast, ionomycin elicited variable responses between experiments, only consistently increasing the proportion of disintegrated nucleus cells over time. When comparing the two stimuli, PMA induced greater levels of both spread and disintegrated nucleus phenotypes than ionomycin, while NETosis was comparable between treatments.

The impact of pre-treatment with GSK484 on the overall levels of each cell type with each NET inducer was assessed. Interestingly, GSK484 alone led to an increase in cell spreading. When combined with PMA, this effect was further amplified (17.1 vs 40.18, $p=0.0066$). However, PAD4 inhibition significantly suppressed the induction of disintegrated nucleus cells and NETosis triggered by PMA. With ionomycin, GSK484 co-treatment significantly reduced the proportion of disintegrated nucleus cells, although levels remained

higher than with GSK484 alone. While NETosis levels were nearly absent in the GSK484 + ionomycin condition, variability between replicates prevented this reduction from reaching statistical significance when compared to ionomycin alone. Notably, GSK + ionomycin resulted in a greater accumulation of disintegrated nucleus cells than GSK484 + PMA (26.64 vs 2.09, p=0.048), suggesting stimulus-specific differences in PAD4-dependent regulation of NETosis.

3.10 Temporal kinetics of NETosis are modulated by stimulus and PAD4 inhibition

When comparing the temporal dynamics of PMA and ionomycin stimulation, ionomycin induced an earlier onset of nuclear disintegration and NETosis, while the subsequent progression rate, as measured by the T_{50} and centroid values, was comparable between the two stimuli (Fig. 3.16). With GSK484 pre-treatment, PMA-induced cell spreading occurred earlier compared to PMA alone. However, no significant differences were observed in the timing of nuclear disintegration and NETosis under PAD4 inhibition with PMA, which is expected given the near absence of these cell types in the GSK + PMA group. In contrast, co-treatment with GSK484 and ionomycin delayed the onset of nuclear disintegration and NETosis relative to ionomycin alone and slowed the progression of disintegrated nucleus cells progression to 50% of their maximum value. Overall, GSK484 attenuated the response to ionomycin across all three phenotypes, as indicated by higher centroid values compared to ionomycin alone. While temporal comparisons between GSK484 + PMA and GSK484 + ionomycin were conducted, the absence of nuclear disintegration and NETosis in the GSK484 + PMA condition limits the relevance of these results.

3.11 NETosis stage composition differs according to stimulus, concentration, and PAD4 activity

To assess compositional differences in the distribution of the three cell phenotypes, stacked area plots were generated to visualize treatment-specific shifts in relative abundance

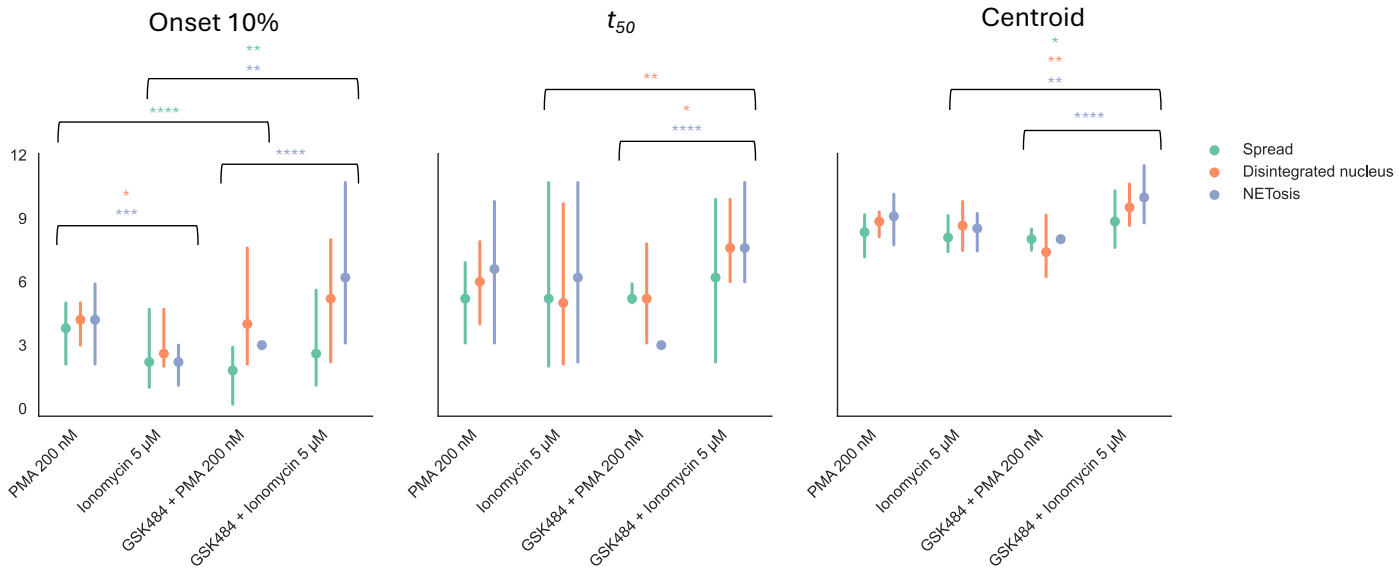

Figure 3.16: NETosis progression timing in response to PMA, ionomycin, and PAD4 inhibition.
Temporal metrics (0nset 10%, t50 and centroid) comparisons between PMA and ionomycin ± GSK484, shown as medians with 95% confidence intervals. Differences between groups were tested using mixed-effect models with experiment used as a random intercept n=experiments and Benjamini-Hochberg applied (n = 5 experiments, N = 15 replicates/treatment).

(Fig. 3.17a). Relative abundances were transformed using the CLR to test for proportional changes between treatments (Fig. 3.17b). A significant difference in overall cell composition was observed between PMA- and ionomycin-stimulated cells in the presence of PAD4 inhibition. In contrast, no significant differences were detected in the distribution of NETosis stages across increasing PMA concentrations or between PMA and ionomycin stimulation alone.

Although global compositional differences between increasing concentrations of PMA were not statistically significant, visual inspection of stacked area plots and pairwise comparisons revealed dose-dependent shifts in the distribution of cell phenotypes. Up to 20 nM, sequential increases in PMA concentration led to shifts in all three phenotypes, although disintegrated nucleus cells and NETosis accounted for ~50% and ~40% of the observed difference, respectively. Between 20 nM and 200 nM, compositional differences were predominantly driven by an increase in NETosis (>30%, $p=0.0001$). Although disintegrated nucleus cells contributed 59.2% of the overall shift, their relative abundance did not differ significantly between the two groups due to high inter-replicate variability ($p=0.232$).

When comparing PMA 200 nM to ionomycin, ionomycin stimulation resulted in a lower abundance of spread cells and a higher abundance of disintegrated nucleus cells compared to PMA 200 nM, accounting for 31.7% and 63% of the observed composition difference, respectively, while NETosis proportion remained similar. Under PAD4 inhibition, 46.3% of the difference in composition between PMA and ionomycin treatments was attributable to a higher abundance of disintegrated nucleus cells in the ionomycin group. Although spread cells also contributed to the shift, the difference was not statistically significant.

a

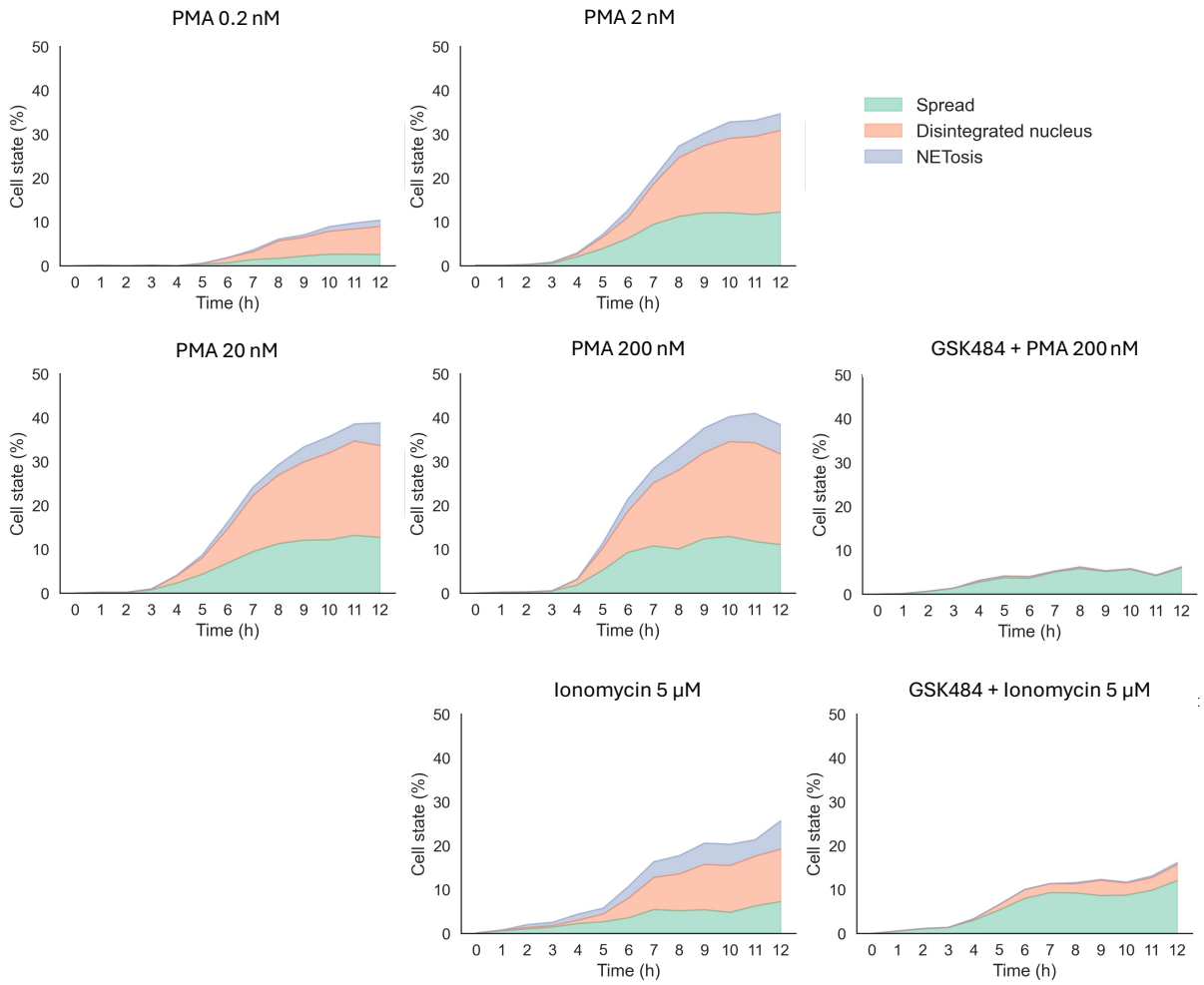

b

Group 1	Group 2	F	p adj	Spread			Disintegrated nucleus			NETosis		
				CLR	Contribution %	p adj	CLR	Contribution %	p adj	CLR	Contribution %	p adj
PMA 0.2 nM	**PMA 2 nM**	0.66	0.55	-0.018	0.2	<0.0001	0.30	53	<0.0001	-0.28	46.8	0.0162
PMA 2 nM	**PMA 20 nM**	0.14	0.93	0.008	0.4	0.0269	-0.088	54.5	<0.0001	0.08	45.1	0.00427
PMA 20 nM	**PMA 200 nM**	1.97	0.31	0.051	2.2	0.207	-0.26	59.2	0.232	0.21	38.6	0.0001
PMA 200 nM	**Ionomycin**	2.88	0.31	0.35	31.7	<0.0001	-0.49	63	<0.0001	0.14	5.3	0.635
GSK484 + PMA	**GSK484 + Ionomycin**	25.7	0.04	-1.54	53.4	0.253	1.44	46.3	0.0214	0.11	0.3	0.104

Figure 3.17: NETosis progression timing in response to PMA concentration, ionomycin and PAD4 inhibition. **a**, Stacked area plot showing the composition of NETosis stages over time per treatment (n = 5 experiments, N = 15 replicates/treatment). **b**, Pairwise comparisons of NETosis stage composition across treatment conditions based on compositional log-ratio (CLR)-transformed data. For each comparison, the F statistic and Benjamini-Hochberg-adjusted p-values are reported. The table shows F-values and adjusted p-values (Benjamini–Hochberg correction) for each comparison, along with CLR differences and p-values per cell type. For NETosis, CLR-based AUC is shown. Significant differences (*p < 0.05) are highlighted.

Together, these analyses of treatment-specific NETosis dynamics revealed progressive phenotype-specific increases in both the rate and magnitude of NETosis stages in response to sequential increases in PMA concentrations, with NETosis abundance primarily driving the shift between the highest concentrations. Ionomycin was observed to induce earlier onset of NETosis than PMA, although overall NET release remained similar. Results also revealed differential responses to PAD4 inhibition between the two stimuli, showing a reduced yet sustained capacity for nuclear disintegration with ionomycin stimulation, whereas this was markedly reduced with PMA. These findings suggest that PMA and ionomycin activate distinct pathways and that nuclear disintegration is not strictly PAD4-dependent under ionomycin stimulation.

3.12 Single-Cell NETosis Stage classification demonstrates high performance with mouse bone marrow neutrophils

The assay was applied to characterize NETosis in mouse bone marrow-derived neutrophils harvested from WT and *Padi4*$^{-/-}$ mice, allowing evaluation of its accuracy in confirming the lack of NET formation in *Padi4*$^{-/-}$ cells and assessing the impact of PAD4 deficiency on NETosis progression. Bone marrow was harvested from one femur of WT and *Padi4*$^{-/-}$ mice by centrifugation, and neutrophils were isolated using magnetic separation (Fig. 3.18a). Cells were resuspended in culture medium containing fluorescent DNA dye and Annexin V probe and were either left untreated or stimulated with 100 nM PMA before being imaged over a 24-hour period. Following feature extraction in CellProfiler, cells were classified into predefined categories: negative, spread, disintegrated nucleus, NETosis, and dead for single-cell classification (Fig. 3.18b).

CPA classifiers trained independently on each bone marrow neutrophil datasets exhibited consistently high performance across experiments (>90% accuracy), with strong discrimination of NETosis phenotypes and limited misclassification between related stages (Fig. 3.19).

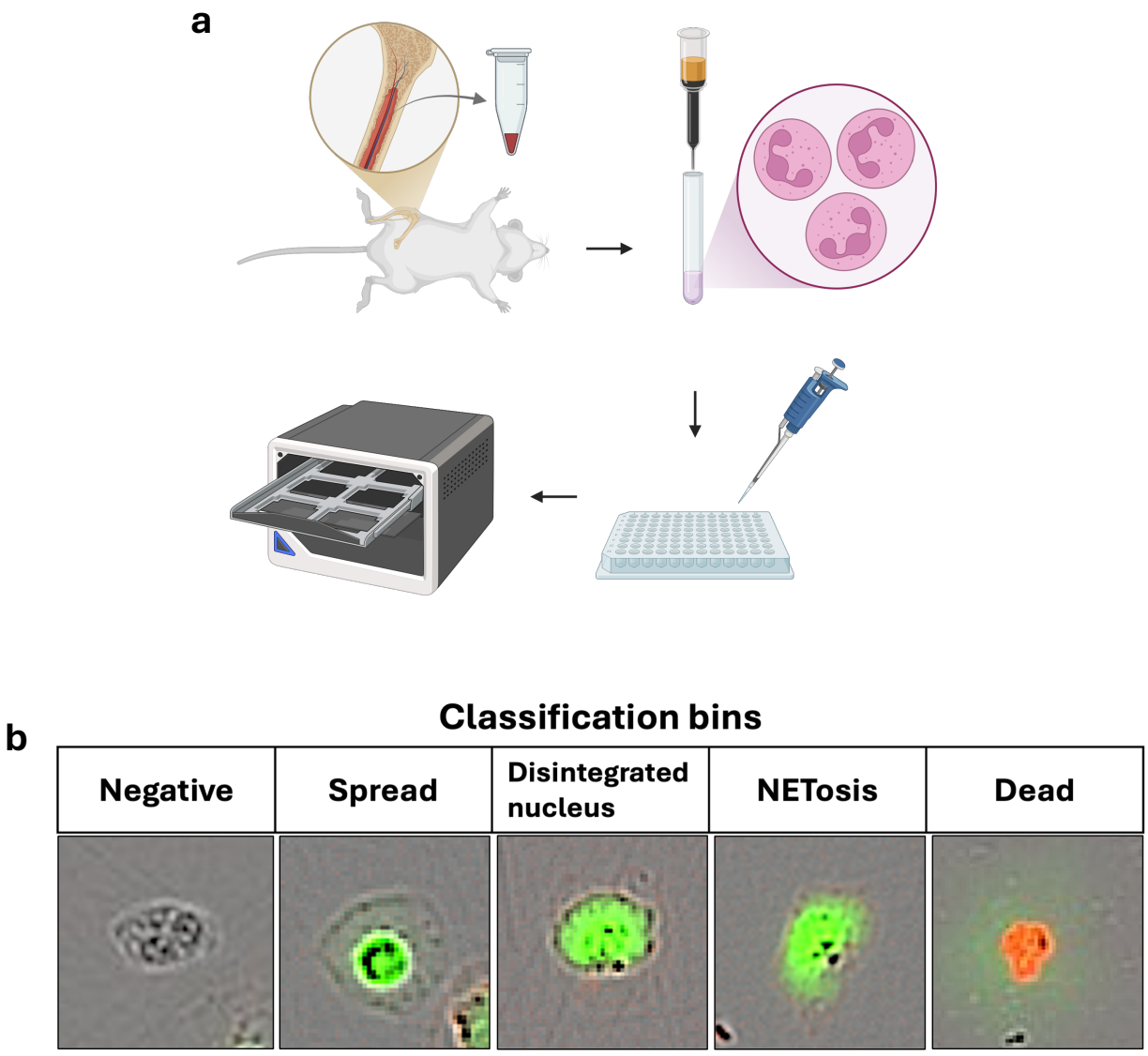

Figure 3.18: Workflow for applying the NET assay to bone marrow-derived neutrophils, with adapted classification of NET stages.

a, Schematic of the workflow for magnetic separation of bone marrow-derived neutrophils and their application in the NET assay. Created in BioRender. **b**, Representative images for each classification bin: Negative, Spread, Disintegrated nucleus, NETosis and Dead.

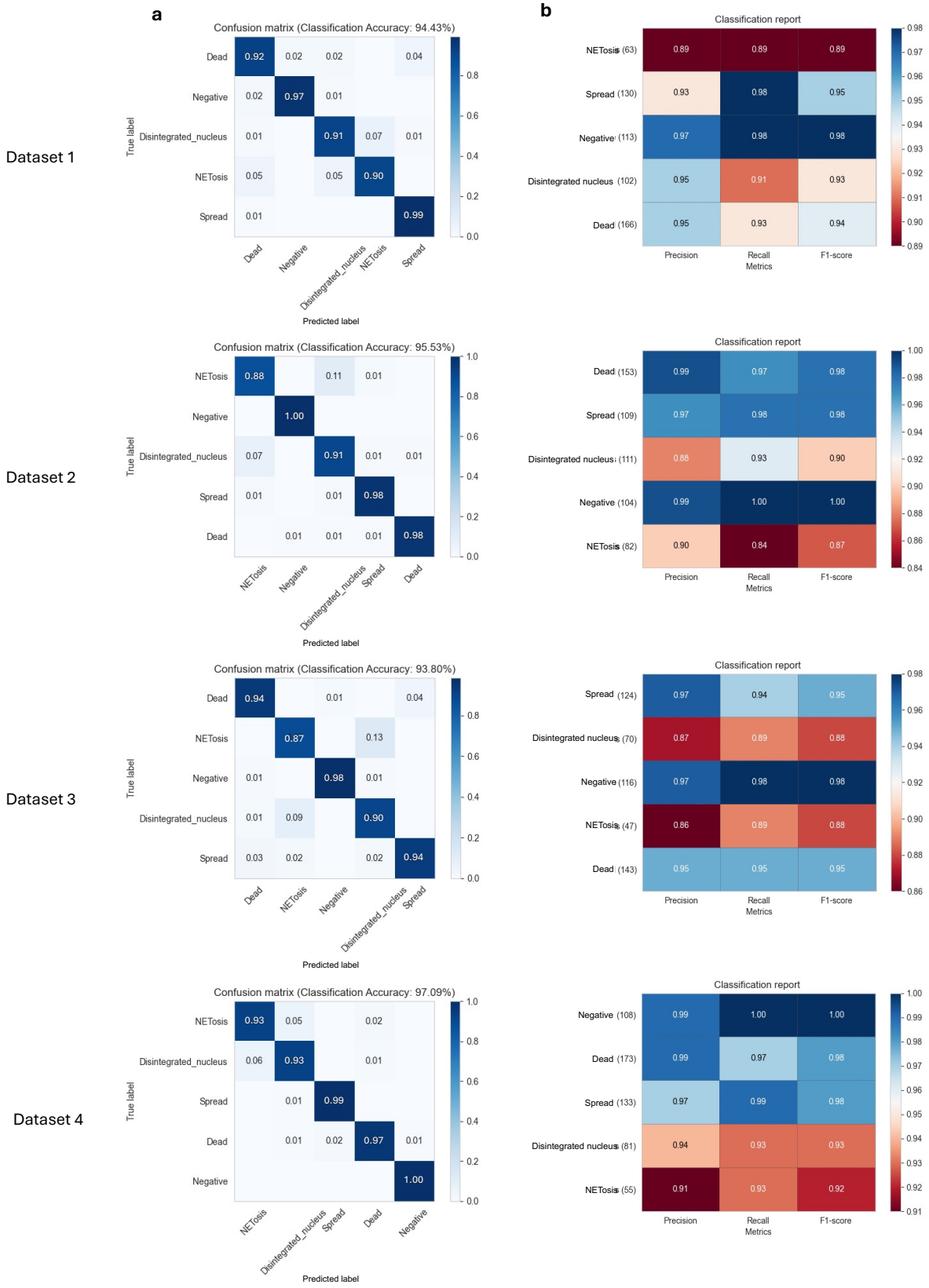

Figure 3.19: CellProfiler Analyst classification performance across mouse bone marrow-derived neutrophil experimental replicates.

a, Confusion matrices and **b**, corresponding performance metrics (precision, recall, and F1-score) obtained from CPA models trained on individual bone marrow neutrophil datasets. Model performance was evaluated using stratified test k-fold cross-validation (k=5) for each of the four experimental replicates. Overall classification accuracy for each dataset is indicated above the corresponding confusion matrix.

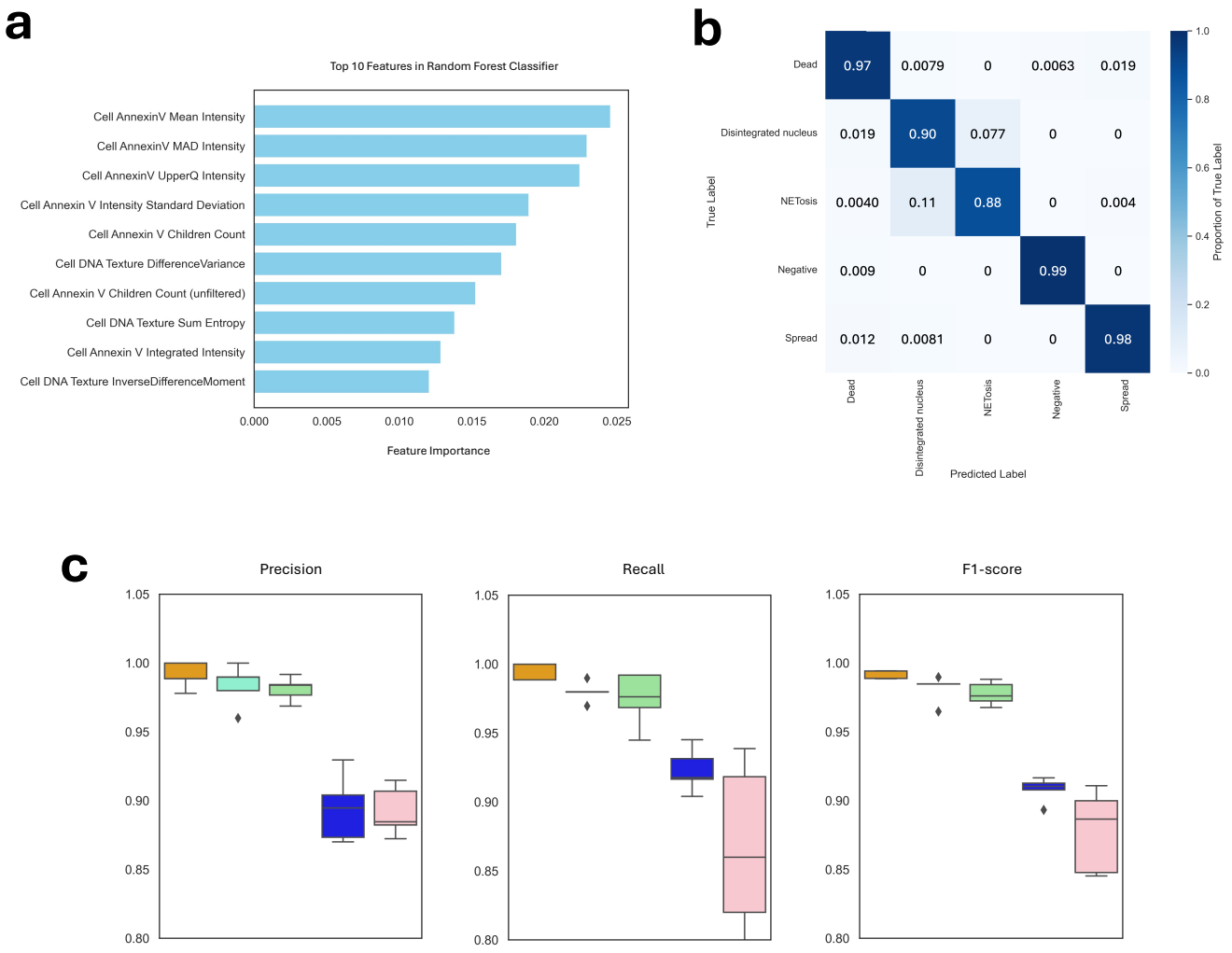

Figure 3.20: Overall CellProfiler Analyst classification performation with bone marrow-derived neutrophils. **a**, Top 10 classification features ranked by importance in the Random Forest model (n = 4 experiments, N = 2183 cells). **b**, Confusion Matrix of classifier predictions on unseen, stratified test data from 5-fold cross validation (k=5). **c**, Classification performance metrics (precision, recall, and F1-score) for each phenotype, evaluated on stratified test data.

A unified classifier was subsequently characterized based on its top-ranking features across experiments to assess their contribution to discriminating between cell phenotypes. Annexin V signal intensity and children count per cell emerged as major discriminators, along with DNA texture features (Fig. 3.20a). Among Annexin V-derived features, mean intensity, MAD intensity, and upper-quartile intensity ranked highest. For the DNA signal features, texture difference variance was the most influential, followed by texture sum entropy and inverse difference moment.

The overall performance of the Random Forest classifier in accurately sorting cells was evaluated using stratified test set validation on unseen data. Mean classification accuracy for each phenotype is summarized in a confusion matrix (Fig. 3.20b), with cell labels matching the training annotations 97% of the time for dead cells, 90% for disintegrated nucleus, 88% for NETosis, 99% for negative cells, and 98% for spread cells. Misclassification was most frequent between disintegrated nucleus and NETotic cells, with 7.7% and 11% of each phenotype misclassified as the other.

Consistent with this, the NETosis class displayed the lowest and most variable median F1-score, largely due to variable recall, followed by the disintegrated nucleus class. In contrast, the negative, spread, and dead cells were detected with high accuracy and precision, with median F1-scores exceeding 0.97 (Fig. 3.20c).

3.13 The NETosis Assay Reliably Distinguishes NETosis Stages and Detects PAD4-Dependent NET Formation in Mouse Bone Marrow Neutrophils

Representative classified images show predominantly disintegrated nucleus and NETotic cells in WT neutrophils treated with PMA, whereas the same treatment in *Padi4*$^{-/-}$ neutrophils resulted mainly in an increase in spread cells (Fig. 3.21).

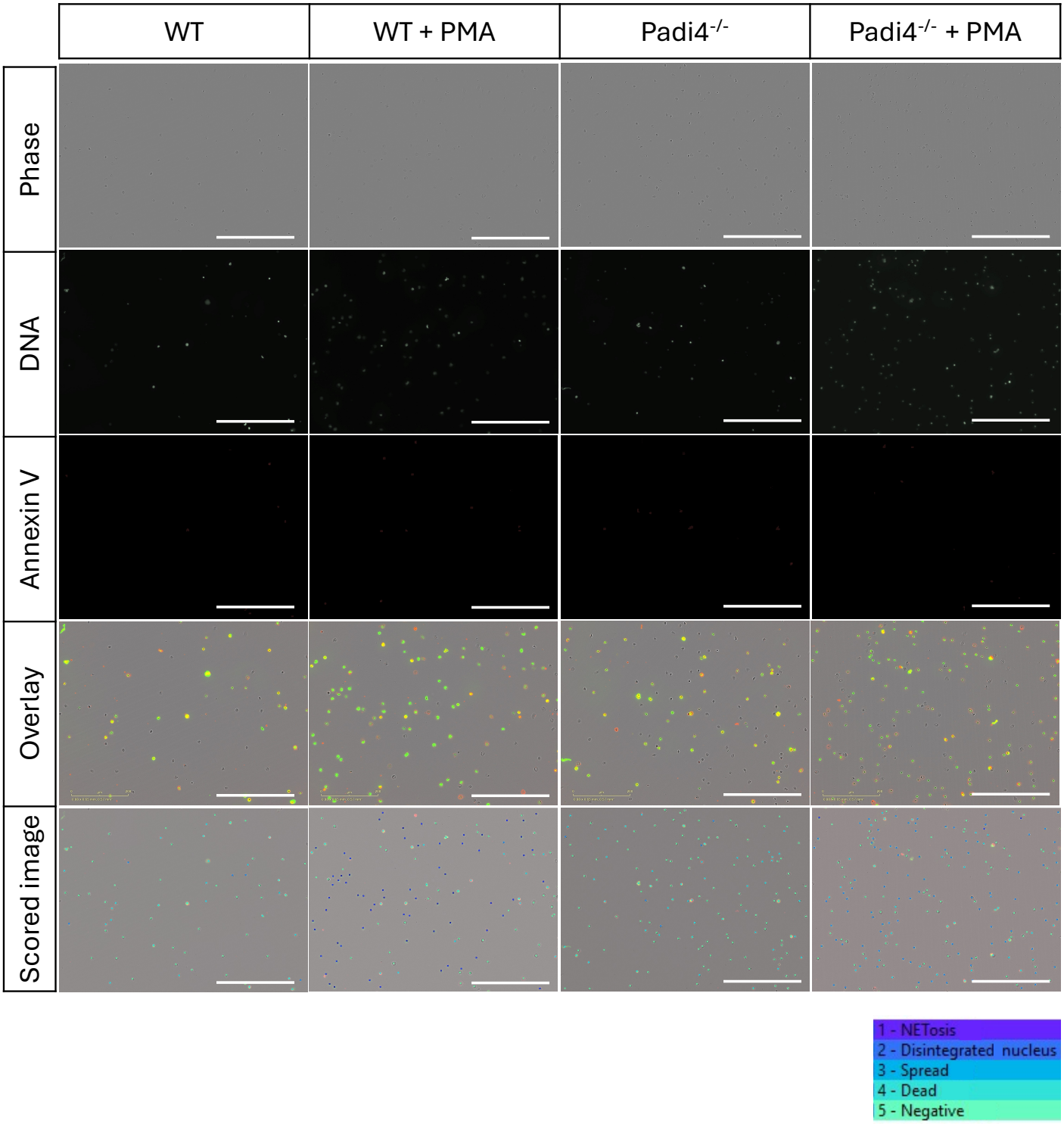

Figure 3.21: Representative images and CellProfiler Analyst-based classification of bone marrow neutrophil NETosis phenotypes.

Representative phase-contrast and fluorescence images of bone marrow neutrophils showing individual channels for DNA (green) and Annexin V (red), alongside composite overlays annotated with CPA-predicted cell phenotypes. Representative fields are shown for neutrophils isolated from WT and *Padi4*$^{-/-}$ mice following 8 h incubation, with or without stimulation with 100 nM PMA. Scale bar = 300 µm.

Time-course analysis of the median percentage of spread cells revealed that this phenotype appeared earliest in PMA-stimulated *Padi4*$^{-/-}$ neutrophils and was significantly higher than in both untreated *Padi4*$^{-/-}$ neutrophils and PMA-stimulated WT neutrophils from 4 hours onward, reaching a maximal response at 20 hours with a median 59% of spread cells (Fig. 3.22a). Accordingly, the median AUC for spread cells in this group showed approximately a 9- and 23-fold increase compared with the other two conditions (Fig. 3.22b).

Spread cells were also detected in unstimulated *Padi4*$^{-/-}$ neutrophils at significantly higher levels than in WT neutrophils across conditions, reaching a maximum of approximately 11%. In WT neutrophils, PMA stimulation induced a faster rise in spread cells (6 hours: WT=0.07% vs WT + PMA=1.22%, p=0.0014). However, at later time points untreated WT neutrophils exhibited higher levels of spreading than PMA-treated WT cells (21 hours: WT=3.82% vs WT + PMA=2.51%, p=0.0042). Despite the temporal differences, the overall magnitude of spread cells, as assessed by AUC, did not differ significantly between these two groups (Fig. 3.22b).

This pattern is consistent with progression of PMA-treated WT neutrophils toward later NETosis stages. Accordingly, disintegrated nucleus cells increased rapidly in PMA-stimulated WT neutrophils, becoming significantly elevated from 4 hours onward compared to untreated WT neutrophils (4 hours: WT=0% vs WT + PMA=1.09%, p=0.0002) and PMA-treated *Padi4*$^{-/-}$ neutrophils ($p<0.0001$). PMA-treated WT neutrophils reached a maximum of 48.4% cells with a disintegrated nucleus. In contrast, disintegrated nucleus cells were essentially absent in *Padi4*$^{-/-}$ neutrophils regardless of treatment and remained minimal in untreated WT neutrophils. These genotype- and treatment-dependent differences were also reflected in the corresponding AUC values (Fig. 3.22b).

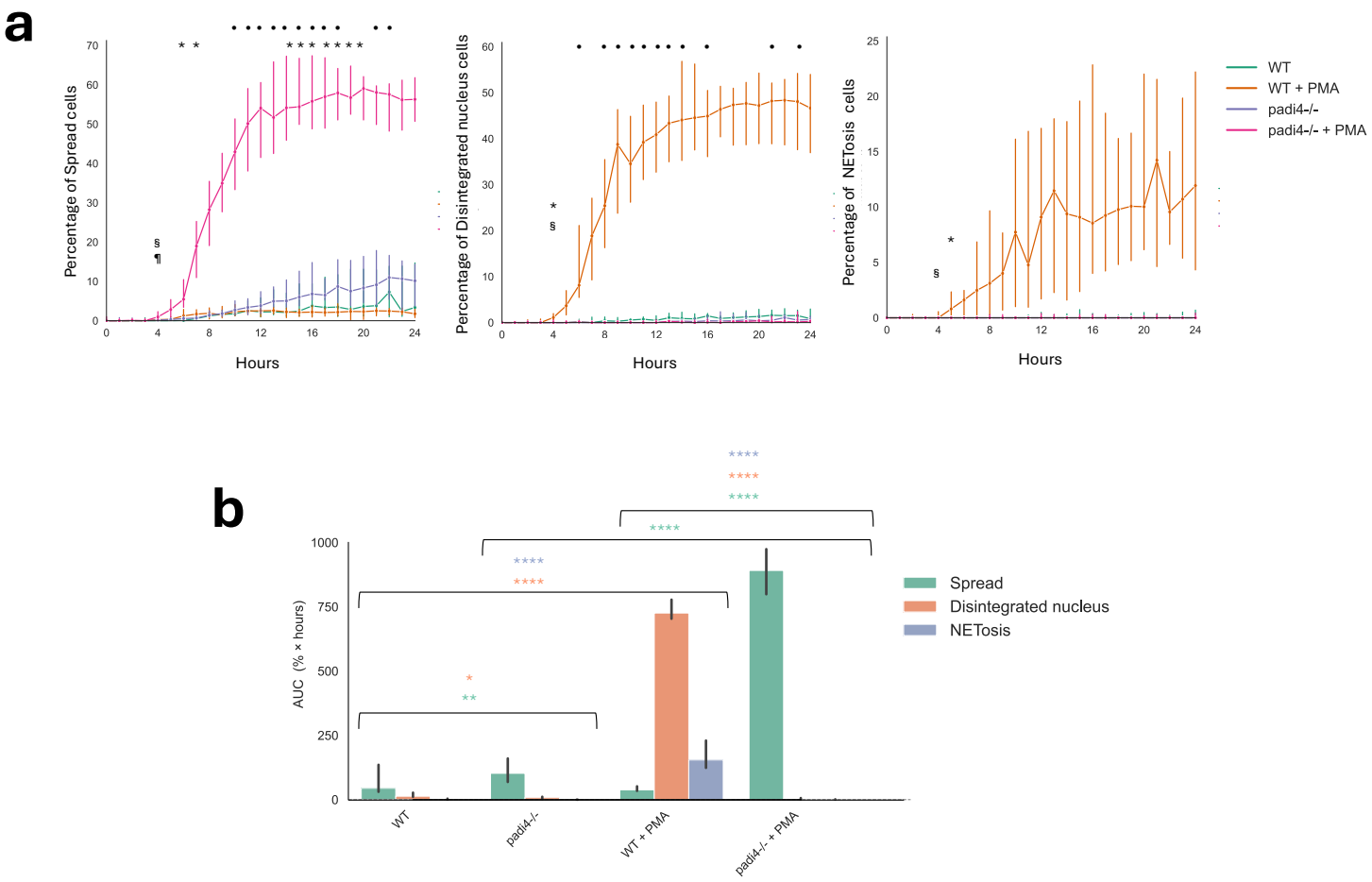

Figure 3.22: NETosis dynamics in WT and *Padi4*$^{-/-}$ mouse bone marrow neutrophils.

a, Line plots showing the median percentage of each NETosis stage over time. Mixed-effects models with experiment as a random intercept were followed by Bonferroni-corrected pairwise comparisons. Symbols are shown only at the first significant time point if significance is maintained for all subsequent time points; otherwise, symbols mark each significant time point. Pairwise comparisons: * WT vs WT + PMA, • WT vs *Padi4*$^{-/-}$, § WT + PMA vs *Padi4*$^{-/-}$ + PMA, ¶ *Padi4*$^{-/-}$ vs *Padi4*$^{-/-}$ + PMA. (n = 4 experiments, N = 12 replicates). **b**, Area under the curve (AUC) for each NETosis phenotype in WT and *Padi4*$^{-/-}$ neutrophils with or without PMA. Mixed-effects modeling with Holm step-down correction was applied. n=4 experiments, N=12 replicates. *p<0.05, **p<0.01, ***p<0.001, ****p<0.0001.

Only PMA-stimulated WT neutrophils progressed to a more advanced NETosis phenotype, representing approximately 12% of cells at 24 hours. Accordingly, this population became significantly elevated relative to untreated WT neutrophils and PMA-stimulated *Padi4*$^{-/-}$ neutrophils, with these differences mirrored in the corresponding AUC values (Fig. 3.22c).

Together, these analyses demonstrate that the NET assay and analysis pipeline can reliably distinguish between NETosis stages in mouse bone marrow-derived neutrophils, with minimal misclassification between disintegrated nucleus and NETotic cells. Consistent with the essential role of PAD4 in NET formation[13], the pipeline accurately captures the absence of NET formation in *Padi4*$^{-/-}$ neutrophils, which showed only accumulation of spread cells following PMA stimulation, while detecting late-stage NETosis exclusively in PMA-treated WT neutrophils, highlighting the assay's ability to resolve PAD4-dependent differences in NET formation.

Chapter 4

Altered NETosis dynamics in experimental hypertension and associated renal injury

4.1 Introduction and Rationale

Hypertension is accompanied by neutrophilia and heightened neutrophil activation, prompting growing interest in whether NETosis contributes to its pathogenesis (256,338). Although circulating NET markers are elevated in hypertensive individuals, the mechanisms driving this increase remain poorly understood (267,339). Both Ang II and mechanical forces associated with elevated vascular pressure have been proposed as triggers of NET formation, suggesting that hypertension may promote NET release beyond the effects of increased circulating neutrophils alone (262,267). Recent findings indicate that NETs may not only arise secondary to hypertension but may also influence blood pressure regulation itself, although their mechanistic contributions to injury remain poorly defined (262). NET accumulation has been observed in the vasculature and kidneys of preclinical hypertension models and in kidney biopsies from patients with essential hypertension, raising the possibility that NETs contribute to local tissue injury and immune activation in hypertensive organs (265,267,268).

The kidney is both a driver and target of hypertensive injury and becomes a site of immune activation when blood pressure is elevated (328). Renal infiltration of neutrophils, macrophages and T cells occurs in response to vascular oxidative stress, promoting a cycle of inflammation, cytokine production, and further oxidative injury that disrupts renal function (340–342). When NETs accumulate within the kidney, they can exacerbate these processes by inducing tubular epithelial injury, endothelial dysfunction, and profibrotic signaling (285,329,343). Despite these observations, the specific contribution of NETs to renal injury in hypertension remains unclear, underscoring the need for experimental models that can dissect how NET formation differs between hypertensive and normotensive conditions and how it shapes renal immune responses and injury.

4.2 NET deficiency does not modify the hypertensive response to Ang II

To investigate the contribution of NETs to hypertension-induced renal immune activation and injury, blood pressure elevation was induced in male and female WT and Padi4$^{-/-}$ mice using subcutaneous infusion of Ang II for 2 weeks (Fig. 4.1). As expected, SBP rose to ~ 166 mmHg in both sexes by week 2 (Table 4.1), consistent with prior Ang II infusion studies (249). SBP elevation was already detectable at week 1, confirming effective induction of hypertension (Figure 4.2a-b). However, in contrast to previous work, NET deficiency did not alter the magnitude or trajectory of the blood pressure response compared to WT controls.

Despite the marked increase in blood pressure, Ang II infusion did not produce detectable changes in normalized kidney or heart weight at study endpoint, indicating no measurable organ enlargement under these conditions (Table 4.1). This likely reflects an early stage of Ang II-induced hypertension, prior to the structural remodeling commonly reported in longer or higher-dose Ang II models (344,345).

4.3 Early renal injury markers show mild, sex-dependent changes with Ang II-induced hypertension, with no clear effect of PAD4 deficiency

To further investigate renal outcomes in this Ang II-induced hypertension model, glomerular morphology and markers of tubular injury were assessed.

Glomeruli were examined in PAS-stained kidney sections from all groups (Fig. 4.3a). Qualitatively, WT mice infused with Ang II exhibited mild mesangial matrix expansion and increased glomerular cellularity relative to WT controls and *Padi4*$^{-/-}$ mice. *Padi4*$^{-/-}$ + Ang II mice displayed glomerular morphology broadly similar to WT + Ang II, with no clear qualitative differences in mesangial expansion or hypercellularity detectable by visual assessment alone.

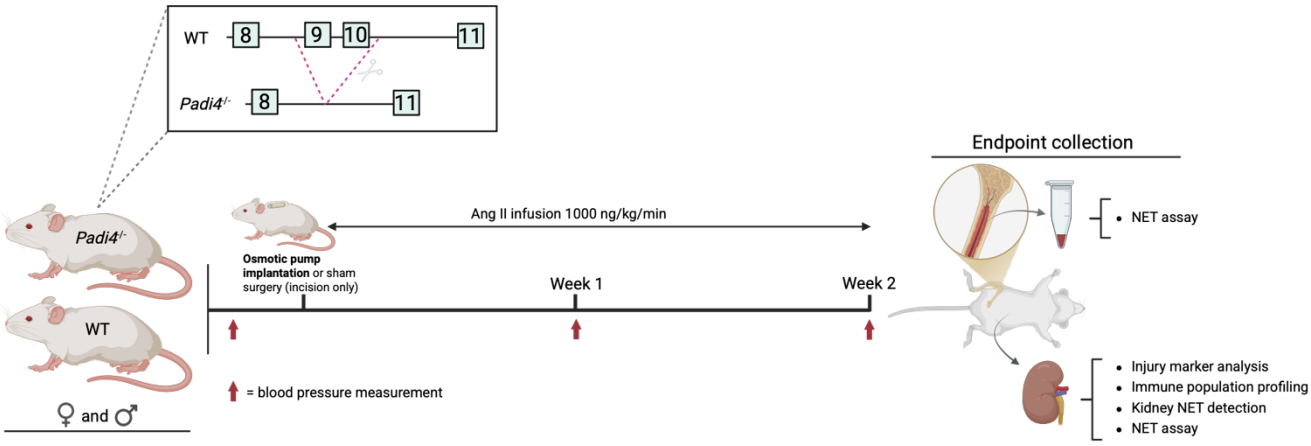

Figure 4.1: Experimental design for assessing NETosis dynamics and kidney injury during Ang II-induced hypertension.

Male and female WT and *Padi4*$^{-/-}$ mice were either implanted with subcutaneous osmotic minipumps delivering Angiotensin II (Ang II; 1000 ng/kg/min) or received sham surgery without pump placement. The schematic inset shows the *Padi4* exon 9-10 deletion that generates NET-deficient mice. Systolic blood pressure was recorded at baseline, week 1, and week 2 of infusion. At the experimental endpoint (week 2), bone marrow and kidney neutrophils were isolated for *ex vivo* NETosis assays, and kidney tissue was collected for injury marker analysis (RT-qPCR), immune cell profiling (IHC), and CitH3 staining to assess PAD4-dependent NETs.

Table 4.1: Endpoint physiological parameters in Ang II-infused mice.

Two weeks after pump implantation, systolic blood pressure (SBP) was measured using tail-cuff plethysmography. Body and organ weights were recorded at the time of tissue collection. Differences between groups were tested using one-way ANOVA with Tukey's multiple-comparison correction. Statistical comparisons are indicated as follows: *= WT vs Ang II; ¶= *Padi4*$^{-/-}$ vs *Padi4*$^{-/-}$ + Ang II. Two symbols=P<0.01, three symbols=P<0.001, four symbols=P<0.0001. N= 6-7 animals per group.

	Males				Females			
	WT	Ang II	*Padi4*$^{-/-}$	*Padi4*$^{-/-}$ + Ang II	WT	Ang II	*Padi4*$^{-/-}$	*Padi4*$^{-/-}$ + Ang II
SBP (mm/Hg)	127.1 ± 2.5	166.5 ± 5.6****	130.8 ± 2.5	162.6 ± 7.3¶¶	126.7 ± 1.9	166.2 ± 11**	128.4 ± 3.9	171.0 ± 5.1¶¶
Weight (g)	29.4 ± 0.8	26.9 ± 0.6	28.3 ± 0.6	25.8 ± 0.5*	23.8 ± 1.2	22.6 ± 0.3	23.9 ± 0.8	22.7 ± 0.5
Kidney weight/tibia (g/mm)	10.2 ± 0.32	9.76 ± 0.19	10.1 ± 0.04	9.14 ± 0.1	7.15 ± 0.01	7.5 ± 0.28	7.35 ± 0.04	6.89 ± 0.37
Heart weight/tibia (g/mm)	7.24 ± 0.36	7.87 ± 0.19	7.22 ± 0.21	7.30 ± 0.3	6.03 ± 0.32	7.04 ± 0.24	6.23 ± 0.4	6.96 ± 0.23

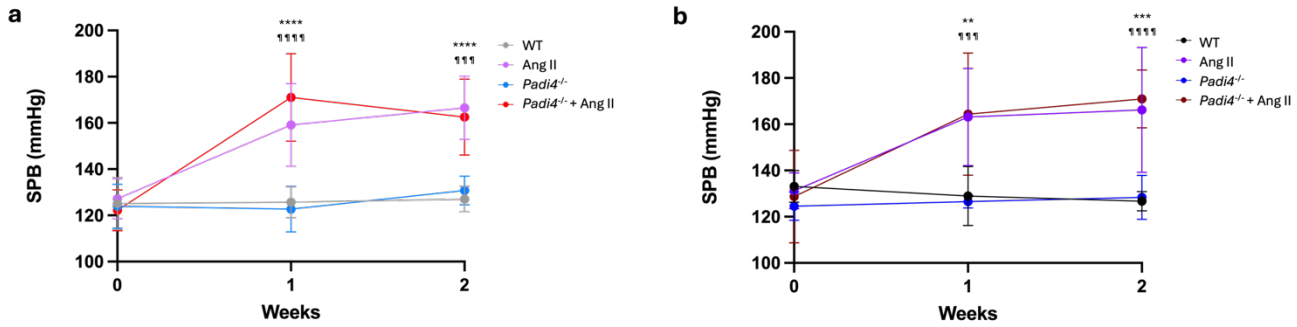

Figure 4.2: Weekly systolic blood pressure (SBP) measurements in Ang II-infused mice.

SBP was measured prior to pump implantation (week 0) and weekly thereafter until study endpoint in **a**, males and **b**, females. Values represent the mean of 7-10 tail-cuff plethysmography readings per mouse. Differences between groups were tested using two-way ANOVA with Tukey's multiple-comparison correction. Statistical comparisons are indicated as follows: *= WT vs Ang II. ¶=*Padi4*$^{-/-}$ vs *Padi4*$^{-/-}$ + Ang II. 2 symbols=P<0.01, 3 symbols=P<0.001, 4 symbols=P<0.0001. N= 6-7 animals per group.

Tubular injury was assessed by quantifying NGAL and KIM-1 mRNA expression in whole-kidney lysates using RT-qPCR (Fig. 4.3b-c). In males, Ang II infusion significantly increased NGAL expression in WT mice compared to WT controls (Fig. 4.3b). In *Padi4*$^{-/-}$ mice, Ang II produced kidney NGAL levels that trended lower than WT + Ang II but remained statistically indistinguishable from both WT baseline and Ang II-treated WT groups. This pattern suggests a possible attenuation of NGAL upregulation in the absence of PAD4, although variability across replicates prevents definitive conclusions.

For KIM-1, male WT + Ang II kidneys showed elevated expression relative to WT controls (Fig. 4.3c). *Padi4*$^{-/-}$ + Ang II mice displayed intermediate KIM-1 that were significantly higher than WT baseline but trended lower than WT + Ang II without achieving statistical significance. As with NGAL, this may reflect a modest reduction in injury signaling in PAD4-deficient mice, though the overlap between groups limits strong interpretation.

In females, neither NGAL nor KIM-1 expression differed significantly across groups, indicating minimal detectable tubular injury after two weeks of Ang II infusion in either genotype (Fig. 4.3b-c). Yet, the absence of measurable tubular injury markers in females highlights a clear sex-dependent difference in susceptibility to Ang II-induced kidney injury.

Overall, these results indicate that two weeks of Ang II infusion produced mild renal injury in males after two weeks, with subtle variable changes across genotypes. While PAD4 deficiency did not markedly alter tubular injury markers, the modest downward trends in NGAL and KIM-1 expression in Padi4$^{-/-}$ + Ang II males suggest a possible attenuation that could not be statistically resolved. Together, these results imply that PAD4-dependent NETosis does not exert a strong effect on early structural or tubular injury in this model of Ang II-induced hypertension,

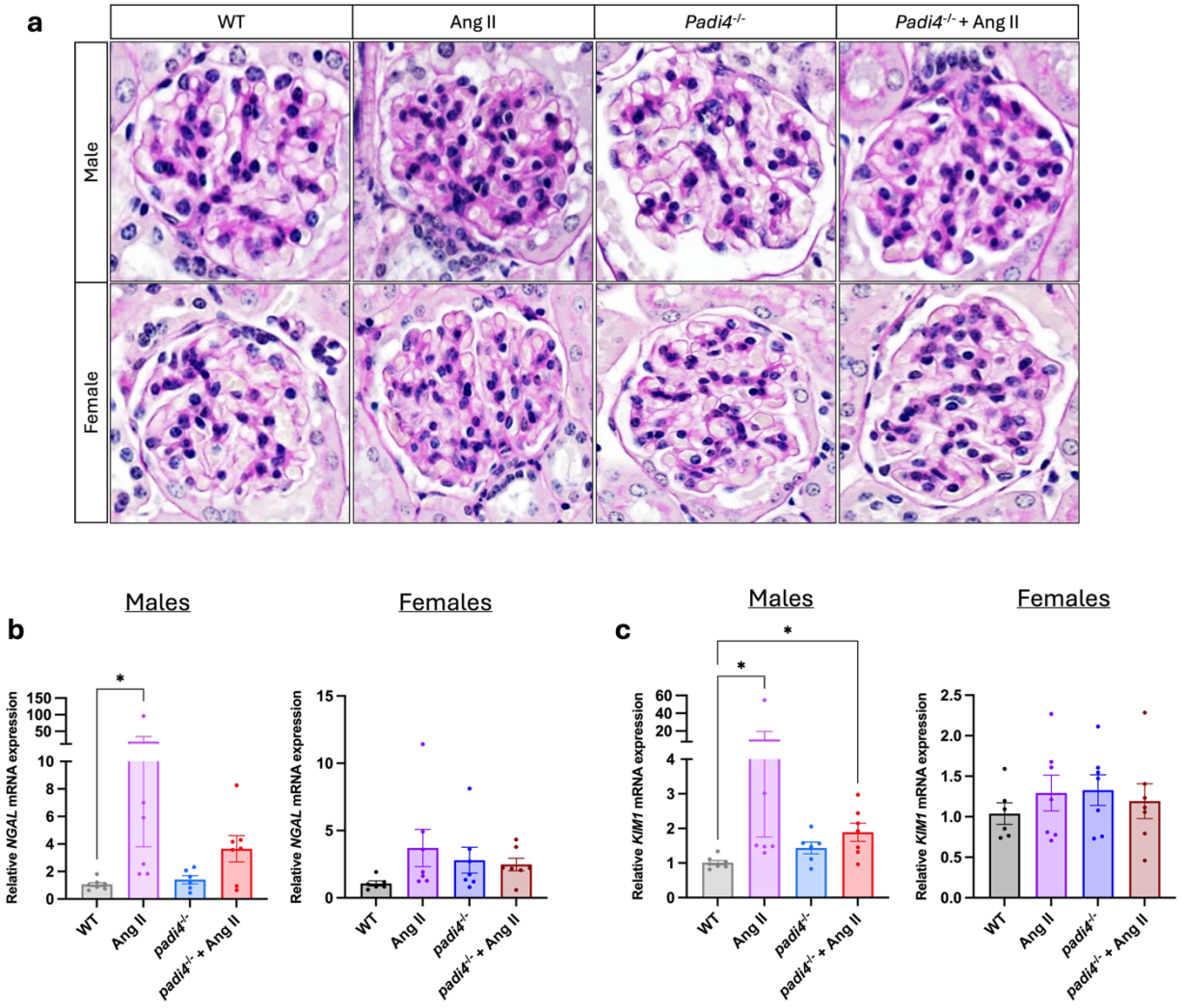

Figure 4.3: Assessment of kidney injury in Ang II-infused mice.

a, Glomerular morphological changes were evaluated in PAS-stained kidney sections from mice infused with Ang II for 2 weeks (63x magnification). **b**, NGAL and **c**, KIM-1 mRNA expression was quantified in kidney tissue by RT-qPCR. Group differences were tested using Kruskal-Wallis or one-way ANOVA with appropriate post-hoc correction. *=P<0.05. N= 6-7 animals per group.

underscoring the need to evaluate immune activation and cellular responses rather than overt tissue damage at this stage.

4.4 Renal immune cell recruitment in Ang II-induced hypertension occurs independently of PAD4-dependent NETosis

Given that renal immune activation is a hallmark of hypertensive kidney injury, immune cell populations were quantified in the kidney to assess whether PAD4-dependent NETosis alters neutrophil, macrophage, or T cell recruitment during Ang II–induced hypertension.

Renal neutrophils were assessed by MPO immunostaining. Representative images show the presence of MPO^+ cells within the renal cortex across all groups (Fig. 4.4). In males, Ang II infusion induced a variable but nonsignificant increase in MPO^+ neutrophils in both WT and *Padi4*$^{-/-}$ kidneys compared to controls. These findings indicate that any neutrophil recruitment to the male kidney is modest at this early hypertensive stage and is not detectably influenced by PAD4 deficiency.

In females, baseline neutrophil levels were lower overall. Yet, Ang II induced a marked increase in renal MPO^+ cells in WT mice, whereas this response was blunted in *Padi4*$^{-/-}$ + Ang II mice. This suggests that PAD4-dependent NETosis may contribute to renal neutrophil recruitment in hypertensive females. Interestingly, untreated *Padi4*$^{-/-}$ females showed a modest increase in MPO^+ cell numbers compared to WT controls, which may reflect compensatory changes in neutrophil activation associated with NETosis deficiency under steady-state conditions (346).

Macrophages are key mediators of renal inflammation in hypertension. Their recruitment to the kidney contributes to oxidative stress, inflammatory signaling, and fibrosis, and has been associated with worsened blood pressure elevation in Ang II–induced and salt-sensitive models (347–349)

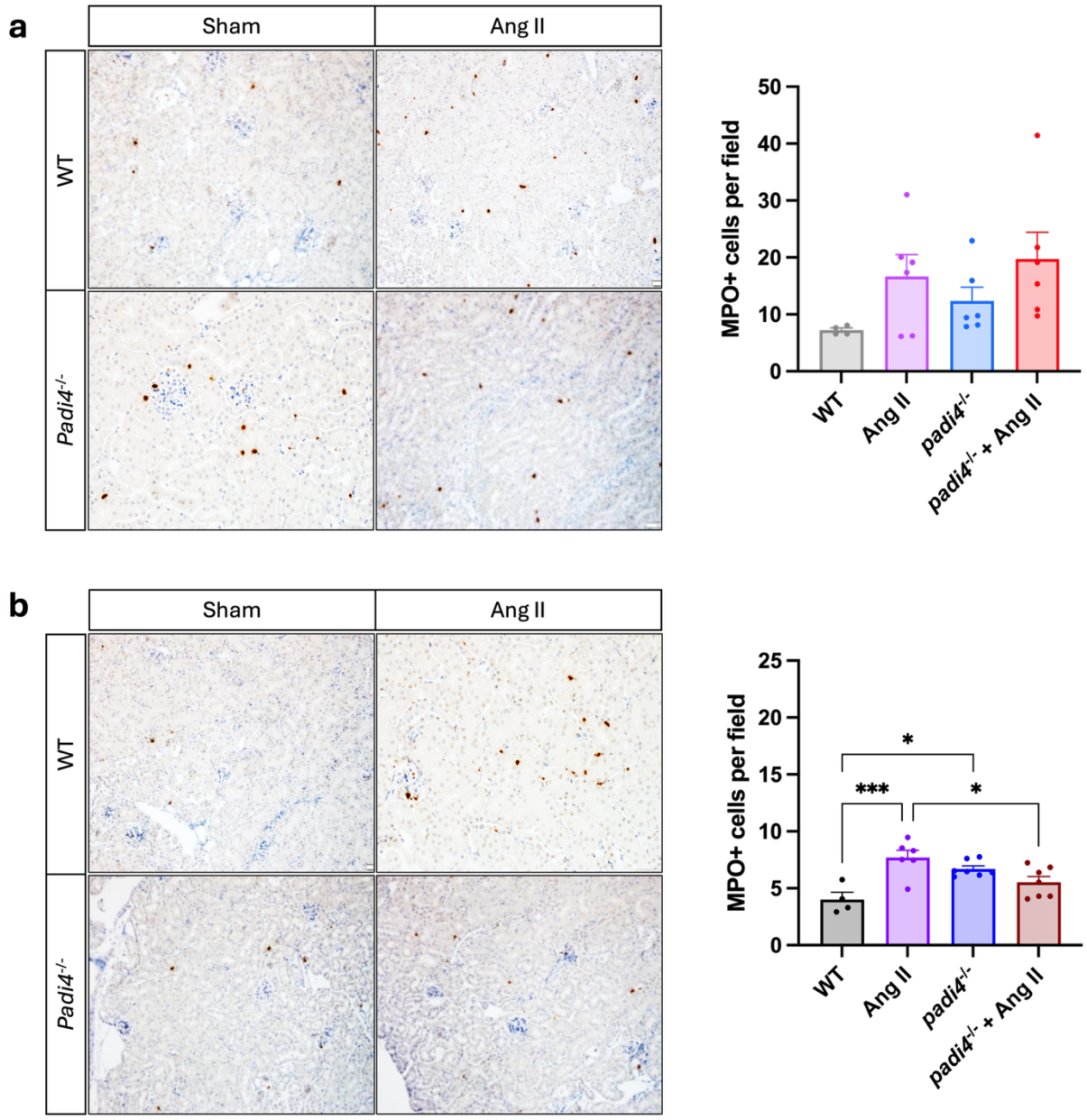

Figure 4.4: Neutrophil staining in kidney sections of Ang II-infused mice.

Neutrophils were detected by MPO immunostaining with DAB in paraffin-embedded kidney sections from **a**, male and **b**, female mice infused with Ang II for 2 weeks. Representative images show MPO^+ cells in WT and *Padi4*$^{-/-}$ mice under sham or Ang II conditions (10x magnification). Quantification reflects the mean number of MPO^+ cells per mouse across 12 fields of view. Group differences were tested using Kruskal-Wallis or one-way ANOVA with appropriate post-hoc correction. *=P<0.05, ***=P<0.001. N= 4-7 animals per group.

Macrophage abundance in the kidney was assessed by F4/80 immunostaining to determine whether PAD4-dependent NETosis influences macrophage recruitment during Ang II–induced hypertension (Fig. 4.5).

In males, Ang II infusion produced a modest increase in $F4/80^{+}$ macrophages in both WT and *Padi4*$^{-/-}$ mice, but only the *Padi4*$^{-/-}$ + Ang II showed a statistically significant elevation compared to WT controls (Fig. 4.5a). This indicates that Ang II-induced hypertension induces kidney macrophage recruitment independently of PAD4-dependent NET formation and may even be slightly more pronounced in the absence of PAD4.

In females, renal macrophage numbers were modestly but significantly elevated in *Padi4*$^{-/-}$ mice compared to control, independent of Ang II infusion (Fig. 4.5b). Ang II treatment did not significantly increase macrophage abundance in WT and did not further amplify macrophage levels in *Padi4*$^{-/-}$ females. These findings suggest that PAD4 deficiency is associated with higher baseline renal macrophage numbers in females, potentially reflecting sex-dependent differences in macrophage homeostasis that appears independent of Ang II stimulation.

T cells are major drivers of hypertensive kidney injury, as their infiltration and activation amplify renal inflammation, oxidative stress, and sodium-retention pathways that promote and sustain elevated blood pressure (341). To evaluate whether PAD4-dependent NETosis influences renal T cell recruitment during Ang II-induced hypertension, kidney sections were stained for cluster of differentiation 3 (CD3), a pan-T cell marker (Fig. 4.6).

In males, Ang II infusion increased renal $CD3^{+}$ T cell numbers in both WT and *Padi4*$^{-/-}$ mice relative to their respective sham controls (Fig. 4.6a). Although WT + Ang II showed a notable numerical rise in T cell infiltration, the variability in this group prevented the increase from reaching statistical significance. In contrast, *Padi4*$^{-/-}$ + Ang II males displayed a robust and

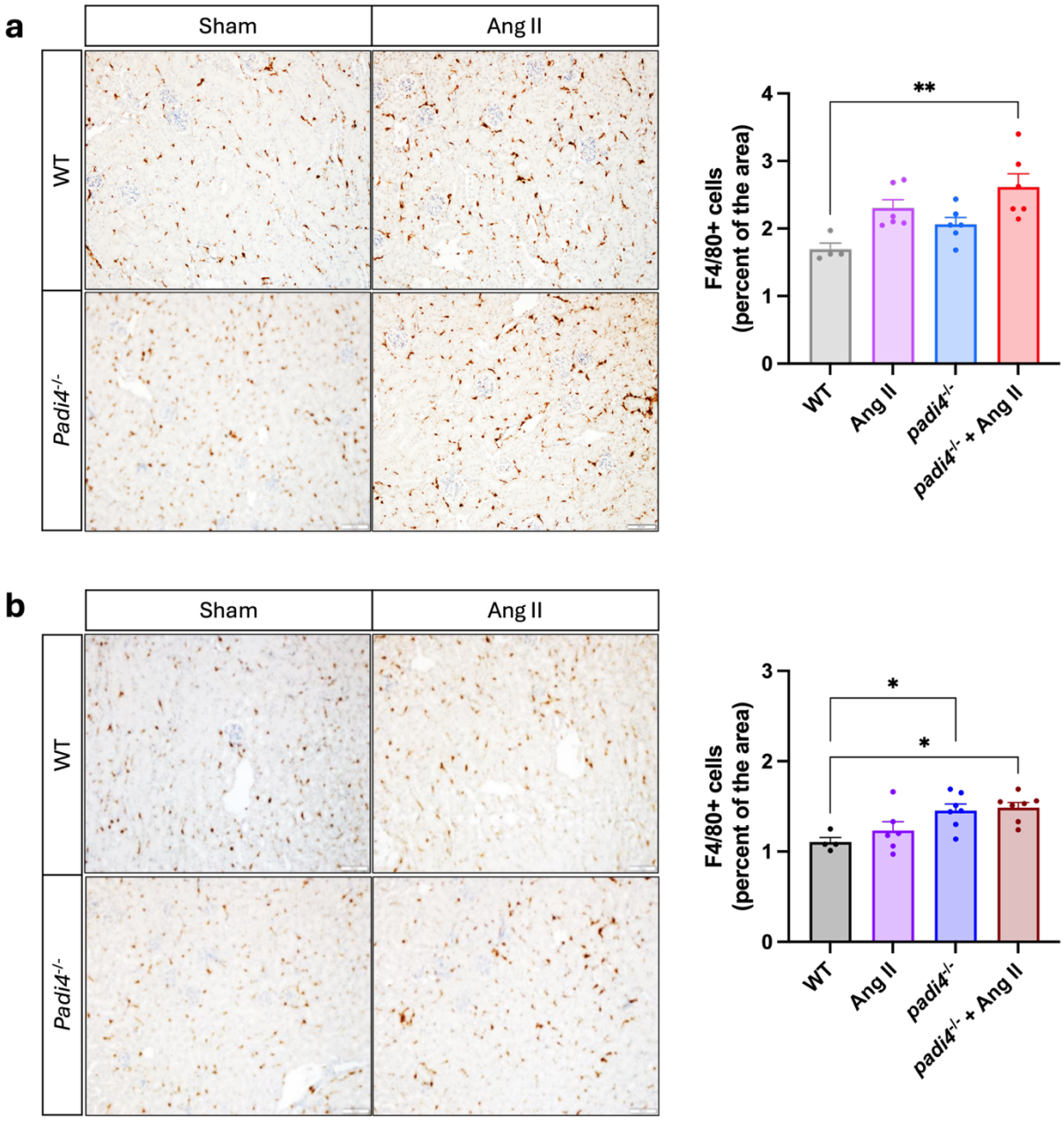

Figure 4.5: Macrophage staining in kidney sections of Ang II-infused mice.

Macrophages were detected by F4/80 immunostaining with DAB in paraffin-embedded kidney sections from **a**, male and **b**, female mice infused with Ang II for 2 weeks. Representative images show F4/80^{+} cells in WT and *Padi4*$^{-/-}$ mice under sham or Ang II conditions (10x magnification). Quantification reflects the mean number of F4/80^{+} cells per mouse across 12 fields of view. Group differences were tested using Kruskal-Wallis or one-way ANOVA with appropriate post-hoc correction. *=P<0.05, **=P<0.01. N= 4-7 animals per group.

significant elevation in $CD3^+$ cells, indicating that Ang II–driven T cell recruitment occurs independently of PAD4.

In females, Ang II significantly increased renal T cell infiltration in both WT and $Padi4^{-/-}$ mice (Fig. 4.6b). The magnitude of T cell accumulation was similar across genotypes, with Ang II elevating $CD3^+$ cell numbers in both groups to a comparable extent. These findings again suggest that PAD4 deficiency does not limit T cell recruitment to the hypertensive kidney.

Together, these data indicate that early renal immune recruitment in Ang II-induced hypertension is mild and proceeds largely independent of PAD4-dependent NETosis, with only subtle sex-specific differences.

4.5 NETs do not deposit in the kidney at two weeks of Ang II-induced hypertension

During inflammatory injury, dysregulated NET formation can lead to NET deposition in the kidney, contributing to structural damage and amplified inflammatory signaling (350). CitH3, a PAD4-dependent NET component, serves as a widely used marker of these deposits (351). To assess whether PAD4-mediated NETs accumulate during Ang II-induced hypertension, we performed CitH3 immunofluorescent staining on fresh-frozen kidney sections. Consistent with our findings that NETs do not drive renal immune cell recruitment in this model, no CitH3-positive areas were detected in any group or sex, suggesting that PAD4-mediated NETs are absent or rapidly cleared at the two-week time point (Fig. 4.7).

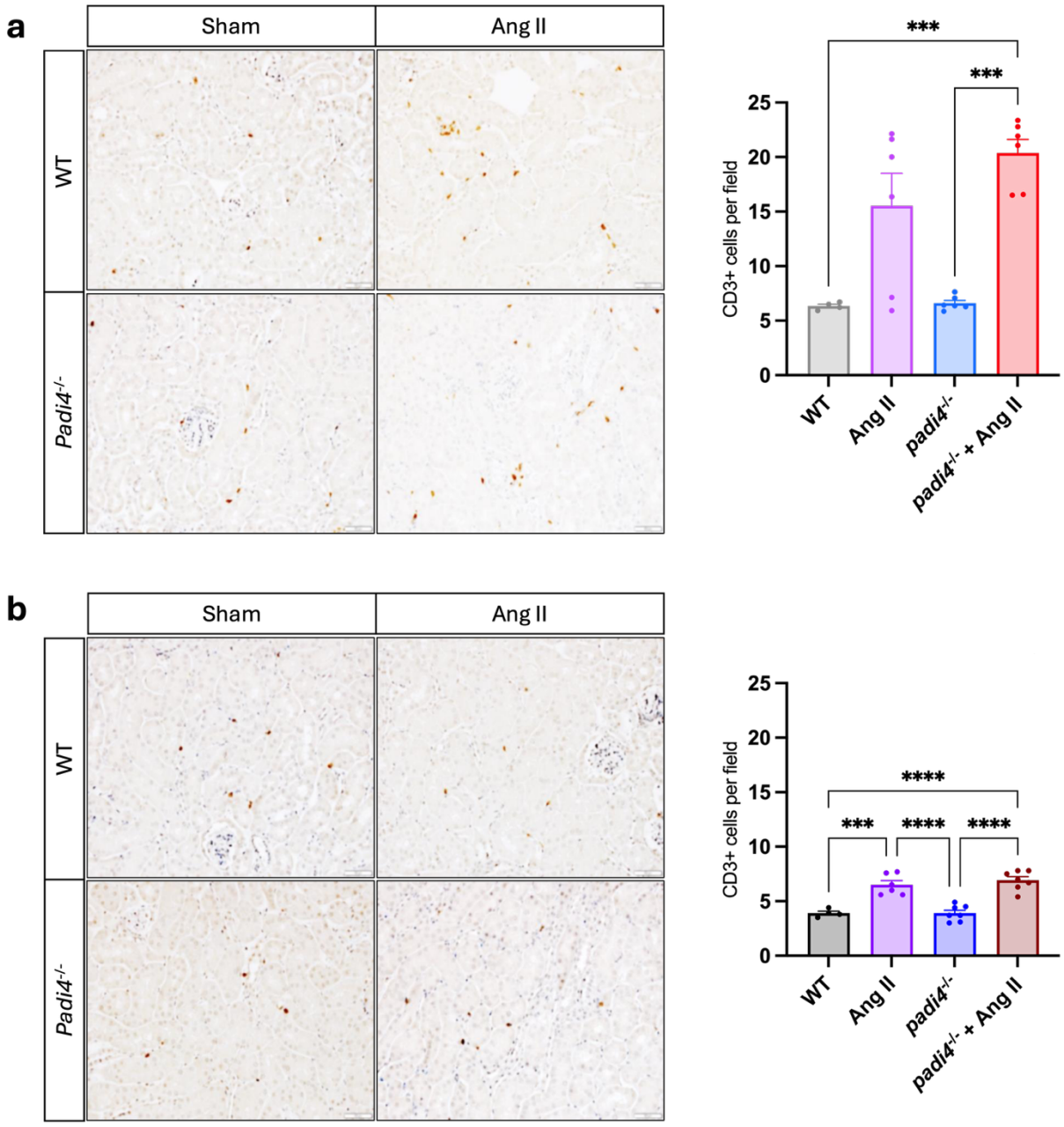

Figure 4.6: T cell staining in kidney sections of Ang II-infused mice.

T cells were detected by CD3 immunostaining with DAB in paraffin-embedded kidney sections from **a**, male and **b**, female mice infused with Ang II for 2 weeks. Representative images show $CD3^+$ cells in WT and *Padi4*$^{-/-}$ mice under sham or Ang II conditions (10x magnification). Quantification reflects the mean number of $CD3^+$ cells per mouse across 12 fields of view. Group differences were tested using Kruskal-Wallis or one-way ANOVA with appropriate post-hoc correction. ***=P<0.001, ****=P<0.0001. N= 4-7 animals per group.

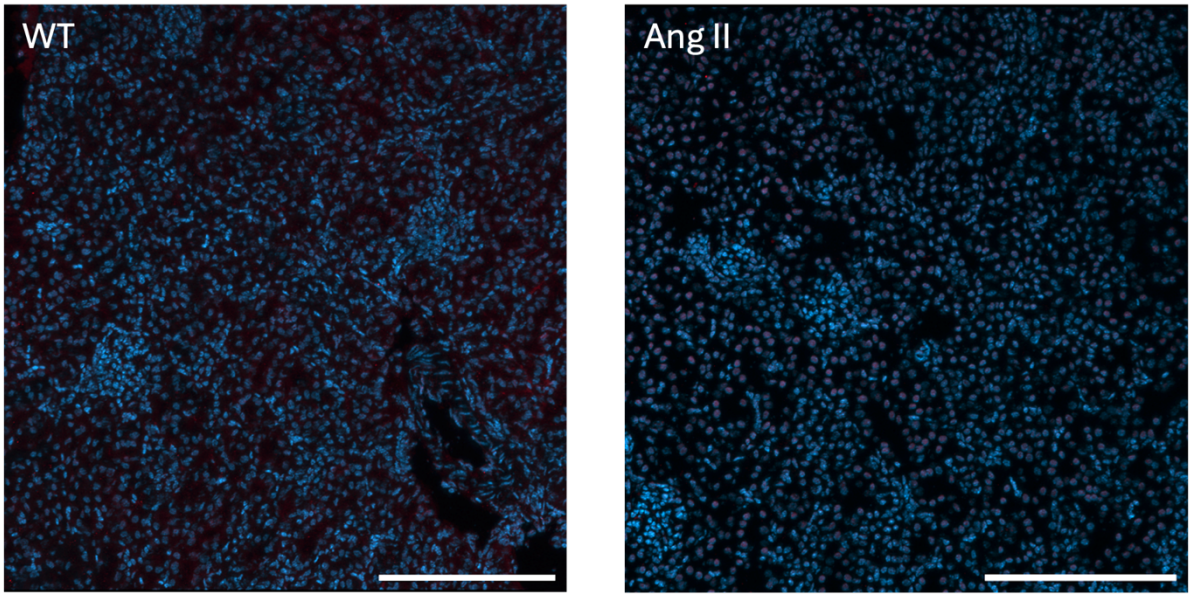

Figure 4.7: Immunofluorescent staining for PAD4-dependent NETs (citrullinated histone H3, CitH3) in kidney sections from Ang II-infused mice.

CitH3 staining was performed on fresh-frozen kidney sections from all groups. Nuclei were counterstained with Hoechst (blue) to visualize tissue architecture**.** Representative images show no detectable CitH3-positive signal (red), indicating an absence of PAD4-dependent NETs across all groups and sexes. Scale bar = 200 µm.

4.6 Kidney neutrophils display distinct NETosis dynamics compared to bone marrow neutrophils

Release of neutrophils from the bone marrow exposes them to diverse biological factors and tissue-derived signals, leading to altered reactivity as they age and acquire tissue-specific characteristics (352). To characterize baseline differences in NETosis dynamics between tissue-resident kidney neutrophils and naïve bone marrow neutrophils, we compared their responses to 100 nM PMA stimulation in untreated WT mice and quantified the distribution of cells across the three NETosis stages (spread, disintegrated nucleus, and complete NETosis) (Fig. 4.8). Unstimulated neutrophils were also assessed, but no spontaneous NETosis occurred, limiting further interpretation (Fig. 4.9).

Overall, kidney- and bone marrow-derived neutrophils displayed significantly different NETosis profiles in both male and female neutrophils. In both sexes, bone marrow neutrophils showed a pronounced accumulation in the disintegrated-nucleus stage, far exceeding that in kidney neutrophils, suggesting a stronger early response to PMA in this compartment (Fig. 4.8b-c). However, only about 1/3 of cells progressed to complete NETosis, particularly in males, indicating potential insufficient activation to initiate final NET release (Fig. 4.8b).

In contrast, kidney neutrophils exhibited lower overall levels of both disintegrated nucleus cell and complete NETosis (Fig. 4.8b-c), yet the time-course plots show a progressive decline in disintegrated-nucleus cells accompanied by a corresponding increase in complete NETosis (Fig. 4.8a). This pattern suggests that, although fewer kidney neutrophils enter the early stages of NETosis, a greater proportion ultimately complete the NET release process, potentially reflecting distinct activation thresholds and tissue-specific priming states.

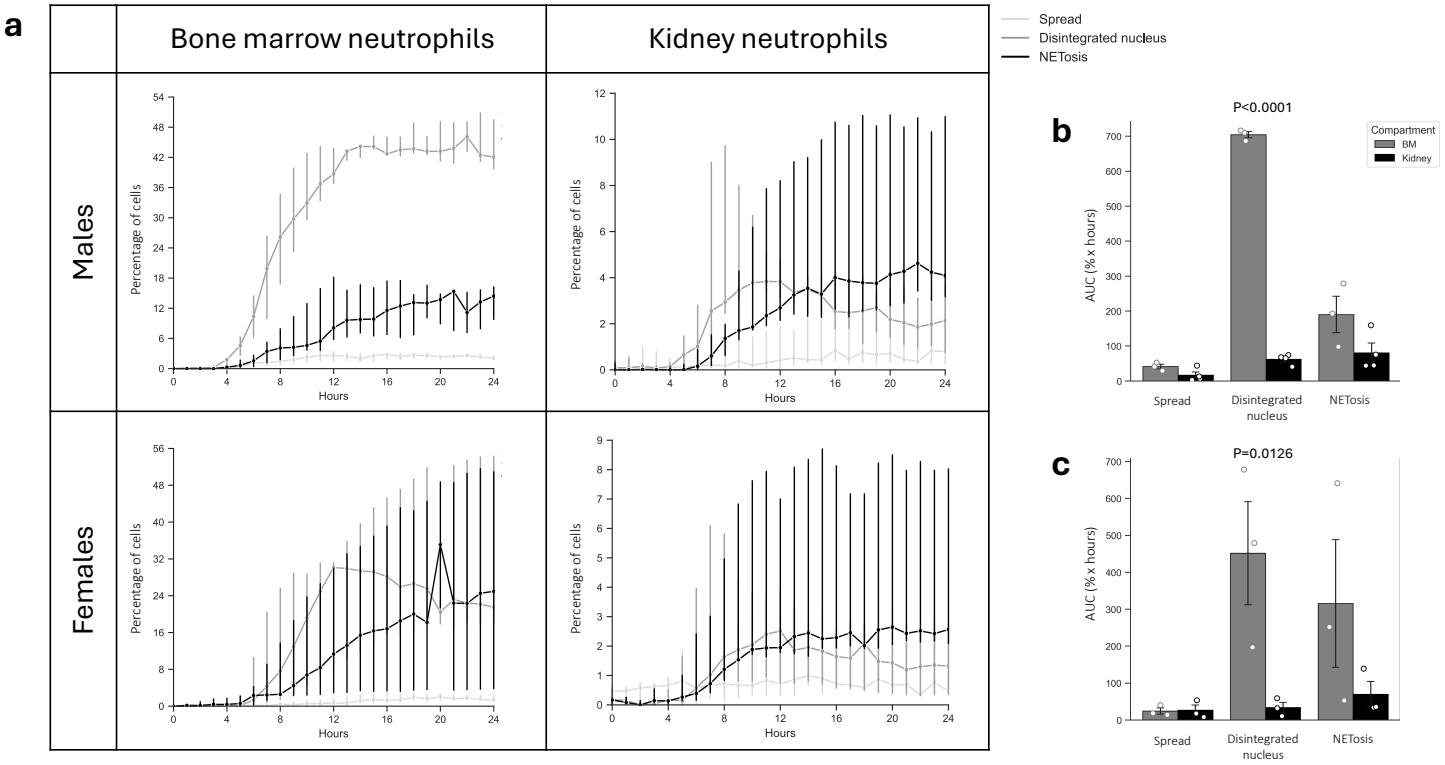

Figure 4.8: Compartment-specific NETosis dynamics in PMA-stimulated neutrophils from males and females.
a, Line plots show the median proportion of each NETosis stage (spread, disintegrated nucleus, NETosis) over time in bone marrow and kidney neutrophils stimulated ex-vivo with 100 nM PMA. Neutrophils were isolated from WT mice using immunomagnetic separation and analyzed using live-cell NETosis assay. **b-c**, Comparison of the AUC for each NETosis stage over time in bone marrow and kidney neutrophils from **b**, males and **c**, females. Compartment-dependent differences were assessed using two-way ANOVA with appropriate post-hoc correction. N= 3-5 animals per group.

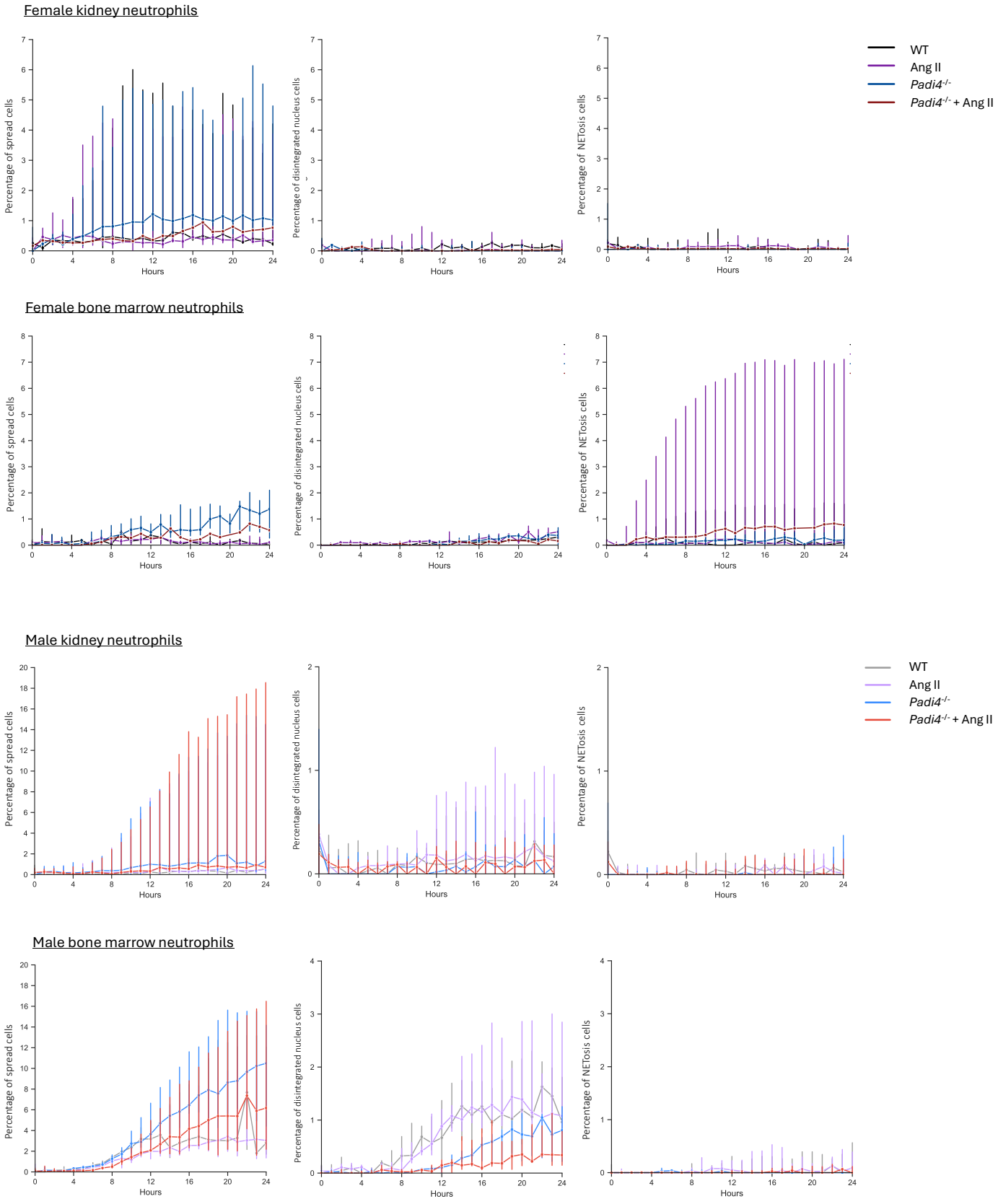

Figure 4.9: Assessment of NETosis in unstimulated neutrophils from Ang II-infused mice.

Line plots show the median proportion of cells in each NETosis stage (spread, disintegrated nucleus, NETosis) over 24 hours. Data are shown for bone marrow and kidney neutrophils isolated from female and male WT and *Padi4*$^{-/-}$ mice under sham or Ang II conditions. N= 3-4 animals per group.

4.7 Female NETosis dynamics are unchanged in Ang II-induced hypertension

To assess whether Ang II-induced hypertension alters the NETosis in female mice, we compared PMA-stimulated (100 nM) NETosis profiles between untreated and Ang II-infused animals in both WT and *Padi4*$^{-/-}$ groups. As expected, PAD4-deficient neutrophils showed greatly impaired nuclear swelling and NET release in both the bone marrow and kidney, confirming the requirement of PAD4 for efficient NET formation (Fig. 4.10-4.11).

In WT female neutrophils, NETosis levels were present but low across both compartments and conditions, resulting in substantial intra-group variability. Nevertheless, WT neutrophils displayed a greater capacity for NET formation than *Padi4*$^{-/-}$ neutrophils, reflected by significantly higher proportions (AUC) of disintegrated nucleus cells in bone marrow (Fig. 4.10b, panel 2) and higher disintegrated nucleus and complete NETosis in kidney neutrophils compared to genotype-matched controls (Fig. 4.11b, panel 2-3).

However, no differences in NETosis stages were observed between WT untreated and WT + Ang II female neutrophils in either compartment, indicating that Ang II-induced hypertension did not alter NETosis progression in female neutrophils (Fig. 4.10-4.11).

Interestingly, *Padi4-/-* neutrophils from the bone marrow exhibited increased spreading (Fig. 4.10b, panel 1), with a similar trend in the kidney (Fig. 4.11b, panel 1). This may reflect either rapid progression of stimulated WT cells toward later NETosis stages or enhanced early in the absence of PAD4. Importantly, these patterns did not differ between neutrophils from untreated and Ang II-infused animals, reinforcing that exposure to hypertensive conditions does not modify NETotic responses in female neutrophils.

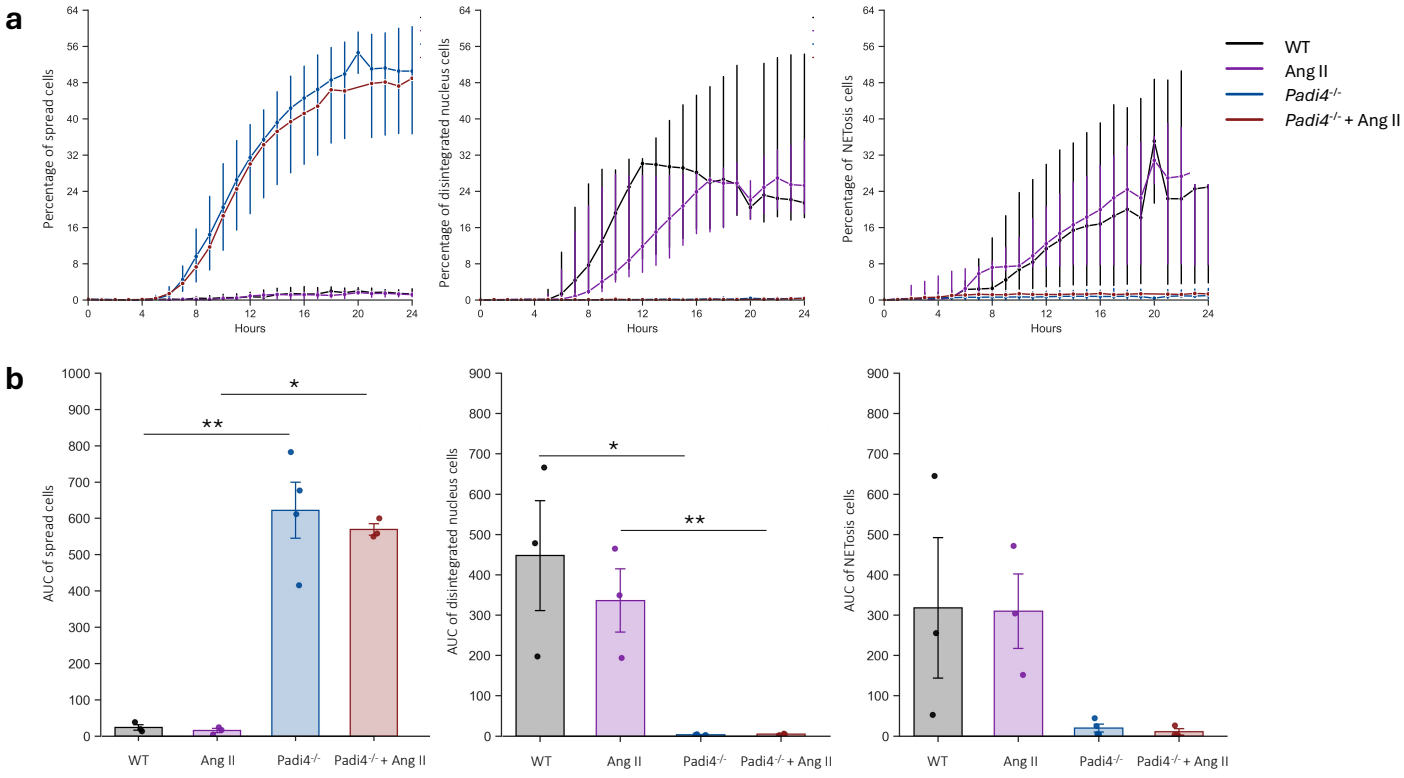

Figure 4.10: Assessment of NETosis dynamics in PMA-stimulated bone marrow neutrophils from Ang II-infused female mice.

a, Line plots show the median proportion of each NETosis stage (spread, disintegrated nucleus, NETosis) over 24 hours in bone marrow neutrophils isolated from female WT and *Padi4*$^{-/-}$ mice under sham or Ang II conditions, stimulated *ex vivo* with 100 nM PMA. **b**, Barplots show the AUC (% x hours) for each NETosis stage, representing the overall magnitude of each phenotype over time. A global Kruskal-Wallis test was performed for each cell state, followed by pairwise Mann-Whitney U tests with Holm correction. *=P<0.05, **=P<0.01. N= 3-4 animals per group.

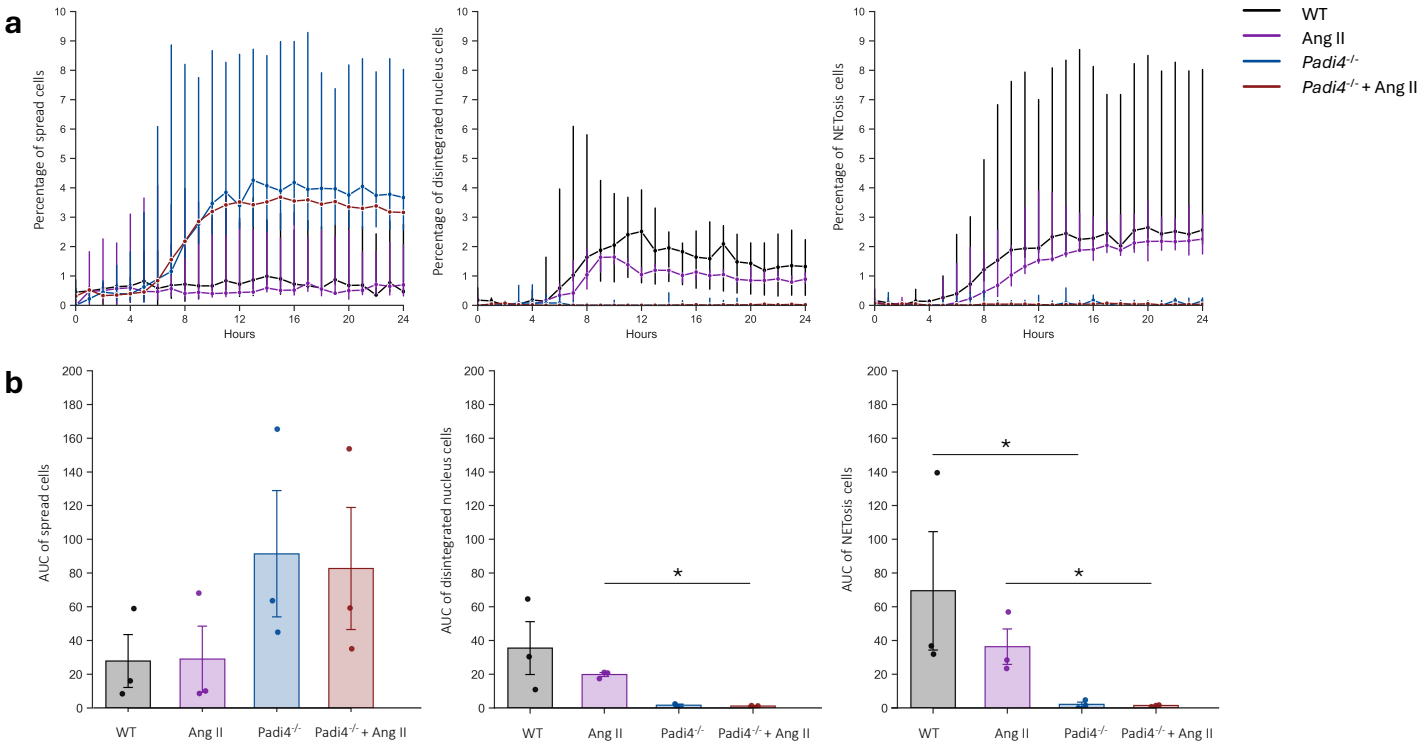

Figure 4.11: Assessment of NETosis dynamics in PMA-stimulated kidney neutrophils from Ang II-infused female mice.

a, Line plots show the median proportion of each NETosis stage (spread, disintegrated nucleus, NETosis) over 24 hours in kidney neutrophils isolated from female WT and *Padi4*$^{-/-}$ mice under sham or Ang II conditions, stimulated *ex vivo* with 100 nM PMA. **b**, Barplots show the AUC (% x hours) for each NETosis stage, representing the overall magnitude of each phenotype over time. A global Kruskal-Wallis test was performed for each cell state, followed by pairwise Mann-Whitney U tests with Holm correction. *=P<0.05. N= 3-4 animals per group.

4.8 Early signs of altered NETosis appear in male bone marrow neutrophils during Ang II–induced hypertension

To determine whether Ang II-induced hypertension alters NETosis in male mice, we compared PMA-stimulated (100 nM) NETosis profiles in bone marrow neutrophils from untreated and Ang II-infused WT and *Padi4*$^{-/-}$ animals. As observed in females, *Padi4*$^{-/-}$ neutrophils showed markedly impaired nuclear swelling and NET release, confirming the requirement of PAD4 for efficient NET formation (Fig. 4.12).

Male WT bone marrow neutrophils exhibited a far more robust NETotic response than females, with cells across NETosis stages comprising roughly 60% of the population by the end of the time course. (Fig. 4.12a) WT neutrophils from both untreated and Ang II-infused males displayed substantially higher AUC values for disintegrated nucleus and complete NETosis stages compared with their *Padi4*$^{-/-}$ controls, which remained near zero (Fig. 4.12b).

Consistent with findings in females, PMA-induced cell spreading was significantly higher in *Padi4*$^{-/-}$ neutrophils than in WT neutrophils, and this effect was unaffected by exposure to hypertensive conditions (Fig. 4.12b, panel 1). Although spreading tended to be slightly lower in neutrophils from Ang II–infused mice, this difference did not reach significance.

To directly assess the impact of Ang II-induced hypertension on NETosis progression *ex vivo*, we compared WT untreated and WT + Ang II groups. Neutrophils from Ang II-infused males displayed a modest reduction in disintegrated nucleus cells (Fig. 4.12, panel 2) accompanied by a corresponding increase in complete NETosis (Fig. 4.12, panel 3). However, these trends did not reach statistical significance. Thus, when each NETosis stage was evaluated independently, Ang II–induced hypertension did not significantly alter the progression of either the disintegrated nucleus or complete NETosis stages in male bone marrow neutrophils.

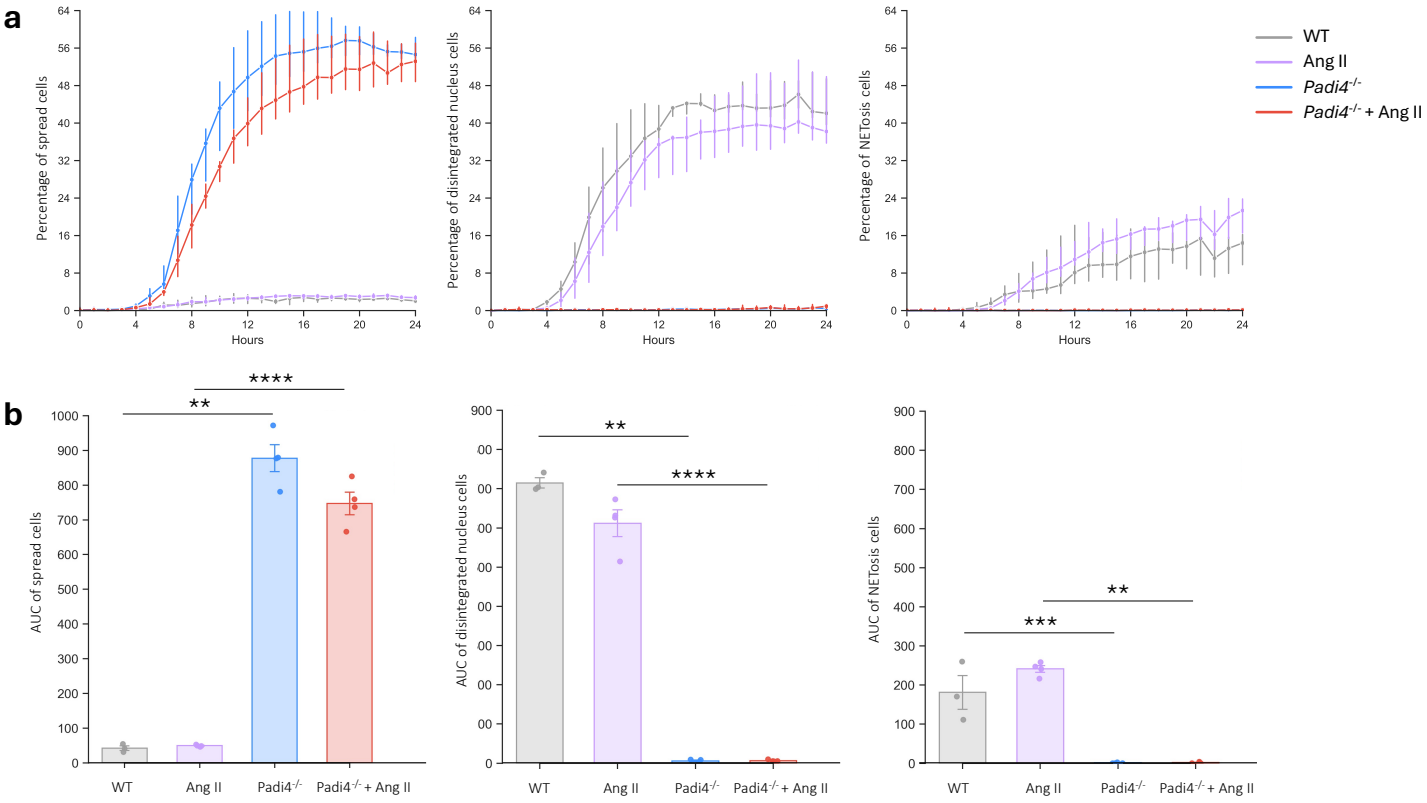

Figure 4.12: Assessment of NETosis dynamics in PMA-stimulated bone marrow neutrophils from Ang II-infused male mice.

a, Line plots show the median proportion of each NETosis stage (spread, disintegrated nucleus, NETosis) over 24 hours in bone marrow neutrophils isolated from male WT and *Padi4*$^{-/-}$ mice under sham or Ang II conditions, stimulated *ex vivo* with 100 nM PMA. **b**, Barplots show the AUC (% x hours) for each NETosis stage, representing the overall magnitude of each phenotype over time. A global Kruskal-Wallis test was performed for each cell state, followed by pairwise Mann-Whitney U tests with Holm correction. **=P<0.01, ***=P<0.001, ****=P<0.0001. N= 4-5 animals per group.

Although the overall magnitude of NETosis was not significantly different between PMA-stimulated neutrophils from untreated and Ang II-infused WT males, we further examined timing and progression metrics to better resolve potential differences (Fig. 4.13a-b).

When assessing the proportion of NETosis-stage cells at 6, 12, and 24 hours, we observed a widening separation over time, with neutrophils from Ang II-infused mice showing a progressively higher proportion of cells in complete NETosis. However, these differences did not reach significance due to inter-group variability (Fig.4.13a).

Temporal NETosis metrics, T50 and peak proportion, were next assessed. T50 values were similar between groups, occurring between 9 and 12 hours, indicating comparable overall NETosis kinetics. In contrast, peak NETosis was approximately 5% higher in the Ang II group, although this trend was not statistically significant (4.13b).

To determine whether the relative distribution of NETosis stages differed between groups, we visualized the proportions of spread, disintegrated nucleus, and complete NETosis using stacked-area plots and quantified overall stage composition using CLR-transformed Euclidean distances (Fig.4.13c). Although the stacked area plots showed a similar proportion of cells across stages overall, the analysis revealed a significant shift in overall stage composition between groups, driven by a decrease in disintegrated nucleus cell and a corresponding increase in complete NETosis in the Ang II group.

Together, these findings suggest that while absolute NETosis output is unchanged, hypertension may bias male neutrophils toward more efficient transition from the disintegrated nucleus stage to late-stage NETosis, indicating a potential shift toward enhanced NET-releasing capacity.

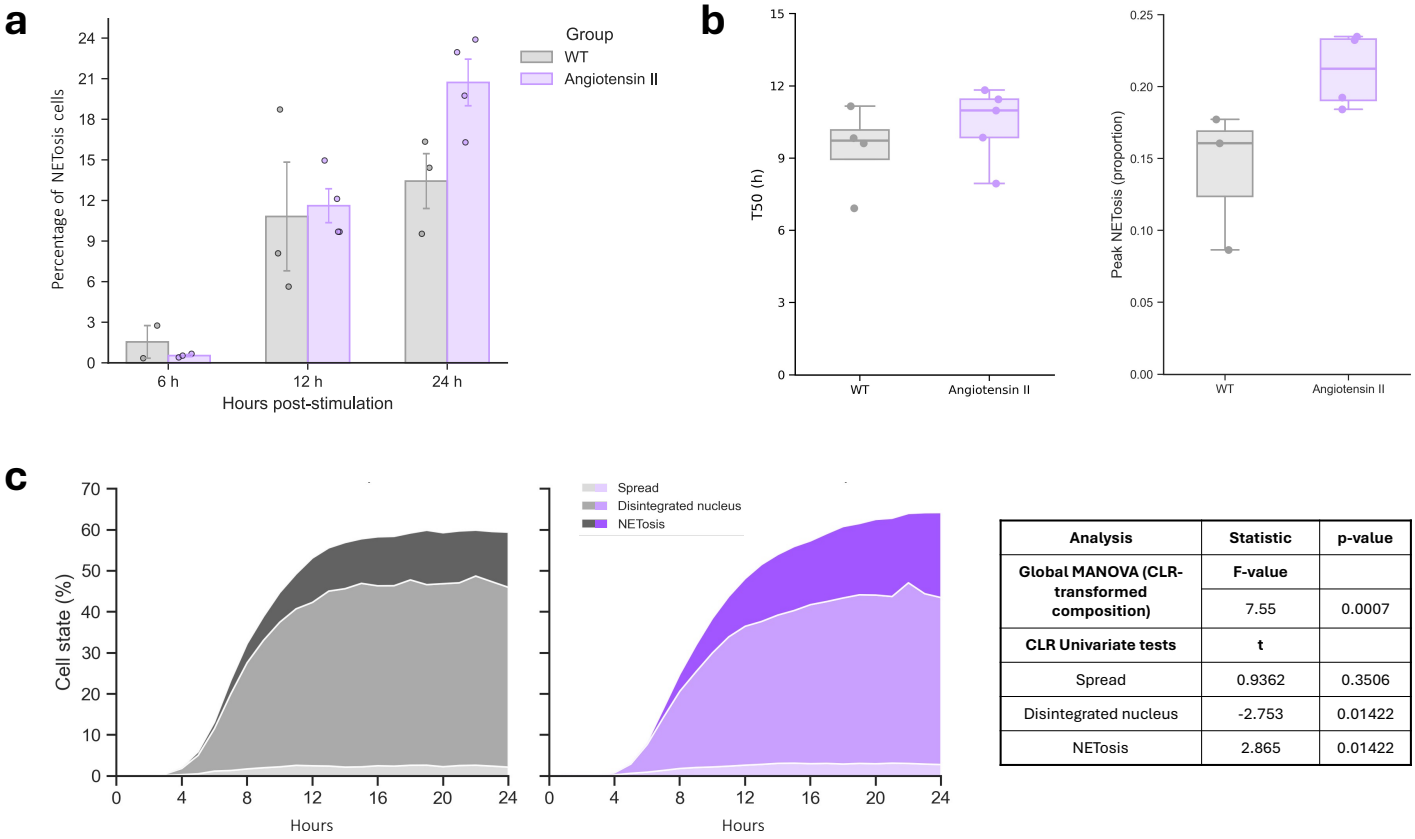

Analysis	Statistic	p-value
Global MANOVA (CLR-transformed composition)	**F-value**	
	7.55	0.0007
CLR Univariate tests	**t**	
Spread	0.9362	0.3506
Disintegrated nucleus	-2.753	0.01422
NETosis	2.865	0.01422

Figure 4.13: Assessment of NETosis kinetics and cell-state dynamics in bone marrow neutrophils from Ang II-infused male mice.

a, Bar plots showing the percentage of NETosis-stage cells at 6, 12, and 24 hours after stimulation with 100 nM PMA in WT and Ang II groups. Pairwise Mann-Whitney U tests with Holm correction were performed at each time point. **b**, Boxplots of key temporal NETosis metrics (t50 and peak NETosis proportion) derived from the NETosis time courses. Mann-Whitney U tests were performed to compare WT and Ang II groups. **c**, Stacked area plots showing the global distribution of neutrophil cell states (spread, disintegrated nucleus, NETosis) over 24 hours. Stage-composition vectors were CLR-transformed and analyzed using a global multivariate PERMANOVA, followed by univariate CLR tests to assess differences between WT and Ang II groups. N= 4-5 animals per group.

4.9 Hypertension promotes early-stage NET release in the kidney

To determine whether Ang II-induced hypertension alters NETosis in tissue-resident kidney neutrophils, we compared PMA-stimulated (100 nM) NETosis profiles from untreated and Ang II-infused WT and *Padi4*$^{-/-}$ male mice (Fig. 4.14). We again observed an absence of disintegrated nucleus and NETosis in *Padi4*$^{-/-}$ neutrophils, with WT neutrophils from both untreated and Ang II-infused males exhibiting higher AUC values for disintegrated nucleus and complete NETosis stages compared with their *Padi4*$^{-/-}$ controls, which remained near zero (Fig. 4.14b). PMA-induced cell spreading was again significantly higher in *Padi4*$^{-/-}$ neutrophils than in WT neutrophils, and this effect was comparable in sham and Ang II groups (Fig. 4.14b, panel 1).

PMA stimulation induced a NETotic response in ~10-15% of WT kidney neutrophils from Ang II-infused males over 24 hours (Fig. 4.14a). By contrast, WT neutrophils from untreated males showed seemingly lower overall NETotic activity, with peak medians around 5% for both disintegrated nucleus and complete NETosis stages.

To quantify these differences, we compared AUC values between untreated and Ang II-infused WT males. Kidney neutrophils from Ang II-infused animals displayed a higher overall burden of disintegrated nucleus cells across time, suggesting enhanced priming or upstream activation of the NETotic program (Fig. 4.14, panel 2). However, this increase did not translate into a proportional rise in complete NETosis. Although, AUC values for late-stage NETosis were numerically higher in the Ang II group, the difference did not reach statistical significance due to inter-group variability (Fig. 4.14, panel 3).

Thus, Ang II–induced hypertension significantly altered the early nuclear swelling phase of NETosis in male kidney neutrophils but did not substantially increase the magnitude of terminal NET release.

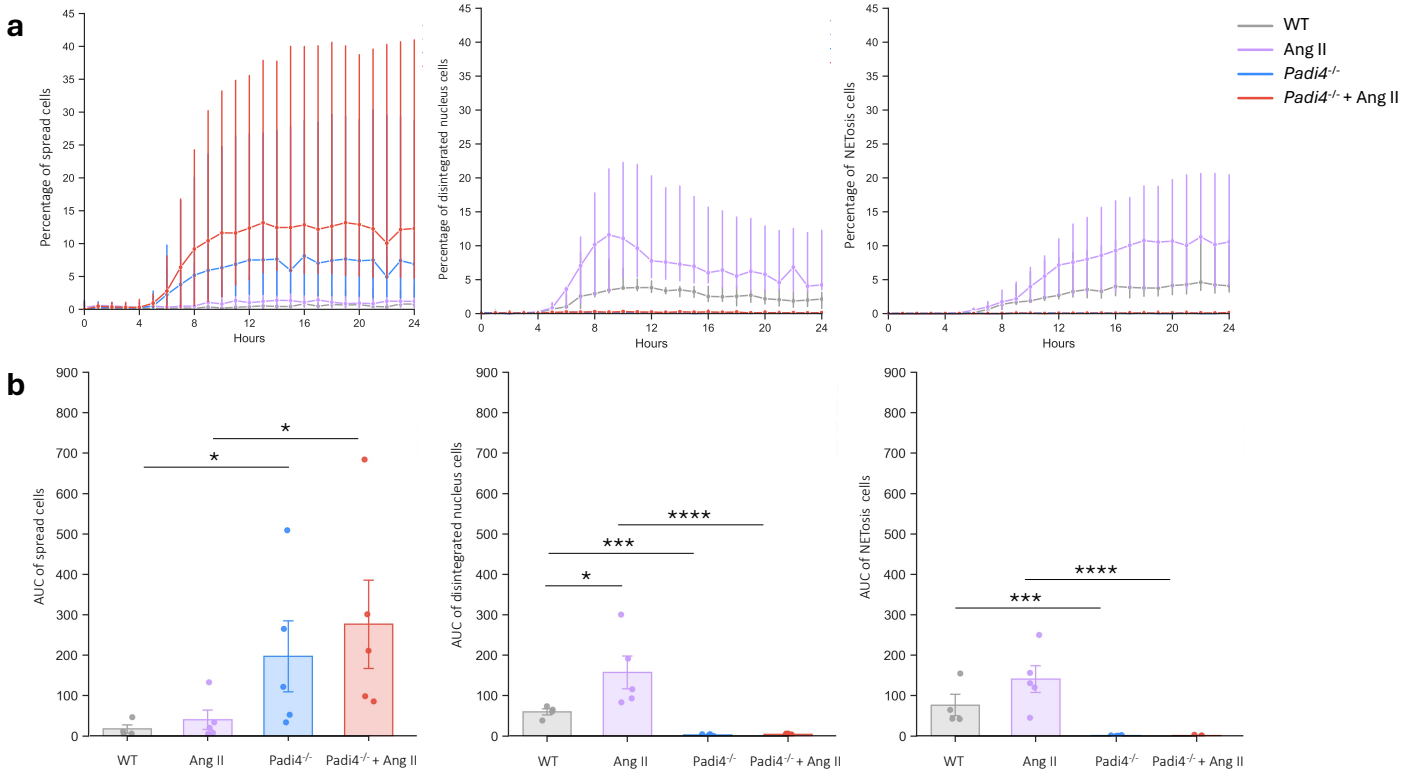

Figure 4.14: Assessment of NETosis dynamics in PMA-stimulated kidney neutrophils from Ang II-infused male mice.

a, Line plots show the median proportion of each NETosis stage (spread, disintegrated nucleus, NETosis) over 24 hours in kidney neutrophils isolated from male WT and *Padi4*$^{-/-}$ mice under sham or Ang II conditions, stimulated *ex vivo* with 100 nM PMA. **b**, Barplots show the AUC (% x hours) for each NETosis stage, representing the overall magnitude of each phenotype over time. A global Kruskal-Wallis test was performed for each cell state, followed by pairwise Mann-Whitney U tests with Holm correction. *=P<0.05, ***=P<0.001, ****=P<0.0001. N= 4-5 animals per group.

We further characterized the progression of disintegrated nucleus and NETosis stages in WT kidney neutrophils from untreated and Ang II–infused male mice and quantified differences in their temporal profiles and overall stage composition (Fig. 4.15).

Comparison of disintegrated nucleus levels at matched time points (6, 12, and 24 hours) showed a pattern consistent with the AUC results. Neutrophils in the Ang II group had significantly higher proportions at 12 and 24 hours, despite both groups displaying the same overall trajectory, in which disintegrated nucleus cells peak and then decline at later time points (Fig. 4.15a). Temporal metrics revealed similar kinetics between groups, with T50 values occurring between 6 and 9 hours (Fig. 4.15c). Although the Ang II group showed a numerically higher peak in disintegrated nucleus cells, likely driving the AUC difference, variability prevented statistical significance (Fig. 4.15c).

Terminal NETosis increased progressively in both groups across 6, 12, and 24 hours, with Ang II neutrophils consistently trending higher. However, variability again limited statistical conclusions (Fig. 4.15b). The similarity in T50 values indicates that terminal NETosis progresses at a comparable rate in both groups (Fig. 4.15d). While the Ang II group showed a modestly higher peak proportion of NETosis, this trend did not achieve statistical significance due to variability (Fig. 4.15d).

To determine whether Ang II-induced hypertension altered the relative distribution of NETosis stages in male kidney neutrophils, we visualized stage proportions using stacked-area plots and quantified overall stage composition using CLR-transformed Euclidean distances (Fig. 4.15e). Kidney neutrophils from Ang II–infused males showed approximately a 2-fold increase in the total proportion of cells engaged across NETosis stages. Composition analysis revealed a significant shift between groups, driven primarily by a higher proportion of

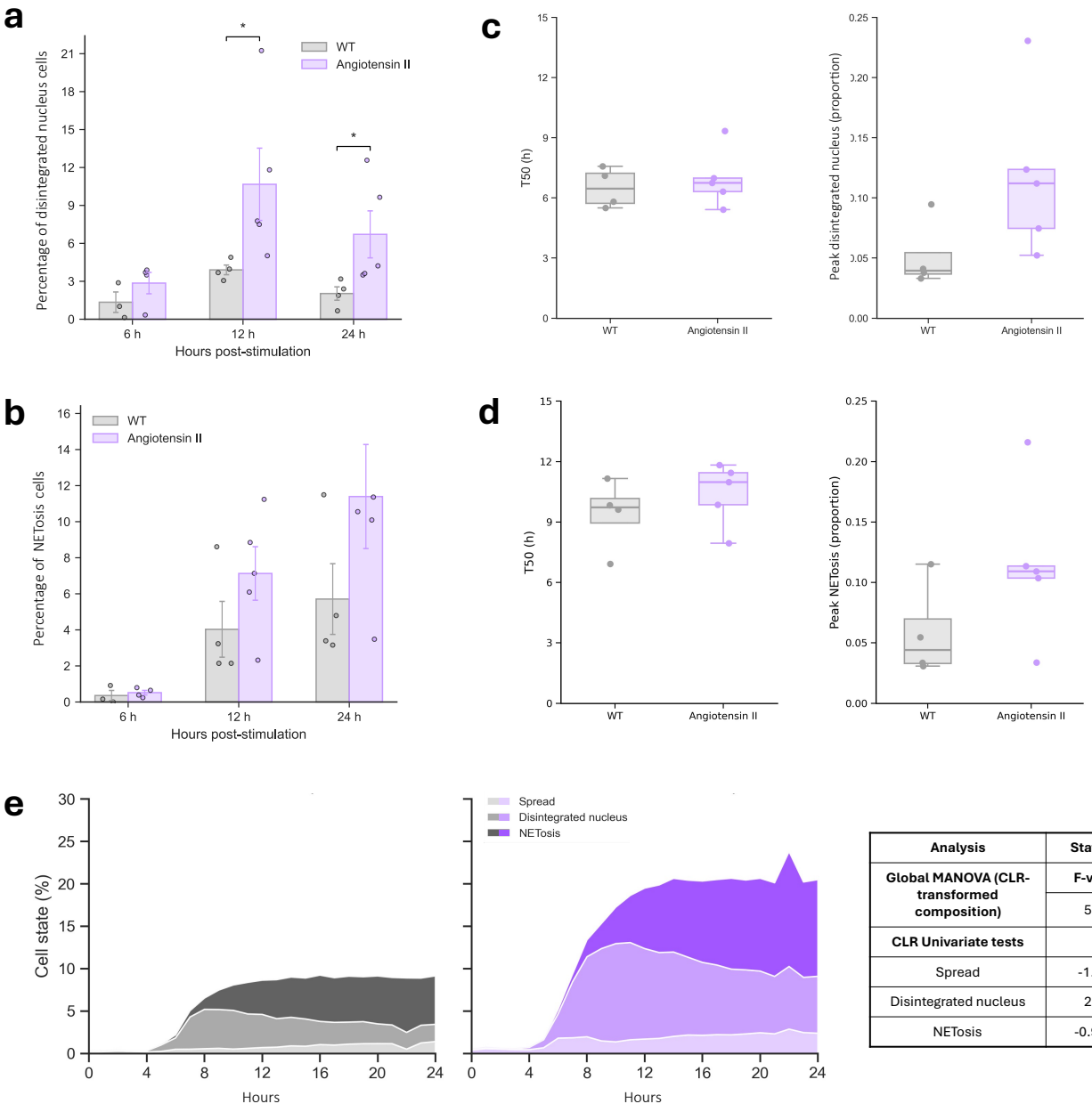

Analysis	Statistic	p-value
Global MANOVA (CLR-transformed composition)	**F-value**	
	5.03	0.0076
CLR Univariate tests	**t**	
Spread	-1.167	0.489
Disintegrated nucleus	2.86	0.014
NETosis	-0.9442	0.489

Figure 4.15: Assessment of NETosis kinetics and cell-state dynamics in kidney neutrophils from Ang II-infused male mice.

a-b, Bar plots showing the percentage of neutrophils in the **(a)** disintegrated nucleus and **(b)** NETosis stages at 6, 12, and 24 hours after stimulation with 100 nM PMA in WT and Ang II groups. Pairwise Mann-Whitney U tests with Holm correction were performed at each time point. **c-d**, Boxplots of key temporal metrics (t50 and peak NETosis proportion) derived from the **(c)** disintegrated nucleus and **(d)** NETosis time courses. Mann-Whitney U tests were performed to compare WT and Ang II groups. **e**, Stacked area plots showing the global distribution of neutrophil cell states (spread, disintegrated nucleus, NETosis) over 24 hours in WT and Ang II groups. Stage-composition vectors were CLR-transformed and tested for differences using a global multivariate PERMANOVA, followed by univariate CLR tests to assess differences between WT and Ang II groups. Results of these analyses are summarized in the accompanying table. N= 4-5 animals per group.

disintegrated nucleus cells in the Ang II group. Importantly, the relative proportion of terminal NETosis was not significantly different, suggesting that increased early-stage activity does not strictly translate into a proportional increase in NET release.

Together, these results indicate that Ang II-induced hypertension primes kidney neutrophils to enter early NETosis stages more readily, but this priming does not consistently translate into full NET release.

Chapter 5

NET- induced senescence-associated reprogramming in endothelial cells

5.1 Introduction and Rationale

ECs play a central role in maintaining vascular homeostasis and are key targets and mediators of vascular inflammation. As such, they are directly exposed to and respond to NET-derived components. A clear link between NETs and tissue damage has been established, positioning NETs as active contributors to vascular injury and necrosis (49). More specifically, NETs have been shown to alter angiogenesis and wound healing (353,354), impair endothelial proliferation and vascular regeneration (326,355), and amplify vascular inflammation, ultimately driving endothelial activation (276,356). Given their central role in disrupting endothelial homeostasis across vascular and inflammatory diseases, there is a critical need to more fully define the mechanisms by which NETs modulate EC function.

Targeted studies have shown that NET-exposed ECs exhibit inflammasome activation (285,357), impaired nitric oxide production (285), increased release of pro-inflammatory cytokines and chemokines (358), and reduced regenerative capacity (326). While these pathway-specific findings highlight the diverse stress responses triggered by NETs, they provide an incomplete picture and underscore the need for an unbiased transcriptomic approach to capture to full spectrum of endothelial pathways altered by NET exposure.

We therefore sought to characterize the global transcriptional response of NET-treated ECs to identify key mechanisms driving NET-induced endothelial injury.

5.2 HL-60-derived NETs dose-dependently impair endothelial cell proliferation

To investigate the mechanisms of NET-induced EC injury, we first established an *in vitro* model in which HUVECs were exposed to NETs generated from differentiated HL-60 cells (359). (Fig. 5.1). NET preparations were collected and used to validate that HL-60–derived NETs elicit measurable biological effects in ECs.

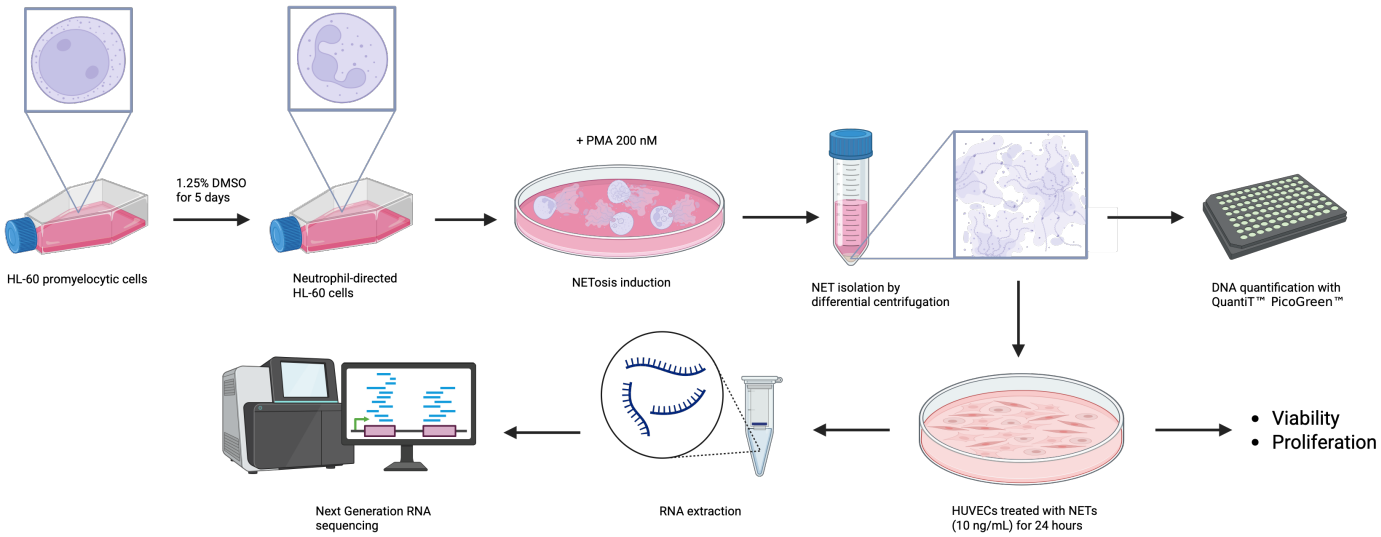

Figure 5.1: Schematic of the *in vitro* model of endothelial NET exposure and downstream experimental readouts. HL-60 cells were differentiated into neutrophil-like cells and stimulated with PMA to induce NET formation. NETs were subsequently isolated, quantified based on DNA content, and applied to cultured HUVECs at an effective concentration of 10 ng/mL for 24 hours. Following NET exposure, endothelial viability and proliferative capacity were assessed, and RNA was extracted for bulk RNA-sequencing and downstream transcriptional analyses.

HUVECs were treated with a range of NET concentrations (0.2-50 ng/mL DNA) for 24 hours, and viability and proliferation were assessed. NETs did not impact EC viability at any concentration tested, but produced a dose-dependent reduction in proliferation, with approximately a 5-fold reduction at the highest concentration (Fig. 5.2). These results were comparable to those reported for NETs generated from primary human neutrophils (326)and confirm that HL-60-derived NETs are biologically active and capable of suppressing endothelial proliferative capacity, establishing this system as an appropriate model to investigate NET-driven endothelial injury *in vitro*.

Given the observed dose-dependent effect of NETs on endothelial proliferation, we selected a mid-range concentration (10 ng/mL) between the two most effective doses (5-50 ng/mL) for all subsequent experiments (Fig. 5.1). The impact of this concentration on viability and proliferation was reassessed using three independent NET preparations, ensuring that 10 ng/mL DNA consistently elicited a measurable biological response while preserving the dynamic range to detect pathway-specific modulation in downstream mechanistic assays (Fig. 5.3).

As expected, the responses induced by 10 ng/mL NETs were consistent with those observed in the dose-response experiment. This concentration did not affect HUVEC viability (Fig. 5.3a) but induced a 2-fold reduction in proliferation (Fig. 5.3b), with low variability across NET samples (Fig. 5.3), validating it as a reliable experimental condition for downstream transcriptomic and mechanistic analyses of NET-induced EC injury.

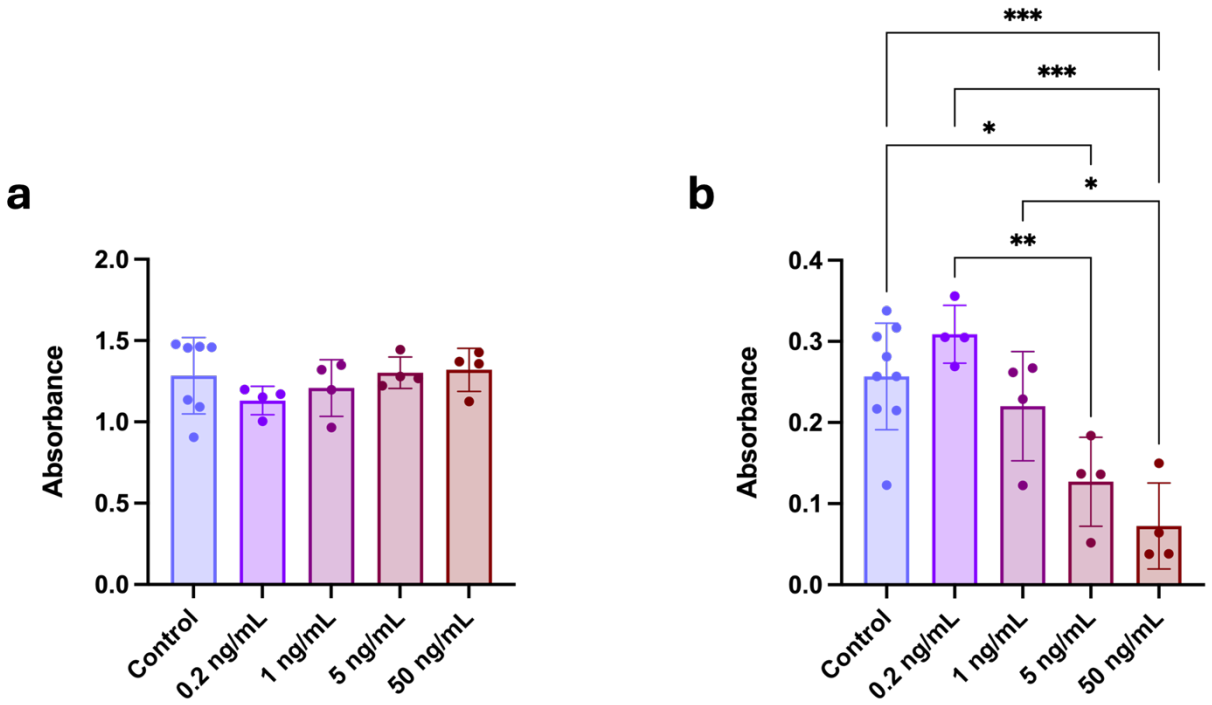

Figure 5.2: Dose-response assessment of NET effects on endothelial cell viability and proliferation. HUVECs were treated with increasing concentrations of NETs (0.2-50 ng/mL) for 24 hours. **a**, Cell viability was measured using an XTT assay. **b**, Cell proliferation was measured using a BrdU incorporation assay. Statistical differences were tested using one-way ANOVA with appropriate post-hoc multiple-comparison correction. Data is presented as mean ± SEM. *=P<0.05, **=P<0.01, ***=P<0.001. N= 4-9 biological replicates per condition.

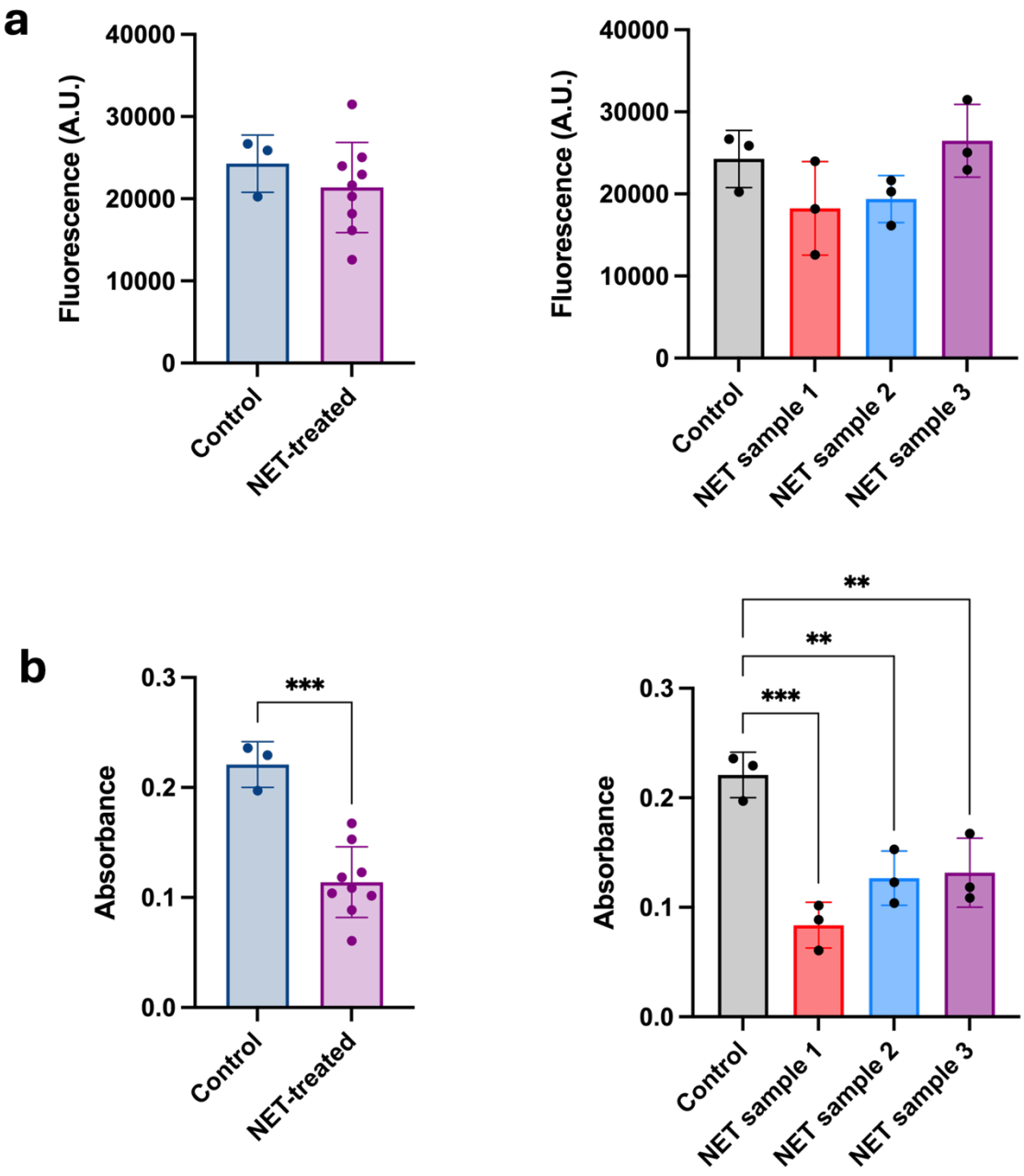

Figure 5.3: Validation of NET-induced functional effects and reproducibility across independent NET preparations at the selected working concentration.

HUVECs were treated with 10 ng/mL NETs for 24 hours. **a**, Cell viability was measured using the PrestoBlue assay, and **b**, proliferation was assessed by BrdU incorporation. Left, summary analysis with data from all NET-treated conditions combined. Right, the same data shown stratified by individual NET preparations. Data is presented as mean ± SEM. Statistical significance was determined using an unpaired two-tailed t-test. ***=P<0.001. N= 3-9 replicates per condition.

5.3 NET-induced transcriptional reprogramming in endothelial cells includes inflammatory activation and cell cycle repression

To broadly characterize the transcriptional changes and identify pathways altered by NET exposure, bulk RNA-sequencing was performed on NET-treated HUVECs and paired controls (Fig. 5.1). PCA demonstrated clear separation between groups, indicating a strong and consistent transcriptional response to NET treatment (Fig. 5.4a). This was further supported by sample-to-sample Euclidean distance analysis, which showed tight clustering within treatment groups and low similarity between NET-treated and control samples (Fig. 5.4b), indicating treatment-specific transcriptional signatures.

Differential expression analysis revealed a substantial number of NET-responsive genes (Fig. 5.5a). After applying thresholds for adjusted $p < 0.05$ and $|\log_2 \text{fold change}| \geq 1$, 2226 genes were significantly upregulated and 2476 were downregulated (Fig. 5.5b). GO and KEGG pathway analyses were performed separately on upregulated and downregulated genes.

Among the top 20 significantly enriched KEGG pathways, upregulated genes were associated with *Pathways in cancer*, several inflammatory signaling pathways (TNF, MAPK, NF-κB, JAK-STAT, IL-17), *Cytokine-cytokine receptor interaction*, *Kaposi sarcoma-associated herpesvirus infection*, *Human cytomegalovirus infection*, *Fluid shear stress and atherosclerosis*, and *Lipid and atherosclerosis* (Fig. 5.6a). *Cellular senescence* was also significantly enriched and is highlighted in Figure 5.6, consistent with the observed reduction in EC proliferation following NET exposure. Together, these pathways indicate a strong inflammatory and stress-response consistent with endothelial dysfunction.

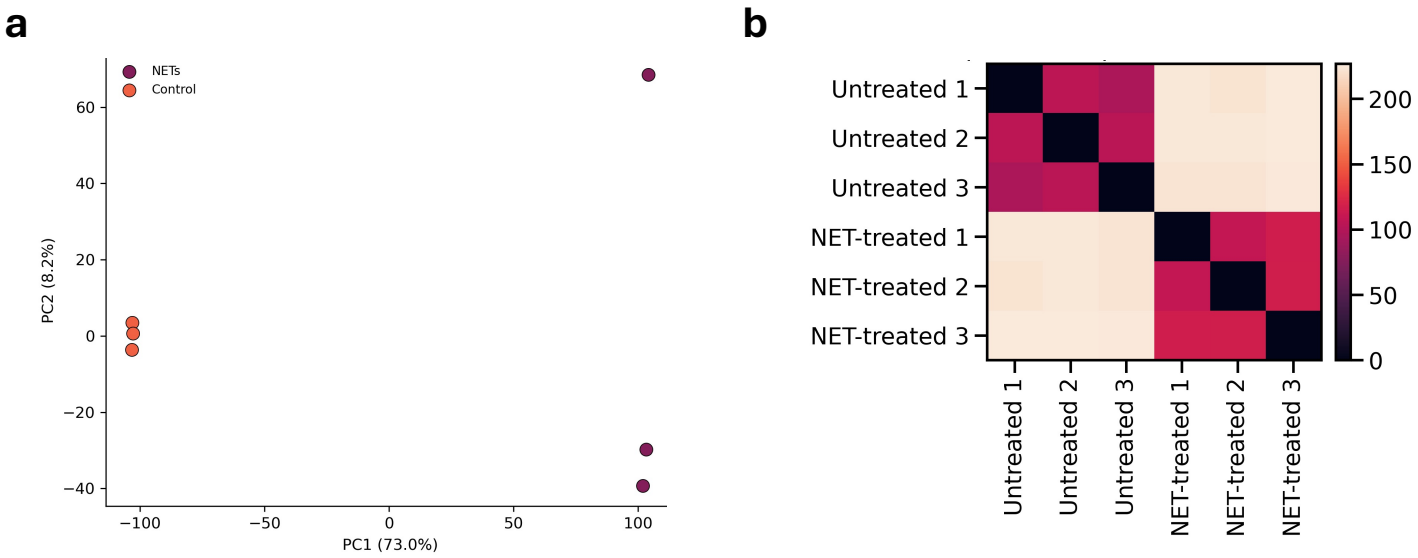

Figure 5.4: Principal component and sample distance analyses of HUVECs RNA-sequencing data.
Bulk-RNA sequencing was performed on HUVECs treated with 10 ng/mL NETs for 24 hours and compared to paired controls. **a**, Principal component analysis (PCA) based on normalized gene expression values from control and NET-treated HUVECs. Each point represents an individual biological replicate. **b**, Sample-to-sample Euclidean distance heatmap generated from normalized expression data across biological replicates.

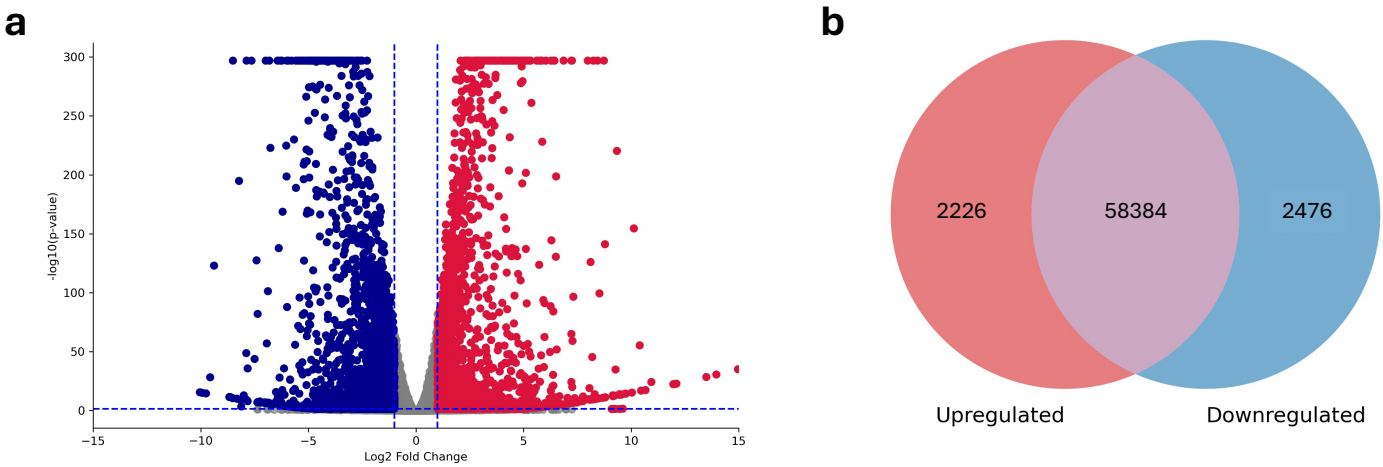

Figure 5.5: Differential gene expression analysis in NET-treated endothelial cells relative to control.
Bulk-RNA sequencing was performed on HUVECs treated with 10 ng/mL NETs for 24 hours and compared to paired controls. **a**, Volcano plot of differentially expressed genes in NET-treated HUVECs relative to control, with downregulated genes shown in blue and upregulated genes shown in red. Each point represents an individual gene. **b**, Venn diagram summarizing the number of significantly upregulated (red) and downregulated (blue) genes, and unchanged genes (purple). Differential expression was defined by $P<0.05$ and $|\log_2 \text{fold}| > 1$.

GO enrichment supported a broad regulatory and developmental shift among NET-treated samples. Significant biological process (BP) terms included regulation of cellular and biological activity and responses to oxygen-containing compounds, reflecting a global stress and signaling response to NET exposure (Fig. 5.6b).

Molecular function (MF) enrichment highlighted modulation of signaling receptor activity and protein kinase regulatory functions, suggesting activation of receptor-mediated signaling and alterations in kinase-driven pathways (Fig. 5.6b). Consistent with this, upregulated genes were strongly associated with the plasma membrane and extracellular components in the cellular component (CC) analysis, including *Cell periphery*, *Plasma membrane*, *Extracellular matrix*, and *Extracellular space* (Fig. 5.6b), supporting the engagement of NETs with cell-surface receptors and extracellular structures.

The KEGG pathway analysis of downregulated genes revealed strong and consistent representation for pathways involved in DNA synthesis and cell cycle progression (*DNA replication, Cell cycle*, and *Homologous recombination*), as well as important pathways for maintaining genome integrity (*Fanconi anemia pathway*, *Mismatch repair*, and *Base excision repair*) (Fig. 5.7a). Together, these results indicate a marked suppression of cell cycle progression and DNA-maintenance programs in NET-treated ECs.

Consistent with this, the most significantly enriched GO BP terms include *Chromosome segregation*, *Nuclear division*, *Mitotic cell cycle*, and *Organelle fission*, all of which reflect impaired mitotic progression (Fig. 5.7b). Correspondingly, enriched MF terms, which include *Microtubule binding*, *Microtubule motor activity*, and *Cytoskeletal protein binding*, further support disruption of mitotic spindle dynamics. In agreement with these patterns, CC enrichment

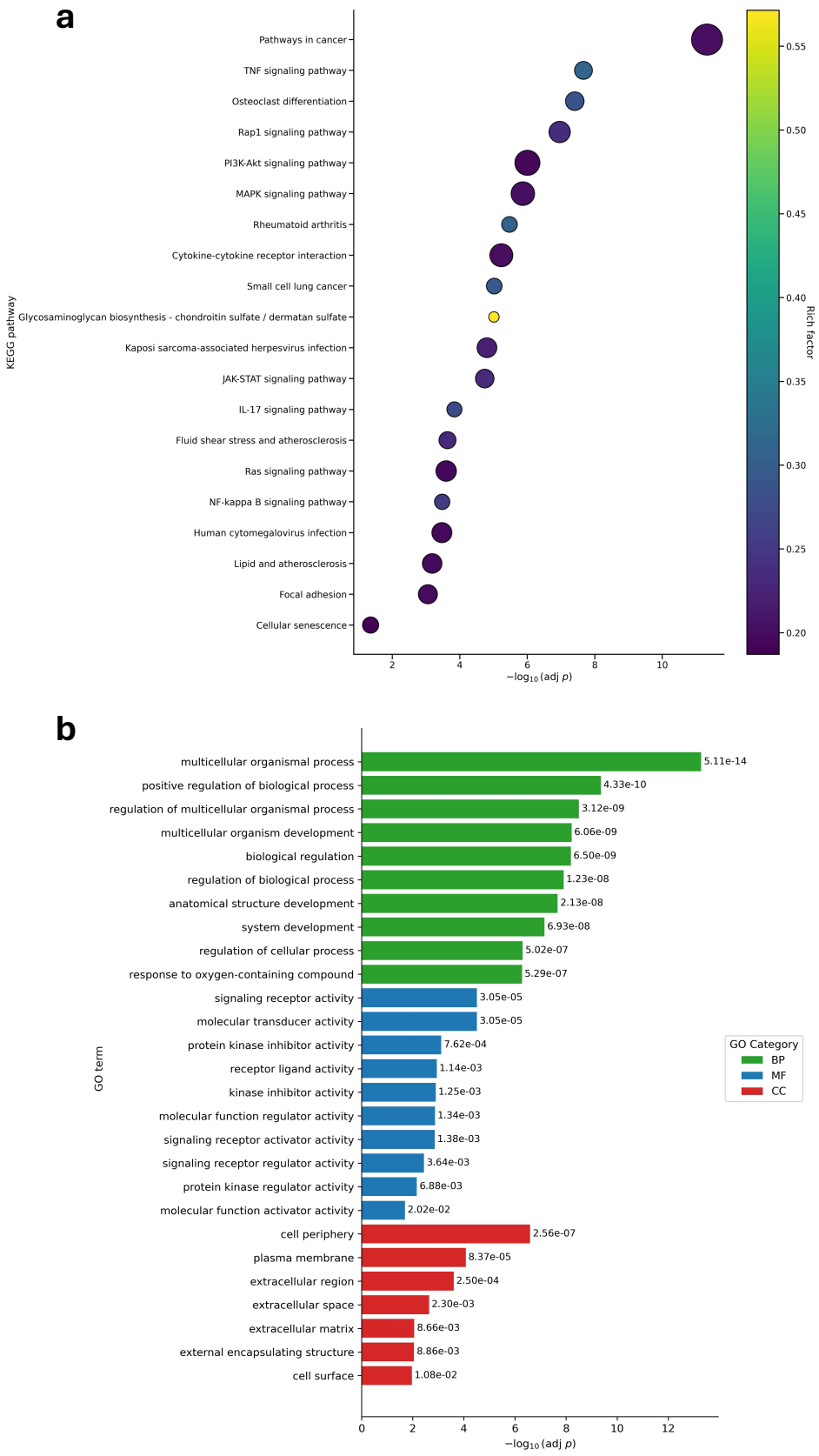

Figure 5.6: Pathway and Gene Ontology enrichment analysis of upregulated genes following NET exposure. **a**, KEGG pathway enrichment analysis showing significantly enriched pathways in NET-treated HUVECs, ranked by adjusted p-value, with dot size representing gene count and color indicating rich factor. The cellular senescence pathway met significance criteria and is shown despite not being among the top-ranked pathways due to its relevance to downstream analyses. **b**, Gene Ontology (GO) enrichment analysis of the same gene set, showing enriched biological process (BP), molecular function (MF), and cellular component (CC) terms, ranked by p-value.

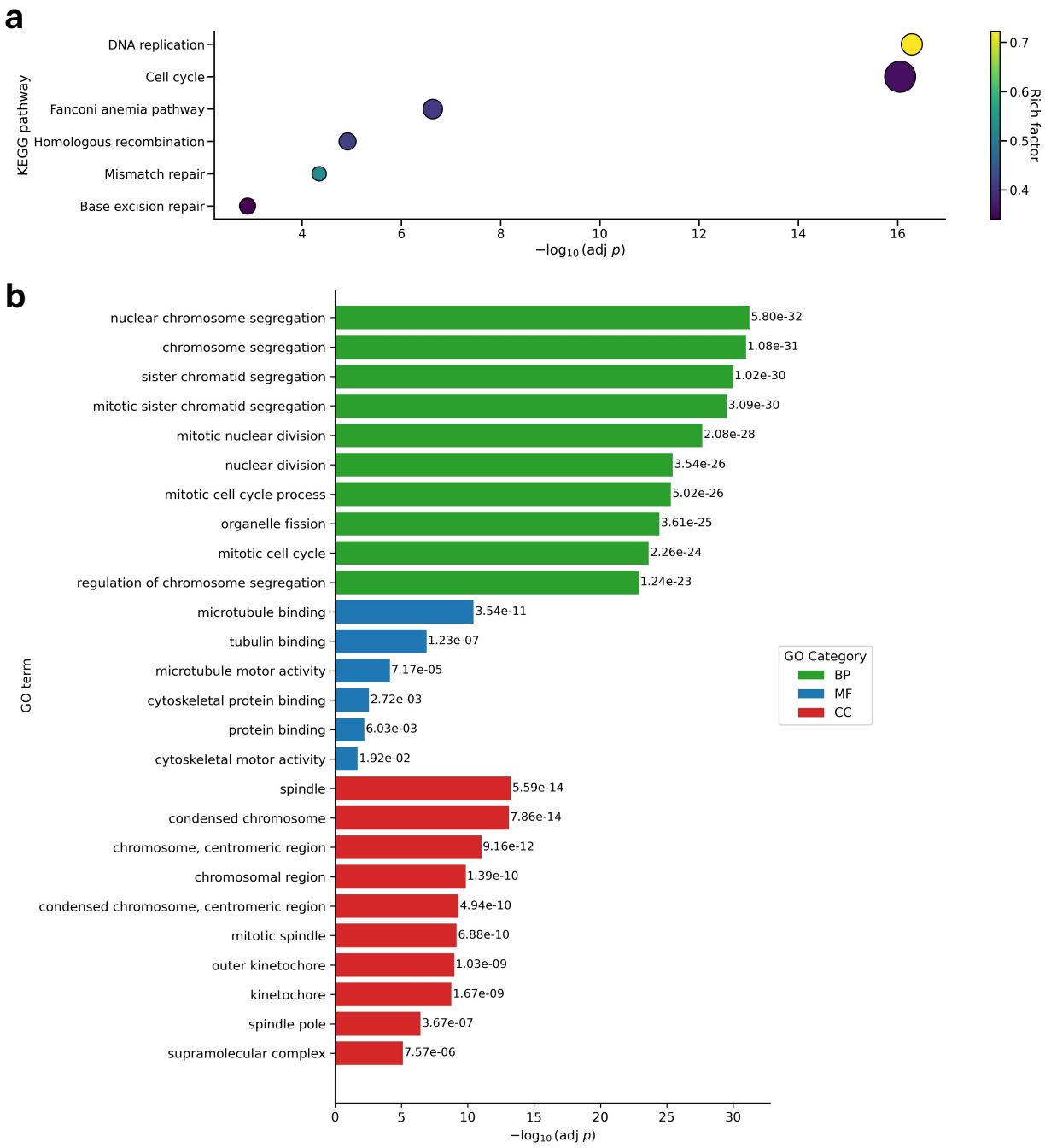

Figure 5.7: Pathway and Gene Ontology enrichment analysis of downregulated genes following NET exposure. **a**, KEGG pathway enrichment analysis showing significantly enriched pathways in NET-treated HUVECs, ranked by adjusted p-value, with dot size representing gene count and color indicating rich factor. **b**, Gene Ontology (GO) enrichment analysis of the same gene set, showing enriched biological process (BP), molecular function (MF), and cellular component (CC) terms, ranked by p-value.

demonstrated overrepresentation of genes associated with the spindle, chromosomal regions, and other structures crucial for cell cycle progression (Fig 5.7b).

Results from the KEGG and GO analyses indicated broad suppression of cell cycle processes along with the activation of inflammatory signaling pathways. To determine whether these reflected coordinated pathway-level transcriptional shifts, GSEA was performed across the entire transcriptome (Fig. 5.8a).

GSEA revealed negative enrichment of pathways that regulate cell cycle progression, including *G2/M checkpoint* essential for mitotic entry, *E2F targets* that drive DNA replication and S-phase entry, and Myc targets which support metabolic activity and proliferative growth (Fig 5.8a). Together, these suppressed pathways align with the function reduction in proliferation observed in NET-treated ECs.

The positively enriched pathways were also consistent with KEGG and GO results, including a coordinated upregulation in *TNF-alpha signaling via NF-κB*, *IL-2/STAT5 signaling*, *IL-6/JAK/STAT3* signaling, and *Coagulation* (Fig. 5.8a), consistent with activation of endothelial inflammatory signaling.

Leading-edge genes driving these pathway enrichments were visualized in a heatmap, which showed NET-induced downregulation of key cell cycle regulators, including the transcription factor *E2F2*, the cyclin-dependent kinase 1 (CDK1) regulator *CDKN3*, the G1/S transition mediator *CDCA3*, and several mitotic machinery components such as *CENPF* and *KIF15* (Fig. 5.8b). Conversely, upregulated genes supported activation of immune and chemokine pathways in NET-treated cells and included components of TNF signaling (TNFRSF4 and TNFSF11(RNAKL)) and NF-κB signaling (*TLR2*) (Fig. 5.8b). Genes involved in

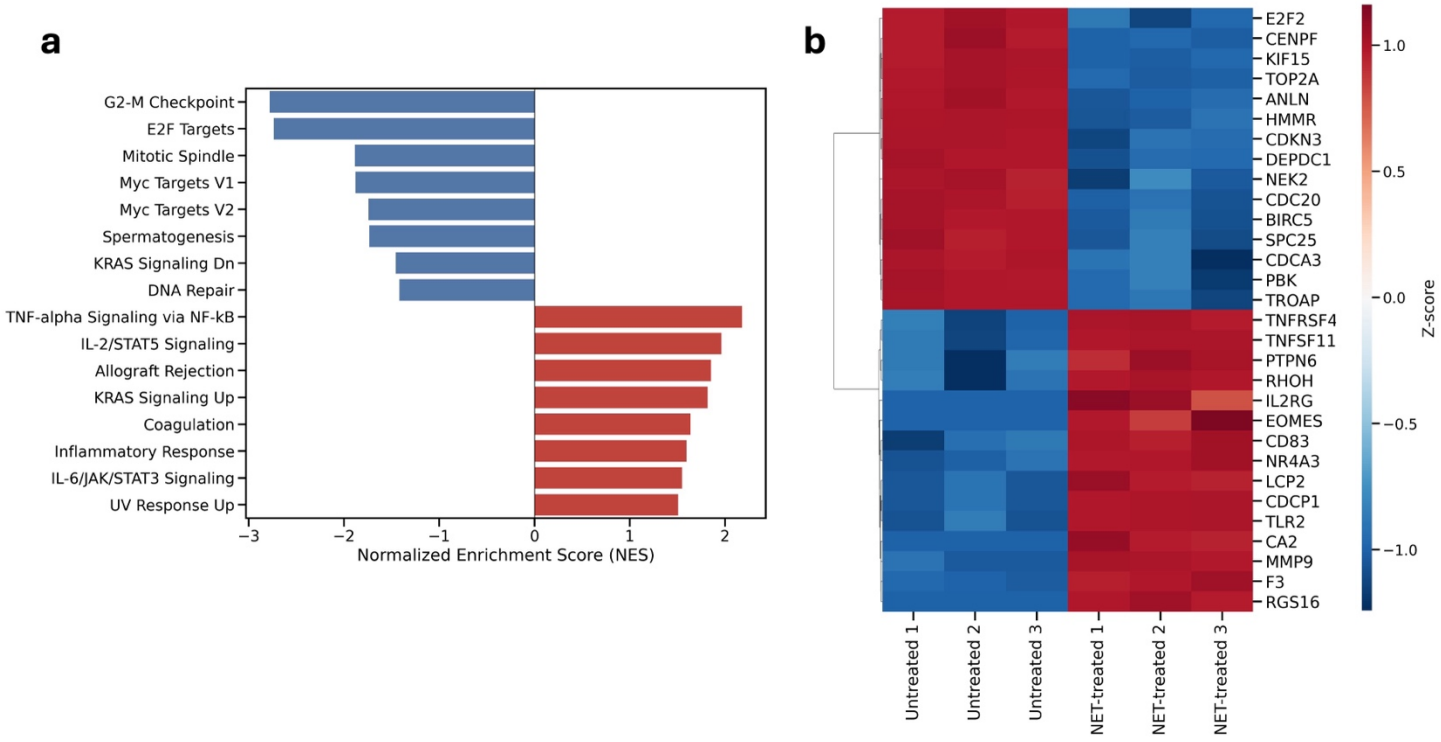

Figure 5.8: Gene set enrichment analysis and leading-edge gene expression in NET-treated endothelial cells.
a, Gene Set Enrichment Analysis (GSEA) of the full ranked transcriptome comparing NET-treated and control HUVECs. Significantly enriched gene sets are shown with positive (red) and negative (blue) normalized enrichment scores (NES), ranked by magnitude of enrichment. **b**, Heatmap of leading-edge genes contributing to enriched gene sets shown in (a). Rows represent genes and columns represent individual biological replicates. Expression values are displayed as row-scaled *z*-scores.

extracellular matrix remodeling (*MMP9* and *CDCPI*) and the pro-coagulant response (*F3*, Tissue Factor), consistent with endothelial inflammatory activation.

5.4 Gene set enrichment analysis identifies senescence-associated transcriptional programs in NET-treated endothelial cells

Together, the enrichment analyses indicate a transcriptional profile characteristic of cellular senescence (360). They reflect well-established senescence-associated DNA-damage signaling and suppression of E2F-driven cell cycle programs that lead to stable G2 to mitosis (G2/M) arrest rather than a reversible G0 quiescent state. Accordingly, NET treatment was associated with downregulation of G2/M regulators and signatures of mitotic failure, a recognized upstream event in senescence, alongside enriched NF-κB signaling, a key driver of the SASP (361–363) (Fig. 5.8).

To further assess whether NETs induce a broad senescence program in ECs, we evaluated their transcriptomes against a unified senescence signature (Fig. 5.9). Given the variability of senescence profiles across cell types and driving mechanisms (360), each sample was first scored using the newly developed transcriptome-based human universal senescence index (hISU), which integrates multiple senescence datasets to capture conserved transcriptional features of senescence (335). The resulting hISU senescence scores were markedly elevated in NET-treated samples, reaching ~ 0.95 on a 0–1 scale, whereas control samples remained below 0.2 (Fig. 5.9a). This significant shift indicates that NETs induce a robust, global transcriptional state reflective of true senescence rather than transient cell cycle arrest in ECs.

GSEA was then performed on senescence-associated mechanistic gene sets, curated from established core senescence signatures (Appendix B), to identify the predominant senescence-related programs contributing to the endothelial transcriptional phenotype induced by NETs (Fig. 5.9b). This revealed strong positive enrichment of SASP-related genes, which showed the largest

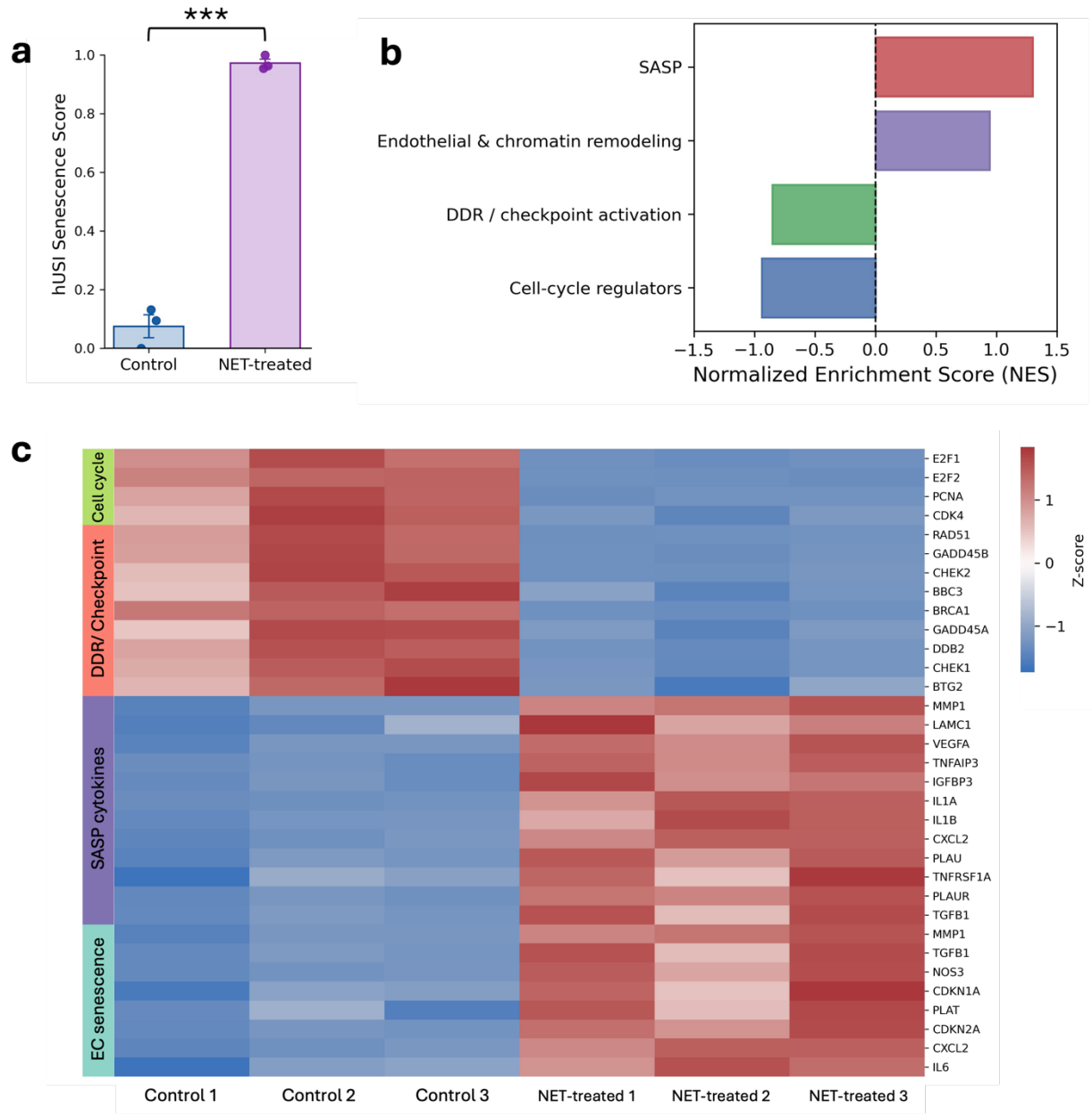

Figure 5.9: Senescence-associated transcriptional signatures in NET-treated endothelial cells.

a, Human Universal Senescence Index (hUSI) scores derived from control and NET-treated HUVEC transcriptomes (10.1038/s43587-025-00886-2). Data is presented as mean ± SEM. ***=P<0.001. **b**, Gene Set Enrichment Analysis (GSEA) of curated senescence-related gene sets comparing NET-treated and control HUVECs, with normalized enrichment scores (NES) for SASP (red), endothelial and chromatin remodeling (purple), DNA damage response (DDR)/ checkpoint activation (green), and cell cycle regulatory (blue) gene sets. c, Heatmap of leading-edge genes driving the senescence-associated enrichment patterns shown in (b), grouped by functional category and displayed as row-scaled *z*-scores.

NES value, together with enrichment of endothelial activation and chromatin remodeling programs characteristic of endothelial senescence (364,365). Conversely, the DNA damage response (DDR) and DNA-integrity checkpoint gene sets were negatively enriched, in line with KEGG results indicating suppression of DNA repair pathways. Cell cycle regulatory genes showed an even stronger negative enrichment, supporting characteristic senescence-associated cell cycle exit (366). A heatmap of leading-edge genes highlights the specific genes driving these enrichments (Fig. 5.9c).

Together, these enrichment patterns are consistent with a senescence-like transcriptional program contributing to NET-induced endothelial injury, integrating suppression of cell cycle and repair pathways with activation of SASP and endothelial-remodeling signatures.

5.5 Targeted validation of G2/M regulators shows modest transcriptional suppression without corresponding protein-level changes following NET exposure

To validate the observed suppression of G2/M regulators, we quantified the expression of key mitotic genes in independently generated NET-treated endothelial samples using RT qPCR (Fig. 5.10). The panel included the central G2/M kinase *CDK1* and its associated cyclins, cyclin B1, cyclin B2, and cyclin A2 (*CCNB1/2, CCNA2*), the mitotic entry regulator polo-like kinase 1 (*PLK1*), and members of the minichromosome maintenance (MCM) protein family as indicators of DNA replication and potential cell cycle exit.

mRNA expression analysis revealed a significant yet modest decrease in *CDK1*, *PLK1*, *CCNB2*, and *MCM2* in NET-treated ECs, consistent with suppression of G2/M transition and cell cycle arrest (Fig. 5.10). The remaining genes showed similar downward trends but did not reach significance, with considerable variability observed across NET-treated samples. This heterogeneity likely reflects differences in NET potency and baseline EC health,

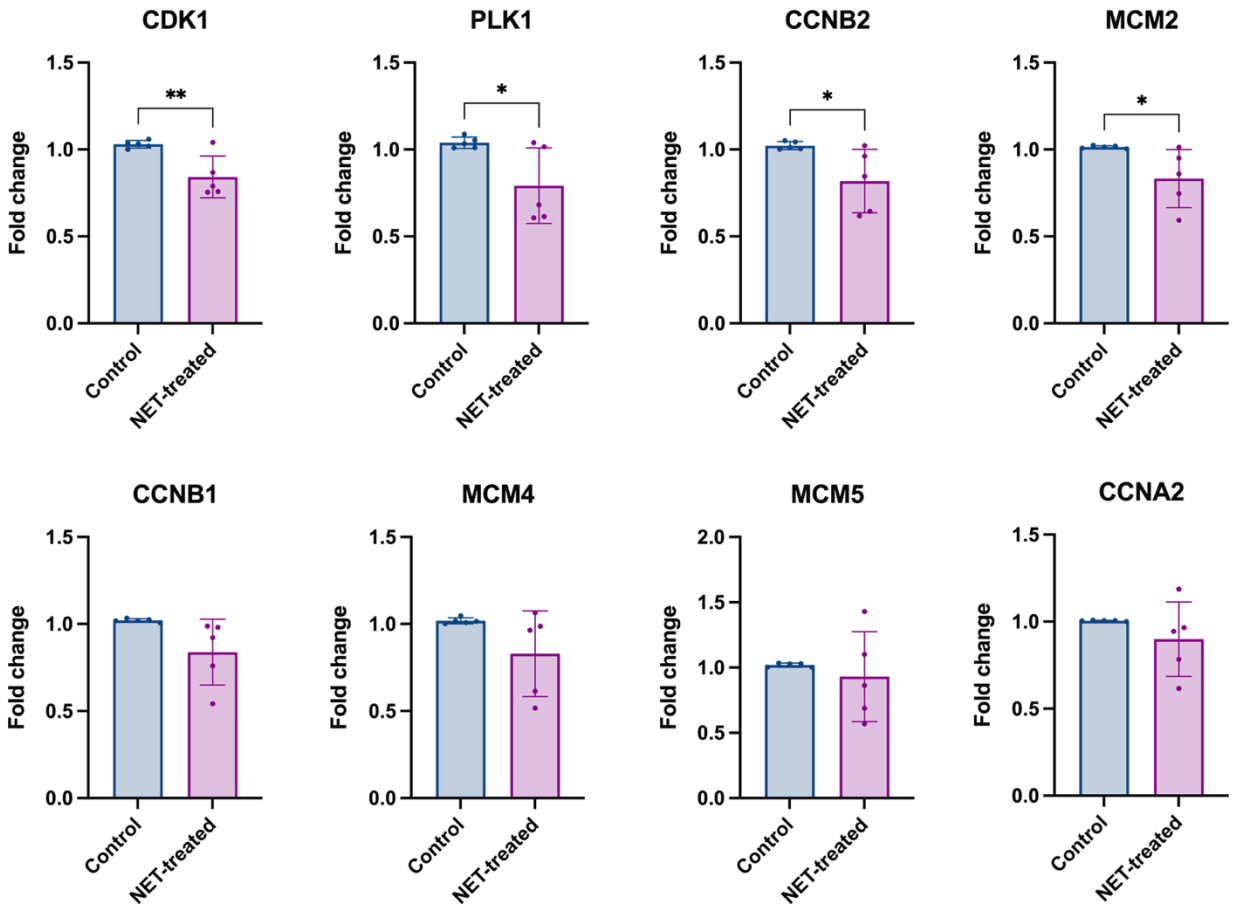

Figure 5.10: Targeted transcriptional validation of G2/M arrest and cell cycle suppression in NET-treated endothelial cells.

mRNA expression levels of selected G2/M and cell cycle–associated genes identified from transcriptomic enrichment analyses were quantified by RT-qPCR in control and NET-treated HUVECs following 24-hour NET exposure. Gene expression was normalized to GAPDH and expressed relative to control samples. Data presented as mean ± SEM. *=P<0.05, **=P<0.01. N=5 biological replicates.

suggesting that the impact of NET exposure on G2/M regulatory genes may vary in magnitude across preparations.

To determine whether reduced transcription of *CDK1* and *PLK1* translated to changes at the protein level, we assessed their expression level in NET-treated cells by Western blot. Levels of CDK1 and PLK1 were not significantly altered after 24 hours of NET exposure, although both kinases showed a modest downward trend (Fig. 5.11). This may be due to the short treatment window, during which transcriptional changes may precede detectable shifts in protein abundance (367).

Together, these G2/M regulator measurements indicate that 24-hour NET exposure leads to modest transcriptional suppression without detectable changes in CDK1 or PLK1 protein abundance. This suggests that the suppression of cell cycle pathways observed in the RNA-sequencing data reflects an early transcriptional reprogramming toward cell cycle exit rather than a fully established arrest.

5.6 NET exposure induces limited and variable functional senescence-associated changes in endothelial cells

To investigate whether the transcriptional suppression of cell cycle genes and the broader senescence-associated transcriptional profiles identified by RNA-sequencing reflect true NET-induced senescence, we next assessed functional markers of senescence in ECs (Fig. 5.12). The levels and activity of endogenous lysosomal senescence-associated β-galactosidase (SA-β-gal), a marker known to increase in senescent cells (368), were compared between control and NET-treated ECs. In contrast, NET-treated cells displayed a modest but consistent increase in enzymatic SA-β-gal activity that reached statistical significance (Fig. 5.12b), indicating altered lysosomal activity associated with senescence.

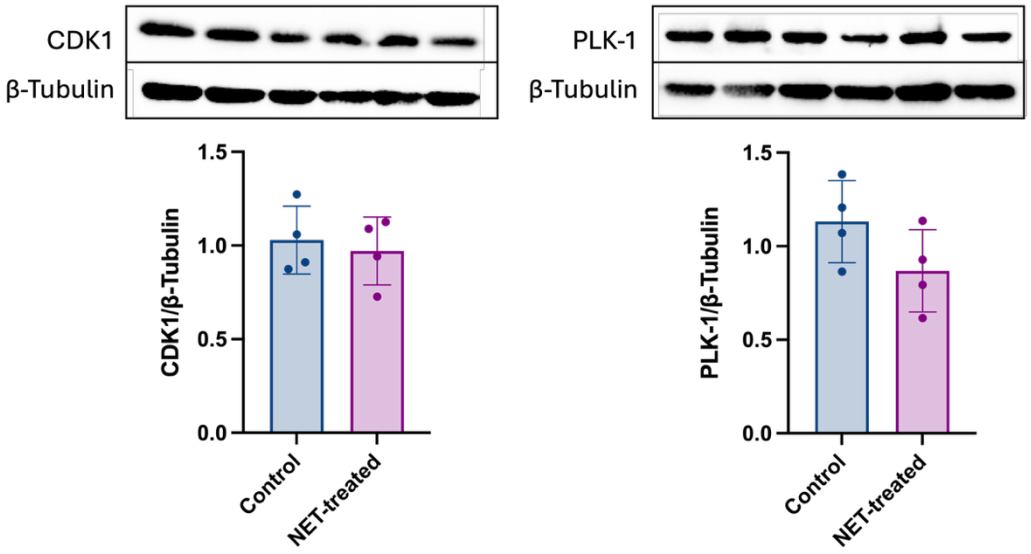

Figure 5.11: Protein-level quantification of G2/M regulatory kinases in NET-treated endothelial cells.
Protein expression of the mitotic entry kinases CDK1 and PLK1 was quantified by Western blot in control and NET-treated HUVECs following 24-hour NET exposure. Protein levels were normalized to β-Tubulin and expressed relative to control samples. Data presented as mean ± SEM. N=4 biological replicates.

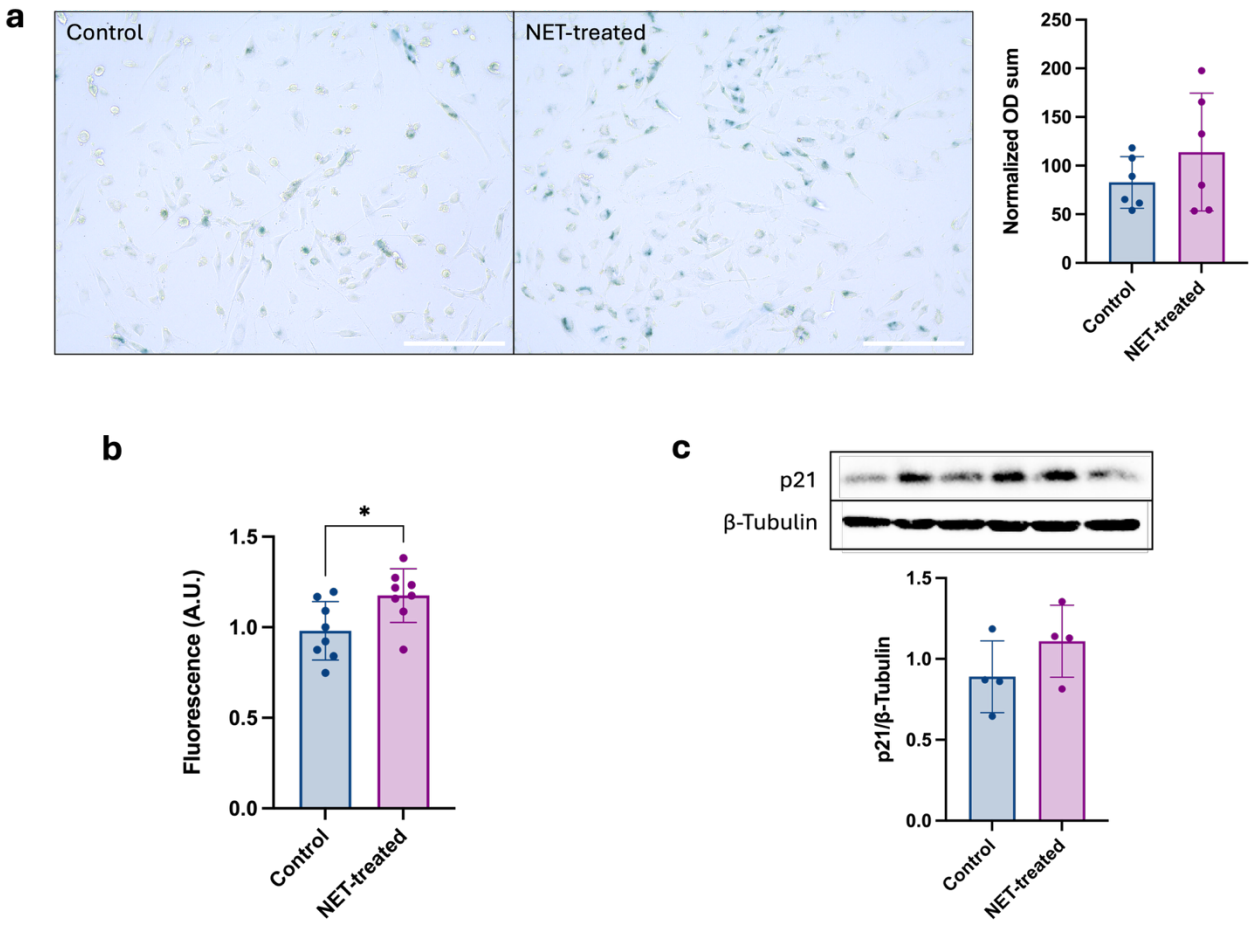

Figure 5.12: Assessment of functional senescence markers in NET-treated endothelial cells.

a, Representative images of SA-β-gal colorimetric staining in control and NET-treated HUVECs with associated quantification presented as mean ± SEM. 20x magnification, scale bar=200µm. N=6 biological replicates. **b**, SA-β-gal enzymatic activity measured in control and NET-treated HUVECs. *=P<0.05. N=8 biological replicates. **c**, Relative p21 expression quantified by Western blot in control and NET-treated HUVECs following 24-hour NET exposure. Protein expression levels were normalized to β-Tubulin. Data presented as mean ± SEM. N=4 biological replicates.

Although colorimetric SA-β-gal staining was increased in some NET-treated samples, responses were highly variable and did not differ significantly from controls (Fig. 5.12a), which may reflect the lower sensitivity of the colorimetric assay compared with the activity-based assay.

The cyclin-dependent kinase inhibitor, p21, a key mediator of senescence-associated cell cycle arrest, has previously been reported to be upregulated in NET-treated ECs (326). To further evaluate whether NET exposure induces functional senescence, we quantified p21 protein levels in NET-treated ECs by Western blot (Fig. 5.12c). Compared with paired controls, NET- treated cells exhibited a consistent upward trend in p21 expression, although this increase did not reach statistical significance. Together, these findings indicate the emergence of early senescence-associated features following NET exposure, while suggesting that a fully consolidated senescent state has not yet been established at this time point.

Overall, the data presented in this chapter demonstrate that 24-hour NET exposure elicits a robust senescence-associated transcriptional signature in ECs, while functional senescence markers remain modest and heterogeneous. This dissociation between transcriptional reprogramming and classical senescence phenotypes suggests that 24-hour NET exposure may induce an early or primed state of senescence rather than a fully established senescent phenotype in ECs. Consideration of the timing, stability, and biological consequences of this response is therefore critical for interpreting the role of NETs in endothelial dysfunction.

Chapter 6
General Discussion

6.1 Summary of Findings

This thesis examined NET formation and NET-mediated cellular responses and injury across complementary *in vivo* and *in vitro* models. A time-resolved imaging and analysis pipeline was developed to characterize NET formation dynamics in response to distinct stimuli and to assess NETosis modulation in an Ang II-induced model of hypertension. Using this approach, altered NETosis dynamics were identified following two weeks of Ang II infusion and were associated with increased tubular injury despite the absence of overt renal NET deposition, implicating altered NETosis dynamics in hypertension-associated kidney injury.

We further characterized NET-induced transcriptional programs in ECs indicative of altered cell cycle regulation and pro-inflammatory activation, consistent with early senescence-associated reprogramming and supported by functional measures suggestive of cell cycle perturbation. These findings identify endothelial senescence as a potential driving mechanism in early NET-induced EC injury.

6.2 Improved NETosis quantification through integrated imaging and machine learning

The high-throughput methodology and analysis pipeline presented in Chapter 3 allows for tracking of NET release across its various morphological stages (39,45,369), enabling inference of underlying mechanisms and progression dynamics. By segmenting and characterizing single-cell features, this comprehensive approach identifies distinguishing traits of each NETosis stage and supports the development of robust algorithms for automated single-cell classification using CPA. The live-cell imaging assay concurrently captures the timing and progression of NETosis under diverse conditions, providing quantitative insights into the magnitude of responses, the sequence of morphological transitions, and the composition of cell populations, and the mechanisms governing temporal dynamics.

The live-cell imaging assay offers distinct advantages over conventional immunofluorescence staining protocols, eliminating the need for extensive sample manipulation and fixation that can alter NET structures and limit temporal resolution (336). Its 96-well format requires fewer cells and minimizes sample preparation time, making it well-suited for high-throughput screening applications.

Our analysis pipeline performs automated quantification of conventional NET metrics over time, including NET count, area and fluorescence intensity, thereby reducing the well-recognized potential for user bias (336). Beyond standard quantification, our pipeline integrates morphological features from phase-contrast images, a source of valuable mechanistic insights (39). By leveraging the ilastik Random Forest classifier in combination with CellProfiler, we achieved improved segmentation of low-contrast cells. Together with DNA and Annexin V staining data, these image features enable characterization of sequential cellular changes and distinction between apoptotic and NETotic cells, a well-recognized pitfall in NET research (39,336). These two pathways of neutrophil cell death exhibit differing morphological features, membrane integrity profiles, and Annexin V staining (39,369), which are more easily discernable with this imaging methodology.

The comprehensive feature characterization of this approach generates sufficient single-cell data to resolve key steps preceding NET release and to capture the full spectrum of NET phenotypes (45,190,194), through supervised classification in CPA. This enhances assay sensitivity and provides a more accurate and comprehensive view of NETosis, enabling detection of subtle dose- and stimulus-dependent differences.

6.3 Adaptable single-cell profiling of NETosis across neutrophil sources

Comprehensive single-cell characterization further supports the adaptability of the pipeline for neutrophils derived from various sources. Human and mouse neutrophils have been reported to exhibit distinct NETting patterns (370), underscoring the need for an adaptable, non-stringent analysis workflow capable of accommodating biological variability. Such flexibility is difficult to achieve with rigid deep-learning-based approaches but is enabled by a Random Forest framework such as the that implemented in CPA (337). The compatibility of CellProfiler and CPA allows unbiased incorporation of all extracted features (334), facilitating the development of classification algorithms that remain robust across experimental contexts.

Consistent with previous reports describing three sequential stages of NETosis, our pipeline resolved these stages across all neutrophil models examined, despite differences in NETosis dynamics and structural features. In human blood neutrophils, PMA stimulation induces cell body spreading within 30 minutes, followed by nuclear swelling filling up the intracellular space in most cells between 80-120 minutes and NETosis release between 120-220 minutes (39,45). In contrast, our results showed a delayed onset of each stage in neutrophil-directed HL-60s (Fig. 3.11) and in mouse bone marrow neutrophils (Fig. 3.22), consistent with reports that they release fewer NETs and form less prominent network structures (370). Despite these kinetic differences, the sequential morphological progression was preserved, supporting the robustness of our methodology for characterizing NET progression across diverse neutrophil sources and validating the use of HL-60 cells as a high-throughput screening model. Accordingly, our approach captured the previously reported differential progression of NETosis between PMA and ionomycin (Fig. 3.16), identifying an earlier onset of cell activation and NETosis with ionomycin (197)

This adaptability was further demonstrated through application of the pipeline to kidney neutrophils in our Ang II–induced hypertension model, where it enabled discrimination of NETosis dynamics between kidney and bone marrow neutrophils (Fig. 4.8) and identified stage-specific alterations in neutrophils from Ang II–infused animals (Fig. 4.12-4.15). Together, these results validate the adaptability of the pipeline across experimental systems and disease contexts.

6.4 Temporal analysis reveals NETosis regulatory features not captured by endpoint measurements

As highlighted in our Ang II-induced hypertension model, differences in neutrophil activation and NETosis priming can manifest as changes that are detectable only through comprehensive temporal analysis of NETosis progression. End-point only measurements of NET release can fail to capture stimulus- or phenotype-dependent differences in NETosis (197), underscoring the importance of defining temporal dynamics. While endpoint NET measures remain a valuable tool and have revealed, for example, PMA dose-dependent increases in NET levels (371,372), our methodology extends these findings by uncovering the dynamic processes underlying concentration-dependent differences, manifesting as changes in both the rate and magnitude of NETosis. Similarly, endpoint analyses have shown that PAD4 inhibition abrogates NET release in response to both PMA and ionomycin (372). While our results are consistent with this and show reduced NET release following PAD4 inhibition, temporal analysis further revealed stimulus-specific effects of PAD4 inhibition on distinct stages of NETosis (Fig. 3.14), as well as a greater propensity for cell spreading in *Padi4*$^{-/-}$ mouse neutrophils (Fig. 3.22), consistent with reports that these cells generate higher levels of ROS and display enhanced activation (346)

6.5 Technical considerations of the NETosis analysis pipeline

A key strength of our methodology is its versatility for mechanistic studies of NETosis. When paired with pharmacological interventions targeting specific NET mediators, it can be used to investigate mechanisms of NETosis inhibition, degradation, and regulation. Its adaptable design allows tracking of single-cell progression through NETosis stages (*TrackObjects* in CellProfiler) (333), enabling detailed examination of associations and transitions between stages. The pipeline is also flexible in its staining requirements. While Annexin V staining provides valuable information for distinguishing NETosis stages, we achieved approximately 88% classification accuracy with DNA staining alone. This allows Annexin V to be replaced with fluorescent labeling of alternative targets for added mechanistic insight, although it may impact classification performance and require optimization. While these features highlight the flexibility of the pipeline, several technical and biological factors should be considered when interpreting results generated using this approach.

Although mean proportions of NETosis stages are generally consistent between cell populations, individual neutrophils exhibit substantial variability in the timing of stage onset and progression (45,369). This intrinsic heterogeneity introduces variability between experiments and necessitates sufficiently large sample sizes to achieve adequate statistical power.

In addition, the low contrast of activated and NETting cells in phase-contrast images can lead to segmentation errors in ilastik, with individual cells occasionally being over-segmented despite extensive annotation of cell morphologies. Such segmentation errors may contribute to misclassification and underestimation of specific NETosis stages. Furthermore, while the general trained CPA model architecture is transferable between experiments, it must be retrained for each dataset to account for differences in imaging conditions and cell populations. Although this

enables identification of experiment-specific phenotypes, it requires a sufficiently large and representative training set to avoid overfitting. Variability in user-generated CPA training datasets may also introduce classification bias. While quantification of terminal NETosis was consistent between users, interpretation of intermediate stages should therefore emphasize relative trends rather than absolute proportions.

Finally, the current pipeline provides only two-dimensional resolution, limiting complete detection of NET structures and accurate reporting of their area. Nuclear swelling preceding NET release has been associated with gradual increases in cell height (45,369), a parameter not captured by the present analysis and therefore excluded as a metric, which may hinder distinction from cells in terminal NETosis. Despite these limitations, the ability of this assay to monitor NETosis at single-cell resolution across defined morphological stages provides a powerful tool for addressing outstanding questions in the field.

6.6 Limited contribution of NETs to early disease features in Ang II-induced hypertension

Results from our study demonstrate that while two weeks of Ang II infusion induces robust blood pressure elevation, this increase is not exacerbated or attributable to NET release (Fig. 4.2). Contrary to reports suggesting a direct role for NETs in driving hypertension (262), SBP levels were comparable between WT and *Padi4*$^{-/-}$ Ang-infused mice in both males and females at the two-week time point. While this finding does not negate the association between NETs and hypertension (267,373), it suggests that NETs may not contribute to early blood pressure elevation and raises the question of when and under what conditions NETs exert pathogenic effects during hypertensive disease progression.

NETs are well established as modulators of immune activation and responses in a range of inflammatory disease contexts, with their deleterious effects often linked to NET deposition in target organs (49,374). In the present model, while Ang II induced renal immune cell

recruitment, these populations were not substantially altered by PAD4 deficiency (Fig. 4.4-4.6), indicating that immune cell recruitment to the kidney is not NET-driven at this stage in the disease model. Immune cell recruitment may rather be attributable to Ang II–mediated activation of renal endothelial and tubular cells, which is well established to promote leukocyte infiltration through chemokine and adhesion molecule signaling (220).

Consistent with a limited role for NETs in this model, we did not detect NET deposition in the kidney following two weeks of Ang II infusion (Fig. 4.7). The absence of renal NET accumulation is consistent with the limited contribution of NETs to blood pressure elevation and immune activation in this model. While NETs have been detected in renal biopsies from hypertensive patients (267)and implicated in some Ang II–induced preclinical models (262,268), differences in mouse strain, disease context, and experimental severity may underlie variability in NET deposition and NET-driven pathology across studies.

NET accumulation has predominantly been reported in settings of sustained inflammation and is often associated with impaired clearance, immune complex binding and complement activation (153,375,376), suggesting that prolonged Ang II exposure and persistent hypertension may be required to trigger the level of immune activation necessary for NET deposition. Although neutrophils represent an early immune cell population recruited during hypertension, NET deposition may arise as a downstream consequence of chronic blood pressure elevation rather than as an initiating event, which could account for the lack of effect of NET depletion on blood pressure or renal immune cell recruitment in this model.

6.7 Sex differences in renal injury during Ang II–induced hypertension

In our model of Ang II-induced hypertension, blood pressure levels were comparable between males and females, yet females exhibited relative protection to kidney injury, as

reflected by lower expression of tubular injury markers KIM-1 and NGAL (Fig. 4.3b-c). This dissociation between blood pressure and renal injury suggests that sex-dependent mechanisms downstream of Ang II contribute to renal protection in females.

Consistent with this, overall renal immune cell infiltration remained lower in females than in males following Ang II infusion (Fig. 4.4-4.6), and WT female neutrophils from both untreated and Ang II-treated groups displayed a reduced capacity to undergo NETosis (Fig. 4.10-4.11). These findings point to sex-dependent differences in immune and neutrophil activation as potential contributors to kidney protection in females.

In the general human population, pre-menopausal women exhibit lower susceptibility to hypertension, with the increased prevalence of hypertension after menopause implicating a prominent role for sex hormones in blood pressure regulation and disease pathogenesis (377). Beyond systemic blood pressure control, sex hormones modulate tissue responses to Ang II through differential regulation of the RAS. Estrogen promotes Ang II signaling toward Ang II-(1-7)-ACE2-Mas and AT2 receptor pathways that favor anti-inflammatory responses, whereas testosterone enhances AT1 receptor-mediated signaling linked to oxidative stress, fibrosis, and immune activation (378,379).

Consistent with our observations, females are reported to exhibit reduced immune cell infiltration and a more anti-inflammatory immune profile in hypertension (380–382), with males exhibiting greater immune-mediated kidney injury (383). Although sex-dependent neutrophil phenotypes in hypertension remain less well defined, available evidence supports greater neutrophil recruitment in males during hypertension (380), and our findings suggest sex-specific differences in neutrophil activation states that may further contribute to differential pathogenicity between sexes.

6.8 Subtle NET-dependent effects in the kidney may not require deposition

While renal NET accumulation was not detected in our model, it does not exclude the possibility of transient or localized NET release without overt deposition. This is supported by the observation that Ang II-infused WT male mice exhibited greater expression of kidney injury markers than *Padi4*$^{-/-}$ males (Fig. 4.3b-c), despite comparable blood pressure levels and no detectable differences in renal immune cell populations or NET deposition. Together, these findings suggest that PAD4-dependent NET release may contribute to renal injury through mechanisms that are not captured by histological detection of NETs or immune cell quantification.

Ang II-induced hypertension was associated with increased renal infiltration of neutrophils, as well as T cells and macrophages (Fig. 4.4-4.6), reflecting a heightened inflammatory milieu, particularly in males. Under such conditions, neutrophils can exhibit prolonged survival, which has been linked to enhanced NET release (384,385). It is therefore plausible that NETs are generated transiently or locally within the kidney and are rapidly cleared, preventing detectable NET deposition.

Such transient NET release may still enable cell-NET interactions that have been shown to exert detrimental effects on renal parenchymal cells through engagement of pattern-recognition receptors, induction of mitochondrial dysfunction, and local activation of complement pathways (293,386,387). In addition, NET-derived granule proteases and histones impair renal cell function through cytotoxic effects, leading to tubular epithelial cell injury, glomerular damage, and activation of cell death pathways (298,329). Collectively, these mechanisms provide biological context for the differential expression of tubular injury markers between Ang II–infused WT and Padi4$^{-/-}$ mice and are consistent with the presence of subtle, PAD4-dependent injury in the absence of detectable NET deposition.

6.9 Compartment-specific modulation of neutrophil reactivity in hypertension

As observed in our model, neutrophil reactivity and NET-releasing behaviour differ between the bone marrow and kidney compartments, even at baseline (Fig. 4.8). This compartment-specific heterogeneity has previously been reported and is commonly attributed to differences in neutrophil maturation and aging, as well as exposure to distinct tissue microenvironmental cues, which collectively drive a phenotypic drift (388,389).

Compared to bone marrow neutrophils, kidney neutrophils exhibited reduced engagement of the early nuclear disintegration stage but a greater transition toward terminal NETosis, resulting in increased overall NET formation in this compartment (Fig. 4.8). Transcriptomic and proteomic profiling studies indicate that aged or tissue-resident neutrophils exhibit features of cellular activation and altered responsiveness (389). This pre-activated state may therefore limit engagement of early NETosis mechanisms in response to stimulation yet promote efficient progression to terminal NET release once initiated.

During hypertension, both the bone marrow niche and the renal microenvironment can shift toward a pro-inflammatory and stress-associated milieu that alter neutrophil phenotypes and functional responsiveness (272,390,391). In our model, alterations in NETotic responses were evident as early as the bone marrow (Fig. 4.13), indicating that Ang II-associated signals may prime neutrophils prior to their release into the circulation, as previously reported (392)

Hypertension is associated with increased sympathetic activation, a feature that has been recapitulated in Ang II–induced hypertension models (392,393). Although sympathetic signaling was not directly assessed here, it is known to remodel the bone marrow niche and modulate mature neutrophil function (272,394). Along with other hypertension-associated changes in the hematopoietic environment (395), this may contribute to the NETotic profile observed in our Ang II–induced hypertension model, characterized by a greater proportion of disintegrated

nucleus–stage cells transitioning to terminal NETosis *ex vivo* (4.13)**,** consistent with a hyperactivated neutrophil phenotype prior to bone marrow egress (3)

The Ang II-associated activation of bone marrow neutrophils was accompanied by altered NETotic behaviour in kidney neutrophils (Fig. 4.14). This aligns with evidence that hypertension can reprogram circulating neutrophils and shape their functional responses following tissue recruitment (256,396). We observed a greater proportion of neutrophils from Ang II-infused male mice entering the disintegrated nucleus stage compared to controls (Fig. 4.14), suggesting that Ang II-associated cues facilitate initiation of NETosis in kidney-resident neutrophils (267,397). Although terminal NET formation increased modestly, this increase did not mirror the extent of nuclear disintegration, indicating that Ang II primarily amplifies early NETotic commitment rather than uniformly driving terminal NET release in kidney neutrophils.

6.10 Neutrophil responses in PAD4-deficient mice

Although PAD4 deficiency is classically associated with impaired NET formation (123), our data indicate that *Padi4*$^{-/-}$ neutrophils retain early activation responses, reflected in normal spreading from PMA stimulation (Fig. 4.12, 4.14). This is consistent with PAD4 acting downstream of early cytoskeletal responses (398,399), and *Padi4*$^{-/-}$ neutrophils maintaining migratory capacity and key effector functions (113,400). Notably, untreated *Padi4*$^{-/-}$ mice displayed increased baseline neutrophil numbers (Fig. 4.4), a phenotype that was more pronounced in females and was mirrored by a similar increase in macrophage abundance. These findings suggest that PAD4 deficiency may alter baseline myeloid composition in the kidney rather than simply abolishing NETotic capacity, raising the possibility that PAD4-dependent immune contexts may engage target tissues through distinct activation or effector programs.

6.11 Early endothelial responses to NET exposure

Our transcriptomic data reveals that NET exposure elicits a coordinated endothelial response characterized by induction of inflammatory signaling pathways and suppression of DNA replication and cell cycle programs (Fig. 5.8). Enrichment of genes associated with extracellular receptor-mediated signaling suggests involvement of EC-surface receptor engagement, consistent with prior reports demonstrating interaction of extracellular histones and other NET-derived molecules with pattern-recognition receptors such as TLR2 and TLR4 (298,401). Receptor-mediated signaling has been shown to underlie NET-induced endothelial activation, promoting a pro-inflammatory and pro-thrombotic phenotype (276). This was recapitulated in our dataset by enrichment of TNF, Nκ-KB and MAPK signaling pathways (Fig. 5.6a), which have previously been implicated in NET-associated endothelial dysfunction (157,354,402).

Notably, enrichment of inflammatory signaling in our model occurred concurrently with transcriptional programs indicative of perturbed cell replication. This was reflected by downregulation of E2F targets and G2/M-associated genes (Fig. 5.8), alongside impaired endothelial proliferation *in vitro* (Fig. 5.3b). Such coupling of inflammatory activation with growth suppression is consistent with reports describing NET-induced impairment of wound healing and endothelial regeneration (157,354), which emerging evidence has linked to enforcement of cell cycle arrest mediated by p21 (326). Mechanistically, TNF- and NF-κB-dependent signaling is known to promote p21 activation, leading to RB- and DREAM-mediated repression of E2F-dependent transcription and inhibition of mitotic entry (403–405).

While NETs increase endothelial oxidative stress and may also contribute to DNA damage–associated cell cycle arrest (358), the concordance between the inflammatory signaling axis described above and the transcriptional profile observed in our data suggests that NET exposure

predominantly promotes a G2/M-associated cell cycle halt through engagement of canonical stress and inflammatory signaling pathways. Together, these findings capture the early development of an adaptive transcriptional reprogramming to NET exposure, resulting in regulated suppression of endothelial proliferation through checkpoint-dominant control mechanisms.

6.12 Early senescence-associated transcriptional reprogramming in NET-treated endothelial cells

The pro-inflammatory phenotype and concurrent disruption of cell cycle programs observed in our transcriptomic data is consistent with early NET-induced senescence-associated transcriptional reprogramming and aligns with the observed impairment of proliferation (406). This pattern suggests that NETs rapidly initiate endothelial states associated with sustained proliferative arrest, rather than transient growth suppression.

A central feature of senescence-associated reprogramming is the SASP, which encompasses coordinated upregulation of cytokine-, chemokine-, and NF-κB-dependent signaling, as well as extracellular matrix–modifying factors (407,408). While the precise composition and induction mechanisms of the SASP vary across cell types and contexts, the transcriptomic profile described here captures several conserved hallmarks of this program (335,409). Notably, enrichment of JAK/STAT signaling, a key regulator of SASP induction and maintenance (410), was observed alongside NF-κB–dependent gene expression (Fig. 5.6a), consistent with the established role of NF-κB as a central transcriptional driver of senescence-associated inflammatory programs (314,360).

In parallel, senescence is enforced through sustained inhibition of cyclin-dependent kinase activity, most prominently via induction of CDK inhibitors such as p21(366). In our model, transcriptional repression of cyclins and mitotic regulators, together with upregulation of

CDK inhibitors CDKN1A (p21) and CDKN2A (p16) (Fig. 5.8b), supports engagement of a G2/M-associated cell cycle arrest (411). Such arrest is widely reported to precede and facilitate establishment of a stable senescent state, particularly when accompanied by downregulation of cyclin A and B1 (411,412), as observed here. Consistent with this transition from checkpoint engagement to loss of mitotic competence, we observed transcriptional downregulation of CDK1 and PLK1 (Fig. 5.10), two central drivers of mitotic entry whose repression is closely associated with commitment to senescence-associated growth arrest (413,414).

Although cell cycle arrest can initially serve as a transient protective response to cellular stress, progression toward senescence is strongly influenced by the efficiency and resolution of DNA repair (415). The transcriptional patterns observed in our data suggest impaired coordination of DNA repair programs, a condition reported to favor sustained p21 signaling and irreversible cell cycle exit rather than re-entry into proliferation. In our model, NET exposure did not induce EC death (Fig. 5.3a), excluding apoptosis as the primary outcome, while the combined persistence of E2F- and G2/M-associated cell-cycle repression and induction of senescence-associated transcriptional signatures argues against reversible quiescence and instead supports progression toward senescence-associated growth arrest (416).

In this regard, our findings are consistent with previous reports describing p21-mediated cell cycle arrest and functional markers of senescence in NET-treated ECs (329,330). However, our data extends this framework by revealing that NET exposure induces a broader senescence-associated transcriptional program that emerges early and may represent a driving response preceding the development of more overt endothelial injury.

6.13 Functional implications of early senescence-associated endothelial reprogramming

Functional assessment of endothelial proliferative capacity and senescence demonstrated that NET exposure markedly impairs EC growth and is associated with a modest senescence-

associated phenotype, as reflected by increased SA-β-galactosidase activity (Fig. 5.12b). However, these functional changes, together with the associated transcriptomic profile, likely reflect commitment toward senescence rather than a fully established senescent state, as transcriptional repression of key G2/M regulators and induction of the senescence driver p21 were not yet accompanied by corresponding protein-level changes (Fig. 5.11, 5.12c) (417,418).

This may be attributable to the relatively short exposure duration of 24 hours, which appears sufficient to induce stress- and inflammatory-signaling and initiate senescence-associated transcriptomic reprogramming, but precedes the emergence of more stable and fully developed senescence features (417,419). While terminal senescence is classically considered irreversible once established, the endothelial state observed here likely represents an early or pre-senescent commitment phase that does not inherently guarantee progression to terminal senescence without continued or sustained insult (420).

Nonetheless, even in the absence of fully consolidated senescence, engagement of early senescence-associated programs is likely sufficient to impair endothelial functions that depend on proliferative capacity, including endothelial repair and barrier integrity (421). Disruption of these processes has previously been linked to NET exposure and is representative of endothelial dysfunction that can arise prior to the establishment of terminal senescence (300).

Taken together, our results indicate that NET exposure elicits a robust endothelial stress response that commits cells to a senescence-associated trajectory, likely preceding and predisposing toward the establishment of a fully consolidated senescent state.

6.14 Limitations and Considerations

Despite the complementary mechanistic insights provided by the *in vivo* Ang II model and the *in vitro* NET–endothelial system, both approaches have inherent limitations in fully

recapitulating human hypertension and NET-mediated injury. The Ang II infusion model captures a defined RAAS-driven hypertensive context and therefore does not encompass the full spectrum of factors contributing to hypertensive kidney injury or NET biology in humans. Moreover, Ang II can exert direct tissue effects that can occur independently of blood pressure elevation, which may complicate separation of pressure-mediated injury from hormone-driven inflammatory remodeling (345), and may be particularly relevant when interpreting NET-associated effects.

Similarly, the *in vitro* NET–endothelial model isolates specific NET-derived signals but does not capture key *in vivo* dynamics such as blood flow, immune–cell interactions, or NET clearance. The transient nature of NET release also limits accurate estimation of physiologically relevant NET exposure levels *in vitro* relative to *in vivo* kinetics, further limiting direct extrapolation to physiological conditions. In both experimental contexts, relatively short exposure durations restrict inference on chronic disease progression and long-term injury outcomes.

With respect to NET specific measurements, assessment of NETs *in vivo* is further complicated by their transient and spatially restricted release, which may limit their detection despite functional effects. While the *ex vivo* NET assay provides insight into neutrophil activation states and NET-forming propensity, these measurements are performed under isolated conditions that limit generalizability. Finally, use of a global *Padi4*$^{-/-}$ model, while informative for NET-associated processes, may influence other immune compartments and thereby confound attribution of observed effects.

6.15 Future Directions

Future studies should extend both the *in vivo* and *in vitro* systems to better resolve the temporal progression and mechanisms of NET-associated renal and endothelial injury. *In vivo*,

longer durations of hypertension, use of complementary hypertensive models, and applying blood-pressure–lowering interventions that do not directly target the RAAS, would help distinguish Ang II–specific effects from pressure-dependent injury and assess the persistence of PAD4-dependent NETosis dynamics. *In vitro*, NET withdrawal followed by extended endothelial culture would enable direct assessment of whether early senescence-associated reprogramming progresses to stable terminal senescence or remains a reversible stress-associated state. Additionally, cross-system approaches integrating NET-primed neutrophils, such as those isolated from hypertensive mice, with endothelial readouts using co-culture systems would provide a mechanistic bridge between neutrophil activation states observed *in vivo* and endothelial dysfunction characterized *in vitro*. Ultimately, assessing ECs isolated directly from hypertensive mice would allow determination of whether features of early senescence-associated reprogramming observed *in vitro* are recapitulated *in vivo*.

6.16 Conclusion

The studies presented in this thesis collectively investigated NET formation at the mechanistic level, examined its regulation and behavior in the context of hypertension, and assessed the downstream impact of NET exposure on ECs. Using a time-resolved approach, NETosis dynamics were shown to be altered under hypertensive conditions and associated with increased kidney injury, supporting a role for altered NET behavior in hypertension-associated pathology. In parallel, NET exposure was found to rapidly induce a broad senescence-associated transcriptomic program in ECs, accompanied by impaired proliferative capacity and consistent with an early stress-driven reprogramming state at the time point examined.

Together, these findings support a framework in which NET activity is dynamically regulated in hypertension and, when encountered by ECs, engages transcriptional programs associated with early functional dysfunction. While these effects were characterized in distinct

experimental contexts, they collectively highlight the pathogenic potential of NETs and provide a conceptual link between altered NET biology in hypertension and endothelial vulnerability to injury. This perspective shifts attention away from static NET detection and acute cytotoxicity toward dynamic regulation of NET formation and early cell-state reprogramming as relevant features of NET-mediated vascular and renal injury in hypertension.

References

1. Lawrence SM, Corriden R, Nizet V. The Ontogeny of a Neutrophil: Mechanisms of Granulopoiesis and Homeostasis. Microbiology and Molecular Biology Reviews. American Society for Microbiology; 2018;82(1). DOI: 10.1128/mmbr.00057-17
2. Rosales C. Neutrophil: A Cell with Many Roles in Inflammation or Several Cell Types? Front Physiol. Front Physiol; 2018;9(FEB). DOI: 10.3389/FPHYS.2018.00113
3. Summers C, Rankin SM, Condliffe AM, Singh N, Peters AM, Chilvers ER. Neutrophil kinetics in health and disease. Trends Immunol. Trends Immunol; 2010;31(8):318–24. DOI: 10.1016/J.IT.2010.05.006
4. Hyun KK, De La Luz Sierra M, Williams CK, Gulino AV, Tosato G. G-CSF down-regulation of CXCR4 expression identified as a mechanism for mobilization of myeloid cells. Blood. Blood; 2006;108(3):812–20. DOI: 10.1182/BLOOD-2005-10-4162
5. Faurschou M, Borregaard N. Neutrophil granules and secretory vesicles in inflammation. Microbes Infect. Elsevier Masson SAS; 2003;5(14):1317–27. DOI: 10.1016/j.micinf.2003.09.008
6. Cowland JB, Borregaard N. Granulopoiesis and granules of human neutrophils. Immunol Rev. Immunol Rev; 2016;273(1):11–28. DOI: 10.1111/IMR.12440
7. Borregaard N, Sørensen OE, Theilgaard-Mönch K. Neutrophil granules: a library of innate immunity proteins. Trends Immunol. Trends Immunol; 2007;28(8):340–5. DOI: 10.1016/J.IT.2007.06.002
8. Lacy P. Mechanisms of Degranulation in Neutrophils. Allergy Asthma Clin Immunol. Springer Science and Business Media LLC; 2006;2(3):98. DOI: 10.1186/1710-1492-2-3-98
9. Borregaard N, Kieldsen L, Sengelov H, Diamond MS, Springer TA, Anderson HC, et al. Changes in subcellular localization and surface expression of L-selectin, alkaline phosphatase, and Mac-1 in human neutrophils during stimulation with inflammatory mediators. J Leukoc Biol. J Leukoc Biol; 1994;56(1):80–7. DOI: 10.1002/JLB.56.1.80
10. Sengeløv H, Kjeldsen L, Borregaard N. Control of exocytosis in early neutrophil activation. The Journal of Immunology. Oxford Academic; 1993;150(4):1535–43. DOI: 10.4049/JIMMUNOL.150.4.1535
11. Ley K, Laudanna C, Cybulsky MI, Nourshargh S. Getting to the site of inflammation: the leukocyte adhesion cascade updated. Nature Reviews Immunology 2007 7:9. Nature Publishing Group; 2007;7(9):678–89. DOI: 10.1038/nri2156
12. McEver RP. Selectins: initiators of leucocyte adhesion and signalling at the vascular wall. Cardiovasc Res. Cardiovasc Res; 2015;107(3):331–9. DOI: 10.1093/CVR/CVV154
13. Springer TA. Traffic signals for lymphocyte recirculation and leukocyte emigration: the multistep paradigm. Cell. Cell; 1994;76(2):301–14. DOI: 10.1016/0092-8674(94)90337-9
14. Hynes RO. Integrins: Bidirectional, allosteric signaling machines. Cell. Cell Press; 2002;110(6):673–87. DOI: 10.1016/S0092-8674(02)00971-6
15. Kjeldsen L, Sengeløv H, Lollike K, Nielsen MH, Borregaard N. Isolation and Characterization of Gelatinase Granules From Human Neutrophils. Blood. Content Repository Only!; 1994;83(6):1640–9. DOI: 10.1182/BLOOD.V83.6.1640.1640
16. Jacobsen LC, Theilgaard-Mönch K, Christensen EI, Borregaard N. Arginase 1 is expressed in myelocytes/metamyelocytes and localized in gelatinase granules of human neutrophils. Blood. Blood; 2007;109(7):3084–7. DOI: 10.1182/BLOOD-2006-06-032599

17. Siqueiros-Cendón T, Arévalo-Gallegos S, Iglesias-Figueroa BF, García-Montoya IA, Salazar-Martínez J, Rascón-Cruz Q. Immunomodulatory effects of lactoferrin. Acta Pharmacol Sin. Acta Pharmacol Sin; 2014;35(5):557–66. DOI: 10.1038/APS.2013.200
18. Eipper S, Steiner R, Lesner A, Sienczyk M, Palesch D, Halatsch ME, et al. Lactoferrin Is an Allosteric Enhancer of the Proteolytic Activity of Cathepsin G. PLoS One. PLoS One; 2016;11(3). DOI: 10.1371/JOURNAL.PONE.0151509
19. Hendrixson DR, Qiu J, Shewry SC, Fink DL, Petty S, Baker EN, et al. Human milk lactoferrin is a serine protease that cleaves Haemophilus surface proteins at arginine-rich sites. Mol Microbiol. Mol Microbiol; 2003;47(3):607–17. DOI: 10.1046/J.1365-2958.2003.03327.X
20. Goetz DH, Holmes MA, Borregaard N, Bluhm ME, Raymond KN, Strong RK. The neutrophil lipocalin NGAL is a bacteriostatic agent that interferes with siderophore-mediated iron acquisition. Mol Cell. Mol Cell; 2002;10(5):1033–43. DOI: 10.1016/S1097-2765(02)00708-6
21. Flo TH, Smith KD, Sato S, Rodriguez DJ, Holmes MA, Strong RK, et al. Lipocalin 2 mediates an innate immune response to bacterial infection by sequestrating iron. Nature 2004 432:7019. Nature Publishing Group; 2004;432(7019):917–21. DOI: 10.1038/nature03104
22. Klebanoff SJ. Myeloperoxidase: friend and foe. J Leukoc Biol. J Leukoc Biol; 2005;77(5):598–625. DOI: 10.1189/JLB.1204697
23. Segal AW. How Neutrophils Kill Microbes. Annu Rev Immunol. 2005;23:197. DOI: 10.1146/ANNUREV.IMMUNOL.23.021704.115653
24. Odobasic D, Kitching AR, Holdsworth SR. Neutrophil-Mediated Regulation of Innate and Adaptive Immunity: The Role of Myeloperoxidase. J Immunol Res. J Immunol Res; 2016;2016. DOI: 10.1155/2016/2349817
25. Burgener SS, Schroder K. Neutrophil Extracellular Traps in Host Defense. 2020; DOI: 10.1101/cshperspect.a037028
26. Parker H, Albrett AM, Kettle AJ, Winterbourn CC. Myeloperoxidase associated with neutrophil extracellular traps is active and mediates bacterial killing in the presence of hydrogen peroxide. J Leukoc Biol. J Leukoc Biol; 2012;91(3):369–76. DOI: 10.1189/JLB.0711387
27. Liu Y, Bühring HJ, Zen K, Burst SL, Schnell FJ, Williams IR, et al. Signal Regulatory Protein (SIRPα), a Cellular Ligand for CD47, Regulates Neutrophil Transmigration. Journal of Biological Chemistry. Elsevier; 2002;277(12):10028–36. DOI: 10.1074/JBC.M109720200
28. Clemmensen SN, Bohr CT, Rørvig S, Glenthøj A, Mora-Jensen H, Cramer EP, et al. Olfactomedin 4 defines a subset of human neutrophils. J Leukoc Biol. J Leukoc Biol; 2012;91(3):495–500. DOI: 10.1189/JLB.0811417
29. Dejas L, Santoni K, Meunier E, Lamkanfi M. Regulated cell death in neutrophils: From apoptosis to NETosis and pyroptosis. Semin Immunol. Academic Press; 2023;70:101849. DOI: 10.1016/J.SMIM.2023.101849
30. Noseykina EM, Schepetkin IA, Atochin DN. Molecular Mechanisms for Regulation of Neutrophil Apoptosis under Normal and Pathological Conditions. J Evol Biochem Physiol. J Evol Biochem Physiol; 2021;57(3):429–50. DOI: 10.1134/S0022093021030017
31. Moulding DA, Akgul C, Derouet M, White MRH, Edwards SW. BCL-2 family expression in human neutrophils during delayed and accelerated apoptosis. DOI: 10.1189/jlb.70.5.783

32. Van Opdenbosch N, Lamkanfi M. Caspases in Cell Death, Inflammation, and Disease. Immunity. Immunity; 2019;50(6):1352–64. DOI: 10.1016/J.IMMUNI.2019.05.020
33. Haslett C. Granulocyte apoptosis and its role in the resolution and control of lung inflammation. Am J Respir Crit Care Med. Am J Respir Crit Care Med; 1999;160(5 Pt 2). DOI: 10.1164/AJRCCM.160.SUPPLEMENT_1.4
34. Kebir D El, Filep JG. Modulation of Neutrophil Apoptosis and the Resolution of Inflammation through β2 Integrins. Front Immunol. 2013;4(MAR):60. DOI: 10.3389/FIMMU.2013.00060
35. Pérez-Figueroa E, Álvarez-Carrasco P, Ortega E, Maldonado-Bernal C. Neutrophils: Many Ways to Die. Front Immunol. Frontiers Media S.A.; 2021;12. DOI: 10.3389/FIMMU.2021.631821/FULL
36. Jorgensen I, Miao EA. Pyroptotic cell death defends against intracellular pathogens. Immunol Rev. Blackwell Publishing Ltd; 2015;265(1):130. DOI: 10.1111/IMR.12287
37. Kroemer G, Levine B. Autophagic cell death: the story of a misnomer. Nature Reviews Molecular Cell Biology 2008 9:12. Nature Publishing Group; 2008;9(12):1004–10. DOI: 10.1038/nrm2529
38. Levine B, Kroemer G. Autophagy in the Pathogenesis of Disease. Cell. 2008;132(1):27. DOI: 10.1016/J.CELL.2007.12.018
39. Fuchs TA, Abed U, Goosmann C, Hurwitz R, Schulze I, Wahn V, et al. Novel cell death program leads to neutrophil extracellular traps. J Cell Biol. J Cell Biol; 2007;176(2):231–41. DOI: 10.1083/JCB.200606027
40. Brinkmann V, Reichard U, Goosmann C, Fauler B, Uhlemann Y, Weiss DS, et al. Neutrophil Extracellular Traps Kill Bacteria. Science (1979). 2004;303(5663):1532–5. DOI: 10.1126/SCIENCE.1092385
41. Savill J, Dransfield I, Gregory C, Haslett C. A blast from the past: clearance of apoptotic cells regulates immune responses. Nat Rev Immunol. Nat Rev Immunol; 2002;2(12):965–75. DOI: 10.1038/NRI957
42. Ortega-Gómez A, Perretti M, Soehnlein O. Resolution of inflammation: an integrated view. EMBO Mol Med. EMBO Mol Med; 2013;5(5):661–74. DOI: 10.1002/EMMM.201202382
43. Stark MA, Huo Y, Burcin TL, Morris MA, Olson TS, Ley K. Phagocytosis of apoptotic neutrophils regulates granulopoiesis via IL-23 and IL-17. Immunity. Immunity; 2005;22(3):285–94. DOI: 10.1016/J.IMMUNI.2005.01.011
44. Martin C, Burdon PCE, Bridger G, Gutierrez-Ramos JC, Williams TJ, Rankin SM. Chemokines acting via CXCR2 and CXCR4 control the release of neutrophils from the bone marrow and their return following senescence. Immunity. Immunity; 2003;19(4):583–93. DOI: 10.1016/S1074-7613(03)00263-2
45. Inozemtsev V, Sergunova V, Vorobjeva N, Kozlova E, Sherstyukova E, Lyapunova S, et al. Stages of NETosis Development upon Stimulation of Neutrophils with Activators of Different Types. 2023; DOI: 10.3390/ijms241512355
46. Papayannopoulos V. Neutrophil extracellular traps in immunity and disease. Nature Reviews. 2018;18(2):134–47. DOI: 10.1038/nri.2017.105
47. Dwyer M, Shan Q, D'Ortona S, Maurer R, Mitchell R, Olesen H, et al. Cystic fibrosis sputum DNA has NETosis characteristics and neutrophil extracellular trap release is regulated by macrophage migration-inhibitory factor. J Innate Immun. J Innate Immun; 2014;6(6):765–79. DOI: 10.1159/000363242

48. Urban CF, Ermert D, Schmid M, Abu-Abed U, Goosmann C, Nacken W, et al. Neutrophil extracellular traps contain calprotectin, a cytosolic protein complex involved in host defense against Candida albicans. PLoS Pathog. PLoS Pathog; 2009;5(10). DOI: 10.1371/JOURNAL.PPAT.1000639
49. Wang H, Kim SJ, Lei Y, Wang S, Wang H, Huang H, et al. Neutrophil extracellular traps in homeostasis and disease. Signal Transduction and Targeted Therapy 2024 9:1. Nature Publishing Group; 2024;9(1):1–40. DOI: 10.1038/s41392-024-01933-x
50. Sørensen, Ole E. and Borregaard N. Neutrophil extracellular traps - the dark side of neutrophils. J Clin Invest. 2016;126(5):1612–20. DOI: 10.1172/JCI84538
51. Yang H, Biermann MH, Brauner JM, Liu Y, Zhao Y, Herrmann M. New Insights into Neutrophil Extracellular Traps: Mechanisms of Formation and Role in Inflammation. Front Immunol. Front Immunol; 2016;7(AUG). DOI: 10.3389/FIMMU.2016.00302
52. Urban CF, Reichard U, Brinkmann V, Zychlinsky A. Neutrophil extracellular traps capture and kill Candida albicans yeast and hyphal forms. Cell Microbiol. John Wiley & Sons, Ltd; 2006;8(4):668–76. DOI: 10.1111/J.1462-5822.2005.00659.X
53. Weinrauch Y, Drujan D, Shapiro SD, Weiss J, Zychlinsky A. Neutrophil elastase targets virulence factors of enterobacteria. Nature. Nature; 2002;417(6884):91–4. DOI: 10.1038/417091A
54. Brinkmann V, Zychlinsky A. Neutrophil extracellular traps : Is immunity the second function of chromatin ? 2012;198(5):773–83. DOI: 10.1083/jcb.201203170
55. Averhoff P, Kolbe M, Zychlinsky A, Weinrauch Y. Single residue determines the specificity of neutrophil elastase for Shigella virulence factors. J Mol Biol. J Mol Biol; 2008;377(4):1053–66. DOI: 10.1016/J.JMB.2007.12.034
56. Hoeksema M, Van Eijk M, Haagsman HP, Hartshorn KL. Histones as mediators of host defense, inflammation and thrombosis. Future Microbiol. Future Microbiol; 2016;11(3):441–53. DOI: 10.2217/FMB.15.151
57. Thanabalasuriar A, Scott BNV, Peiseler M, Willson ME, Zeng Z, Warrener P, et al. Neutrophil Extracellular Traps Confine Pseudomonas aeruginosa Ocular Biofilms and Restrict Brain Invasion. Cell Host Microbe. Cell Press; 2019;25(4):526. DOI: 10.1016/J.CHOM.2019.02.007
58. Díaz-Godínez C, Carrero JC. The state of art of neutrophil extracellular traps in protozoan and helminthic infections. Biosci Rep. Biosci Rep; 2019;39(1). DOI: 10.1042/BSR20180916
59. Barr FD, Ochsenbauer C, Wira CR, Rodriguez-Garcia M. Neutrophil extracellular traps prevent HIV infection in the female genital tract. Mucosal Immunol. Mucosal Immunol; 2018;11(5):1420–8. DOI: 10.1038/S41385-018-0045-0
60. Mojoli A, Gonçalves BS, Temerozo JR, Cister-Alves B, Geddes V, Herlinger A, et al. Neutrophil extracellular traps from healthy donors and HIV-1-infected individuals restrict HIV-1 production in macrophages. Scientific Reports 2020 10:1. Nature Publishing Group; 2020;10(1):19603-. DOI: 10.1038/s41598-020-75357-2
61. Saitoh T, Komano J, Saitoh Y, Misawa T, Takahama M, Kozaki T, et al. Neutrophil extracellular traps mediate a host defense response to human immunodeficiency virus-1. Cell Host Microbe. Cell Host Microbe; 2012;12(1):109–16. DOI: 10.1016/J.CHOM.2012.05.015
62. He Y, Liu J, Chen Y, Yan L, Wu J. Neutrophil Extracellular Traps in Candida albicans Infection. Front Immunol. Front Immunol; 2022;13. DOI: 10.3389/FIMMU.2022.913028

63. Bianchi M, Niemiec MJ, Siler U, Urban CF, Reichenbach J. Restoration of anti-Aspergillus defense by neutrophil extracellular traps in human chronic granulomatous disease after gene therapy is calprotectin-dependent. J Allergy Clin Immunol. J Allergy Clin Immunol; 2011;127(5):1243-1252.e7. DOI: 10.1016/J.JACI.2011.01.021
64. Rosales C. Neutrophils at the crossroads of innate and adaptive immunity. J Leukoc Biol. Oxford Academic; 2020;108(1):377–96. DOI: 10.1002/JLB.4MIR0220-574RR
65. An Z, Li J, Yu J, Wang X, Gao H, Zhang W, et al. Neutrophil extracellular traps induced by IL-8 aggravate atherosclerosis via activation NF-κB signaling in macrophages. Cell Cycle. Cell Cycle; 2019;18(21):2928–38. DOI: 10.1080/15384101.2019.1662678
66. Monteith AJ, Miller JM, Maxwell CN, Chazin WJ, Skaar EP. Neutrophil extracellular traps enhance macrophage killing of bacterial pathogens. Sci Adv. American Association for the Advancement of Science; 2021;7(37). DOI: 10.1126/SCIADV.ABJ2101/SUPPL_FILE/SCIADV.ABJ2101_SM.PDF
67. Chen L, Zhao Y, Lai D, Zhang P, Yang Y, Li Y, et al. Neutrophil extracellular traps promote macrophage pyroptosis in sepsis. Cell Death & Disease 2018 9:6. Nature Publishing Group; 2018;9(6):597-. DOI: 10.1038/s41419-018-0538-5
68. Sutton JAF, Carnell OT, Lafage L, Gray J, Biboy J, Gibson JF, et al. Staphylococcus aureus cell wall structure and dynamics during host-pathogen interaction. PLoS Pathog. Public Library of Science; 2021;17(3):e1009468. DOI: 10.1371/JOURNAL.PPAT.1009468
69. Guimarães-Costa AB, Rochael NC, Oliveira F, Echevarria-Lima J, Saraiva EM. Neutrophil Extracellular Traps Reprogram IL-4/GM-CSF-Induced Monocyte Differentiation to Anti-inflammatory Macrophages. Front Immunol. Front Immunol; 2017;8(MAY). DOI: 10.3389/FIMMU.2017.00523
70. Matta B, Barnes BJ. Coordination between innate immune cells, type I IFNs and IRF5 drives SLE pathogenesis. Cytokine. Cytokine; 2020;132. DOI: 10.1016/J.CYTO.2019.05.018
71. Barrientos L, Bignon A, Gueguen C, de Chaisemartin L, Gorges R, Sandré C, et al. Neutrophil extracellular traps downregulate lipopolysaccharide-induced activation of monocyte-derived dendritic cells. J Immunol. J Immunol; 2014;193(11):5689–98. DOI: 10.4049/JIMMUNOL.1400586
72. Shrestha S, Hong CW. Extracellular Mechanisms of Neutrophils in Immune Cell Crosstalk. Immune Netw. Immune Netw; 2023;23(5). DOI: 10.4110/IN.2023.23.E38
73. Tate MD, Brooks AG, Reading PC, Mintern JD. Neutrophils sustain effective CD8(+) T-cell responses in the respiratory tract following influenza infection. Immunol Cell Biol. Immunol Cell Biol; 2012;90(2):197–205. DOI: 10.1038/ICB.2011.26
74. Bert S, Nadkarni S, Perretti M. Neutrophil-T cell crosstalk and the control of the host inflammatory response. Immunol Rev. Immunol Rev; 2023;314(1):36–49. DOI: 10.1111/IMR.13162
75. Fang H, Shao S, Xue K, Yuan X, Qiao P, Zhang J, et al. Neutrophil extracellular traps contribute to immune dysregulation in bullous pemphigoid via inducing B-cell differentiation and antibody production. FASEB J. FASEB J; 2021;35(7). DOI: 10.1096/FJ.202100145R

76. Hahn J, Schauer C, Czegley C, Kling L, Petru L, Schmid B, et al. Aggregated neutrophil extracellular traps resolve inflammation by proteolysis of cytokines and chemokines and protection from antiproteases. FASEB J. FASEB J; 2019;33(1):1401–14. DOI: 10.1096/FJ.201800752R
77. Wang Y, Li M, Stadler S, Correll S, Li P, Wang D, et al. Histone hypercitrullination mediates chromatin decondensation and neutrophil extracellular trap formation. J Cell Biol. J Cell Biol; 2009;184(2):205–13. DOI: 10.1083/JCB.200806072
78. Hakkim A, Fuchs TA, Martinez NE, Hess S, Prinz H, Zychlinsky A, et al. Activation of the Raf-MEK-ERK pathway is required for neutrophil extracellular trap formation. Nat Chem Biol. Nat Chem Biol; 2011;7(2):75–7. DOI: 10.1038/NCHEMBIO.496
79. Neeli I, Radic M. Opposition between PKC isoforms regulates histone deimination and neutrophil extracellular chromatin release. Front Immunol. Front Immunol; 2013;4(FRB). DOI: 10.3389/FIMMU.2013.00038
80. Boeltz S, Amini P, Anders H-J, Andrade F, Bilyy R, Chatfield S, et al. To NET or not to NET:current opinions and state of the science regarding the formation of neutrophil extracellular traps. Cell Death Differ. 2019;26:28. DOI: 10.1038/s41418-018-0261-x
81. Keshari RS, Jyoti A, Dubey M, Kothari N, Kohli M, Bogra J, et al. Cytokines Induced Neutrophil Extracellular Traps Formation: Implication for the Inflammatory Disease Condition. PLoS One. PLOS; 2012;7(10):48111. DOI: 10.1371/JOURNAL.PONE.0048111
82. El Benna J, Jiahuai H, Park JW, Schmid E, Ulevitch RJ, Babior BM. Activation of p38 in stimulated human neutrophils: Phosphorylation of the oxidase component p47(phox) by p38 and ERK but not by JNK. Arch Biochem Biophys. Academic Press Inc.; 1996;334(2):395–400. DOI: 10.1006/abbi.1996.0470
83. Metzler KD, Goosmann C, Lubojemska A, Zychlinsky A, Papayannopoulos V. A myeloperoxidase-containing complex regulates neutrophil elastase release and actin dynamics during NETosis. Cell Rep. Cell Rep; 2014;8(3):883–96. DOI: 10.1016/J.CELREP.2014.06.044
84. Metzler KD, Fuchs TA, Nauseef WM, Reumaux D, Roesler J, Schulze I, et al. Myeloperoxidase is required for neutrophil extracellular trap formation: implications for innate immunity. Blood. Blood; 2011;117(3):953–9. DOI: 10.1182/BLOOD-2010-06-290171
85. Wu X, You D, Pan M, Weng M, Xie Q, Guan Y, et al. Knockout of the C3a receptor protects against renal ischemia reperfusion injury by reduction of NETs formation. Cellular and Molecular Life Sciences. Springer Science and Business Media Deutschland GmbH; 2023;80(11):1–17. DOI: 10.1007/S00018-023-04967-6/FIGURES/10
86. Mohammed BM, Fisher BJ, Kraskauskas D, Farkas D, Brophy DF, Fowler III AA, et al. Vitamin C: A novel regulator of neutrophil extracellular trap formation. Nutrients. 2013;5(8):3131–51. DOI: 10.3390/nu5083131
87. Papayannopoulos V, Metzler KD, Hakkim A, Zychlinsky A. Neutrophil elastase and myeloperoxidase regulate the formation of neutrophil extracellular traps. J Cell Biol. J Cell Biol; 2010;191(3):677–91. DOI: 10.1083/JCB.201006052
88. Sollberger G, Choidas A, Burn GL, Habenberger P, Lucrezia R Di, Kordes S, et al. Gasdermin D plays a vital role in the generation of neutrophil extracellular traps. Sci Immunol. Sci Immunol; 2018;3(26). DOI: 10.1126/SCIIMMUNOL.AAR6689

89. Hidalgo A, Libby P, Soehnlein O, Aramburu IV, Papayannopoulos V, Silvestre-Roig C. Neutrophil extracellular traps: from physiology to pathology. Cardiovasc Res. Cardiovasc Res; 2022;118(13):2737–53. DOI: 10.1093/CVR/CVAB329
90. Mor-Vaknin N, Saha A, Legendre M, Carmona-Rivera C, Amin MA, Rabquer BJ, et al. DEK-targeting DNA aptamers as therapeutics for inflammatory arthritis. Nature Communications 2017 8:1. Nature Publishing Group; 2017;8(1):14252-. DOI: 10.1038/ncomms14252
91. Chen KW, Monteleone M, Boucher D, Sollberger G, Ramnath D, Condon ND, et al. Noncanonical inflammasome signaling elicits gasdermin D-dependent neutrophil extracellular traps. Sci Immunol. Sci Immunol; 2018;3(26). DOI: 10.1126/SCIIMMUNOL.AAR6676
92. Tatsiy O, McDonald PP. Physiological stimuli induce PAD4-Dependent, ROS-Independent NETosis, with early and late events controlled by discrete signaling pathways. Front Immunol. 2018;9(SEP). DOI: 10.3389/fimmu.2018.02036
93. Tatsiy O, de Carvalho Oliveira V, Mosha HT, McDonald PP. Early and Late Processes Driving NET Formation, and the Autocrine/Paracrine Role of Endogenous RAGE Ligands. Front Immunol. Front Immunol; 2021;12. DOI: 10.3389/FIMMU.2021.675315
94. Van Der Linden M, Westerlaken GHA, Van Der Vlist M, Van Montfrans J, Meyaard L. Differential Signalling and Kinetics of Neutrophil Extracellular Trap Release Revealed by Quantitative Live Imaging. Sci Rep. 2017;7(1). DOI: 10.1038/s41598-017-06901-w
95. Zhu F, Jing D, Zhou H, Hu Z, Wang Y, Jin G, et al. Blockade of Syk modulates neutrophil immune-responses via the mTOR/RUBCNL-dependent autophagy pathway to alleviate intestinal inflammation in ulcerative colitis. Precis Clin Med. 2023;6(4). DOI: 10.1093/pcmedi/pbad025
96. Maugeri N, Campana L, Gavina M, Covino C, De Metrio M, Panciroli C, et al. Activated platelets present high mobility group box 1 to neutrophils, inducing autophagy and promoting the extrusion of neutrophil extracellular traps. Journal of Thrombosis and Haemostasis. 2014;12(12):2074–88. DOI: 10.1111/jth.12710
97. Xu Q, Shi M, Ding L, Xia Y, Luo L, Lu X, et al. High expression of P-selectin induces neutrophil extracellular traps via the PSGL-1/Syk/Ca2+/PAD4 pathway to exacerbate acute pancreatitis. Front Immunol. 2023;14. DOI: 10.3389/fimmu.2023.1265344
98. Gupta AK, Giaglis S, Hasler P, Hahn S. Efficient Neutrophil Extracellular Trap Induction Requires Mobilization of Both Intracellular and Extracellular Calcium Pools and Is Modulated by Cyclosporine A. PLoS One. PLOS; 2014;9(5). DOI: 10.1371/JOURNAL.PONE.0097088
99. Kenny EF, Herzig A, Krüger R, Muth A, Mondal S, Thompson PR, et al. Diverse stimuli engage different neutrophil extracellular trap pathways. Elife. eLife Sciences Publications Ltd; 2017;6. DOI: 10.7554/ELIFE.24437
100. Kayagaki N, Stowe IB, Lee BL, O'Rourke K, Anderson K, Warming S, et al. Caspase-11 cleaves gasdermin D for non-canonical inflammasome signalling. Nature 2015 526:7575. Nature Publishing Group; 2015;526(7575):666–71. DOI: 10.1038/nature15541
101. Shi J, Zhao Y, Wang K, Shi X, Wang Y, Huang H, et al. Cleavage of GSDMD by inflammatory caspases determines pyroptotic cell death. Nature 2015 526:7575. Nature Publishing Group; 2015;526(7575):660–5. DOI: 10.1038/nature15514

102. Wang Y, Li Y, Chen Z, Yuan Y, Su Q, Ye K, et al. GSDMD-dependent neutrophil extracellular traps promote macrophage-to-myofibroblast transition and renal fibrosis in obstructive nephropathy. Cell Death Dis. Cell Death Dis; 2022;13(8). DOI: 10.1038/S41419-022-05138-4
103. Yipp BG, Kubes P. NETosis: how vital is it? Blood. Blood; 2013;122(16):2784–94. DOI: 10.1182/BLOOD-2013-04-457671
104. Pilsczek FH, Salina D, Poon KKH, Fahey C, Yipp BG, Sibley CD, et al. A novel mechanism of rapid nuclear neutrophil extracellular trap formation in response to Staphylococcus aureus. J Immunol. J Immunol; 2010;185(12):7413–25. DOI: 10.4049/JIMMUNOL.1000675
105. Yipp BG, Petri B, Salina D, Jenne CN, Scott BN V, Zbytnuik LD, et al. Infection-induced NETosis is a dynamic process involving neutrophil multitasking in vivo. Nat Med. 2012; DOI: 10.1038/nm.2847
106. Jorch SK, Kubes P. An emerging role for neutrophil extracellular traps in noninfectious disease. Nature Medicine 2017 23:3. Nature Publishing Group; 2017;23(3):279–87. DOI: 10.1038/NM.4294
107. Lewis HD, Liddle J, Coote JE, Atkinson SJ, Barker MD, Bax BD, et al. Inhibition of PAD4 activity is sufficient to disrupt mouse and human NET formation. Nat Chem Biol. Nat Chem Biol; 2015;11(3):189–91. DOI: 10.1038/NCHEMBIO.1735
108. Pieterse E, Rother N, Yanginlar C, Hilbrands LB, van der Vlag J. Neutrophils discriminate between lipopolysaccharides of different bacterial sources and selectively release neutrophil extracellular traps. Front Immunol. Frontiers Media S.A.; 2016;7(NOV):484. DOI: 10.3389/FIMMU.2016.00484/FULL
109. Byrd AS, O'Brien XM, Johnson CM, Lavigne LM, Reichner JS. An extracellular matrix-based mechanism of rapid neutrophil extracellular trap formation in response to Candida albicans. J Immunol. J Immunol; 2013;190(8):4136–48. DOI: 10.4049/JIMMUNOL.1202671
110. Wu X, You D, Cui J, Yang L, Lin L, Chen Y, et al. Reduced Neutrophil Extracellular Trap Formation During Ischemia Reperfusion Injury in C3 KO Mice: C3 Requirement for NETs Release. Front Immunol. Frontiers Media S.A.; 2022;13. DOI: 10.3389/FIMMU.2022.781273/FULL
111. Vossenaar ER, Zendman AJW, van Venrooij WJ, Pruijn GJM. PAD, a growing family of citrullinating enzymes: genes, features and involvement in disease. BioEssays. 2003;25(11):1106–18. DOI: 10.1002/bies.10357
112. Rohrbach AS, Slade DJ, Thompson PR, Mowen KA. Activation of PAD4 in NET formation. Front Immunol. Frontiers; 2012;3:360. DOI: 10.3389/fimmu.2012.00360
113. Hemmers S, Teijaro JR, Arandjelovic S, Mowen KA. PAD4-Mediated Neutrophil Extracellular Trap Formation Is Not Required for Immunity against Influenza Infection. PLoS One. Public Library of Science; 2011;6(7):e22043. DOI: 10.1371/JOURNAL.PONE.0022043
114. Nakashima K, Arai S, Suzuki A, Nariai Y, Urano T, Nakayama M, et al. PAD4 regulates proliferation of multipotent haematopoietic cells by controlling c-myc expression. Nat Commun. Nat Commun; 2013;4. DOI: 10.1038/NCOMMS2862
115. Arita K, Hashimoto H, Shimizu T, Nakashima K, Yamada M, Sato M. Structural basis for Ca(2+)-induced activation of human PAD4. Nat Struct Mol Biol. Nat Struct Mol Biol; 2004;11(8):777–83. DOI: 10.1038/NSMB799

116. Shirai H, Blundell TL, Mizuguchi K. A novel superfamily of enzymes that catalyze the modification of guanidino groups. Trends Biochem Sci. Trends Biochem Sci; 2001;26(8):465–8. DOI: 10.1016/S0968-0004(01)01906-5
117. Kearney PL, Bhatia M, Jones NG, Yuan L, Glascock MC, Catchings KL, et al. Kinetic characterization of protein arginine deiminase 4: a transcriptional corepressor implicated in the onset and progression of rheumatoid arthritis. Biochemistry. Biochemistry; 2005;44(31):10570–82. DOI: 10.1021/BI050292M
118. Raijmakers R, Zendman AJW, Egberts WV, Vossenaar ER, Raats J, Soede-Huijbregts C, et al. Methylation of arginine residues interferes with citrullination by peptidylarginine deiminases in vitro. J Mol Biol. J Mol Biol; 2007;367(4):1118–29. DOI: 10.1016/J.JMB.2007.01.054
119. Douda DN, Khan MA, Grasemann H, Palaniyar N. SK3 channel and mitochondrial ROS mediate NADPH oxidase-independent NETosis induced by calcium influx. Proc Natl Acad Sci U S A. National Academy of Sciences; 2015;112(9):2817–22. DOI: 10.1073/PNAS.1414055112/SUPPL_FILE/PNAS.201414055SI.PDF
120. de Souza CN, Breda LCD, Khan MA, de Almeida SR, Câmara NOS, Sweezey N, et al. Alkaline pH Promotes NADPH Oxidase-Independent Neutrophil Extracellular Trap Formation: A Matter of Mitochondrial Reactive Oxygen Species Generation and Citrullination and Cleavage of Histone. Front Immunol. Front Immunol; 2018;8(JAN). DOI: 10.3389/FIMMU.2017.01849
121. Willemze A, Trouw LA, Toes REM, Huizinga TWJ. The influence of ACPA status and characteristics on the course of RA. Nat Rev Rheumatol. Nat Rev Rheumatol; 2012;8(3):144–52. DOI: 10.1038/NRRHEUM.2011.204
122. Suzuki A, Yamada R, Chang X, Tokuhiro S, Sawada T, Suzuki M, et al. Functional haplotypes of PADI4, encoding citrullinating enzyme peptidylarginine deiminase 4, are associated with rheumatoid arthritis. Nat Genet. Nat Genet; 2003;34(4):395–402. DOI: 10.1038/NG1206
123. Li P, Li M, Lindberg MR, Kennett MJ, Xiong N, Wang Y. PAD4 is essential for antibacterial innate immunity mediated by neutrophil extracellular traps. J Exp Med. J Exp Med; 2010;207(9):1853–62. DOI: 10.1084/JEM.20100239
124. Leshner M, Wang S, Lewis C, Zheng H, Chen XA, Santy L, et al. PAD4 mediated histone hypercitrullination induces heterochromatin decondensation and chromatin unfolding to form neutrophil extracellular trap-like structures. Front Immunol. Frontiers; 2012;3:307. DOI: 10.3389/fimmu.2012.00307
125. Tsourouktsoglou TD, Warnatsch A, Ioannou M, Hoving D, Wang Q, Papayannopoulos V. Histones, DNA, and Citrullination Promote Neutrophil Extracellular Trap Inflammation by Regulating the Localization and Activation of TLR4. Cell Rep. Cell Rep; 2020;31(5). DOI: 10.1016/J.CELREP.2020.107602
126. Knight JS, Zhao W, Luo W, Subramanian V, O'Dell AA, Yalavarthi S, et al. Peptidylarginine deiminase inhibition is immunomodulatory and vasculoprotective in murine lupus. Journal of Clinical Investigation. 2013;123(7):2981–93. DOI: 10.1172/JCI67390
127. Paunel-Görgülü A, Conforti A, Mierau N, Zierden M, Xiong X, Wahlers T. Peptidylarginine deiminase 4 deficiency in bone marrow cells prevents plaque progression without decreasing atherogenic inflammation in apolipoprotein E-knockout mice. Front Cardiovasc Med. 2022;9. DOI: 10.3389/fcvm.2022.1046273

128. Seri Y, Shoda H, Suzuki A, Matsumoto I, Sumida T, Fujio K, et al. Peptidylarginine deiminase type 4 deficiency reduced arthritis severity in a glucose-6-phosphate isomerase-induced arthritis model. 2015; DOI: 10.1038/srep13041
129. Branzk N, Lubojemska A, Hardison SE, Wang Q, Gutierrez MG, Brown GD, et al. Neutrophils sense microbe size and selectively release neutrophil extracellular traps in response to large pathogens. Nat Immunol. Nat Immunol; 2014;15(11):1017–25. DOI: 10.1038/NI.2987
130. Eby JC, Gray MC, Hewlett EL. Cyclic AMP-mediated suppression of neutrophil extracellular trap formation and apoptosis by the Bordetella pertussis adenylate cyclase toxin. Infect Immun. Infect Immun; 2014;82(12):5256–69. DOI: 10.1128/IAI.02487-14
131. Eisenbeis J, Saffarzadeh M, Peisker H, Jung P, Thewes N, Preissner KT, et al. The Staphylococcus aureus Extracellular Adherence Protein Eap Is a DNA Binding Protein Capable of Blocking Neutrophil Extracellular Trap Formation. Front Cell Infect Microbiol. Front Cell Infect Microbiol; 2018;8(JUL). DOI: 10.3389/FCIMB.2018.00235
132. Kolaczkowska E, Jenne CN, Surewaard BGJ, Thanabalasuriar A, Lee WY, Sanz MJ, et al. Molecular mechanisms of NET formation and degradation revealed by intravital imaging in the liver vasculature. Nat Commun. Nat Commun; 2015;6. DOI: 10.1038/NCOMMS7673
133. Farrera C, Fadeel B. Macrophage clearance of neutrophil extracellular traps is a silent process. J Immunol. J Immunol; 2013;191(5):2647–56. DOI: 10.4049/JIMMUNOL.1300436
134. Haider P, Kral-Pointner JB, Mayer J, Richter M, Kaun C, Brostjan C, et al. Neutrophil Extracellular Trap Degradation by Differently Polarized Macrophage Subsets. Arterioscler Thromb Vasc Biol. Arterioscler Thromb Vasc Biol; 2020;40(9):2265–78. DOI: 10.1161/ATVBAHA.120.314883
135. Lauková L, Konečná B, Janovičová L, Vlková B, Celec P. Deoxyribonucleases and Their Applications in Biomedicine. Biomolecules. Biomolecules; 2020;10(7):1–20. DOI: 10.3390/BIOM10071036
136. Jiménez-Alcázar M, Napirei M, Panda R, Köhler EC, Kremer Hovinga JA, Mannherz HG, et al. Impaired DNase1-mediated degradation of neutrophil extracellular traps is associated with acute thrombotic microangiopathies. J Thromb Haemost. J Thromb Haemost; 2015;13(5):732–42. DOI: 10.1111/JTH.12796
137. Huang KW, Liu TC, Liang RY, Chu LY, Cheng H Lo, Chu JW, et al. Structural basis for overhang excision and terminal unwinding of DNA duplexes by TREX1. PLoS Biol. PLoS Biol; 2018;16(5). DOI: 10.1371/JOURNAL.PBIO.2005653
138. Lazzaretto B, Fadeel B. Intra- and Extracellular Degradation of Neutrophil Extracellular Traps by Macrophages and Dendritic Cells. J Immunol. J Immunol; 2019;203(8):2276–90. DOI: 10.4049/JIMMUNOL.1800159
139. Nakazawa D, Shida H, Kusunoki Y, Miyoshi A, Nishio S, Tomaru U, et al. The responses of macrophages in interaction with neutrophils that undergo NETosis. J Autoimmun. J Autoimmun; 2016;67:19–28. DOI: 10.1016/J.JAUT.2015.08.018
140. Iba T, Levi M, Levy JH. Intracellular communication and immunothrombosis in sepsis. Journal of Thrombosis and Haemostasis. John Wiley and Sons Inc; 2022;20(11):2475. DOI: 10.1111/JTH.15852

141. Bukong TN, Cho Y, Iracheta-Vellve A, Saha B, Lowe P, Adejumo A, et al. Abnormal neutrophil traps and impaired efferocytosis contribute to liver injury and sepsis severity after binge alcohol use. J Hepatol. J Hepatol; 2018;69(5):1145–54. DOI: 10.1016/J.JHEP.2018.07.005
142. Silva CMS, Wanderley CWS, Veras FP, Sonego F, Nascimento DC, Gonçalves A V., et al. Gasdermin D inhibition prevents multiple organ dysfunction during sepsis by blocking NET formation. Blood. Blood; 2021;138(25):2702–13. DOI: 10.1182/BLOOD.2021011525
143. Abrams ST, Zhang N, Manson J, Liu T, Dart C, Baluwa F, et al. Circulating histones are mediators of trauma-associated lung injury. Am J Respir Crit Care Med. Am J Respir Crit Care Med; 2013;187(2):160–9. DOI: 10.1164/RCCM.201206-1037OC
144. Block H, Rossaint J, Zarbock A. The Fatal Circle of NETs and NET-Associated DAMPs Contributing to Organ Dysfunction. Cells. Cells; 2022;11(12). DOI: 10.3390/CELLS11121919
145. Barnes BJ, Adrover JM, Baxter-Stoltzfus A, Borczuk A, Cools-Lartigue J, Crawford JM, et al. Targeting potential drivers of COVID-19: Neutrophil extracellular traps. J Exp Med. J Exp Med; 2020;217(6). DOI: 10.1084/JEM.20200652
146. Abrams ST, Du M, Shaw RJ, Johnson C, McGuinness D, Schofield J, et al. Damage-associated cellular markers in the clinical and pathogenic profile of vaccine-induced immune thrombotic thrombocytopenia. J Thromb Haemost. J Thromb Haemost; 2024;22(4):1145–53. DOI: 10.1016/J.JTHA.2023.12.008
147. McDonald B, Davis RP, Kim SJ, Tse M, Esmon CT, Kolaczkowska E, et al. Platelets and neutrophil extracellular traps collaborate to promote intravascular coagulation during sepsis in mice. Blood. Blood; 2017;129(10):1357–67. DOI: 10.1182/BLOOD-2016-09-741298
148. Liu Y, Lightfoot YL, Seto N, Carmona-Rivera C, Moore E, Goel R, et al. Peptidylarginine deiminases 2 and 4 modulate innate and adaptive immune responses in TLR-7-dependent lupus. JCI Insight. JCI Insight; 2018;3(23). DOI: 10.1172/JCI.INSIGHT.124729
149. Gestermann N, Di Domizio J, Lande R, Demaria O, Frasca L, Feldmeyer L, et al. Netting Neutrophils Activate Autoreactive B Cells in Lupus. J Immunol. J Immunol; 2018;200(10):3364–71. DOI: 10.4049/JIMMUNOL.1700778
150. Lande R, Ganguly D, Facchinetti V, Frasca L, Conrad C, Gregorio J, et al. Neutrophils activate plasmacytoid dendritic cells by releasing self-DNA-peptide complexes in systemic lupus erythematosus. Sci Transl Med. Sci Transl Med; 2011;3(73). DOI: 10.1126/SCITRANSLMED.3001180
151. Rahman S, Sagar D, Hanna RN, Lightfoot YL, Mistry P, Smith CK, et al. Low-density granulocytes activate T cells and demonstrate a non-suppressive role in systemic lupus erythematosus. Ann Rheum Dis. Ann Rheum Dis; 2019;78(7):957–66. DOI: 10.1136/ANNRHEUMDIS-2018-214620
152. Lyons PA, McKinney EF, Rayner TF, Hatton A, Woffendin HB, Koukoulaki M, et al. Novel expression signatures identified by transcriptional analysis of separated leucocyte subsets in systemic lupus erythematosus and vasculitis. Ann Rheum Dis. Ann Rheum Dis; 2010;69(6):1208–13. DOI: 10.1136/ARD.2009.108043

153. Hakkim A, Fürnrohr BG, Amann K, Laube B, Abed UA, Brinkmann V, et al. Impairment of neutrophil extracellular trap degradation is associated with lupus nephritis. Proc Natl Acad Sci U S A. Proc Natl Acad Sci U S A; 2010;107(21):9813–8. DOI: 10.1073/PNAS.0909927107/-/DCSUPPLEMENTAL/PNAS.200909927SI.PDF
154. Wang H, Li T, Chen S, Gu Y, Ye S. Neutrophil Extracellular Trap Mitochondrial DNA and Its Autoantibody in Systemic Lupus Erythematosus and a Proof-of-Concept Trial of Metformin. Arthritis Rheumatol. Arthritis Rheumatol; 2015;67(12):3190–200. DOI: 10.1002/ART.39296
155. Li Y, Cao X, Liu Y, Zhao Y, Herrmann M. Neutrophil Extracellular Traps Formation and Aggregation Orchestrate Induction and Resolution of Sterile Crystal-Mediated Inflammation. Front Immunol. Front Immunol; 2018;9(JUL). DOI: 10.3389/FIMMU.2018.01559
156. Giovenzana A, Carnovale D, Phillips B, Petrelli A, Giannoukakis N. Neutrophils and their role in the aetiopathogenesis of type 1 and type 2 diabetes. Diabetes Metab Res Rev. John Wiley and Sons Ltd; 2022;38(1). DOI: 10.1002/DMRR.3483
157. Wong SL, Demers M, Martinod K, Gallant M, Wang Y, Goldfine AB, et al. Diabetes primes neutrophils to undergo NETosis, which impairs wound healing. Nat Med. 2015; DOI: 10.1038/nm.3887
158. Shen Y, You Q, Wu Y, Wu J. Inhibition of PAD4-mediated NET formation by cl-amidine prevents diabetes development in nonobese diabetic mice. Eur J Pharmacol. Elsevier; 2022;916:174623. DOI: 10.1016/J.EJPHAR.2021.174623
159. Liu C, Yalavarthi S, Tambralli A, Zeng L, Rysenga CE, Alizadeh N, et al. Inhibition of neutrophil extracellular trap formation alleviates vascular dysfunction in type 1 diabetic mice. Sci Adv. American Association for the Advancement of Science; 2023;9(43). DOI: 10.1126/SCIADV.ADJ1019
160. Döring Y, Soehnlein O, Weber C. Neutrophil Extracellular Traps in Atherosclerosis and Atherothrombosis. Circ Res. 2017;120(4):736–43. DOI: 10.1161/CIRCRESAHA.116.309692
161. Vallés J, Lago A, Santos MT, Latorre AM, Tembl JI, Salom JB, et al. Neutrophil extracellular traps are increased in patients with acute ischemic stroke: prognostic significance. Thromb Haemost. Thromb Haemost; 2017;117(10):1919–29. DOI: 10.1160/TH17-02-0130
162. Yao M, Ma J, Wu D, Fang C, Wang Z, Guo T, et al. Neutrophil extracellular traps mediate deep vein thrombosis: from mechanism to therapy. Vol. 14, Frontiers in Immunology Frontiers Media SA; 2023.
163. Herre M, Cedervall J, Mackman N, Olsson AK. Neutrophil extracellular traps in the pathology of cancer and other inflammatory diseases. Physiol Rev. Physiol Rev; 2023;103(1):277–312. DOI: 10.1152/PHYSREV.00062.2021
164. Thålin C, Demers M, Blomgren B, Wong SL, Von Arbin M, Von Heijne A, et al. NETosis promotes cancer-associated arterial microthrombosis presenting as ischemic stroke with troponin elevation. Thromb Res. Elsevier Ltd; 2016;139:56. DOI: 10.1016/J.THROMRES.2016.01.009
165. Rosell A, Martinod K, Mackman N, Thålin C. Neutrophil extracellular traps and cancer-associated thrombosis. Thromb Res. 2022;213:S35–41. DOI: 10.1016/j.thromres.2021.12.018

166. Wang H, Zhang Y, Wang Q, Wei X, Wang H, Gu K. The regulatory mechanism of neutrophil extracellular traps in cancer biological behavior. Cell Biosci. Cell Biosci; 2021;11(1). DOI: 10.1186/S13578-021-00708-Z
167. Fadini GP, Menegazzo L, Rigato M, Scattolini V, Poncina N, Bruttocao A, et al. NETosis Delays Diabetic Wound Healing in Mice and Humans. Diabetes. Diabetes; 2016;65(4):1061–71. DOI: 10.2337/DB15-0863
168. Knight JS, Luo W, O'Dell AA, Yalavarthi S, Zhao W, Subramanian V, et al. Peptidylarginine deiminase inhibition reduces vascular damage and modulates innate immune responses in murine models of atherosclerosis. Circ Res. 2014; DOI: 10.1161/CIRCRESAHA.114.303312
169. Kawakami T, He J, Morita H, Yokoyama K, Kaji H, Tanaka C, et al. Rab27a Is Essential for the Formation of Neutrophil Extracellular Traps (NETs) in Neutrophil-Like Differentiated HL60 Cells. PLoS One. Public Library of Science; 2014;9(1):e84704. DOI: 10.1371/JOURNAL.PONE.0084704
170. Guo Y, Gao F, Wang Q, Wang K, Pan S, Pan Z, et al. Differentiation of HL-60 cells in serum-free hematopoietic cell media enhances the production of neutrophil extracellular traps. Exp Ther Med. Spandidos Publications; 2021;21(4). DOI: 10.3892/ETM.2021.9784
171. Bhakta SB, Lundgren SM, Sesti BN, Flores BA, Akdogan E, Collins SR, et al. Neutrophil-like cells derived from the HL-60 cell-line as a genetically-tractable model for neutrophil degranulation. PLoS One. PLoS One; 2024;19(2). DOI: 10.1371/JOURNAL.PONE.0297758
172. Manda-Handzlik A, Bystrzycka W, Wachowska M, Sieczkowska S, Stelmaszczyk-Emmel A, Demkow U, et al. The influence of agents differentiating HL-60 cells toward granulocyte-like cells on their ability to release neutrophil extracellular traps. Immunol Cell Biol. John Wiley & Sons, Ltd; 2018;96(4):413–25. DOI: 10.1111/IMCB.12015
173. Rincón E, Rocha-Gregg BL, Collins SR. A map of gene expression in neutrophil-like cell lines. BMC Genomics. BMC Genomics; 2018;19(1). DOI: 10.1186/S12864-018-4957-6
174. Malavez-Cajigas SJ, Marini-Martinez FI, Lacourt-Ventura M, Rosario-Pacheco KJ, Ortiz-Perez NM, Velazquez-Perez B, et al. HL-60 cells as a valuable model to study LPS-induced neutrophil extracellular traps release. Heliyon. Elsevier Ltd; 2024;10(16):e36386. DOI: 10.1016/J.HELIYON.2024.E36386
175. Hsieh YT, Chou YC, Kuo PY, Tsai HW, Yen YT, Shiau AL, et al. Down-regulated miR-146a expression with increased neutrophil extracellular traps and apoptosis formation in autoimmune-mediated diffuse alveolar hemorrhage. J Biomed Sci. J Biomed Sci; 2022;29(1). DOI: 10.1186/S12929-022-00849-4
176. Sano M, Maejima Y, Nakagama S, Shiheido-Watanabe Y, Tamura N, Hirao K, et al. Neutrophil extracellular traps-mediated Beclin-1 suppression aggravates atherosclerosis by inhibiting macrophage autophagy. Front Cell Dev Biol. Front Cell Dev Biol; 2022;10. DOI: 10.3389/FCELL.2022.876147
177. Zhao J, Zhen N, Zhou Q, Lou J, Cui W, Zhang G, et al. NETs Promote Inflammatory Injury by Activating cGAS-STING Pathway in Acute Lung Injury. Int J Mol Sci. Multidisciplinary Digital Publishing Institute (MDPI); 2023;24(6):5125. DOI: 10.3390/IJMS24065125/S1

178. Raup-Konsavage WM, Wang Y, Wang WW, Feliers D, Ruan H, Reeves WB. Neutrophil peptidyl arginine deiminase-4 has a pivotal role in ischemia/reperfusion-induced acute kidney injury. Kidney Int. Kidney Int; 2018;93(2):365–74. DOI: 10.1016/J.KINT.2017.08.014
179. Wang S, Wang Y. Peptidylarginine deiminases in citrullination, gene regulation, health and pathogenesis. Biochim Biophys Acta. Biochim Biophys Acta; 2013;1829(10):1126–35. DOI: 10.1016/J.BBAGRM.2013.07.003
180. Du M, Yang W, Schmull S, Gu J, Xue S. Inhibition of peptidyl arginine deiminase-4 protects against myocardial infarction induced cardiac dysfunction. Int Immunopharmacol. Int Immunopharmacol; 2020;78. DOI: 10.1016/J.INTIMP.2019.106055
181. Kaltenmeier C, Yazdani HO, Morder K, Geller DA, Simmons RL, Tohme S. Neutrophil Extracellular Traps Promote T Cell Exhaustion in the Tumor Microenvironment. Front Immunol. Front Immunol; 2021;12. DOI: 10.3389/FIMMU.2021.785222
182. BRILL A, FUCHS TA, SAVCHENKO AS, THOMAS GM, MARTINOD K, DE MEYER SF, et al. Neutrophil extracellular traps promote deep vein thrombosis in mice. Journal of Thrombosis and Haemostasis. Wiley/Blackwell (10.1111); 2012;10(1):136–44. DOI: 10.1111/j.1538-7836.2011.04544.x
183. Stoimenou M, Tzoros G, Skendros P, Chrysanthopoulou A. Methods for the Assessment of NET Formation: From Neutrophil Biology to Translational Research. Int J Mol Sci. 2022;23(24). DOI: 10.3390/ijms232415823
184. Henry BM, De Oliveira MHS, Cheruiyot I, Benoit J, Rose J, Favaloro EJ, et al. Cell-Free DNA, Neutrophil extracellular traps (NETs), and Endothelial Injury in Coronavirus Disease 2019- (COVID-19-) Associated Acute Kidney Injury. Mediators Inflamm. Mediators Inflamm; 2022;2022. DOI: 10.1155/2022/9339411
185. Lee KH, Cavanaugh L, Leung H, Yan F, Ahmadi Z, Chong BH, et al. Quantification of NETs-associated markers by flow cytometry and serum assays in patients with thrombosis and sepsis. Int J Lab Hematol. 2018;40(4):392–9. DOI: 10.1111/ijlh.12800
186. Thålin C, Hisada Y, Lundström S, Mackman N, Wallén H. Neutrophil Extracellular Traps: Villains and Targets in Arterial, Venous, and Cancer-Associated Thrombosis. Arterioscler Thromb Vasc Biol. Arterioscler Thromb Vasc Biol; 2019;39(9):1724–38. DOI: 10.1161/ATVBAHA.119.312463
187. Mauracher L-M, Posch F, Martinod K, Grilz E, Däullary T, Hell L, et al. Citrullinated histone H3, a biomarker of neutrophil extracellular trap formation, predicts the risk of venous thromboembolism in cancer patients. Journal of Thrombosis and Haemostasis. 2018;16(3):508–18. DOI: 10.1111/jth.13951
188. Zharkova O, Tay SH, Lee HY, Shubhita T, Ong WY, Lateef A, et al. A Flow Cytometry-Based Assay for High-Throughput Detection and Quantification of Neutrophil Extracellular Traps in Mixed Cell Populations. Cytometry Part A. 2019;95(3):268–78. DOI: 10.1002/cyto.a.23672
189. Brinkmann V, Goosmann C, Kühn LI, Zychlinsky A. Automatic quantification of in vitro NET formation. Front Immunol. 2012;3(JAN). DOI: 10.3389/FIMMU.2012.00413
190. Brinkmann V, Laube B, Abed UA, Goosmann C, Zychlinsky A. Neutrophil extracellular traps: how to generate and visualize them. J Vis Exp. J Vis Exp; 2010;(36). DOI: 10.3791/1724

191. Kasprzycka W, Homa-Mlak I, Mlak R, Małecka-Massalska T. Direct and indirect methods of evaluating the NETosis process. Journal of Pre-Clinical and Clinical Research. 2019;13(1):50–6. DOI: 10.26444/jpccr/105563
192. Naccache PH, Fernandes MJG. Challenges in the characterization of neutrophil extracellular traps: The truth is in the details. Eur J Immunol. 2016;46(1):52–5. DOI: 10.1002/eji.201546022
193. Kaplan MJ, Radic M. Neutrophil extracellular traps: double-edged swords of innate immunity. J Immunol. J Immunol; 2012;189(6):2689–95. DOI: 10.4049/JIMMUNOL.1201719
194. Kumra Ahnlide J, Thelaus L, Kahn F, van Breda S, Nordenfelt P. NETQUANT2: automated web-based quantification of neutrophil extracellular traps from fluorescence microscopy. Front Immunol. Front Immunol; 2024;15. DOI: 10.3389/FIMMU.2024.1459933
195. Rebernick R, Fahmy L, Glover C, Bawadekar M, Shim D, Holmes CL, et al. DNA Area and NETosis Analysis (DANA): A High-Throughput Method to Quantify Neutrophil Extracellular Traps in Fluorescent Microscope Images. Biol Proced Online. 2018;20(1). DOI: 10.1186/s12575-018-0072-y
196. Coelho LP, Pato C, Friães A, Neumann A, Von Köckritz-Blickwede M, Ramirez M, et al. Automatic determination of NET (neutrophil extracellular traps) coverage in fluorescent microscopy images. Bioinformatics. Bioinformatics; 2015;31(14):2364–70. DOI: 10.1093/BIOINFORMATICS/BTV156
197. Hoppenbrouwers T, Autar ASA, Sultan AR, Abraham TE, Van Cappellen WA, Houtsmuller AB, et al. In vitro induction of NETosis: Comprehensive live imaging comparison and systematic review. PLoS One. PLoS One; 2017;12(5). DOI: 10.1371/JOURNAL.PONE.0176472
198. Mohanty T, Sørensen OE, Nordenfelt P. NETQUANT: Automated quantification of neutrophil extracellular traps. Front Immunol. Frontiers Media S.A.; 2018;8(JAN). DOI: 10.3389/FIMMU.2017.01999
199. Manda-Handzlik A, Fiok K, Cieloch A, Heropolitanska-Pliszka E, Demkow U. Convolutional Neural Networks-Based Image Analysis for the Detection and Quantification of Neutrophil Extracellular Traps. Cells. 2020;9(2):508. DOI: 10.3390/cells9020508
200. Mohanty T, Nordenfelt P. Automated image-based quantification of neutrophil extracellular traps using netquant. Journal of Visualized Experiments. 2019;2019(153). DOI: 10.3791/58528
201. Olsen MH, Angell SY, Asma S, Boutouyrie P, Burger D, Chirinos JA, et al. A call to action and a lifecourse strategy to address the global burden of raised blood pressure on current and future generations: the Lancet Commission on hypertension. Lancet. Lancet; 2016;388(10060):2665–712. DOI: 10.1016/S0140-6736(16)31134-5
202. Bundy JD, Li C, Stuchlik P, Bu X, Kelly TN, Mills KT, et al. Systolic Blood Pressure Reduction and Risk of Cardiovascular Disease and Mortality: A Systematic Review and Network Meta-analysis. JAMA Cardiol. American Medical Association; 2017;2(7):775. DOI: 10.1001/JAMACARDIO.2017.1421
203. Sarathy H, Salman LA, Lee C, Cohen JB. Evaluation and Management of Secondary Hypertension. Med Clin North Am. W.B. Saunders; 2022;106(2):269. DOI: 10.1016/J.MCNA.2021.11.004

204. Mills KT, Stefanescu A, He J. The global epidemiology of hypertension. Nat Rev Nephrol. Nature Research; 2020;16(4):223. DOI: 10.1038/S41581-019-0244-2
205. Zhou B, Perel P, Mensah GA, Ezzati M. Global epidemiology, health burden and effective interventions for elevated blood pressure and hypertension. Nat Rev Cardiol. Nature Research; 2021;18(11):785. DOI: 10.1038/S41569-021-00559-8
206. Harrison DG, Coffman TM, Wilcox CS. Pathophysiology of Hypertension: The Mosaic Theory and Beyond. Circ Res. Lippincott Williams and Wilkins; 2021;128(7):847–63. DOI: 10.1161/CIRCRESAHA.121.318082/ASSET/CCB9929F-2796-40B1-919B-CBA056777917/ASSETS/IMAGES/LARGE/CIRCRESAHA.121.318082.FIG03.JPG
207. Guessoum O, de Goes Martini A, Sequeira-Lopez MLS, Gomez RA. Deciphering the Identity of Renin Cells in Health and Disease. Trends Mol Med. Trends Mol Med; 2021;27(3):280–92. DOI: 10.1016/J.MOLMED.2020.10.003
208. Forrester SJ, Booz GW, Sigmund CD, Coffman TM, Kawai T, Rizzo V, et al. Angiotensin II Signal Transduction: An Update on Mechanisms of Physiology and Pathophysiology. Physiol Rev. Physiol Rev; 2018;98(3):1627–738. DOI: 10.1152/PHYSREV.00038.2017
209. Braith RW, Mills RM, Wilcox CS, Davis GL, Wood CE. Breakdown of blood pressure and body fluid homeostasis in heart transplant recipients. J Am Coll Cardiol. J Am Coll Cardiol; 1996;27(2):375–83. DOI: 10.1016/0735-1097(95)00467-X
210. Jia G, Habibi J, Aroor AR, Martinez-Lemus LA, De Marco VG, Ramirez-Perez FI, et al. Endothelial mineralocorticoid receptor mediates diet-induced aortic stiffness in females. Circ Res. Lippincott Williams and Wilkins; 2016;118(6):935–43. DOI: 10.1161/CIRCRESAHA.115.308269/-/DC1
211. DiBona GF. Neural control of the kidney: Functionally specific renal sympathetic nerve fibers. Am J Physiol Regul Integr Comp Physiol. American Physiological Society; 2000;279(5 48-5). DOI: 10.1152/AJPREGU.2000.279.5.R1517/ASSET/IMAGES/LARGE/H61100203006.JPEG
212. Saleem M, Hodgkinson CP, Xiao L, Gimenez-Bastida JA, Rasmussen ML, Foss J, et al. Sox6 as a new modulator of renin expression in the kidney. Am J Physiol Renal Physiol. Am J Physiol Renal Physiol; 2020;318(2):F285–97. DOI: 10.1152/AJPRENAL.00095.2019
213. Lifton RP, Gharavi AG, Geller DS. Molecular mechanisms of human hypertension. Cell. Cell; 2001;104(4):545–56. DOI: 10.1016/S0092-8674(01)00241-0
214. McDonough AA, Nguyen MTX. Maintaining Balance under Pressure: Integrated Regulation of Renal Transporters during Hypertension. Hypertension. Lippincott Williams and Wilkins; 2015;66(3):450–5. DOI: 10.1161/HYPERTENSIONAHA.115.04593/ASSET/A4A78331-3CC8-4BBB-A55F-3739A13C9E29/ASSETS/GRAPHIC/450FIG01.JPEG
215. Diedrich A, Jordan J, Tank J, Shannon JR, Robertson R, Luft FC, et al. The sympathetic nervous system in hypertension: assessment by blood pressure variability and ganglionic blockade. J Hypertens. J Hypertens; 2003;21(9):1677–86. DOI: 10.1097/00004872-200309000-00017
216. Cao W, Shi M, Wu L, Li J, Yang Z, Liu Y, et al. Adipocytes initiate an adipose-cerebral-peripheral sympathetic reflex to induce insulin resistance during high-fat feeding. Clin Sci (Lond). Clin Sci (Lond); 2019;133(17):1883–99. DOI: 10.1042/CS20190412

217. Welch WJ, Chabrashvili T, Solis G, Chen Y, Gill PS, Aslam S, et al. Role of extracellular superoxide dismutase in the mouse angiotensin slow pressor response. Hypertension. Hypertension; 2006;48(5):934–41. DOI: 10.1161/01.HYP.0000242928.57344.92
218. Rajagopalan S, Meng XP, Ramasamy S, Harrison DG, Galis ZS. Reactive oxygen species produced by macrophage-derived foam cells regulate the activity of vascular matrix metalloproteinases in vitro. Implications for atherosclerotic plaque stability. J Clin Invest. J Clin Invest; 1996;98(11):2572–9. DOI: 10.1172/JCI119076
219. Somers MJ, Mavromatis K, Galis ZS, Harrison DG. Vascular superoxide production and vasomotor function in hypertension induced by deoxycorticosterone acetate-salt. Circulation. Circulation; 2000;101(14):1722–8. DOI: 10.1161/01.CIR.101.14.1722
220. Harrison DG, Guzik TJ, Lob HE, Madhur MS, Marvar PJ, Thabet SR, et al. Inflammation, immunity, and hypertension. Hypertension. Lippincott Williams & WilkinsHagerstown, MD; 2011;57(2):132–40. DOI: 10.1161/HYPERTENSIONAHA.110.163576/ASSET/1F1ADA12-6D94-4212-983B-792F286D0C1D/ASSETS/GRAPHIC/ZHY0021111990002.JPEG
221. Li Q, Youn JY, Cai H. Mechanisms and consequences of endothelial nitric oxide synthase dysfunction in hypertension. J Hypertens. J Hypertens; 2015;33(6):1128–36. DOI: 10.1097/HJH.0000000000000587
222. FOLKOW B, GRIYBY G, THULESIUS. O. Adaptive structural changes of the vascular walls in hypertension and their relation to the control of the peripheral resistance. Acta Physiol Scand. Acta Physiol Scand; 1958;44(3–4):255–72. DOI: 10.1111/J.1748-1716.1958.TB01626.X
223. Vasan RS, Larson MG, Leip EP, Evans JC, O'Donnell CJ, Kannel WB, et al. Impact of high-normal blood pressure on the risk of cardiovascular disease. N Engl J Med. N Engl J Med; 2001;345(18):1291–7. DOI: 10.1056/NEJMOA003417
224. Cooper LL, Rong J, Benjamin EJ, Larson MG, Levy D, Vita JA, et al. Components of Hemodynamic Load and Cardiovascular Events: The Framingham Heart Study. Circulation. Lippincott Williams and Wilkins; 2014;131(4):354. DOI: 10.1161/CIRCULATIONAHA.114.011357
225. Vasan RS, Short MI, Niiranen TJ, Xanthakis V, DeCarli C, Cheng S, et al. Interrelations Between Arterial Stiffness, Target Organ Damage, and Cardiovascular Disease Outcomes. J Am Heart Assoc. American Heart Association Inc.; 2019;8(14). DOI: 10.1161/JAHA.119.012141/ASSET/D42445F0-873C-417B-89C9-344173377789/ASSETS/GRAPHIC/JAH34250-FIG-0005.PNG
226. Deng LY, Li JS, Schiffrin EL. Endothelium-dependent relaxation of small arteries from essential hypertensive patients: mechanisms and comparison with normotensive subjects and with responses of vessels from spontaneously hypertensive rats. Clin Sci (Lond). Clin Sci (Lond); 1995;88(6):611–22. DOI: 10.1042/CS0880611
227. Endemann DH, Schiffrin EL. Endothelial dysfunction. J Am Soc Nephrol. J Am Soc Nephrol; 2004;15(8):1983–92. DOI: 10.1097/01.ASN.0000132474.50966.DA
228. Oparil S, Acelajado MC, Bakris GL, Berlowitz DR, Cífková R, Dominiczak AF, et al. Hypertension. Nature Reviews Disease Primers 2018 4:1. Nature Publishing Group; 2018;4(1):18014-. DOI: 10.1038/nrdp.2018.14
229. Schiffrin EL. Vascular remodeling in hypertension: mechanisms and treatment. Hypertension. Hypertension; 2012;59(2):367–74. DOI: 10.1161/HYPERTENSIONAHA.111.187021

230. Britten MB, Zeiher AM, Schächinger V. Microvascular dysfunction in angiographically normal or mildly diseased coronary arteries predicts adverse cardiovascular long-term outcome. Coron Artery Dis. Coron Artery Dis; 2004;15(5):259–64. DOI: 10.1097/01.MCA.0000134590.99841.81
231. Zhu XY, Chade AR, Rodriguez-Porcel M, Bentley MD, Ritman EL, Lerman A, et al. Cortical microvascular remodeling in the stenotic kidney: Role of increased oxidative stress. Arterioscler Thromb Vasc Biol. Lippincott Williams & Wilkins; 2004;24(10):1854–9. DOI: 10.1161/01.ATV.0000142443.52606.81/SUPPL_FILE/ATVB2782_FIGUREI.PDF
232. Chade AR. Small Vessels, Big Role: Renal Microcirculation and Progression of Renal Injury. Hypertension. Lippincott Williams and Wilkins; 2017;69(4):551–63. DOI: 10.1161/HYPERTENSIONAHA.116.08319/ASSET/A10A9496-3F7B-43FA-BBB2-47909A9CE12D/ASSETS/GRAPHIC/551FIG02.JPEG
233. Faraco G, Iadecola C. Hypertension: A harbinger of stroke and dementia. Hypertension. Lippincott Williams & WilkinsHagerstown, MD; 2013;62(5):810–7. DOI: 10.1161/HYPERTENSIONAHA.113.01063/ASSET/F81B6AEE-5578-4A85-BD44-8FA2CB6492AC/ASSETS/GRAPHIC/810FIG03.JPEG
234. Matsushita K, Kuriyama Y, Nagatsuka K, Nakamura M, Sawada T, Omae T. Periventricular white matter lucency and cerebral blood flow autoregulation in hypertensive patients. Hypertension. Hypertension; 1994;23(5):565–8. DOI: 10.1161/01.HYP.23.5.565
235. Savoia C, Schiffrin EL. Vascular inflammation in hypertension and diabetes: molecular mechanisms and therapeutic interventions. Clin Sci (Lond). Clin Sci (Lond); 2007;112(7):375–84. DOI: 10.1042/CS20060247
236. Guzik TJ, Nosalski R, Maffia P, Drummond GR. Immune and inflammatory mechanisms in hypertension. Nat Rev Cardiol. Nat Rev Cardiol; 2024;21(6):396–416. DOI: 10.1038/S41569-023-00964-1
237. Kirabo A, Fontana V, De Faria APC, Loperena R, Galindo CL, Wu J, et al. DC isoketal-modified proteins activate T cells and promote hypertension. J Clin Invest. J Clin Invest; 2014;124(10):4642–56. DOI: 10.1172/JCI74084
238. McMaster WG, Kirabo A, Madhur MS, Harrison DG. Inflammation, immunity, and hypertensive end-organ damage. Circ Res. Circ Res; 2015;116(6):1022–33. DOI: 10.1161/CIRCRESAHA.116.303697
239. Amador CA, Barrientos V, Peña J, Herrada AA, González M, Valdés S, et al. Spironolactone decreases DOCA-salt-induced organ damage by blocking the activation of T helper 17 and the downregulation of regulatory T lymphocytes. Hypertension. Hypertension; 2014;63(4):797–803. DOI: 10.1161/HYPERTENSIONAHA.113.02883
240. Madhur MS, Lob HE, McCann LA, Iwakura Y, Blinder Y, Guzik TJ, et al. Interleukin 17 promotes angiotensin II-induced hypertension and vascular dysfunction. Hypertension. Hypertension; 2010;55(2):500–7. DOI: 10.1161/HYPERTENSIONAHA.109.145094
241. Shao J, Nangaku M, Miyata T, Inagi R, Yamada K, Kurokawa K, et al. Imbalance of T-cell subsets in angiotensin II-infused hypertensive rats with kidney injury. Hypertension. Hypertension; 2003;42(1):31–8. DOI: 10.1161/01.HYP.0000075082.06183.4E

242. Barhoumi T, Kasal DA, Li MW, Shbat L, Laurant P, Neves MF, et al. T regulatory lymphocytes prevent angiotensin II-induced hypertension and vascular injury. Hypertension. Hypertension; 2011;57(3):469–76. DOI: 10.1161/HYPERTENSIONAHA.110.162941
243. Calvillo L, Gironacci MM, Crotti L, Meroni PL, Parati G. Neuroimmune crosstalk in the pathophysiology of hypertension. Nature Reviews Cardiology 2019 16:8. Nature Publishing Group; 2019;16(8):476–90. DOI: 10.1038/s41569-019-0178-1
244. Xiao L, do Carmo LS, Foss JD, Chen W, Harrison DG. Sympathetic Enhancement of Memory T-Cell Homing and Hypertension Sensitization. Circ Res. Circ Res; 2020;126(6):708–21. DOI: 10.1161/CIRCRESAHA.119.314758
245. Ruggeri Barbaro N, Van Beusecum J, Xiao L, Do Carmo L, Pitzer A, Loperena R, et al. Sodium activates human monocytes via the NADPH oxidase and isolevuglandin formation. Cardiovasc Res. Cardiovasc Res; 2021;117(5):1358–71. DOI: 10.1093/CVR/CVAA207
246. Jantsch J, Schatz V, Friedrich D, Schröder A, Kopp C, Siegert I, et al. Cutaneous Na+ storage strengthens the antimicrobial barrier function of the skin and boosts macrophage-driven host defense. Cell Metab. Cell Metab; 2015;21(3):493–501. DOI: 10.1016/J.CMET.2015.02.003
247. Kleinewietfeld M, Manzel A, Titze J, Kvakan H, Yosef N, Linker RA, et al. Sodium chloride drives autoimmune disease by the induction of pathogenic TH17 cells. Nature. Nature; 2013;496(7446):518–22. DOI: 10.1038/NATURE11868
248. Nguyen H, Chiasson VL, Chatterjee P, Kopriva SE, Young KJ, Mitchell BM. Interleukin-17 causes Rho-kinase-mediated endothelial dysfunction and hypertension. Cardiovasc Res. Cardiovasc Res; 2013;97(4):696–704. DOI: 10.1093/CVR/CVS422
249. Guzik TJ, Hoch NE, Brown KA, McCann LA, Rahman A, Dikalov S, et al. Role of the T cell in the genesis of angiotensin II–induced hypertension and vascular dysfunction. J Exp Med. 2007;204(10):2449. DOI: 10.1084/JEM.20070657
250. Libby P, Ridker PM, Hansson GK. Inflammation in atherosclerosis: from pathophysiology to practice. J Am Coll Cardiol. J Am Coll Cardiol; 2009;54(23):2129–38. DOI: 10.1016/J.JACC.2009.09.009
251. Bomfim GF, dos Santos RA, Oliveira MA, Giachini FR, Akamine EH, Tostes RC, et al. Toll-like receptor 4 contributes to blood pressure regulation and vascular contraction in spontaneously hypertensive rats. Clin Sci (Lond). Clin Sci (Lond); 2012;122(11):535–43. DOI: 10.1042/CS20110523
252. Biancardi VC, Bomfim GF, Reis WL, Al-Gassimi S, Nunes KP. The interplay between Angiotensin II, TLR4 and hypertension. Pharmacol Res. Pharmacol Res; 2017;120:88–96. DOI: 10.1016/J.PHRS.2017.03.017
253. Sreejit G, Johnson J, Jaggers RM, Dahdah A, Murphy AJ, Hanssen NMJ, et al. Neutrophils in cardiovascular disease: warmongers, peacemakers, or both? Cardiovasc Res. Oxford University Press; 2021;118(12):2596. DOI: 10.1093/CVR/CVAB302
254. Silvestre-Roig C, Fridlender ZG, Glogauer M, Scapini P. Neutrophil Diversity in Health and Disease. Trends Immunol. Trends Immunol; 2019;40(7):565–83. DOI: 10.1016/J.IT.2019.04.012

255. Itani HA, McMaster WG, Saleh MA, Nazarewicz RR, Mikolajczyk TP, Kaszuba AM, et al. Activation of Human T Cells in Hypertension: Studies of Humanized Mice and Hypertensive Humans. Hypertension. Hypertension; 2016;68(1):123–32. DOI: 10.1161/HYPERTENSIONAHA.116.07237
256. Araos P, Figueroa S, Amador CA. The Role of Neutrophils in Hypertension. Int J Mol Sci. MDPI AG; 2020;21(22):8536. DOI: 10.3390/IJMS21228536
257. Sarejloo S, Dehesh M, Fathi M, Khanzadeh M, Lucke-Wold B, Ghaedi A, et al. Meta-analysis of differences in neutrophil to lymphocyte ratio between hypertensive and non-hypertensive individuals. BMC Cardiovasc Disord. BioMed Central Ltd; 2023;23(1):1–16. DOI: 10.1186/S12872-023-03304-W/FIGURES/6
258. Tsukimori K, Nakano H, Wake N. Difference in neutrophil superoxide generation during pregnancy between preeclampsia and essential hypertension. Hypertension. Hypertension; 2007;49(6):1436–41. DOI: 10.1161/HYPERTENSIONAHA.106.086751
259. Chatterjee M, Saluja R, Tewari S, Barthwal MK, Goel SK, Dikshit M. Augmented nitric oxide generation in neutrophils: oxidative and pro-inflammatory implications in hypertension. Free Radic Res. Free Radic Res; 2009;43(12):1195–204. DOI: 10.3109/10715760903247256
260. Kolaczkowska E, Kubes P. Neutrophil recruitment and function in health and inflammation. Nat Rev Immunol. Nat Rev Immunol; 2013;13(3):159–75. DOI: 10.1038/NRI3399
261. Silvestre-Roig C, Braster Q, Wichapong K, Lee EY, Teulon JM, Berrebeh N, et al. Externalized histone H4 orchestrates chronic inflammation by inducing lytic cell death. Nature 2019 569:7755. Nature Publishing Group; 2019;569(7755):236–40. DOI: 10.1038/s41586-019-1167-6
262. Krishnan J, Hennen EM, Ao M, Kirabo A, Ahmad T, de la Visitación N, et al. NETosis Drives Blood Pressure Elevation and Vascular Dysfunction in Hypertension. Circ Res. 2024;134(11):1483–94. DOI: 10.1161/CIRCRESAHA.123.323897
263. Petrie JR, Guzik TJ, Touyz RM. Diabetes, Hypertension, and Cardiovascular Disease: Clinical Insights and Vascular Mechanisms. Can J Cardiol. Can J Cardiol; 2018;34(5):575–84. DOI: 10.1016/J.CJCA.2017.12.005
264. Li J, Tong D, Song B, Xie F, Zhang G, Hao X, et al. Inflammatory cytokines induce neutrophil extracellular traps interaction with activated platelets and endothelial cells exacerbate coagulation in moderate and severe essential hypertension. J Hypertens. Lippincott Williams and Wilkins; 2022;40(11):2219–29. DOI: 10.1097/HJH.0000000000003250
265. Fang X, Ma L, Wang Y, Ren F, Yu Y, Yuan Z, et al. Neutrophil extracellular traps accelerate vascular smooth muscle cell proliferation via Akt/CDKN1b/TK1 accompanying with the occurrence of hypertension. J Hypertens. J Hypertens; 2022;40(10):2045–57. DOI: 10.1097/HJH.0000000000003231
266. Dong Y, Zhang Y, Yang X, Yan C, Feng Y. Recent Insights into Neutrophil Extracellular Traps in Cardiovascular Diseases. J Clin Med. J Clin Med; 2022;11(22). DOI: 10.3390/JCM11226662
267. Chrysanthopoulou A, Gkaliagkousi E, Lazaridis A, Arelaki S, Pateinakis P, Ntinopoulou M, et al. Angiotensin II triggers release of neutrophil extracellular traps, linking thromboinflammation with essential hypertension. JCI Insight. JCI Insight; 2021;6(18). DOI: 10.1172/JCI.INSIGHT.148668

268. Krishnan J, De La Visitación N, Hennen EM, Amarnath V, Harrison DG, Patrick DM. IsoLGs (Isolevuglandins) Drive Neutrophil Migration in Hypertension and Are Essential for the Formation of Neutrophil Extracellular Traps. Hypertension. Hypertension; 2022;79(8):1644–55. DOI: 10.1161/HYPERTENSIONAHA.122.19305
269. Namin SS, Zhu YP, Croker BA, Tan Z. Turning Neutrophil Cell Death Deadly in the Context of Hypertensive Vascular Disease. Can J Cardiol. Can J Cardiol; 2024;40(12):2356–67. DOI: 10.1016/J.CJCA.2024.09.015
270. Morton J, Coles B, Wright K, Gallimore A, Morrow JD, Terry ES, et al. Circulating neutrophils maintain physiological blood pressure by suppressing bacteria and IFNgamma-dependent iNOS expression in the vasculature of healthy mice. Blood. Blood; 2008;111(10):5187–94. DOI: 10.1182/BLOOD-2007-10-117283
271. Blanco-Camarillo C, Alemán OR, Rosales C. Low-Density Neutrophils in Healthy Individuals Display a Mature Primed Phenotype. Front Immunol. Frontiers Media SA; 2021;12:672520. DOI: 10.3389/FIMMU.2021.672520/FULL
272. Al-Sharea A, Lee MKS, Whillas A, Michell DL, Shihata WA, Nicholls AJ, et al. Chronic sympathetic driven hypertension promotes atherosclerosis by enhancing hematopoiesis. Haematologica. Ferrata Storti Foundation; 2019;104(3):456–67. DOI: 10.3324/HAEMATOL.2018.192898,
273. Yang X, Ma Y, Chen X, Zhu J, Xue W, Ning K. Mechanisms of neutrophil extracellular trap in chronic inflammation of endothelium in atherosclerosis. Life Sci. Pergamon; 2023;328:121867. DOI: 10.1016/J.LFS.2023.121867
274. Sorvillo N, Cherpokova D, Martinod K, Wagner DD. Extracellular DNA NET-Works With Dire Consequences for Health. Circ Res. Circ Res; 2019;125(4):470–88. DOI: 10.1161/CIRCRESAHA.119.314581
275. Ambler WG, Kaplan MJ. Vascular damage in systemic lupus erythematosus. Nat Rev Nephrol. Nat Rev Nephrol; 2024;20(4):251–65. DOI: 10.1038/S41581-023-00797-8
276. Zhang H, Wang Y, Qu M, Li W, Wu D, Cata JP, et al. Neutrophil, neutrophil extracellular traps and endothelial cell dysfunction in sepsis. Clin Transl Med. John Wiley & Sons, Ltd; 2023;13(1):e1170. DOI: 10.1002/CTM2.1170
277. Yu S, Liu J, Yan N. Endothelial Dysfunction Induced by Extracellular Neutrophil Traps Plays Important Role in the Occurrence and Treatment of Extracellular Neutrophil Traps-Related Disease. Int J Mol Sci. Int J Mol Sci; 2022;23(10). DOI: 10.3390/IJMS23105626
278. Arai Y, Yamashita K, Kuriyama K, Shiokawa M, Kodama Y, Sakurai T, et al. Plasmacytoid Dendritic Cell Activation and IFN-α Production Are Prominent Features of Murine Autoimmune Pancreatitis and Human IgG4-Related Autoimmune Pancreatitis. J Immunol. J Immunol; 2015;195(7):3033–44. DOI: 10.4049/JIMMUNOL.1500971
279. Incalza MA, D'Oria R, Natalicchio A, Perrini S, Laviola L, Giorgino F. Oxidative stress and reactive oxygen species in endothelial dysfunction associated with cardiovascular and metabolic diseases. Vascul Pharmacol. Vascul Pharmacol; 2018;100:1–19. DOI: 10.1016/J.VPH.2017.05.005
280. Gupta AK, Joshi MB, Philippova M, Erne P, Hasler P, Hahn S, et al. Activated endothelial cells induce neutrophil extracellular traps and are susceptible to NETosis-mediated cell death. FEBS Lett. FEBS Lett; 2010;584(14):3193–7. DOI: 10.1016/J.FEBSLET.2010.06.006

281. Edfeldt K, Agerberth B, Rottenberg ME, Gudmundsson GH, Wang XB, Mandal K, et al. Involvement of the antimicrobial peptide LL-37 in human atherosclerosis. Arterioscler Thromb Vasc Biol. Arterioscler Thromb Vasc Biol; 2006;26(7):1551–7. DOI: 10.1161/01.ATV.0000223901.08459.57
282. Qi H, Yang S, Zhang L. Neutrophil Extracellular Traps and Endothelial Dysfunction in Atherosclerosis and Thrombosis. Front Immunol. Front Immunol; 2017;8(AUG). DOI: 10.3389/FIMMU.2017.00928
283. Campos J, Ponomaryov T, de Prendergast A, Whitworth K, Smith CW, Khan AO, et al. Neutrophil extracellular traps and inflammasomes cooperatively promote venous thrombosis in mice. Blood Adv. American Society of Hematology; 2021;5(9):2319–24. DOI: 10.1182/BLOODADVANCES.2020003377
284. Shahzad K, Bock F, Dong W, Wang H, Kopf S, Kohli S, et al. Nlrp3-inflammasome activation in non-myeloid-derived cells aggravates diabetic nephropathy. Kidney Int. Kidney Int; 2015;87(1):74–84. DOI: 10.1038/KI.2014.271
285. Gupta A, Singh K, Fatima S, Ambreen S, Zimmermann S, Younis R, et al. Neutrophil Extracellular Traps Promote NLRP3 Inflammasome Activation and Glomerular Endothelial Dysfunction in Diabetic Kidney Disease. Nutrients. Nutrients; 2022;14(14). DOI: 10.3390/NU14142965
286. Allam R, Darisipudi MN, Tschopp J, Anders HJ. Histones trigger sterile inflammation by activating the NLRP3 inflammasome. Eur J Immunol. Eur J Immunol; 2013;43(12):3336–42. DOI: 10.1002/EJI.201243224
287. Huang H, Evankovich J, Yan W, Nace G, Zhang L, Ross M, et al. Endogenous histones function as alarmins in sterile inflammatory liver injury through Toll-like receptor 9 in mice. Hepatology. Hepatology; 2011;54(3):999–1008. DOI: 10.1002/HEP.24501
288. Xu J, Zhang X, Monestier M, Esmon NL, Esmon CT. Extracellular histones are mediators of death through TLR2 and TLR4 in mouse fatal liver injury. J Immunol. J Immunol; 2011;187(5):2626–31. DOI: 10.4049/JIMMUNOL.1003930
289. Liu D, Yang P, Gao M, Yu T, Shi Y, Zhang M, et al. NLRP3 activation induced by neutrophil extracellular traps sustains inflammatory response in the diabetic wound. Clin Sci (Lond). Clin Sci (Lond); 2019;133(4):565–82. DOI: 10.1042/CS20180600
290. Morales-Primo AU, Becker I, Zamora-Chimal J. Neutrophil extracellular trap-associated molecules: a review on their immunophysiological and inflammatory roles. Int Rev Immunol. Int Rev Immunol; 2022;41(2):253–74. DOI: 10.1080/08830185.2021.1921174
291. Hansson GK, Hermansson A. The immune system in atherosclerosis. Nature Immunology 2011 12:3. Nature Publishing Group; 2011;12(3):204–12. DOI: 10.1038/ni.2001
292. Döring Y, Manthey HD, Drechsler M, Lievens D, Megens RTA, Soehnlein O, et al. Auto-antigenic protein-DNA complexes stimulate plasmacytoid dendritic cells to promote atherosclerosis. Circulation. Circulation; 2012;125(13):1673–83. DOI: 10.1161/CIRCULATIONAHA.111.046755
293. Kajana X, Caridi G, Bruschi M, Spinelli S, Lugani F, Ghiggeri GM, et al. The Crosstalk Between NETs and the Complement Cascade: An Overview in Nephrological Autoimmune Disease. Int J Mol Sci. Int J Mol Sci; 2025;26(6). DOI: 10.3390/IJMS26062789
294. Kessenbrock K, Krumbholz M, Schönermarck U, Back W, Gross WL, Werb Z, et al. Netting neutrophils in autoimmune small-vessel vasculitis. Nature Medicine 2009 15:6. Nature Publishing Group; 2009;15(6):623–5. DOI: 10.1038/nm.1959

295. Söderberg D, Segelmark M. Neutrophil Extracellular Traps in ANCA-Associated Vasculitis. Front Immunol. Front Immunol; 2016;7(JUN). DOI: 10.3389/FIMMU.2016.00256
296. Rubartelli A, Sozzani S, Maugeri N, Fafutis-Morris M, Delgado-Rizo V, Martínez-Guzmán MA, et al. Neutrophil extracellular Traps and its implications in inflammation: An Overview. Neutrophil Extracellular Traps and Its Implications in Inflammation: An Overview Front Immunol. 2017;8:81. DOI: 10.3389/fimmu.2017.00081
297. Pieterse E, Rother N, Garsen M, Hofstra JM, Satchell SC, Hoffmann M, et al. Neutrophil Extracellular Traps Drive Endothelial-to-Mesenchymal Transition. Arterioscler Thromb Vasc Biol. Arterioscler Thromb Vasc Biol; 2017;37(7):1371–9. DOI: 10.1161/ATVBAHA.117.309002
298. Kumar SVR, Kulkarni OP, Mulay SR, Darisipudi MN, Romoli S, Thomasova D, et al. Neutrophil Extracellular Trap-Related Extracellular Histones Cause Vascular Necrosis in Severe GN. J Am Soc Nephrol. J Am Soc Nephrol; 2015;26(10):2399–413. DOI: 10.1681/ASN.2014070673
299. Saffarzadeh M, Juenemann C, Queisser MA, Lochnit G, Barreto G, Galuska SP, et al. Hartl D, editor. Neutrophil Extracellular Traps Directly Induce Epithelial and Endothelial Cell Death: A Predominant Role of Histones. PLoS One. Public Library of Science; 2012;7(2):e32366. DOI: 10.1371/journal.pone.0032366
300. Villanueva E, Yalavarthi S, Berthier CC, Hodgin JB, Khandpur R, Lin AM, et al. Netting Neutrophils Induce Endothelial Damage, Infiltrate Tissues, and Expose Immunostimulatory Molecules in Systemic Lupus Erythematosus. The Journal of Immunology. American Association of Immunologists; 2011;187(1):538–52. DOI: 10.4049/JIMMUNOL.1100450
301. Meegan JE, Yang X, Beard RS, Jannaway M, Chatterjee V, Taylor-Clark TE, et al. Citrullinated Histone 3 Causes Endothelial Barrier Dysfunction. Biochem Biophys Res Commun. Elsevier B.V.; 2018;503(3):1498. DOI: 10.1016/J.BBRC.2018.07.069
302. Sternlicht MD, Werb Z. How matrix metalloproteinases regulate cell behavior. Annu Rev Cell Dev Biol. Annu Rev Cell Dev Biol; 2001;17:463–516. DOI: 10.1146/ANNUREV.CELLBIO.17.1.463
303. Carmona-Rivera C, Zhao W, Yalavarthi S, Kaplan MJ. Neutrophil extracellular traps induce endothelial dysfunction in systemic lupus erythematosus through the activation of matrix metalloproteinase-2. Ann Rheum Dis. Ann Rheum Dis; 2015;74(7):1417–24. DOI: 10.1136/ANNRHEUMDIS-2013-204837
304. Jackson PL, Xu X, Wilson L, Weathington NM, Clancy JP, Blalock JE, et al. Human neutrophil elastase-mediated cleavage sites of MMP-9 and TIMP-1: implications to cystic fibrosis proteolytic dysfunction. Mol Med. Mol Med; 2010;16(5–6):159–66. DOI: 10.2119/MOLMED.2009.00109
305. Wiedow O, Meyer-Hoffert U. Neutrophil serine proteases: potential key regulators of cell signalling during inflammation. J Intern Med. J Intern Med; 2005;257(4):319–28. DOI: 10.1111/J.1365-2796.2005.01476.X
306. Chu AJ. Tissue factor mediates inflammation. Arch Biochem Biophys. Arch Biochem Biophys; 2005;440(2):123–32. DOI: 10.1016/J.ABB.2005.06.005

307. Gora IM, Ciechanowska A, Ladyzynski P, Gora IM, Ciechanowska A, Ladyzynski P. NLRP3 Inflammasome at the Interface of Inflammation, Endothelial Dysfunction, and Type 2 Diabetes. Cells 2021, Vol 10,. Multidisciplinary Digital Publishing Institute; 2021;10(2):1–29. DOI: 10.3390/CELLS10020314
308. Thai T, Zhong F, Dang L, Chan E, Ku J, Malle E, et al. Endothelial-transcytosed myeloperoxidase activates endothelial nitric oxide synthase via a phospholipase C-dependent calcium signaling pathway. Free Radic Biol Med. Free Radic Biol Med; 2021;166:255–64. DOI: 10.1016/J.FREERADBIOMED.2020.12.448
309. Etwebi Z, Landesberg G, Preston K, Eguchi S, Scalia R. Mechanistic Role of the Calcium-Dependent Protease Calpain in the Endothelial Dysfunction Induced by MPO (Myeloperoxidase). Hypertension. Hypertension; 2018;71(4):761–70. DOI: 10.1161/HYPERTENSIONAHA.117.10305
310. Knight JS, Subramanian V, O'dell AA, Yalavarthi S, Zhao W, Smith CK, et al. Peptidylarginine deiminase inhibition disrupts NET formation and protects against kidney, skin and vascular disease in lupus-prone MRL/lpr mice HHS Public Access. Ann Rheum Dis. 2015;74(12):2199–206. DOI: 10.1136/annrheumdis-2014-205365
311. Schommer N, Gendron N, Krauel K, Van Bruggen S, Jarrot P-A, Maier A, et al. Neutrophil extracellular traps and peptidylarginine deiminase 4–mediated inflammasome activation link diabetes to cardiorenal injury and heart failure. Eur Heart J. 2025; DOI: 10.1093/EURHEARTJ/EHAF963
312. Rossman MJ, Kaplon RE, Hill SD, McNamara MN, Santos-Parker JR, Pierce GL, et al. Endothelial cell senescence with aging in healthy humans: prevention by habitual exercise and relation to vascular endothelial function. Am J Physiol Heart Circ Physiol. Am J Physiol Heart Circ Physiol; 2017;313(5):H890–5. DOI: 10.1152/AJPHEART.00416.2017
313. Gandhi M, Haider S, Chang HZY, Kazlauskas A, Gandhi M, Haider S, et al. The Role of Endothelial Senescence in the Pathogenesis of Diabetic Retinopathy. International Journal of Molecular Sciences 2025, Vol 26,. Multidisciplinary Digital Publishing Institute; 2025;26(11). DOI: 10.3390/IJMS26115211
314. Chien Y, Scuoppo C, Wang X, Fang X, Balgley B, Bolden JE, et al. Control of the senescence-associated secretory phenotype by NF-κB promotes senescence and enhances chemosensitivity. Genes Dev. Genes Dev; 2011;25(20):2125–36. DOI: 10.1101/GAD.17276711
315. Acosta JC, Banito A, Wuestefeld T, Georgilis A, Janich P, Morton JP, et al. A complex secretory program orchestrated by the inflammasome controls paracrine senescence. Nature Cell Biology 2013 15:8. Nature Publishing Group; 2013;15(8):978–90. DOI: 10.1038/ncb2784
316. Van Deursen JM. The role of senescent cells in ageing. Nature 2014 509:7501. Nature Publishing Group; 2014;509(7501):439–46. DOI: 10.1038/nature13193
317. Di Micco R, Krizhanovsky V, Baker D, d'Adda di Fagagna F. Cellular senescence in ageing: from mechanisms to therapeutic opportunities. Nature Reviews Molecular Cell Biology 2020 22:2. Nature Publishing Group; 2020;22(2):75–95. DOI: 10.1038/s41580-020-00314-w
318. Donato AJ, Morgan RG, Walker AE, Lesniewski LA. Cellular and molecular biology of aging endothelial cells. J Mol Cell Cardiol. J Mol Cell Cardiol; 2015;89(Pt B):122–35. DOI: 10.1016/J.YJMCC.2015.01.021

319. Lähteenvuo J, Rosenzweig A. Effects of aging on angiogenesis. Circ Res. Circ Res; 2012;110(9):1252–63. DOI: 10.1161/CIRCRESAHA.111.246116
320. Hoffmann J, Haendeler J, Aicher A, Rössig L, Vasa M, Zeiher AM, et al. Aging enhances the sensitivity of endothelial cells toward apoptotic stimuli: Important role of nitric oxide. Circ Res. Lippincott Williams and Wilkins; 2001;89(8):709–15. DOI: 10.1161/HH2001.097796/ASSET/B0BA74BE-FF5E-49F3-9E47-009BE14C6D87/ASSETS/GRAPHIC/G11FF6.JPEG
321. Graves SI, Baker DJ. Implicating endothelial cell senescence to dysfunction in the ageing and diseased brain. Basic Clin Pharmacol Toxicol. Basic Clin Pharmacol Toxicol; 2020;127(2):102–10. DOI: 10.1111/BCPT.13403
322. Taddei S, Virdis A, Ghiadoni L, Versari D, Salvetti A. Endothelium, aging, and hypertension. Curr Hypertens Rep. Curr Hypertens Rep; 2006;8(1):84–9. DOI: 10.1007/S11906-006-0045-4
323. Han Y, Kim SY. Endothelial senescence in vascular diseases: current understanding and future opportunities in senotherapeutics. Experimental & Molecular Medicine 2022 55:1. Nature Publishing Group; 2023;55(1):1–12. DOI: 10.1038/s12276-022-00906-w
324. Zieman SJ, Melenovsky V, Kass DA. Mechanisms, pathophysiology, and therapy of arterial stiffness. Arterioscler Thromb Vasc Biol. Arterioscler Thromb Vasc Biol; 2005;25(5):932–43. DOI: 10.1161/01.ATV.0000160548.78317.29
325. Li Z, Li Z, Hu Y, Xie Y, Shi Y, Chen G, et al. Neutrophil extracellular traps potentiate effector T cells via endothelial senescence in uveitis. JCI Insight. JCI Insight; 2025;10(2). DOI: 10.1172/JCI.INSIGHT.180248
326. Zhu S, Yu Y, Hong Q, Li C, Zhang H, Guo K. Neutrophil Extracellular Traps Upregulate p21 and Suppress Cell Cycle Progression to Impair Endothelial Regeneration after Inflammatory Lung Injury. J Clin Med. 2024;13(5). DOI: 10.3390/jcm13051204
327. Binet F, Cagnone G, Crespo-Garcia S, Hata M, Neault M, Dejda A, et al. Neutrophil extracellular traps target senescent vasculature for tissue remodeling in retinopathy. Science (1979). American Association for the Advancement of Science; 2020;369(6506). DOI: 10.1126/SCIENCE.AAY5356/SUPPL_FILE/AAY5356-BINET-SM.PDF
328. Chen XL, Sun L, Xuan K, Zong A. The role of immune mechanisms in hypertension and advances in immunomodulatory research. Clin Exp Hypertens. Clin Exp Hypertens; 2025;47(1). DOI: 10.1080/10641963.2025.2535328
329. Nakazawa D, Kumar S V., Marschner J, Desai J, Holderied A, Rath L, et al. Histones and neutrophil extracellular traps enhance tubular necrosis and remote organ injury in ischemic AKI. Journal of the American Society of Nephrology. American Society of Nephrology; 2017;28(6):1753–68. DOI: 10.1681/ASN.2016080925/-/DCSUPPLEMENTAL
330. Amend SR, Valkenburg KC, Pienta KJ. Murine Hind Limb Long Bone Dissection and Bone Marrow Isolation. J Vis Exp. J Vis Exp; 2016;2016(110). DOI: 10.3791/53936
331. Collins SJ, Ruscetti FW, Gallagher RE, Gallo RC. Terminal differentiation of human promyelocytic leukemia cells induced by dimethyl sulfoxide and other polar compounds. Proc Natl Acad Sci U S A. Proc Natl Acad Sci U S A; 1978;75(5):2458–62. DOI: 10.1073/PNAS.75.5.2458
332. Berg S, Kutra D, Kroeger T, Straehle CN, Kausler BX, Haubold C, et al. ilastik: interactive machine learning for (bio)image analysis. Nat Methods. Nat Methods; 2019;16(12):1226–32. DOI: 10.1038/S41592-019-0582-9

333. Stirling DR, Swain-Bowden MJ, Lucas AM, Carpenter AE, Cimini BA, Goodman A. CellProfiler 4: improvements in speed, utility and usability. BMC Bioinformatics. BMC Bioinformatics; 2021;22(1). DOI: 10.1186/S12859-021-04344-9
334. Stirling DR, Carpenter AE, Cimini BA. CellProfiler Analyst 3.0: accessible data exploration and machine learning for image analysis. Bioinformatics. Bioinformatics; 2021;37(21):3992–4. DOI: 10.1093/BIOINFORMATICS/BTAB634
335. Wang J, Zhou X, Yu P, Yao J, Guo P, Xu Q, et al. A transcriptome-based human universal senescence index (hUSI) robustly predicts cellular senescence under various conditions. Nature Aging 2025 5:6. Nature Publishing Group; 2025;5(6):1159–75. DOI: 10.1038/s43587-025-00886-2
336. Henneck T, Krüger C, Nerlich A, Langer M, Fingerhut L, Bonilla MC, et al. Comparison of NET quantification methods based on immunofluorescence microscopy: Hand-counting, semi-automated and automated evaluations. Heliyon. Elsevier; 2023;9(6):e16982. DOI: 10.1016/J.HELIYON.2023.E16982
337. Criminisi A, Shotton J, Konukoglu E. Decision Forests: A Unified Framework for Classification, Regression, Density Estimation, Manifold Learning and Semi-Supervised Learning. Foundations and Trends® in Computer Graphics and Vision. Now Publishers, Inc.; 2012;7(2–3):81–227. DOI: 10.1561/0600000035
338. Ramasamy R, Maqbool M, Mohamed AL, Noah RM. Elevated neutrophil respiratory burst activity in essential hypertensive patients. Cell Immunol. Cell Immunol; 2010;263(2):230–4. DOI: 10.1016/J.CELLIMM.2010.04.004
339. Lazaridis A, Malliora A, Natsi A-M, Papadopoulos V, Antoniadou C, Gavriilidis E, et al. HYPERTENSION RELATED NETOSIS IS STRONGLY DEPENDENT ON NIGHTTIME BLOOD PRESSURE IN A COHORT OF NEWLY DIAGNOSED, TREATMENT NAÏVE HYPERTENSIVE PATIENTS. J Hypertens. Ovid Technologies (Wolters Kluwer Health); 2024;42(Suppl 1):e247. DOI: 10.1097/01.HJH.0001022016.94433.EA
340. Mattson DL. Infiltrating immune cells in the kidney in salt-sensitive hypertension and renal injury. Am J Physiol Renal Physiol. Am J Physiol Renal Physiol; 2014;307(5). DOI: 10.1152/AJPRENAL.00258.2014
341. Norlander AE, Madhur MS, Harrison DG. The immunology of hypertension. J Exp Med. J Exp Med; 2018;215(1):21–33. DOI: 10.1084/JEM.20171773
342. Lu X, Crowley SD. Actions of immune cells in the hypertensive kidney. Curr Opin Nephrol Hypertens. Lippincott Williams and Wilkins; 2020;29(5):515–22. DOI: 10.1097/MNH.0000000000000635
343. Zhang Y, Li C, Jiang Q, Jiang Y, Xu G, Kao G, et al. Unraveling neutrophil extracellular traps: A new frontier in kidney disease therapy. Life Sci. Pergamon; 2025;379:123892. DOI: 10.1016/J.LFS.2025.123892
344. Cambier L, Giani JF, Liu W, Ijichi T, Echavez AK, Valle J, et al. Angiotensin II-Induced End-Organ Damage in Mice Is Attenuated by Human Exosomes and by an Exosomal y RNA Fragment. Hypertension. Lippincott Williams and Wilkins; 2018;72(2):370–80. DOI: 10.1161/HYPERTENSIONAHA.118.11239/SUPPL_FILE/HYP_HYPE201811239D_SUPP1.PDF

345. Crowley SD, Gurley SB, Herrera MJ, Ruiz P, Griffiths R, Kumar AP, et al. Angiotensin II causes hypertension and cardiac hypertrophy through its receptors in the kidney. Proc Natl Acad Sci U S A. Proc Natl Acad Sci U S A; 2006;103(47):17985–90. DOI: 10.1073/PNAS.0605545103
346. Eghbalzadeh K, Georgi L, Louis T, Zhao H, Keser U, Weber C, et al. Compromised Anti-inflammatory Action of Neutrophil Extracellular Traps in PAD4-Deficient Mice Contributes to Aggravated Acute Inflammation After Myocardial Infarction. Front Immunol. Front Immunol; 2019;10. DOI: 10.3389/FIMMU.2019.02313
347. Peter JK, Umene R, Wu CH, Nakamura Y, Washimine N, Yamamoto R, et al. Macrophage depletion lowers blood pressure and reduces renal fibrosis progression in existing hypertension mice model. J Physiol Sci. J Physiol Sci; 2025;75(3). DOI: 10.1016/J.JPHYSS.2025.100049
348. Peter JK, Umene R, Wu CH, Nakamura Y, Washimine N, Yamamoto R, et al. Renal macrophages induce hypertension and kidney fibrosis in Angiotensin II salt mice model. Biochem Biophys Res Commun. Academic Press; 2024;715:149997. DOI: 10.1016/J.BBRC.2024.149997
349. Liao TD, Yang XP, Liu YH, Shesely EG, Cavasin MA, Kuziel WA, et al. Role of inflammation in the development of renal damage and dysfunction in angiotensin II-induced hypertension. Hypertension. Lippincott Williams & Wilkins; 2008;52(2):256–63. DOI: 10.1161/HYPERTENSIONAHA.108.112706/ASSET/86E600C9-7CDD-4769-8C8D-F113BC87886F/ASSETS/GRAPHIC/34FF8.JPEG
350. Nakazawa D, Masuda S, Nishibata Y, Watanabe-Kusunoki K, Tomaru U, Ishizu A. Neutrophils and NETs in kidney disease. Nature Reviews Nephrology 2025 21:6. Nature Publishing Group; 2025;21(6):383–98. DOI: 10.1038/s41581-025-00944-3
351. Chen Y, Tetz ZA, Zeng X, Go SJ, Ouyang W, Lee KE, et al. CitH3, a Druggable Biomarker for Human Diseases Associated with Acute NETosis and Chronic Immune Dysfunction. Pharmaceutics. Pharmaceutics; 2025;17(7). DOI: 10.3390/PHARMACEUTICS17070809
352. Zhang F, Xia Y, Su J, Quan F, Zhou H, Li Q, et al. Neutrophil diversity and function in health and disease. Signal Transduction and Targeted Therapy 2024 9:1. Nature Publishing Group; 2024;9(1):343-. DOI: 10.1038/s41392-024-02049-y
353. Ozel I, Duerig I, Domnich M, Lang S, Pylaeva E, Jablonska J, et al. The Good, the Bad, and the Ugly: Neutrophils, Angiogenesis, and Cancer. Cancers 2022, Vol 14,. Multidisciplinary Digital Publishing Institute; 2022;14(3):536. DOI: 10.3390/CANCERS14030536
354. Zhu S, Yu Y, Ren Y, Xu L, Wang H, Ling X, et al. The emerging roles of neutrophil extracellular traps in wound healing. Cell Death & Disease 2021 12:11. Nature Publishing Group; 2021;12(11):984-. DOI: 10.1038/s41419-021-04294-3
355. Kang L, Yu H, Yang X, Zhu Y, Bai X, Wang R, et al. Neutrophil extracellular traps released by neutrophils impair revascularization and vascular remodeling after stroke. Nat Commun. Nat Commun; 2020;11(1). DOI: 10.1038/S41467-020-16191-Y
356. Folco EJ, Mawson TL, Vromman A, Bernardes-Souza B, Franck G, Persson O, et al. Neutrophil extracellular traps induce endothelial cell activation and tissue factor production through interleukin-1α and cathepsin G. Arterioscler Thromb Vasc Biol. Lippincott Williams and Wilkins; 2018;38(8):1901–12. DOI: 10.1161/ATVBAHA.118.311150/FORMAT/EPUB

357. Zhao P, Zhu J, Bai L, Ma W, Li F, Zhang C, et al. Neutrophil extracellular traps induce pyroptosis of pulmonary microvascular endothelial cells by activating the NLRP3 inflammasome. Clin Exp Immunol. Clin Exp Immunol; 2024;217(1):89–98. DOI: 10.1093/CEI/UXAE028
358. Wang J, Li L, Xu J, Gheyret D, Li K, Zhang X, et al. Neutrophil extracellular traps induce endothelial damage and exacerbate vasospasm in traumatic brain injury. Theranostics. Ivyspring International Publisher; 2025;15(17):9221–39. DOI: 10.7150/THNO.115746
359. Koga T, Morotomi-Yano K, Sakugawa T, Saitoh H, Yano K ichi. Nanosecond pulsed electric fields induce extracellular release of chromosomal DNA and histone citrullination in neutrophil-differentiated HL-60 cells. Scientific Reports 2019 9:1. Nature Publishing Group; 2019;9(1):8451-. DOI: 10.1038/s41598-019-44817-9
360. Kumari R, Jat P. Mechanisms of Cellular Senescence: Cell Cycle Arrest and Senescence Associated Secretory Phenotype. Front Cell Dev Biol. Frontiers Media S.A.; 2021;9:645593. DOI: 10.3389/FCELL.2021.645593/XML
361. Gire V, Dulic V. Senescence from G2 arrest, revisited. Cell Cycle. Cell Cycle; 2015;14(3):297–304. DOI: 10.1080/15384101.2014.1000134
362. Wang B, Han J, Elisseeff JH, Demaria M. The senescence-associated secretory phenotype and its physiological and pathological implications. Nat Rev Mol Cell Biol. Nat Rev Mol Cell Biol; 2024;25(12):958–78. DOI: 10.1038/S41580-024-00727-X
363. Coppé JP, Desprez PY, Krtolica A, Campisi J. The Senescence-Associated Secretory Phenotype: The Dark Side of Tumor Suppression. Annu Rev Pathol. 2010;5:99. DOI: 10.1146/ANNUREV-PATHOL-121808-102144
364. Honda S, Ikeda K, Urata R, Yamazaki E, Emoto N, Matoba S. Cellular senescence promotes endothelial activation through epigenetic alteration, and consequently accelerates atherosclerosis. Scientific Reports 2021 11:1. Nature Publishing Group; 2021;11(1):14608-. DOI: 10.1038/s41598-021-94097-5
365. El-Osta A. Transcriptional Control of Endothelial Senescence and Vascular Repair. Circ Res. Lippincott Williams & WilkinsHagerstown, MD; 2023;133(10):858–60. DOI: 10.1161/CIRCRESAHA.123.323716
366. Ajoolabady A, Pratico D, Bahijri S, Tuomilehto J, Uversky VN, Ren J. Hallmarks of cellular senescence: biology, mechanisms, regulations. Experimental & Molecular Medicine 2025 57:7. Nature Publishing Group; 2025;57(7):1482–91. DOI: 10.1038/s12276-025-01480-7
367. Liu Y, Beyer A, Aebersold R. On the Dependency of Cellular Protein Levels on mRNA Abundance. Cell. Cell; 2016;165(3):535–50. DOI: 10.1016/J.CELL.2016.03.014
368. Dimri GP, Lee X, Basile G, Acosta M, Scott G, Roskelley C, et al. A biomarker that identifies senescent human cells in culture and in aging skin in vivo. Proc Natl Acad Sci U S A. National Academy of Sciences; 1995;92(20):9363. DOI: 10.1073/PNAS.92.20.9363
369. Neubert E, Meyer D, Rocca F, Günay G, Kwaczala-Tessmann A, Grandke J, et al. Chromatin swelling drives neutrophil extracellular trap release. Nature Communications 2018 9:1. Nature Publishing Group; 2018;9(1):3767-. DOI: 10.1038/s41467-018-06263-5
370. Jiang D, Saffarzadeh M, Scharffetter-Kochanek K. In vitro Demonstration and Quantification of Neutrophil Extracellular Trap Formation. Bio Protoc. 2017;7(13):e2386. DOI: 10.21769/BioProtoc.2386

371. Val S, Krueger A, Hussain A, Tomney A, Chen Y, Lazarski C, et al. MUC5B induces in vitro neutrophil extracellular trap formation: Implication in otitis media. Laryngoscope Investig Otolaryngol. 2020;5(3):536–45. DOI: 10.1002/lio2.396
372. Moussavi-Harami SF, Mladinich KM, Sackmann EK, Shelef MA, Starnes TW, Guckenberger DJ, et al. Microfluidic device for simultaneous analysis of neutrophil extracellular traps and production of reactive oxygen species. Integrative Biology. 2016;8(2):243–52. DOI: 10.1039/C5IB00225G
373. Yu F, Chen J, Zhang X, Ma Z, Wang J, Wu Q. Role of Neutrophil Extracellular Traps in Hypertension and Their Impact on Target Organs. Journal of Clinical Hypertension John Wiley and Sons Inc; 2024.
374. Senda A, Sasai R, Kato K, Nishibata Y, Masuda S, Ishizu A, et al. Involvement of neutrophil extracellular traps in the pathogenesis of glomerulonephritis in a case of systemic lupus erythematosus and antineutrophil cytoplasmic antibody-associated vasculitis overlap syndrome. CEN Case Rep. CEN Case Rep; 2022;11(3):339–46. DOI: 10.1007/S13730-021-00682-Y
375. Leffler J, Gullstrand B, Jönsen A, Nilsson JÅ, Martin M, Blom AM, et al. Degradation of neutrophil extracellular traps co-varies with disease activity in patients with systemic lupus erythematosus. Arthritis Res Ther. Arthritis Res Ther; 2013;15(4). DOI: 10.1186/AR4264
376. Bengtsson AM, Blom Tydén C, Lood L, Truedsson AAJ, Leffler M, Martin B, et al. Disease Activate Complement Exacerbating the Degraded in Systemic Lupus Erythematosus Neutrophil Extracellular Traps That Are Not. 2018; DOI: 10.4049/jimmunol.1102404
377. Coylewright M, Reckelhoff JF, Ouyang P. Menopause and hypertension: An age-old debate. Hypertension. Lippincott Williams & Wilkins; 2008;51(4 PART 2 SUPPL.):952–9. DOI: 10.1161/HYPERTENSIONAHA.107.105742/ASSET/2A31D8D6-95FC-4AD9-AF52-B69C7FD42C38/ASSETS/GRAPHIC/38FF2.JPEG
378. Reckelhoff JF. Gender differences in the regulation of blood pressure. Hypertension. Lippincott Williams and Wilkins; 2001;37(5):1199–208. DOI: 10.1161/01.HYP.37.5.1199/ASSET/2F1E1260-892A-4BE1-8F59-89777DF33697/ASSETS/GRAPHIC/HY0511628010.JPEG
379. Medina D, Mehay D, Arnold AC. Sex differences in cardiovascular actions of the renin-angiotensin system. Clin Auton Res. Clin Auton Res; 2020;30(5):393–408. DOI: 10.1007/S10286-020-00720-2
380. Comeau KD, Shokoples BG, Schiffrin EL. Sex Differences in the Immune System in Relation to Hypertension and Vascular Disease. Can J Cardiol. Can J Cardiol; 2022;38(12):1828–43. DOI: 10.1016/J.CJCA.2022.05.010
381. Nwia SM, Leite APO, Li XC, Zhuo JL. Sex differences in the renin-angiotensin-aldosterone system and its roles in hypertension, cardiovascular, and kidney diseases. Front Cardiovasc Med. Frontiers Media SA; 2023;10:1198090. DOI: 10.3389/FCVM.2023.1198090/XML
382. Colafella KMM, Denton KM. Sex-specific differences in hypertension and associated cardiovascular disease. Nat Rev Nephrol. Nat Rev Nephrol; 2018;14(3):185–201. DOI: 10.1038/NRNEPH.2017.189

383. Zimmerman MA, Baban B, Tipton AJ, O'Connor PM, Sullivan JC. Chronic ANG II infusion induces sex-specific increases in renal T cells in Sprague-Dawley rats. Am J Physiol Renal Physiol. American Physiological Society; 2015;308(7):F706–12. DOI: 10.1152/AJPRENAL.00446.2014/ASSET/IMAGES/LARGE/ZH20041575190003.JPEG
384. Song C, Li H, Mao Z, Peng L, Liu B, Lin F, et al. Delayed neutrophil apoptosis may enhance NET formation in ARDS. Respir Res. Respir Res; 2022;23(1). DOI: 10.1186/S12931-022-02065-Y
385. Gray RD, Hardisty G, Regan KH, Smith M, Robb CT, Duffin R, et al. Delayed neutrophil apoptosis enhances NET formation in cystic fibrosis. Thorax. Thorax; 2018;73(2):134–44. DOI: 10.1136/THORAXJNL-2017-210134
386. Allam R, Scherbaum CR, Darisipudi MN, Mulay SR, Hägele H, Lichtnekert J, et al. Histones from dying renal cells aggravate kidney injury via TLR2 and TLR4. Journal of the American Society of Nephrology. American Society of Nephrology; 2012;23(8):1375–88. DOI: 10.1681/ASN.2011111077/-/DCSUPPLEMENTAL
387. Zhuang S, Xia S, Huang P, Wu J, Qu J, Chen R, et al. Targeting P2RX1 alleviates renal ischemia/reperfusion injury by preserving mitochondrial dynamics. Pharmacol Res. Pharmacol Res; 2021;170. DOI: 10.1016/J.PHRS.2021.105712
388. Ballesteros I, Rubio-Ponce A, Genua M, Lusito E, Kwok I, Fernández-Calvo G, et al. Co-option of Neutrophil Fates by Tissue Environments. Cell. Cell Press; 2020;183(5):1282-1297.e18. DOI: 10.1016/J.CELL.2020.10.003
389. Adrover JM, Nicolás-Ávila JA, Hidalgo A. Aging: A Temporal Dimension for Neutrophils. Trends Immunol. Elsevier Current Trends; 2016;37(5):334–45. DOI: 10.1016/J.IT.2016.03.005
390. Montaniel KRC, Harrison DG. Is Hypertension a Bone Marrow Disease? Circulation. Lippincott Williams and Wilkins; 2016;134(18):1369–72. DOI: 10.1161/CIRCULATIONAHA.116.024520,
391. Maier-Begandt D, consortium on behalf of the T, Alonso-Gonzalez N, consortium on behalf of the T, Klotz L, consortium on behalf of the T, et al. Neutrophils—biology and diversity. Nephrology Dialysis Transplantation. Oxford Academic; 2024;39(10):1551–64. DOI: 10.1093/NDT/GFAD266
392. Young CN, Davisson RL. Angiotensin-II, the brain, and hypertension: An update. Hypertension. Lippincott Williams and Wilkins; 2015;66(5):920–6. DOI: 10.1161/HYPERTENSIONAHA.115.03624/ASSET/7EEBCD3B-10E2-48AC-953F-7EADE30A03CF/ASSETS/GRAPHIC/920FIG01.JPEG
393. Grassi G, Ram VS. Evidence for a critical role of the sympathetic nervous system in hypertension. J Am Soc Hypertens. J Am Soc Hypertens; 2016;10(5):457–66. DOI: 10.1016/J.JASH.2016.02.015
394. Felkle D, Jarczyński M, Kaleta K, Zięba K, Nazimek K. The immunomodulatory effects of antihypertensive therapy: A review. Biomed Pharmacother. Biomed Pharmacother; 2022;153. DOI: 10.1016/J.BIOPHA.2022.113287
395. Hennen EM, Uppuganti S, de la Visitación N, Chen W, Krishnan J, Vecchi LA, et al. Hypertension promotes bone loss and fragility by favoring bone resorption in mouse models. J Clin Invest. American Society for Clinical Investigation; 2025;135(20). DOI: 10.1172/JCI184325

396. Pérez-Olivares L, Soehnlein O, Pérez-Olivares L, Soehnlein O. Contemporary Lifestyle and Neutrophil Extracellular Traps: An Emerging Link in Atherosclerosis Disease. Cells 2021, Vol 10,. Multidisciplinary Digital Publishing Institute; 2021;10(8). DOI: 10.3390/CELLS10081985
397. Nabah YNA, Mateo T, Estellés R, Mata M, Zagorski J, Sarau H, et al. Angiotensin II induces neutrophil accumulation in vivo through generation and release of CXC chemokines. Circulation. Circulation; 2004;110(23):3581–6. DOI: 10.1161/01.CIR.0000148824.93600.F3
398. Thiama HR, Wong SL, Qiu R, Kittisopikul M, Vahabikashi A, Goldman AE, et al. NETosis proceeds by cytoskeleton and endomembrane disassembly and PAD4-mediated chromatin decondensation and nuclear envelope rupture. Proc Natl Acad Sci U S A. National Academy of Sciences; 2020;117(13):7326–37. DOI: 10.1073/PNAS.1909546117/SUPPL_FILE/PNAS.1909546117.SM22.AVI
399. Wong SL, Wagner DD. Peptidylarginine deiminase 4: a nuclear button triggering neutrophil extracellular traps in inflammatory diseases and aging. FASEB J. FASEB J; 2018;32(12):6358–70. DOI: 10.1096/FJ.201800691R
400. Guiducci E, Lemberg C, Küng N, Schraner E, Theocharides APA, LeibundGut-Landmann S. Candida albicans-Induced NETosis Is Independent of Peptidylarginine Deiminase 4. Front Immunol. Front Immunol; 2018;9(JUL). DOI: 10.3389/FIMMU.2018.01573
401. Yang X, Li L, Liu J, Lv B, Chen F. Extracellular histones induce tissue factor expression in vascular endothelial cells via TLR and activation of NF-κB and AP-1. Thromb Res. Pergamon; 2016;137:211–8. DOI: 10.1016/J.THROMRES.2015.10.012
402. Xu J, Zhang X, Pelayo R, Monestier M, Ammollo CT, Semeraro F, et al. Extracellular histones are major mediators of death in sepsis. Nat Med. Nat Med; 2009;15(11):1318–21. DOI: 10.1038/NM.2053
403. Engeland K. Cell cycle arrest through indirect transcriptional repression by p53: I have a DREAM. Cell Death & Differentiation 2018 25:1. Nature Publishing Group; 2017;25(1):114–32. DOI: 10.1038/cdd.2017.172
404. Abbas T, Dutta A. p21 in cancer: intricate networks and multiple activities. Nature Reviews Cancer 2009 9:6. Nature Publishing Group; 2009;9(6):400–14. DOI: 10.1038/nrc2657
405. Perkins ND. Integrating cell-signalling pathways with NF-κB and IKK function. Nature Reviews Molecular Cell Biology 2007 8:1. Nature Publishing Group; 2007;8(1):49–62. DOI: 10.1038/nrm2083
406. Hernandez-Segura A, Nehme J, Demaria M. Hallmarks of Cellular Senescence. Trends Cell Biol. Trends Cell Biol; 2018;28(6):436–53. DOI: 10.1016/J.TCB.2018.02.001
407. Coppé JP, Patil CK, Rodier F, Sun Y, Muñoz DP, Goldstein J, et al. Senescence-Associated Secretory Phenotypes Reveal Cell-Nonautonomous Functions of Oncogenic RAS and the p53 Tumor Suppressor. PLoS Biol. Public Library of Science; 2008;6(12):e301. DOI: 10.1371/JOURNAL.PBIO.0060301
408. Salama R, Sadaie M, Hoare M, Narita M. Cellular senescence and its effector programs. Genes Dev. Genes Dev; 2014;28(2):99–114. DOI: 10.1101/GAD.235184.113
409. Basisty N, Kale A, Jeon OH, Kuehnemann C, Payne T, Rao C, et al. A proteomic atlas of senescence-associated secretomes for aging biomarker development. PLoS Biol. Public Library of Science; 2020;18(1):e3000599. DOI: 10.1371/JOURNAL.PBIO.3000599

410. Xu M, Tchkonia T, Ding H, Ogrodnik M, Lubbers ER, Pirtskhalava T, et al. JAK inhibition alleviates the cellular senescence-associated secretory phenotype and frailty in old age. Proc Natl Acad Sci U S A. National Academy of Sciences; 2015;112(46):E6301–10. DOI: 10.1073/PNAS.1515386112/SUPPL_FILE/PNAS.201515386SI.PDF
411. Johmura Y, Shimada M, Misaki T, Naiki-Ito A, Miyoshi H, Motoyama N, et al. Necessary and sufficient role for a mitosis skip in senescence induction. Mol Cell. Mol Cell; 2014;55(1):73–84. DOI: 10.1016/J.MOLCEL.2014.05.003
412. Baus F, Gire V, Fisher D, Piette J, Dulić V. Permanent cell cycle exit in G2 phase after DNA damage in normal human fibroblasts. The EMBO Journal 2003 22:15. Springer; 2003;22(15):3992–4002. DOI: 10.1093/EMBOJ/CDG387
413. Santamaría D, Barrière C, Cerqueira A, Hunt S, Tardy C, Newton K, et al. Cdk1 is sufficient to drive the mammalian cell cycle. Nature. Nature; 2007;448(7155):811–5. DOI: 10.1038/NATURE06046
414. Driscoll DL, Chakravarty A, Bowman D, Shinde V, Lasky K, Shi J, et al. Plk1 Inhibition Causes Post-Mitotic DNA Damage and Senescence in a Range of Human Tumor Cell Lines. PLoS One. Public Library of Science; 2014;9(11):e111060. DOI: 10.1371/JOURNAL.PONE.0111060
415. Feringa FM, Raaijmakers JA, Hadders MA, Vaarting C, Macurek L, Heitink L, et al. Persistent repair intermediates induce senescence. Nature Communications 2018 9:1. Nature Publishing Group; 2018;9(1):3923-. DOI: 10.1038/s41467-018-06308-9
416. Coller HA, Sang L, Roberts JM. A New Description of Cellular Quiescence. PLoS Biol. Public Library of Science; 2006;4(3):e83. DOI: 10.1371/JOURNAL.PBIO.0040083
417. Hernandez-Segura A, de Jong T V., Melov S, Guryev V, Campisi J, Demaria M. Unmasking Transcriptional Heterogeneity in Senescent Cells. Curr Biol. Curr Biol; 2017;27(17):2652-2660.e4. DOI: 10.1016/J.CUB.2017.07.033
418. Deschênes M, Chabot B. The emerging role of alternative splicing in senescence and aging. Aging Cell. Blackwell Publishing Ltd; 2017;16(5):918. DOI: 10.1111/ACEL.12646
419. Passos JF, Saretzki G, Ahmed S, Nelson G, Richter T, Peters H, et al. Mitochondrial Dysfunction Accounts for the Stochastic Heterogeneity in Telomere-Dependent Senescence. PLoS Biol. Public Library of Science; 2007;5(5):e110. DOI: 10.1371/JOURNAL.PBIO.0050110
420. Campisi J, D'Adda Di Fagagna F. Cellular senescence: when bad things happen to good cells. Nature Reviews Molecular Cell Biology 2007 8:9. Nature Publishing Group; 2007;8(9):729–40. DOI: 10.1038/nrm2233
421. Minamino T, Miyauchi H, Yoshida T, Ishida Y, Yoshida H, Komuro I. Endothelial cell senescence in human atherosclerosis: role of telomere in endothelial dysfunction. Circulation. Circulation; 2002;105(13):1541–4. DOI: 10.1161/01.CIR.0000013836.85741.17
422. Kuilman T, Michaloglou C, Mooi WJ, Peeper DS. The essence of senescence. Genes Dev. Genes Dev; 2010;24(22):2463–79. DOI: 10.1101/GAD.1971610
423. Childs BG, Durik M, Baker DJ, Van Deursen JM. Cellular senescence in aging and age-related disease: from mechanisms to therapy. Nat Med. Nat Med; 2015;21(12):1424–35. DOI: 10.1038/NM.4000
424. D'Adda Di Fagagna F. Living on a break: cellular senescence as a DNA-damage response. Nat Rev Cancer. Nat Rev Cancer; 2008;8(7):512–22. DOI: 10.1038/NRC2440

425. Rodier F, Campisi J. Four faces of cellular senescence. J Cell Biol. J Cell Biol; 2011;192(4):547–56. DOI: 10.1083/JCB.201009094
426. Gorgoulis V, Adams PD, Alimonti A, Bennett DC, Bischof O, Bishop C, et al. Cellular Senescence: Defining a Path Forward. Cell. Cell; 2019;179(4):813–27. DOI: 10.1016/J.CELL.2019.10.005
427. Narita M, Nũnez S, Heard E, Narita M, Lin AW, Hearn SA, et al. Rb-mediated heterochromatin formation and silencing of E2F target genes during cellular senescence. Cell. Elsevier B.V.; 2003;113(6):703–16. DOI: 10.1016/S0092-8674(03)00401-X
428. Childs BG, Gluscevic M, Baker DJ, Laberge RM, Marquess D, Dananberg J, et al. Senescent cells: an emerging target for diseases of ageing. Nature Reviews Drug Discovery 2017 16:10. Nature Publishing Group; 2017;16(10):718–35. DOI: 10.1038/nrd.2017.116

Appendix A: NETosis assay de tails and supplementary data

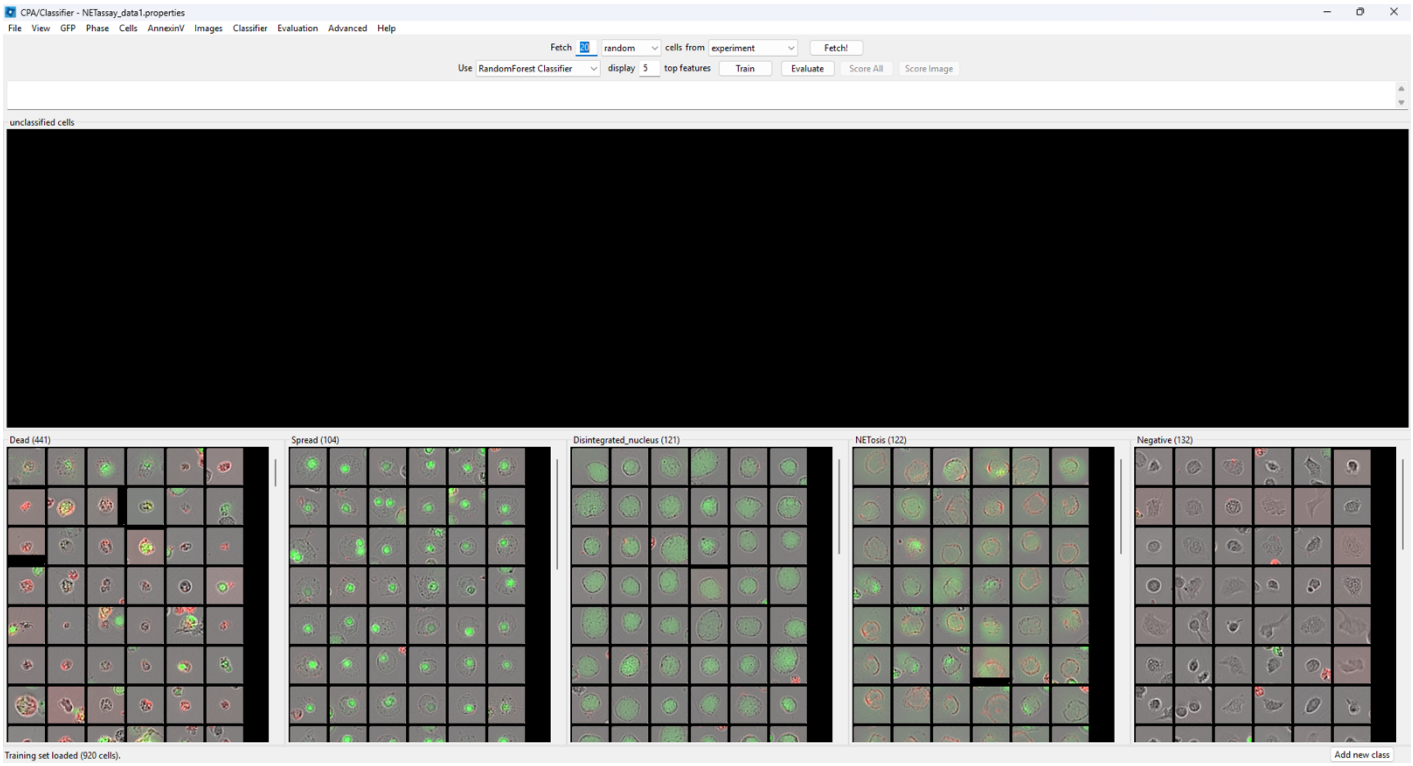

Figure A.1: CellProfiler Analyst classifier interface.

Individual cells are assigned to one of five classification bins: 1) Dead, 2) Spread, 3) Disintegrated nucleus, 4) NETosis, and 5) Negative to train a Random Forest classifier.

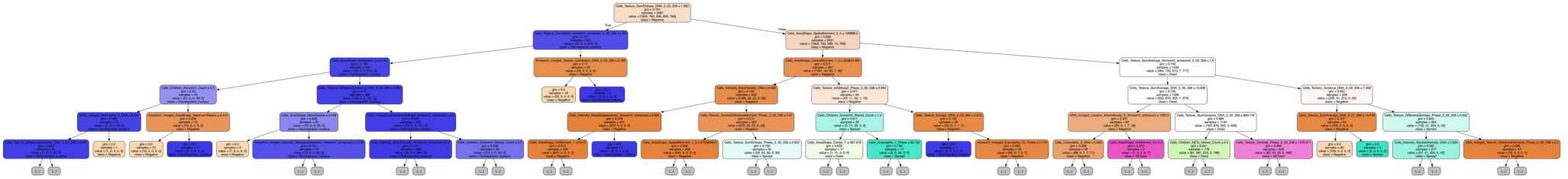

Figure A.2: Example of classifier tree used for classifying NETosis stages.

Single classification tree (maximum depth = 5) generated from the CellProfiler Analyst training datasets and associated CellProfiler-extracted features.

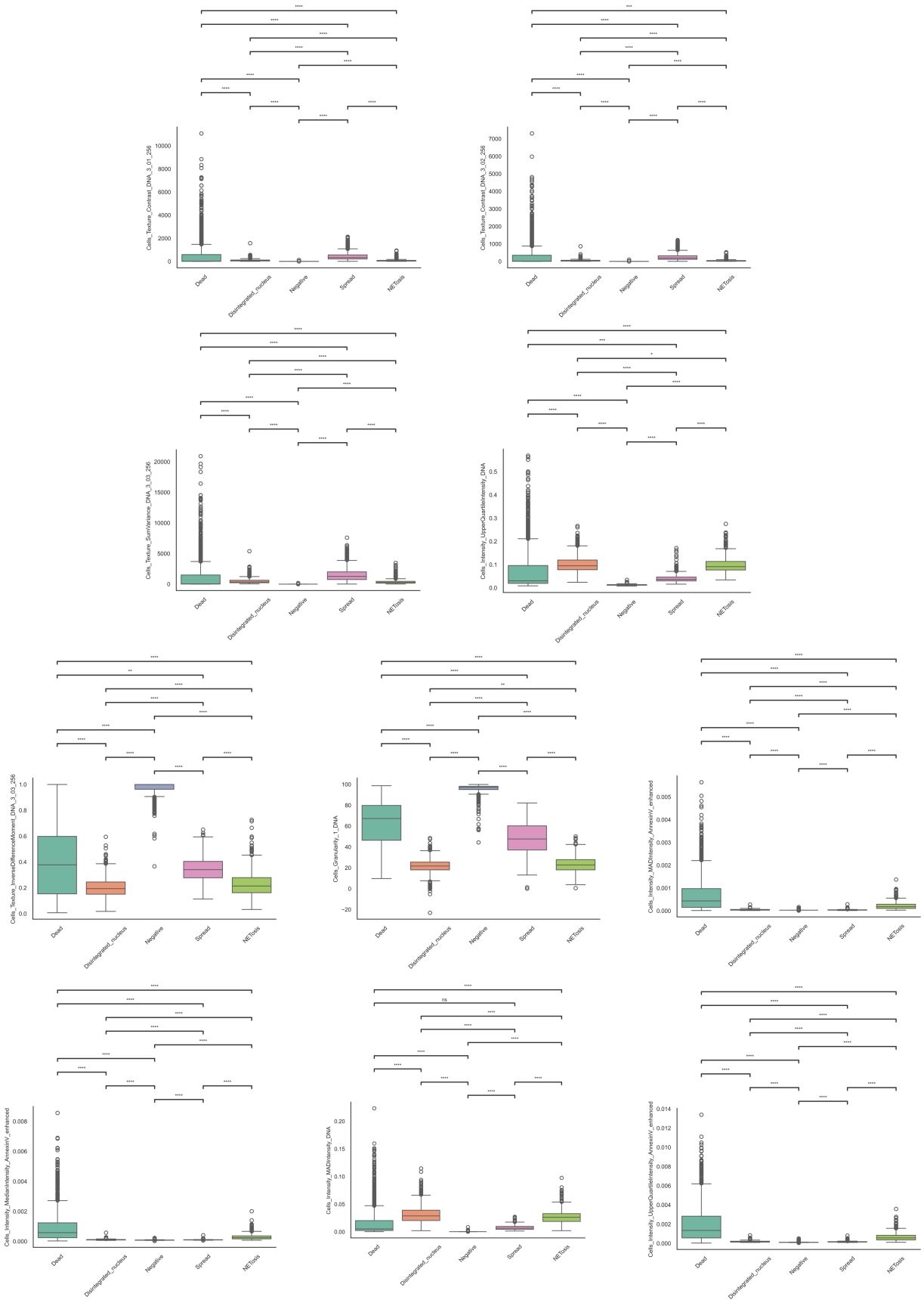

Figure A.3: Top 10 classification features for neutrophil-directed HL-60 cell sorting.

Boxplots showing the distribution of each feature across classified cell types (n = 5 experiments, N = 4,886 cells). Mann-Whitney test and Holm-Bonferroni correction performed ****p<0.0001.

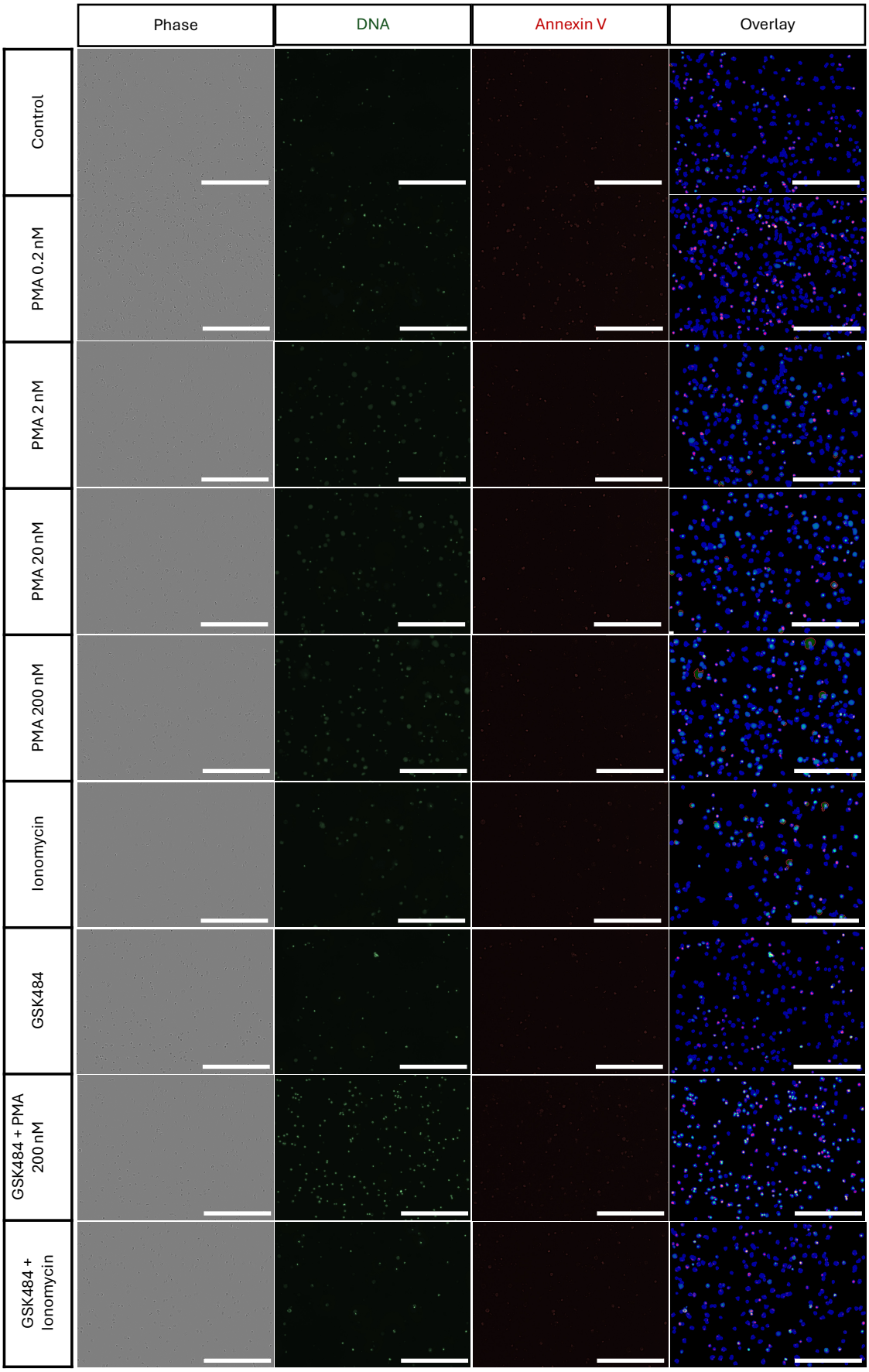

Figure A.4: Individual channel images corresponding to the overlays shown in Figures 3.11 and 3.14. Representative images are presented for each channel: 1) phase-contrast, 2) DNA (green), 3) Annexin V (red), and 4) the composite overlay. Scale bar = 30 µm.

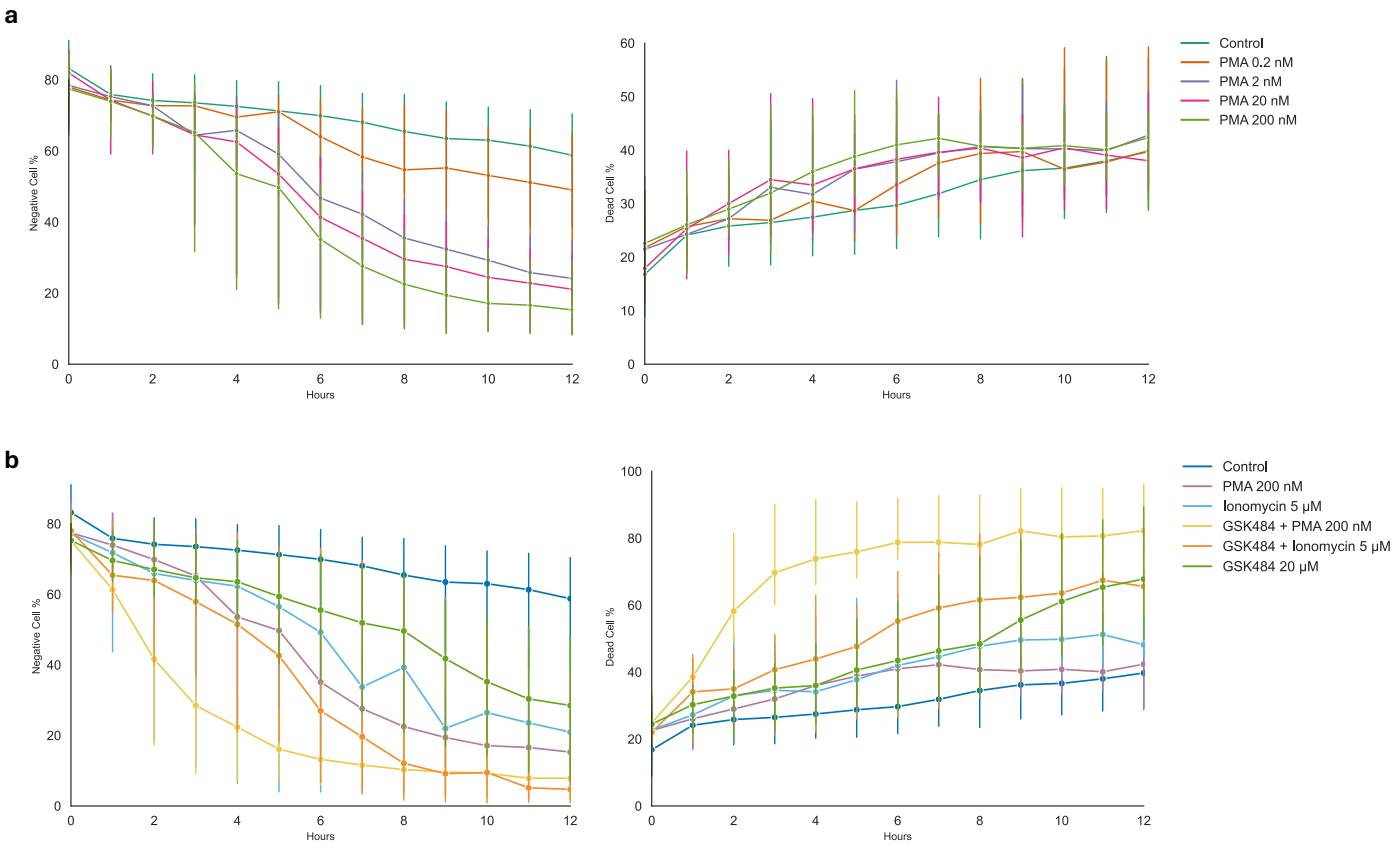

Figure A.5: Line plots of the percentage of negative and dead cells over time in dHL-60 experiments.
a, Proportions of cells with increasing PMA concentrations. **b**, Proportions of cells compared between PMA- and ionomycin-stimulated cells, with or without PAD4 inhibition with GSK484. Median proportions with 95% confidence interval are shown.

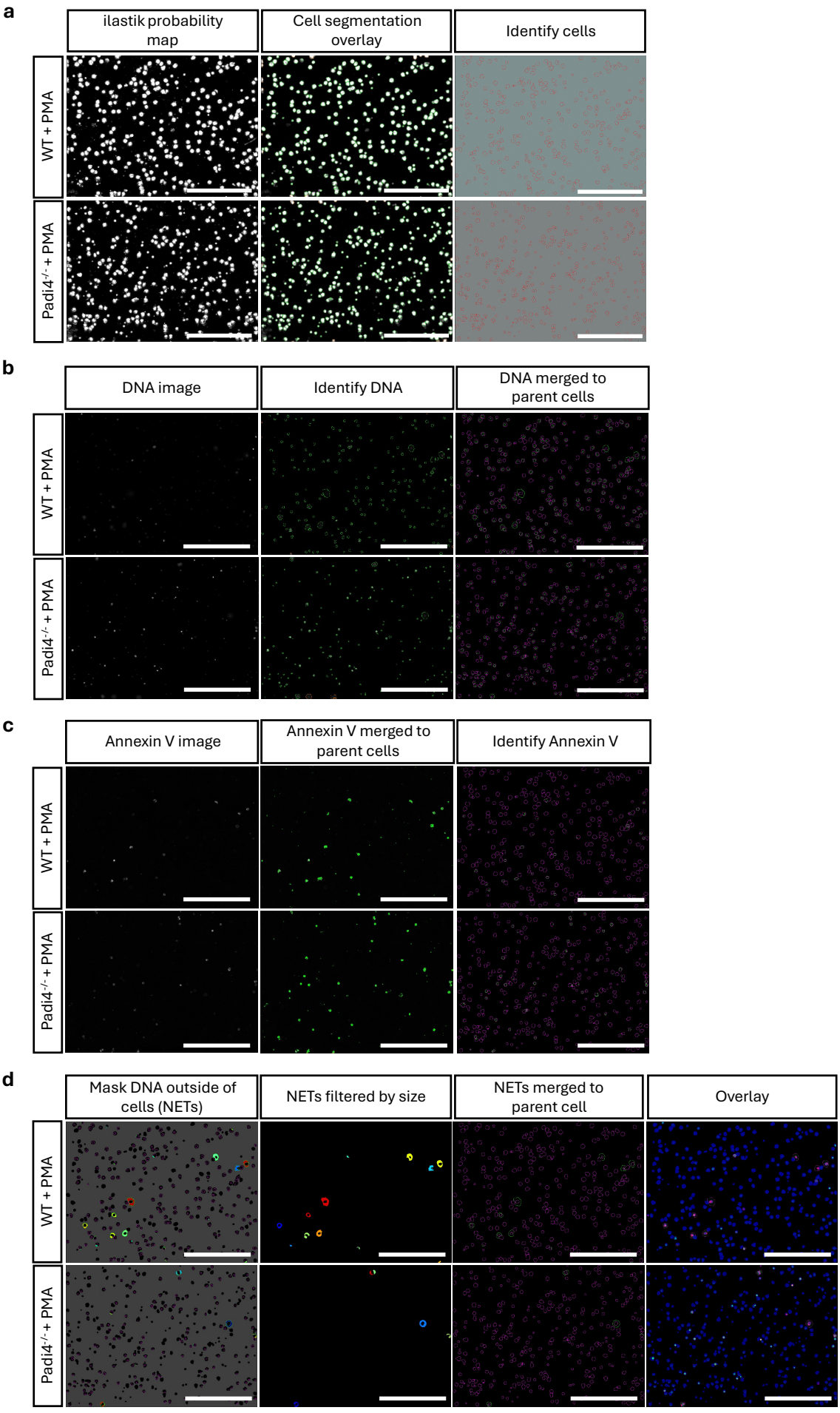
a
ilastik probability map
Cell segmentation overlay
Identify cells
WT + PMA
Padi4-/- + PMA
b
DNA image
Identify DNA
DNA merged to parent cells
WT + PMA
Padi4-/- + PMA
c
Annexin V image
Annexin V merged to parent cells
Identify Annexin V
WT + PMA
Padi4-/- + PMA
d
Mask DNA outside of cells (NETs)
NETs filtered by size
NETs merged to parent cell
Overlay
WT + PMA
Padi4-/- + PMA

Figure A.6: CellProfiler object-based segmentation and NET detection in mouse bone marrow-derived neutrophils. (a-d), Representative steps of the CellProfiler pipeline for segmenting cells, DNA, Annexin V and NETs, shown for WT and padi4$^{-/-}$ cells treated with 100 nM of PMA at 12 hours. Scale bar = 30 μm. **a**, Ilastik-generated probability maps and corresponding CellProfiler segmentations overlaid on phase contrast images. **b**, Raw green fluorescence images (DNA) image, DNA object identification by CellProfiler and mapping to parent cells. **c**, Raw red fluorescence images (Annexin V), CellProfiler-identified Annexin V-positive regions, and their association with parent cells. **d**, NET segmentation from masking of DNA areas outside of segmented cells in CellProfiler and mapping to parent cells, with resulting composite overlays showing segmented cells (blue), DNA (green) and Annexin V (red) with NETs outlined in red.

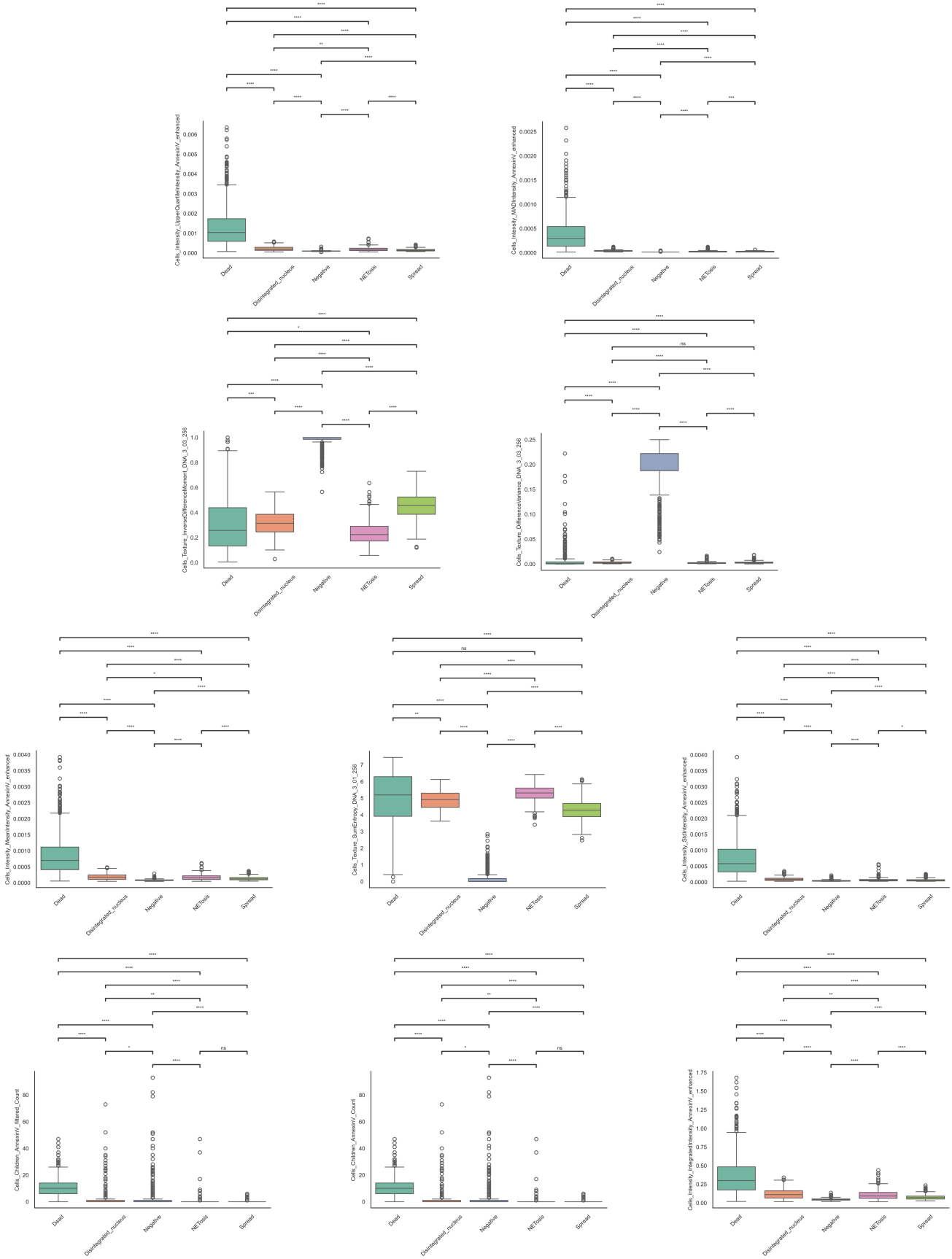

Figure A.7: Top 10 classification features for mouse bone marrow-derived neutrophil sorting.

Boxplots showing the distribution of each feature across classified cell types (n = 4 experiments, N = 2,183 cells). Mann-Whitney test and Bonferroni correction performed *P<0.05, **P<0.01, ***P<0.001, ****P<0.0001.

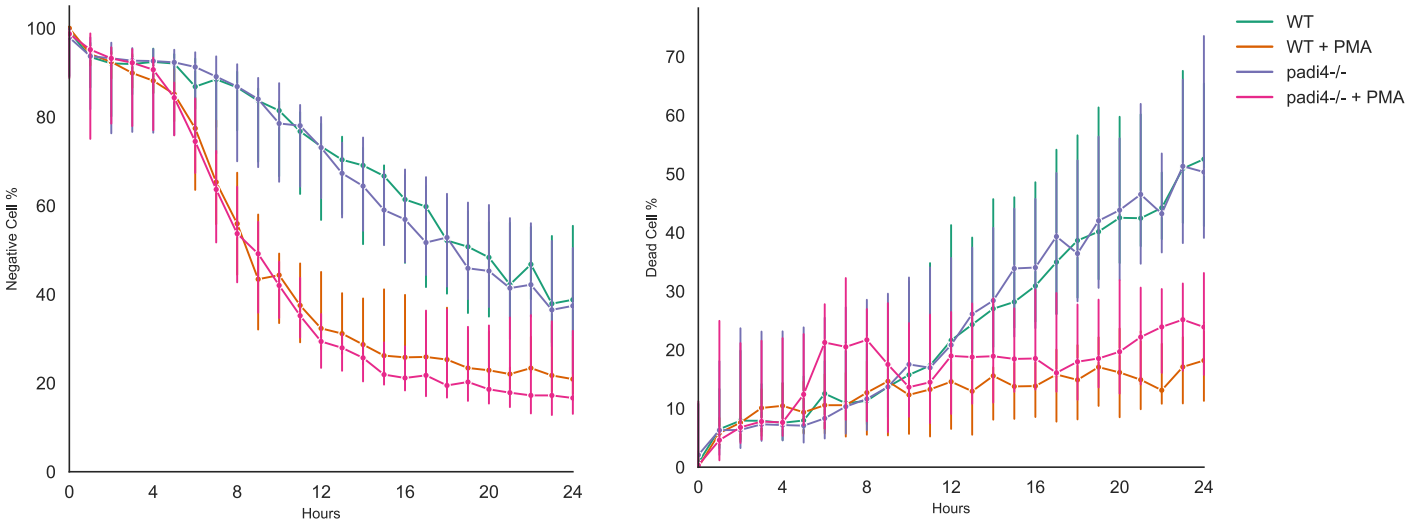

Figure A.8: Line plots of the percentage of negative and dead cells over time in bone marrow-derived neutrophil experiments.

Median proportions with 95% confidence interval are shown for WT and *Padi4*$^{-/-}$ neutrophils with or without PMA stimulation.

Appendix B: Senescence-associated gene sets for GSEA

Table B.1: Curated senescence-associated gene sets used for GSEA on NET treated ECs

Senescence-associated gene sets were curated based on established literature and used for GSEA of endothelial transcriptomic data. Listed genes represent core components of each biological theme, with references indicating the primary sources supporting gene set composition.

Gene set	Biological theme	Genes	Key references
Cell cycle regulators	Cell cycle arrest and proliferative suppression	CCND1, CCND2, CCNE1, CCNE2, CDK2, CDK4, CDK6, E2F1, E2F2, RB1, CDKN1A, CDKN2A	(420,422,423)
DDR/Checkpoint	Persistent DNA damage response and checkpoint activation	ATM, ATR, CHEK1, CHEK2, TP53, MDM2, H2AFX, RAD51, RAD50, MRE11, NBN, BRCA1, BRCA2, FANCD2, FANCI, XRCC5, XRCC6, GADD45A, GADD45B, CDKN1A, CDC25A, CDC25C, SESN1	(424–426)
SASP	Senescence-associated secretory phenotype (inflammatory and paracrine signaling)	IL1A, IL1B, IL6, CXCL8, CXCL1, CXCL2, CXCL3, CXCL10, CCL2, CCL5, CSF2, TNF, TGFB1, VEGFA, ICAM1, VCAM1, SELE, MMP1, MMP3, MMP9, SERPINE1, IGFBP3, IGFBP7, PLAUR, PTGS2, FOS, JUN, STAT3, NFKB1, RELA, CEBPB, CEBPD, SOD2, NOX4, TGFB2, TGFB3, EDN1, ANGPT2	(363,366,407)
Endothelial/chromatin remodeling	Endothelial senescence identity and chromatin remodeling	HMGA1, HMGA2, EZH2, SUZ12, EED, BMI1, CBX7, CBX8, SUV39H1, SETDB1, KDM6B, KDM5A, KDM5B, DNMT1, DNMT3A, DNMT3B, HIST1H1C, HIST1H1D, HIST1H2AC, HIST1H2BD, HIST1H3A, HIST1H4A, LBR, LMNA, LMNB1, LMNB2, SP100, PML, ATRX, DAXX, FOXO1, KLF2, KLF4, NOS3, VCAM1, ICAM1, SELE, TGFB1, THBS1, ANGPT2	(417,427,428)